Composition- structure and size/shape-controlled synthesis and characterization of high coercivity ferrite nanocrystals

by

Yarilyn Cedeño-Mattei

A dissertation submitted in partial fulfillment of the requirements for the degree of

DOCTOR OF PHILOSOPHY
in
APPLIED CHEMISTRY
(Chemistry of Materials)

UNIVERSITY OF PUERTO RICO
MAYAGÜEZ CAMPUS
2010

Approved by:

Félix Román, PhD Member, Graduate Committee	Date
Enrique Meléndez, PhD Member, Graduate Committee	Date
Carlos Rinaldi, PhD Member, Graduate Committee	Date
Oscar Perales-Pérez, PhD President, Graduate Committee	Date
Pedro Quintero, PhD Representative of Graduate Studies	Date
Francis Patrón, PhD Chairperson of the Department	Date

ABSTRACT

Cobalt ferrite ($CoFe_2O_4$) possesses excellent chemical stability, good mechanical hardness and a large positive first order magnetocrystalline anisotropy constant, making it a promising candidate for magneto-optical recording media. In addition to precise control of the composition and structure of $CoFe_2O_4$, its practical application will require the capability to control particle size at the nanoscale.

It has been well-established that a fine tuning in cobalt ferrite nanocrystals size within the magnetic single domain region would lead to the achievement of extremely high coercivity values at room-temperature. The development of a size-sensitive phase separation method for cobalt ferrite nanocrystals that is based on selective dissolution of the superparamagnetic fraction and subsequent size-sensitive magnetic separation of single-domain nanoparticles is presented. The attained colossal room temperature coercivity value of 11.9 kOe was mainly attributed to the enlargement of the average crystal size within the single domain region coupled with the removal of the superparamagnetic fraction in the ferrite powders. The strong influence of crystal size, ferrite composition, cations distribution in the ferrite lattice and lattice distortion on the corresponding magnetic properties at the nanoscale, was also confirmed.

The superparamagnetic and magnetic single domain limits were experimentally determined by synthesizing extremely small (4 nm) and large (over 100 nm) single crystals of cobalt

ferrite. The first ones were produced using sodium oleate in-synthesis whereas the large crystals were produced by thermal treatment of starting 16 nm cobalt ferrite nanocrystals.

RESUMEN

La ferrita de cobalto ($CoFe_2O_4$) posee excelente estabilidad química, adecuada resistencia mecánica así como una alta y positiva constante de anisotropía magnetocristalina, lo que la convierte en un candidato prometedor para ser usado en sistemas de grabación magneto-ópticos. Además de un control preciso en la composición y estructura de $CoFe_2O_4$, su aplicación práctica dependerá de la capacidad de controlar el tamaño de partícula de esta ferrita a la nanoescala.

Se entiende que solo un fino control en el tamaño de nanocristales de ferrita de cobalto dentro de la región de monodominios magnéticos permitiría la obtención de valores de coercividad extremadamente altos a temperatura ambiente. El desarrollo de un método para la separación por tamaños de los nanocristales de ferrita de cobalto, basado en la disolución selectiva de la fracción superparamagnética y la subsecuente separación magnética sensitiva a tamaños de nanopartículas monodominio, es presentado. La altísima coercividad obtenida a temperatura ambiente, 11.9 kOe, fue principalmente atribuida al incremento del tamaño promedio del cristal en la región de monodominios en adición a la eliminación de la fracción superparamagnética en la ferrita. La gran influencia del tamaño de cristal, composición de la ferrita, distribución de cationes en la celda unitaria y la distorsión de esta celda, sobre las propiedades magnéticas correspondientes a escala nanométrica, también fue confirmado.

Los limites superparamagnético y de monodominios magnéticos se determinaron experimentalmente mediante la síntesis de monocristales de ferrita de cobalto extremadamente pequeños (4 nm) y de mayor tamaño (100 nm +). Los primeros fueron sintetizados mediante el uso de oleato de sodio durante la síntesis, en tanto que los cristales de mayor tamaño fueron producidos mediante el tratamiento térmico de nanocristales con un tamaño promedio inicial de 16 nm.

Copyright © by
Yarilyn Cedeño-Mattei
2010

.

Dedicated to my family . . .

my parents *Marilyn* and *Félix*,

my husband *Andrés Felipe*,

my sister *Marieli* and my brother *Félix Javier*

…for their unconditional love and support.

ACKNOWLEDGEMENTS

My graduate studies at the University of Puerto Rico have been possible thanks to the support, collaboration and advice of some persons and institutions. This is why I want to dedicate this section to express my gratitude to them.

First of all, I want to express my gratitude to my advisor, Dr. Oscar Perales-Pérez for his trust and guidance across these years of study and research.

I want to thank everyone that allowed me access to their characterization facilities:

Dr. Carlos Rinaldi for the SQUID measurements.

Dr. Oswald Uwakweh for the High-energy ball milling equipment and Mössbauer Spectroscopy measurements and analyses.

Dr. Félix Román and Diana Sánchez for the ICP measurements.

Dr. Mauricio Cabrera, Matilde Sánchez, and Yareni Patricia Lara for their help on the development and analysis of the experimental design.

Dr. Samuel Hernandez and Eduardo Espinosa for FT-IR measurements.

Dr. Yan Xin and Dr. Andrew Ozarowski, from the National High Magnetic Field Laboratory, for the Transmission Electron Microscopy and Mössbauer Spectroscopy facilities.

Dr. Paul Voyles and Dr. Mark Rzchowski, from the University of Wisconsin – Madison, for allowing me to work in their facilities during the four months internship.

I also want to acknowledge my friends and coworkers from the Nanomaterials Processing Laboratory.

I am also grateful with all the persons and institutions that supported this research project: Dr. Marcelo Suárez and the Synergistic Partnership for Research and Education on Functional and Nanostructured Materials (PREM); Dr. Manuel Gómez and the NSF-EPSCoR Institute for Functional Nanomaterials Fellowship (IFN); the Department of Energy Savanna River Research Scholarship (UPRM/DoE-SR), the Alfred P. Sloan Foundation Graduate Scholarship Program, in addition to the Department of Engineering Science and Materials and the Department of Chemistry of the University of Puerto Rico, Mayagüez Campus.

Table of Contents

ABSTRACT ..... **II**

RESUMEN ..... **IV**

ACKNOWLEDGEMENTS ..... **VIII**

TABLE OF CONTENTS ..... **X**

TABLE LIST ..... **XIII**

FIGURE LIST ..... **XVI**

1 INTRODUCTION **2**

1.1 MOTIVATION AND JUSTIFICATION 2
1.2 OBJECTIVES 5
1.2.1 Main Objective *5*
1.2.2 Specific Objectives *5*
1.3 DISSERTATION CONTENTS 6

2 THEORETICAL BACKGROUND **7**

2.1 FUNDAMENTALS OF MAGNETISM 7
2.2 MAGNETIC BEHAVIORS 8
2.2.1 Diamagnetism *8*
2.2.2 Paramagnetism *9*
2.2.3 Ferro- and Ferri- magnetism *10*
2.2.4 Antiferromagnetism *12*
2.2.5 Superparamagnetism *12*
2.3 MAGNETIC DOMAINS 13
2.3.1 Single Magnetic Domains *13*
2.3.2 Magnetic Multi-domains *14*
2.4 MAGNETIC HYSTERESIS 16
2.4.1 Coercivity *17*
2.4.2 Saturation Magnetization *18*
2.4.3 Remanence *20*
2.4.4 Squareness ratio *20*
2.4.5 Magnetic Anisotropy *20*
2.5 FERRITES 23
2.5.1 Spinel structure of the ferrite *23*
2.5.2 The cobalt ferrite *27*
2.6 CRYSTALS NUCLEATION AND GROWTH PROCESSES 29
2.7 MAGNETIC PROPERTIES AND PARTICLE SIZE 31
2.8 FUNDAMENTALS OF EXPERIMENTAL DESIGN APPLIED TO MAGNETIC PROPERTIES OF MATERIALS 33

3 LITERATURE REVIEW **37**

3.1 FERRITE SYNTHESIS 37

3.1.1 Cobalt ferrite synthesis: Possibilities and Limitations *37*
3.2 FERRITES AND DATA STORAGE SYSTEMS 41
3.2.1 Current status *41*
3.2.2 Limitations and Challenges *43*

4 METHODOLOGY 45

4.1 EXPERIMENTAL PROCEDURES 45
4.1.1 Materials *45*
4.1.2 Conventional coprecipitation method *46*
4.1.3 Modified coprecipitation method *48*
4.1.4 Combined acid-washing and magnetically-assisted size-sensitive separation *48*
4.1.5 Effect of the ferrite composition *51*
4.1.6 Heterogeneous nucleation experiments: Seed-mediated growth *51*
4.1.7 Size reduction by high-energy ball milling *52*
4.1.8 Shape modification by hydrothermal synthesis *54*
4.1.9 Post-synthesis thermal treatment of ferrite powders *56*
4.1.10 Inhibition of crystal growth by using surfactants or polymers *56*
4.2 CHARACTERIZATION TECHNIQUES 58
4.2.1 X-Ray Diffractometry (XRD) *58*
4.2.2 Vibrating Sample Magnetometry (VSM) *61*
4.2.3 The Semiconducting Quantum Interference Device (SQUID) *63*
4.2.4 Scanning Electron Microscopy (SEM) *64*
4.2.5 High-Resolution Transmission Electron Microscopy (HR-TEM) and its analytical techniques: Electron Diffraction (ED) and Energy Dispersive X-Ray Spectroscopy (EDS) *66*
4.2.6 Surface Area Analyzer (BET) *68*
4.2.7 Mössbauer Spectroscopy *70*

5 RESULTS AND DISCUSSION 73

5.1 OPTIMIZATION OF SYNTHESIS PARAMETERS 73
5.1.1 Reaction time *73*
5.1.2 Effect of flow-rate at which the reactants are mixed *77*
5.1.3 Effect of NaOH concentration *81*
5.1.4 Experimental design *84*
5.2 COMBINED ACID-WASHING AND MAGNETICALLY-ASSISTED SIZE-SENSITIVE SEPARATION 93
5.2.1 Single acid washing process *94*
5.2.2 Double acid washing process *104*
5.3 EFFECT OF THE FERRITE COMPOSITION 111
5.3.1 Variation of the Fe:Co mole ratio *111*
5.3.2 Transition metals-substituted cobalt ferrite *131*
5.3.3 Co substitution by Mn species *131*
5.3.4 Co substitution by Ni species *136*
5.4 HETEROGENEOUS NUCLEATION SEED-MEDIATED CRYSTAL GROWTH 142
5.4.1 Effect of the ferrite/seed weight ratio, 'r' *142*
5.4.2 Seeding and re-seeding experiments at 'r'=1.0 and flow-rate controlled synthesis conditions *148*
5.4.3 Seeding-assisted synthesis of Ni-substituted cobalt ferrite ('r'=1.0) *151*
5.5 CRYSTAL SIZE REDUCTION BY HIGH-ENERGY 155
5.5.1 Effect of high-intensity ball milling time on structural, specific surface area and magnetic properties of cobalt ferrite powders *156*
5.6 SHAPE MODIFICATION BY HYDROTHERMAL SYNTHESIS 169
5.6.1 Comparison between nanoparticles synthesized by coprecipitation and hydrothermal processes... ..... *174*

5.7 POST-SYNTHESIS THERMAL TREATMENT OF FERRITE POWDERS 177
5.8 INHIBITION OF CRYSTAL GROWTH: USE OF SURFACTANTS OR POLYMERS DURING THE FERRITE CRYSTAL FORMATION 183
5.8.1 Effect of the type of surfactant 185
5.8.2 Synthesis of superparamagnetic particles by inhibition of crystal growth using Na-oleate 188
5.9 ZFC/FC AND M-T MEASUREMENTS AS A FUNCTION OF FERRITE CRYSTAL SIZE 195
5.10 REVISITED DEPENDENCE OF COERCIVITY WITH PARTICLE SIZE 204

6 REFERENCES 208

APPENDIX A 214

Table List

Tables **Page**

TABLE 1: Magnetic moments of some simple ferrites (magnetic moment [μ_B]). 19
TABLE 2: Magnetocrystalline anisotropy constant of some ferrites. 22
TABLE 3: Angles in the spinel structure for the different types of lattice site interactions.. 25
TABLE 4: Interionic distances in the spinel structure for the different types of lattice site interactions. 25
TABLE 5: Ionic radius of metal ions in spinel ferrites. 26
TABLE 6: Lattice parameter of some cubic ferrites. 27
TABLE 7: Main requirements for high-density recording media. 44
TABLE 8: Surfactants and their chemical structure. 57
TABLE 9: Lattice parameter, 'a', and average crystallite size, 't', for $CoFe_2O_4$ powders synthesized at different reaction times. 74
TABLE 10: Coercivity and magnetization for ferrite nanocrystals synthesized at different reaction times. 77
TABLE 11: Lattice parameter, 'a', and average crystallite size, 't', for $CoFe_2O_4$ nanoparticles synthesized at different flow rates of the addition of reactants. 79
TABLE 12: Coercivity and magnetization values corresponding to the ferrite nanocrystals synthesized at different flow rates. The reaction time was 60 minutes. 80
TABLE 13: Lattice parameter, 'a', and average crystallite size, 't', for $CoFe_2O_4$ nanoparticles synthesized at different NaOH concentrations. 82
TABLE 14: Coercivity, H_c, and magnetization, M_{max}, values corresponding to the ferrite nanocrystals synthesized at different NaOH concentrations. The reaction time was 60 minutes. 84
TABLE 15: Low and high levels employed in the 2^3 factorial design. 85
TABLE 16: Experimental conditions for the 2^3 factorial design and the corresponding response: room-temperature coercivity, H_c. 86
TABLE 17: P-values corresponding to the analysis of CCF, CCI, and CCF + CCI experimental designs. 89
TABLE 18: Structural properties of the sample submitted to the acid treatment and magnetically-assisted separation stages (1st and 2nd cycle). 109
TABLE 19: Magnetic properties of the sample submitted to the acid treatment and magnetically-assisted separation stages (1st and 2nd cycle). 109
TABLE 20: Average crystallite size, 't', and lattice parameter, 'a', of cobalt ferrite synthesized at various Fe:Co mole ratios with and without control of the flow-rate. .. 114
TABLE 21: Summary of Fe:Co mole ratios of cobalt ferrite synthesized with and without control on flow-rate. 116

TABLE 22: Coercivity, H_c, and maximum magnetization, M_{max}, of cobalt ferrite synthesized with and without control on flow-rate. 120
TABLE 23: Mössbauer parameters for sample synthesized at 2:1 Fe:Co mole ratio and 0.67 mL/min flow-rate. 124
TABLE 24: Mössbauer parameters for sample synthesized at 1.7:1 mole ratio and 0.67 mL/min flow-rate. 125
TABLE 25: Mössbauer parameters for sample synthesized at 1.4:1 mole ratio and 0.67 mL/min flow-rate. 128
TABLE 26: Mössbauer parameters for sample synthesized at 1.4:1 mole ratio without control on flow-rate. 129
TABLE 27: Average crystallite size, 't', and lattice parameter, 'a' of Mn-substituted cobalt ferrite. 133
TABLE 28: Coercivity, H_c, maximum magnetization, M_{max}, and squareness ratio of Mn-substituted cobalt ferrite powders synthesized at different 'x' values. 135
TABLE 29: Average crystallite size, 't', and lattice parameter, 'a' in Ni-substituted cobalt ferrite nanocrystals. 137
TABLE 30: Summary of magnetic properties of Ni-substituted cobalt ferrite powders. 139
TABLE 31: Average crystallite size, 't', and lattice parameter, 'a', in cobalt ferrite nanocrystals after seeding and re-seeding processes at different 'r' values. 144
TABLE 32: Coercivity, H_c, and magnetization, M_{max}, values of cobalt ferrite nanocrystals treated by seeding and re-seeding cycles at different 'r' values. 146
TABLE 33: Average crystallite size, 't', and lattice parameter, 'a', of cobalt ferrite nanocrystals treated by seeding and re-seeding (r = 1.0) at 0.81 mL/min. 149
TABLE 34: Coercivity, H_c, and magnetization, M_{max}, values of cobalt ferrite nanocrystals treated by seeding and re-seeding cycles at different 'r' values and 0.81 mL/min. 150
TABLE 35: Average crystallite size, 't', and lattice parameter, 'a', of Ni-doped cobalt ferrite nanocrystals (y = 0.7) submitted to seeding and re-seeding processes at 'r' = 1.0..... 152
TABLE 36: Coercivity, H_c, and magnetization, M_{max}, values of Ni-substituted cobalt ferrite (y = 0.7) treated by seeding and re-seeding cycles at 'r' = 1.0. 154
TABLE 37: Variation in average crystallite size, 't', lattice parameter, 'a', and specific surface area (SSA) measurements of ball-milled cobalt ferrite nanocrystals with initial average crystallite size of 12 nm. 160
TABLE 38: Variation in average crystallite size and surface area as a function of milling time of 12 nm-cobalt ferrite. The dot line shown in the figure is a visual guide to show the decreasing trend in both, average crystallite size and SSA. 161
TABLE 39: Coercivity, H_c, and maximum magnetization, M_{max}, of cobalt ferrite submitted to high-energy ball milling. The initial average crystallite size was 12 nm. 165
TABLE 40: Coercivity, H_c, and maximum magnetization, M_{max}, of cobalt ferrite submitted to high-energy ball milling. The initial average crystallite size was 18 nm. 167
TABLE 41: Summary of structural properties of cobalt ferrite powders produced by the hydrothermal process. 171

TABLE 42: Summary of magnetic properties of cobalt ferrite synthesized by the hydrothermal process. 174
TABLE 43: Comparison between main features of the nanoparticles synthesized by conventional coprecipitation and hydrothermal processes. 175
TABLE 44: Lattice parameter of cobalt ferrite nanocrystals submitted to thermal treatment in air. 178
TABLE 45: Summary of magnetic properties of cobalt ferrite nanocrystals submitted to thermal treatment in air. 181
TABLE 46: Average crystallite size, ‘t’, and lattice parameter, ‘a’, of cobalt ferrite nanocrystals produced using different types of surfactants. 186
TABLE 47: Magnetic properties of cobalt ferrite synthesized using different types of surfactants. 187
TABLE 48: Magnetic properties of cobalt ferrite nanocrystals produced with and without Na-oleate. 192
TABLE 49: Magnetic properties of cobalt ferrite with different crystal sizes measured at 2 K and 300 K. 200
TABLE 50: Demagnetization temperature, T_d, of cobalt ferrite with different crystal sizes. The external magnetic field was 5000 Oe. 201

Figure List

Figures **Page**

Figure 1: Applications of ferrites. 3
Figure 2: Origin of magnetism. 7
Figure 3: Diamagnetic response in absence or presence of an external magnetic field. 8
Figure 4: Paramagnetic response in absence or presence of an external magnetic field. 9
Figure 5: Ferromagnetic response in absence or presence of an external magnetic field..... 10
Figure 6: Ferrimagnetic response in absence or presence of an external magnetic field. 11
Figure 7: Distribution of spin magnetic moments for Fe^{3+} and Co^{2+} in a unit cell of $CoFe_2O_4$. The arrow represents the magnetic moment orientation of each cation. 11
Figure 8: Antiferromagnetic response in absence or presence of an external magnetic field. 12
Figure 9: Scheme of a magnetic single domain. 13
Figure 10: Scheme of a magnetic multi-domains. 15
Figure 11: Magnetic hysteresis loop. 17
Figure 12: The spinel structure. 24
Figure 13: Tetrahedral site (left) and octahedral site (right) in the spinel structure. 24
Figure 14: Cations arrangement in the lattice interstices of cobalt ferrite. 28
Figure 15: Nucleation and growth processes. 29
Figure 16: Dependence of coercivity with particle diameter for cobalt ferrite. 32
Figure 17: Experimental points for a 2^3 factorial design. 34
Figure 18: Different functional layers of perpendicular recording medium. 42
Figure 19: General Experimental Scheme: *The Coprecipitation Method* 47
Figure 20: The acid-washing treatment stage. 49
Figure 21: The magnetically-assisted separation. 49
Figure 22: Images of the different fractions after the acid treatment and magnetically-assisted separation stages. 50
Figure 23: IKA T-8 basic homogenizer used to re-disperse the seeds in aqueous solution. . 52
Figure 24: Fritsch Pulverisette-4 milling media (top) and the tungsten carbide jars, balls used for the milling of cobalt ferrite nanocrystals (center), and the three types of impacts involved in the milling process (bottom). 54
Figure 25: Autoclave reactor used for synthesis of cobalt ferrite by the hydrothermal method. 55
Figure 26: Schematic image of the 4575 model HP/HT Pressure Reactor from Parr Instruments Company. 55
Figure 27: The diffraction phenomenon. 58
Figure 28: Siemens D500 X-Ray Diffractometer. 60

Figure 29: LakeShore 7400 Series Vibrating Sample Magnetometer (top) and schematic diagram of a vibrating sample magnetometer (bottom). 62
Figure 30: Quantum Design MPMSXL Superconducting Quantum Interference Device (top) and the general scheme of the device (bottom). 64
Figure 31: JEOL model JSM-5410 LV Scanning Electron Microscope (top) and general scheme of a scanning electron microscope (bottom). 65
Figure 32: JEOL 2011 Transmission Electron Microscope (top) and general scheme of a transmission electron microscope (bottom). 68
Figure 33: Horiba SA – 9600 series Surface Area Analyzer. 70
Figure 34: WEBRES spectrometer operating in the transmission mode, with a 50 mCi ^{57}Co source in a Rh matrix from Ritverc, GmbH (top) and the basic scheme of a Mössbauer spectrometer (bottom). 72
Figure 35: XRD patterns for $CoFe_2O_4$ powders synthesized at different reaction times with no control of flow-rate. 74
Figure 36: TEM pictures for $CoFe_2O_4$ nanoparticles produced after 5 minutes (a), and 60 minutes (b) of reaction. The flow-rate was 10 mL/min. (c) TEM-ED pattern for $CoFe_2O_4$ nanoparticles synthesized after 10 minutes of reaction. 75
Figure 37: M-H plots (a) and loops (b) at 300K for $CoFe_2O_4$ synthesized at different reaction times with no control of flow-rate. 76
Figure 38: XRD patterns for $CoFe_2O_4$ powders synthesized at different flow rates. The reaction time was 60 minutes. 78
Figure 39: M-H loops at 300K for $CoFe_2O_4$ synthesized at different flow-rates. The reaction time was 60 minutes. 79
Figure 40: Cobalt ferrite coercivity and average crystallite size as function of flow rate. 81
Figure 41: XRD patterns for $CoFe_2O_4$ powders synthesized at different NaOH concentrations. The reaction time was 60 minutes. 82
Figure 42: M-H loops at 300K for $CoFe_2O_4$ synthesized at different NaOH concentrations. The reaction time was 60 minutes. 83
Figure 43: M-H loops at 300K for $CoFe_2O_4$ synthesized at different flow-rates (0.85 mL/min, combination ‘a’, or 20 mL/min, combination ‘ab’). The corresponding reaction time and NaOH concentration were 180 minutes and 0.34M, respectively. 86
Figure 44: 2^3 factorial design collapsed to 2^2 factorial design. 87
Figure 45: Contour plot of the collapsed 2^2 factorial design. 87
Figure 46: Experimental combinations for the additional experimental designs. 88
Figure 47: Contour plot of the CCF + CCI experimental design. 90
Figure 48: Experimental points for the maximization of coercivity experiments. 91
Figure 49: XRD patterns of $CoFe_2O_4$ powders before (a) and after acidic treatment with 10% HCl followed by magnetically-assisted separation. The patterns correspond to the solids contained in the fractions collected after 4 minutes, (b), and 6 minutes, (c), of magnetic separation and the sediment at the end of this stage, (d). 95

Figure 50: TEM images of $CoFe_2O_4$ powders before, (a), and after acidic treatment with 5% HCl v/v, (b,) or 10% HCl v/v, (c), followed by magnetically-assisted separation for 6 minutes. 97
Figure 51: TEM images of $CoFe_2O_4$ powders before, (a), and after acidic treatment with 10% HCl followed by magnetically-assisted separation at different times (b-e). The images correspond to the solids contained in the fractions collected after 2 minutes, (b), 4 minutes, (c), and 6 minutes, (d), of magnetic separation and the sediment at the end of this stage, (e). 98
Figure 52: Electron diffraction pattern (ED) and High-resolution TEM image of a 16 nm cobalt ferrite nanocrystal showing high crystallinity. 99
Figure 53: Room-temperature M-H loops of $CoFe_2O_4$ powders before and after acidic treatment followed by magnetically-assisted separation for 6 minutes. The HCl concentrations for the acidic treatment of the samples were 5% v/v and 10% v/v. 101
Figure 54: Room-temperature Mössbauer spectrum of the $CoFe_2O_4$ powders without acidic treatment, (a). The spectrum in (b) corresponds to the sample recovered at the end of the acidic treatment (HCl 10 % v/v) and magnetic separation stages. 103
Figure 55: XRD patterns of $CoFe_2O_4$ powders before, (a), and after acidic treatment with 10% HCl followed by magnetically-assisted separation. The patterns correspond to the solids contained in the fractions collected after 2 minutes, (b), 4 minutes (c), and 6 minutes, (d) of magnetic separation. 105
Figure 56: Room temperature M-H measurements of $CoFe_2O_4$ powders before (a) and after acidic treatment with 10% HCl followed by magnetically-assisted separation. The patterns correspond to the solids contained in the fractions collected after 2 minutes, (b), 4 minutes (c), and 6 minutes, (d) of magnetic separation. 106
Figure 57: XRD patterns of $CoFe_2O_4$ powders submitted to two cycles of acid treatment and magnetically-assisted separation stages. Sample (a) corresponds to the ferrite before treatment, sample (c) corresponds to the second fraction of the first cycle, samples (e) and (f) are the fractions obtained after the second cycle of the size-sensitive phase separation. Average crystallite sizes of 16 nm and 23 nm were obtained for the sample before and after the two cycles of size-sensitive phase separation, respectively. 107
Figure 58: Room temperature M-H measurements of $CoFe_2O_4$ powders submitted to two cycles of acid treatment and magnetically-assisted separation stages. 108
Figure 59: XRD patterns of cobalt ferrite nanocrystals synthesized without control on flow-rate at different Fe:Co mole ratios. The peak with the asterisk corresponds to hematite, α-Fe_2O_3 (entry # *00-03-0800 from Match!* software). 113
Figure 60: XRD patterns of cobalt ferrite nanocrystals synthesized at 0.67 mL/min and various Fe:Co mole ratios. 113
Figure 61: TEM images of cobalt ferrite nanocrystals produced with, (a), and without, (b), the flow-rate. The Fe:Co mole ratio was 1.4:1. 115
Figure 62: TEM images of cobalt ferrite nanocrystals synthesized without control on flow-rate at different Fe:Co mole ratios: 1.4:1 (a), 1.7:1 (b), and 2:1 (c). 115

Figure 63: Room temperature M-H loops of cobalt ferrite nanocrystals produced without control on flow-rate and different Fe:Co mole ratios. The inset shows the loops around the origin. 118
Figure 64: Room temperature M-H loops of cobalt ferrite nanocrystals synthesized at 0.67 mL/min and different Fe:Co mole ratios. The inset shows the loops around the origin. 119
Figure 65: Room temperature M-H loops of cobalt ferrite nanocrystals synthesized under controlled, (a), and non-controlled flow-rate conditions, (b). The Fe:Co mole ratio was 1.7:1. The inset shows the loops around the origin..... 120
Figure 66: Unfitted Mössbauer spectra of cobalt ferrite nanocrystals synthesized at 0.67 mL/min and Fe:Co mole ratios of 1.4:1, (a), 1.7:1, (b), and 2:1, (c). 123
Figure 67: Fitted Mössbauer spectra corresponding to cobalt ferrite nanocrystals synthesized at 0.67 mL/min and nominal Fe:Co mole ratios of 2:1, (a,) and 1.7:1, (b). The green, blue, cyan, and magenta fittings correspond to sites 1, 2, 3, and 4, respectively. 124
Figure 68: Unfitted Mössbauer spectra of cobalt ferrite nanocrystals produced at 1.4:1 Fe:Co mole ratio and 0.67 mL/min, (a), and without control of the flow-rate, (b). 127
Figure 69: Fitted spectra with the sub-sites indicated. The sub-sites are listed arranged from the last to the first from top to bottom. They correspond to cobalt ferrite nanocrystals produced at a nominal Fe:Co mole ratio of 1.4:1, controlling (a) and not controlling (b) the flow-rate. The green, blue, cyan, and magenta fittings correspond to Site 1, 2, 3, and 4, respectively. 128
Figure 70: XRD patterns of Mn-substituted cobalt ferrite powders synthesized at different Mn atomic fraction, ‘x’, values..... 132
Figure 71: Variation of lattice parameter with Mn atomic fraction in cobalt ferrite. 133
Figure 72: Room temperature M-H loops for Mn-substituted cobalt ferrite synthesized at different Mn atomic fractions, ‘x’..... 134
Figure 73: Variation in coercivity and maximum magnetization as a function of Mn atomic fraction, ‘x’. 135
Figure 74: XRD patterns of Ni-substituted cobalt ferrite at different Ni atomic fraction, ‘y’, values. 137
Figure 75: Variation of lattice parameter, ‘a’, as a function of Ni atomic fraction, ‘y’..... 138
Figure 76: Room temperature M-H loops of Ni-substituted cobalt ferrite at different Ni atomic fractions, ‘y’. 139
Figure 77: Variation in coercivity and maximum magnetization as a function of Ni atomic fraction, ‘y’. 140
Figure 78: XRD patterns of seeds and seeded products of cobalt ferrite at a starting ferrite/seeds w/w ratio, ‘r’, of 1.0. 143
Figure 79: Room temperature M-H loops of cobalt ferrite nanocrystals treated by three cycles of seeding and re-seeding at r = 1.0. 145
Figure 80: Variation in coercivity, H_c, and maximum magnetization, M_{max}, of cobalt ferrite crystals as a function of the ferrite/seed w/w ratio, ‘r’. The samples correspond to the third re-seeding cycle. 147

Figure 81: XRD patterns of cobalt ferrite treated by seeding and re-seeding cycles (r = 1.0) under flow-rate controlled synthesis conditions (0.81 mL/min)..... 149
Figure 82: Room temperature M-H loops of cobalt ferrite nanocrystals treated by seeding and re-seeding cycles (r = 1.0) and 0.81 mL/min. 150
Figure 83: XRD patterns of Ni-substituted cobalt ferrite (y = 0.7) treated by seeding and re-seeding cycles and r = 1.0. 152
Figure 84: Room temperature M-H loops of Ni-substituted cobalt ferrite (y = 0.7) treated by seeding and re-seeding cycles at 'r' = 1.0..... 153
Figure 85: XRD patterns of 12 nm-cobalt ferrite nanocrystals ball-milled at different times. 158
Figure 86: XRD patterns of 18 nm-cobalt ferrite nanocrystals ball-milled at different times. 158
Figure 87: Average crystallite size and surface area versus milling time of cobalt ferrite with initial average crystallite size of 12 nm. The dot line shown in the figure is a visual guide to show the decreasing trend in both, average crystallite size and SSA. 160
Figure 88: Variation in average crystallite size and surface area as a function of milling time of 18 nm-cobalt ferrite particles..... 161
Figure 89: High-Resolution TEM images of cobalt ferrite with average crystallite sizes of 12 nm (left) and 18 nm (right) before milling..... 162
Figure 90: TEM images of cobalt ferrite nanocrystals before (left) and after 5 hours of high-intensity ball milling (right). The average crystallite in the starting sample was 12 nm. 163
Figure 91: TEM images of cobalt ferrite nanocrystals before (left) and after 5 hours of high-intensity ball milling (right). The average crystallite in the starting samples was 18 nm. 163
Figure 92: Room temperature M-H measurements of ball-milled cobalt ferrite nanocrystals with an initial average crystallite size of 12 nm. 165
Figure 93: Variation in coercivity and specific surface area with milling time of cobalt ferrite with initial average crystallite size of 12 nm. 166
Figure 94: Room temperature M-H loops of ball-milled cobalt ferrite nanocrystals with initial average crystallite size of 18 nm. The inset shows the MH data around the origin. 166
Figure 95: Variation in coercivity and specific surface area with milling time of cobalt ferrite with initial average crystallite size of 18 nm. 167
Figure 96: XRD patterns of cobalt ferrite synthesized by the hydrothermal method at different temperatures. 170
Figure 97: TEM image of cobalt ferrite synthesized by hydrothermal method at 250 ºC... 172
Figure 98: TEM image of cobalt ferrite synthesized by the hydrothermal method at 350 ºC (left). Right-hand figure shows the corresponding High-Resolution TEM image. 172
Figure 99: Room temperature M-H measurements of cobalt ferrite synthesized by the hydrothermal method at different temperatures..... 173

Figure 100: XRD patterns of cobalt ferrite powders thermally treated in air at various temperatures. The XRD pattern of the starting powder synthesized under flow-rate controlled conditions is also included for comparison purposes. 178
Figure 101: SEM images of cobalt ferrite submitted to thermal treatment at different temperatures. 179
Figure 102: Electron diffraction pattern (ED) and TEM image of cobalt ferrite submitted at 900 ºC thermal treatment in air. 180
Figure 103: M-H room temperature loops of cobalt ferrite submitted to thermal treatment. 181
Figure 104: Mechanism of inhibition of crystal growth by means of steric effect enhanced by surfactants adsorption onto nanoparticles surface. 184
Figure 105: XRD patterns of cobalt ferrite synthesized using Na-oleate, CTAB, SDS, and PVP. 185
Figure 106: Room temperature M-H loops of cobalt ferrite synthesized using different types of surfactants. 187
Figure 107: XRD patterns of cobalt ferrite produced with and without 0.011M Na-oleate. The ferrite powders were removed right after the metal solution was fully added into the boiling hydroxide solution. 189
Figure 108: XRD pattern corresponding to the 4 nm cobalt ferrite nanocrystals. 189
Figure 109: TEM images of cobalt ferrite nanocrystals synthesized in presence of 0.011 M Na-oleate. 190
Figure 110: Infrared spectra of bare and Na-oleate coated cobalt ferrite. 191
Figure 111: M-H loops of cobalt ferrite synthesized with and without Na-oleate. 192
Figure 112: M-H loops at 2 K of 4 nm cobalt ferrite powders. 193
Figure 113: Mössbauer spectrum of cobalt ferrite synthesized using Na-oleate. 194
Figure 114: XRD patterns of cobalt ferrite with different average crystallite sizes. 196
Figure 115: Zero-field-cooled (closed symbols) and field-cooled (open symbols) (ZFC/FC) magnetization curves of 4nm-cobalt ferrite crystals. 197
Figure 116: M-H loops at 2 K of cobalt ferrite powders with different average crystallite sizes. 198
Figure 117: M-H loops at 300 K of cobalt ferrite powders with different average crystallite size. 199
Figure 118: M-H loops of 23 nm cobalt ferrite nanocrystals analyzed in a Quantum Design SQUID unit at 2 K and 300 K. The external magnetic field was 7 T. 199
Figure 119: M-T measurements for cobalt ferrite with different sizes. The external magnetic field was 5000 Oe. 201
Figure 120: XRD patterns of cobalt ferrite samples after M-T measurements. 203
Figure 121: Variation of coercivity with particle size in cobalt ferrite particles synthesized in the present study. 204

1 INTRODUCTION

1.1 Motivation and Justification

Nanometric cobalt-ferrite ($CoFe_2O_4$) particles display unusual properties that increase their attractiveness for advanced technological applications ranging from ferrofluids to biomedical treatment agents[1,2] (Figure 1). In particular, good chemical stability, large positive first order magnetocrystalline anisotropy constant and room-temperature high coercivity values makes this nano-size ferrite a promising candidate for magneto-optical recording media[3]. Control on particle size and shape, ions distribution, and/or structure could allow a fine tuning on the magnetic properties of ferrites[4-7]. In this regard, magnetic nanocrystals exhibit strong size-dependent properties that may provide valuable information to estimate the scaling limits of magnetic storage while contributing to the development of high-density data storage devices.

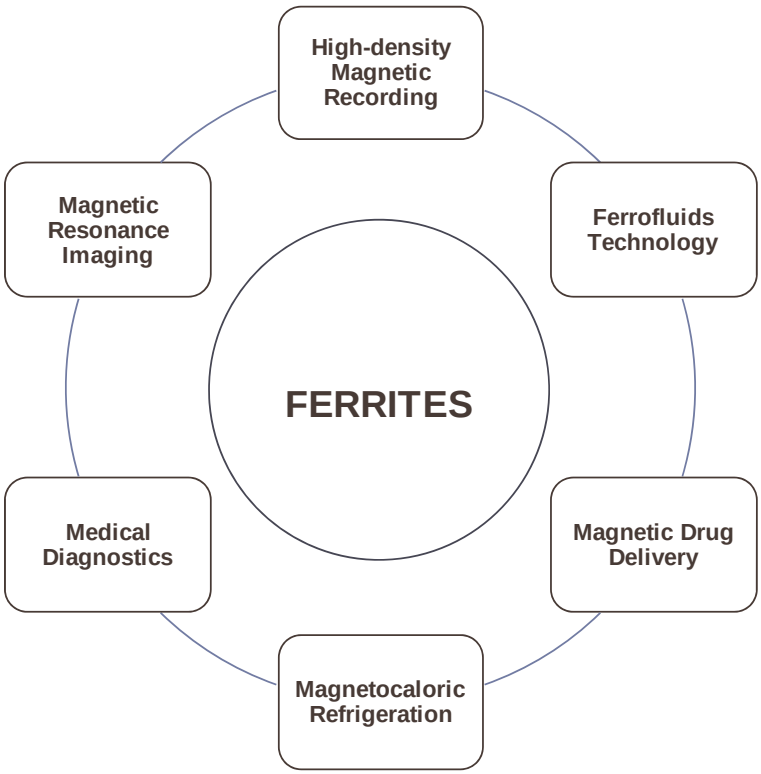

Figure 1: Applications of ferrites.

To our understanding, there is still a lack of a systematic effort to restrict the growth of single nanocrystals within the magnetic single domain region where enhancement of coercivity could be achieved. Theoretically, the single domain region ranges between 5 nm and 40 nm[8]. Maximum coercivity value of around 5.3 kOe[9] has also been reported for 40 nm nanocrystals. Since coercivity is strongly dependent of particle size, any attempt to achieve higher coercivity values in cobalt ferrite must consider the development of an alternative approaches in order to obtain more homogeneous crystal sizes with less or null presence of superparamagnetic particles which has near-zero coercivity.

It is desired to select a synthesis procedure capable of produce nanocrystals with a narrow size distribution due to the above mentioned direct dependence of coercivity with crystal size. Synthesis approaches as reverse micelles and thermal decomposition meet this criterion but the excessive consumption of resources, namely, synthesis reagents and experimental time must be minimized. The consumption of toxic solvents and surfactants make these processes less attractive. On the other hand, aqueous based synthesis (i.e. coprecipitation method) are environmentally friendly, the experimental time and synthesis reagents are minimum and, the most important, can allow a fine tuning on crystal size.

Although coercivity is mainly governed by the magnetocrystalline anisotropy energy, contribution from surface anisotropy becomes important in some cases at the nanoscale. These types of anisotropy are consequence of the spin-orbit coupling. The strain anisotropy and shape anisotropy also contribute to the magnetic anisotropy. The introduction of strain or modification of particle shape and their effect on magnetic properties are part of this work. The effect of composition will be also evaluated due to their effect on magnetocrystalline anisotropy and superexchange interaction.

Based on the above, the present research addresses the optimization of high coercivity ferrite nanocrystals. A systematic study on composition, size, shape, and cation distribution allowed determining the limits of the single and multi-domain regions experimentally as function of crystal size.

1.2 Objectives

1.2.1 Main Objective

- To determine the limits of the single domain and multi-domain regions as a function of the composition, structure, and crystal size in ferrimagnetic ferrites. The effect of particle shape on the magnetic behavior of ferrites was also attempted.

1.2.2 Specific Objectives

- To determine the optimum synthesis conditions to tune crystal size of ferrites within the single- and multi-domain regions.
- To enhance growth of ferrite crystals by promoting heterogeneous nucleation at the nanoscale. For this purpose, formation of ferrite crystal under seed-assisted and/or oversaturation-controlled precipitation conditions will be evaluated.
- To improve size monodispersity of produced nanocrystals through selective dissolution and/or size-sensitive phase separation.
- To determine the effect of ferrite composition (variation in Fe:Co mole ratio and transition metals substituted cobalt ferrite) on magnetic properties.
- To determine the relationship between processing conditions (including thermal treatment and creation of defects in produced nanocrystals), crystal size or shape and magnetic properties of produced ferrites at the nanoscale.

1.3 Dissertation Contents

The present dissertation was structured in the following way:

Chapter 1, Introduction, includes the motivation and justification of the research work as well as the objectives. The theoretical background, including the relation between magnetic properties and crystal size, in addition to fundamental concepts on experimental design, are discussed in Chapter 2. Literature review about ferrites and data storage systems is summarized in Chapter 3. Chapter 4 describes the syntheses protocols and the corresponding characterization of cobalt ferrite. The results obtained from the optimization of synthesis parameters, the size-selective phase separation method, the evaluation of the ferrite composition, seed-mediated growth experiments, size reduction by high-energy ball milling, shape modification by hydrothermal synthesis, post-synthesis thermal treatment of ferrite powders as well as the inhibition of crystal growth by using surfactants are discussed in Chapter 5. Finally, the general remarks are summarized in Chapter 6.

2 THEORETICAL BACKGROUND

2.1 Fundamentals of Magnetism

There are some legends behind the origin of the word magnetism. One of them tells that it comes from a little shepherd from ancient Greece. Magnus, the shepherd, was tending his flock at Mount Ida when accidentally placed the tip of his cane on a big stone. The stone exerted such force that Magnus was unable to release his cane. A second legend derives the word magnetism from the strange stones discovered in an ancient country of Asia Minor called Magnesia. These magnetic stones were actually a kind of iron ore now called magnetite.

Magnetism is a physical phenomenon by which a material exerts forces of attraction or repulsion on other materials. It is the product of orbital motion of the electron around the nucleus and the intrinsic magnetic field of the electron (spin), as shown in Figure 2.

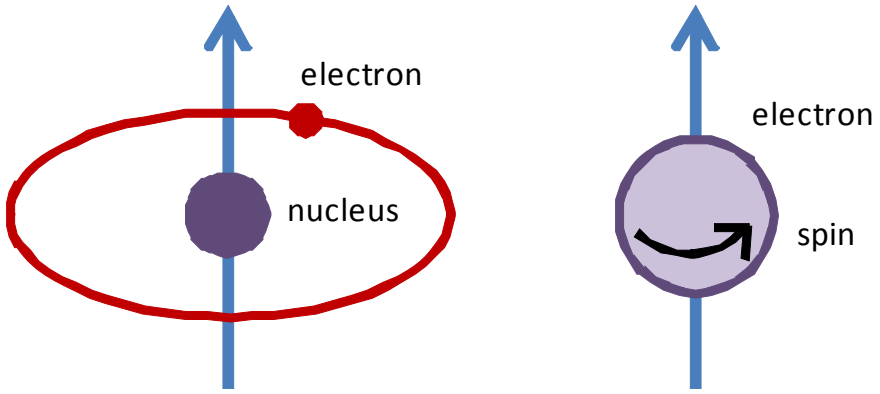

Figure 2: Origin of magnetism.

2.2 Magnetic Behaviors

2.2.1 Diamagnetism

Elements with all electrons paired exhibit diamagnetism. It is a form of magnetism that is only exhibited by a material in presence of an external magnetic field. The external magnetic field alters the orbital velocity of electrons around their nuclei, changing the magnetic dipole moment in the direction opposing the external field, causing a repulsive effect. They are the so-called 'non-magnetic' materials. The response of a material to an applied field H is characterized by the magnetic susceptibility, χ. Materials are classified depending on its susceptibility:

$$\chi = \frac{M}{H} \tag{1}$$

For a diamagnetic material, a negative susceptibility is present when a magnetic field is applied. It is the range between 10^{-6} and 10^{-5}.

Some elements and materials that exhibit diamagnetism are Cu, Au, and Al_2O_3.

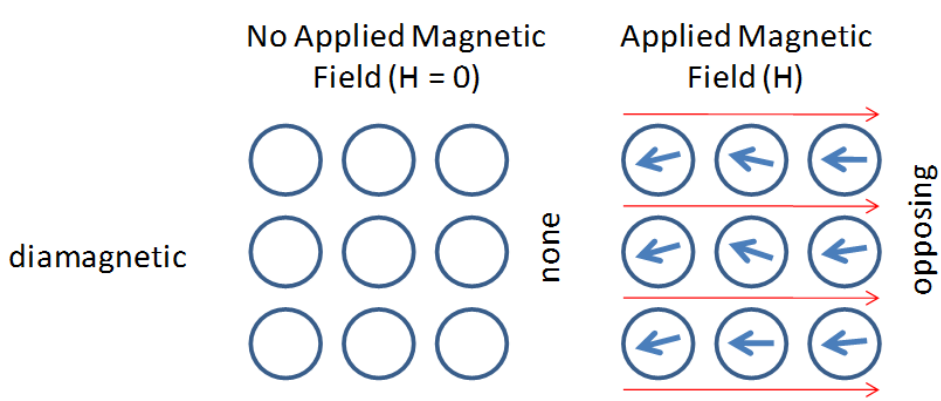

Figure 3: Diamagnetic response in absence or presence of an external magnetic field.

2.2.2 Paramagnetism

Paramagnetic elements have permanent magnetic moments (dipoles), even in the absence of an applied field, arising from unpaired electrons in the valence shell of the atoms. In pure paramagnetism, the dipoles do not interact with one another and are randomly oriented in the absence of an external field due to thermal agitation, resulting in zero net magnetic moment. When an external magnetic field is applied, the magnetic dipoles will partially line up with it, giving rise to a positive induced magnetic moment. Paramagnetic materials have a positive susceptibility when a magnetic field is applied. Typical susceptibility ranges between 10^{-3} and 10^{-5}.

Some elements that exhibit paramagnetism are Pt, Al, and Mn.

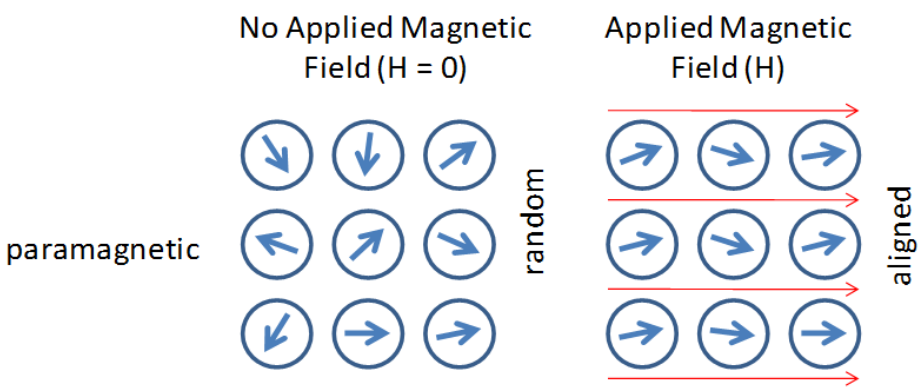

Figure 4: Paramagnetic response in absence or presence of an external magnetic field.

2.2.3 Ferro- and Ferri- magnetism

A ferromagnetic material has permanent and large magnetizations which result from the parallel alignment of neighboring magnetic moments. They can be magnetized by an external magnetic field and remain magnetized after the external field is removed. Metallic Co, Fe and Ni are examples of ferromagnetic materials.

In a ferrimagnetic material, the magnetic moments of the atoms on different sublattices are opposed; however, the opposing moments are unequal and a spontaneous magnetization remains. Susceptibility values for ferromagnetic and ferrimagnetic materials are large and positive, > 10^{-3}. For the cobalt ferrite case, the magnetic moments Fe^{3+} located at the tetrahedral site completely cancel with the magnetic moments of Fe^{3+} in the octahedral site. This ferrimagnetic behavior is shown in Figure 7 (modified from reference [10]).

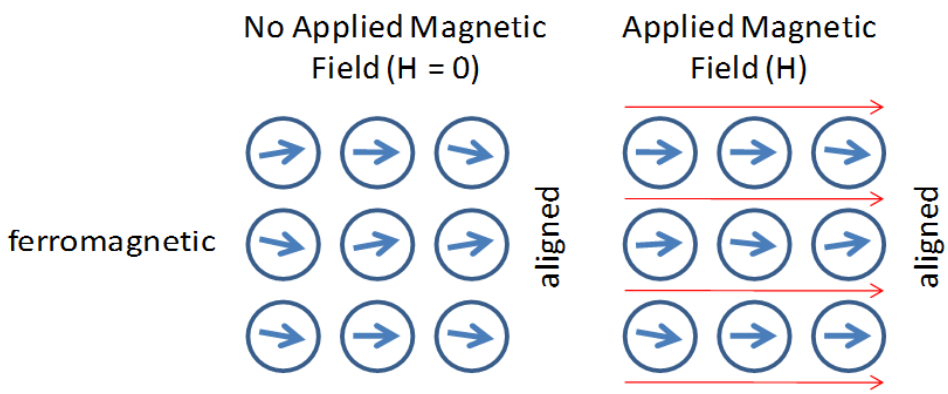

Figure 5: Ferromagnetic response in absence or presence of an external magnetic field.

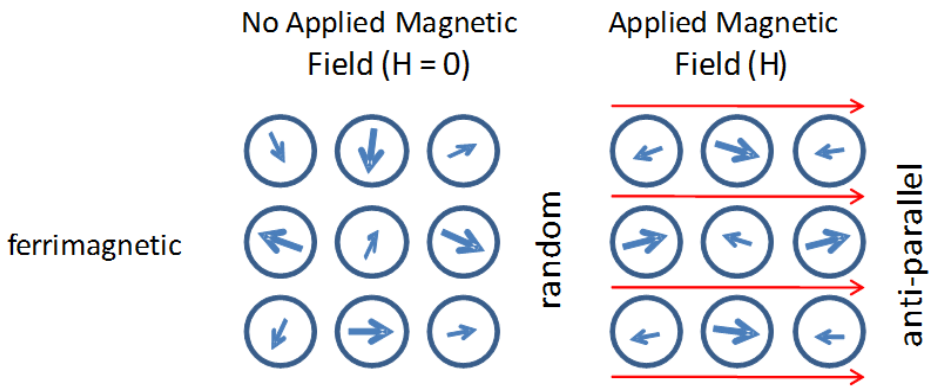

Figure 6: Ferrimagnetic response in absence or presence of an external magnetic field.

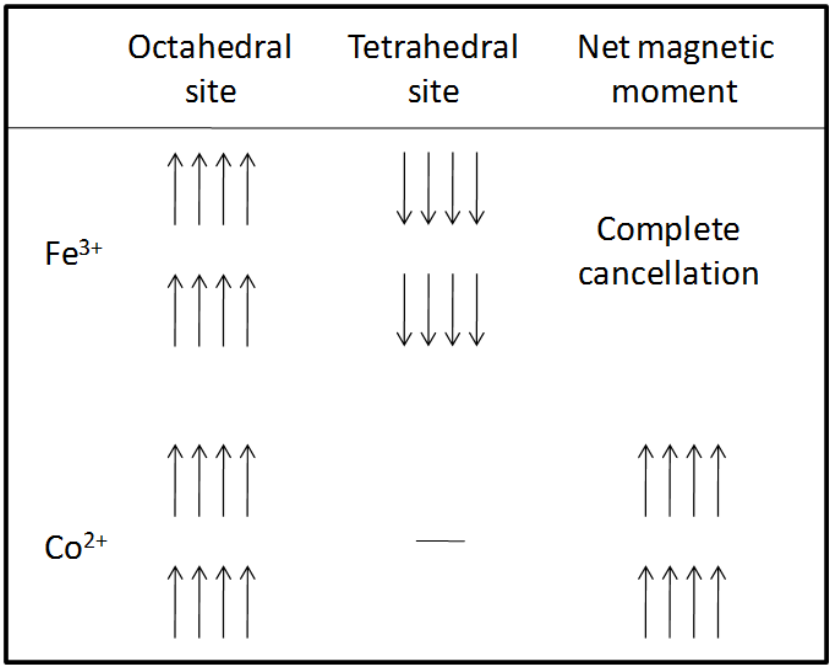

Figure 7: Distribution of spin magnetic moments for Fe^{3+} and Co^{2+} in a unit cell of $CoFe_2O_4$. The arrow represents the magnetic moment orientation of each cation.

2.2.4 Antiferromagnetism

In this case, the magnetic moments of atoms or molecules align in a regular pattern with neighboring spins pointing in opposite directions causing the net magnetization to be zero. It is a manifestation of ordered magnetism. CoO and MnS exhibit antiferromagnetism.

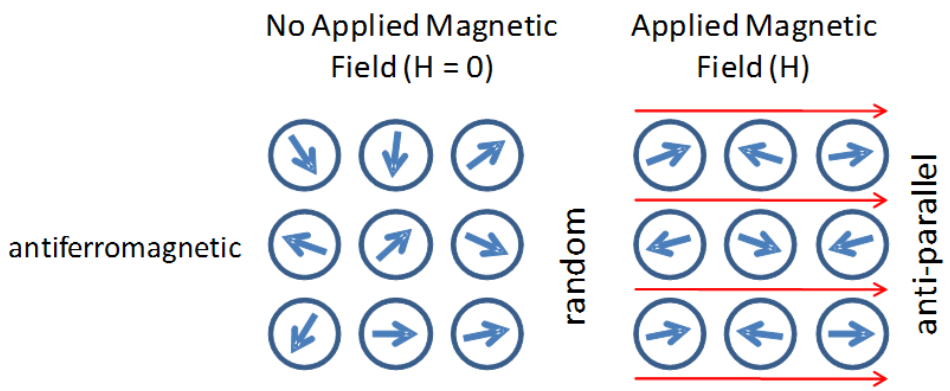

Figure 8: Antiferromagnetic response in absence or presence of an external magnetic field.

2.2.5 Superparamagnetism

This type of magnetism appears in small ferromagnetic or ferrimagnetic nanoparticles. In small enough nanoparticles, magnetization can randomly flip direction under the influence of temperature. The typical time between two flips is called the Néel relaxation time. In the absence of external magnetic field, when the time used to measure the magnetization of the nanoparticles is much longer than the Néel relaxation time, their magnetization appears to be in average zero: they are said to be in the superparamagnetic state. In this state, an external magnetic field is able to magnetize the nanoparticles, similarly to a paramagnet. However, their magnetic susceptibility is much larger than the one of paramagnets.

2.3 Magnetic Domains

2.3.1 Single Magnetic Domains

A representation of a single magnetic domain[11] is shown in Figure 9. The single magnetic domain describes a region within a magnetic material which has uniform magnetization, i.e., the individual magnetic moments of the atoms are aligned with one another and pointed in the same direction. When heated above a particular temperature (*Curie temperature*), a ferromagnetic material undergoes a phase transition, and the uniform magnetization within a domain spontaneously disappears: each atom has its own direction of magnetic moment, independent from his neighboring atoms (typical of the paramagnetic state). Magnetic domain structure is responsible for the magnetic behavior of ferromagnetic materials like iron, nickel, cobalt and their alloys, ferrites etc.

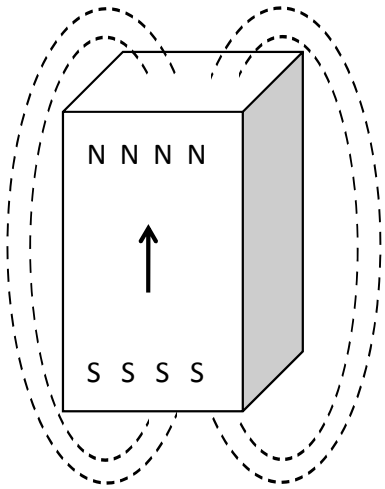

Figure 9: Scheme of a magnetic single domain[11].

2.3.2 Magnetic Multi-domains

Regions inside a material where all the magnetic moments are aligned in the same direction are called domains. The regions separating magnetic domains are called domain walls, where the magnetization rotates coherently from the direction in one domain to that in the next domain. The existence of magnetic multi-domains[11] (Figure 10) is a result of energy minimization. In 1935, Landau and Lifschitz[12] pointed out that the primary reason for the existence of domains within a crystal is that their formation reduces the magnetostatic energy. The breakup of the magnetization into domains provides for flux closure at the end of the material reducing the magnetostatic energy. The magnetostatic energy of a single-domain particle is given by:

$$E = \frac{\mu_0}{2} N_d M^2 \qquad \textbf{(2)}$$

In equation (2), N_d is the demagnetization factor and M is the magnetization. This equation also suggests that if M is reduced by the emergence of domains, the magnetostatic energy will also be reduced.

The size of the domains will be determined by the domain wall energy. The domain wall energy is defined as the difference in energy of the magnetic moments when they are part of the wall and when they are part of the main body of the domain. Subdivision into domains cannot be indefinitely because the production and maintenance of them requires energy.

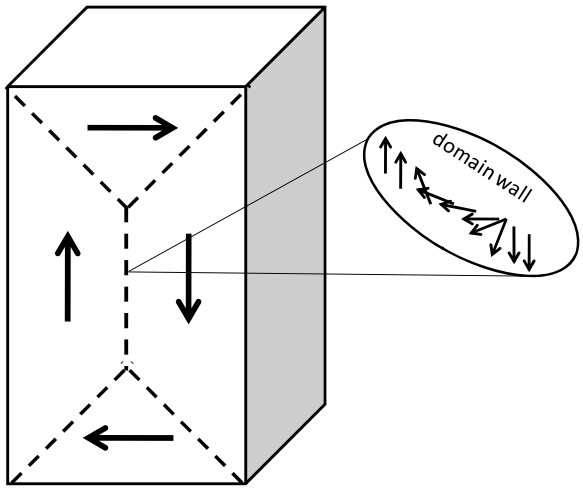

Figure 10: Scheme of a magnetic multi-domains[11].

2.4 Magnetic Hysteresis

The hysteresis loop represents the variation of the magnetic flux density (or magnetization) as function of applied magnetic field (magnetizing force). This loop shows the magnetic behavior of materials when it is exposed to an external magnetic field. Application of a magnetic field causes the magnetization to increase in the direction of the applied magnetic field. If the magnetic field is increased indefinitely the magnetization reaches saturation at some point. It means that all the magnetic moments are aligned with the magnetic field direction and any additional increment in the field does not causes a further increment in magnetization. If the magnetic field is reversed, the magnetization will gradually align in the new field direction until reach saturation in the opposite way. Diamagnetic and paramagnetic materials show negative and positive magnetization, respectively, in the presence of a magnetic field that disappears almost immediately when it is removed. Ferromagnetic materials have positive magnetization that persists after the magnetic field removal and give rise to the hysteresis loop (Figure 11) that determines the technological applications of the material. Some magnetic properties as coercivity, saturation magnetization, and remanence are obtained from it.

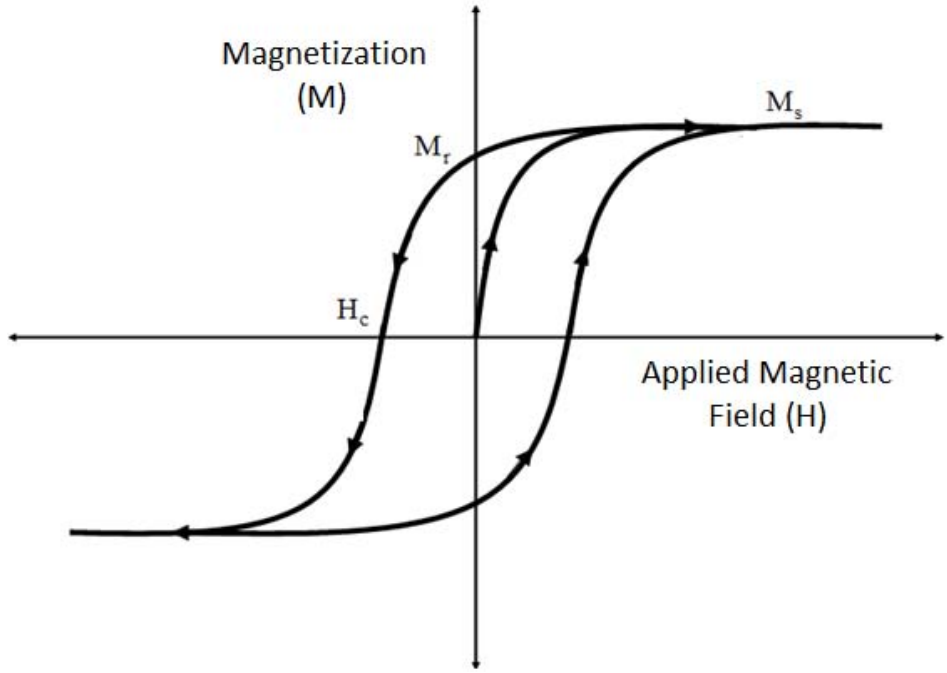

Figure 11: Magnetic hysteresis loop.

2.4.1 Coercivity

Coercivity, also called coercive field (H_c), refers to the applied magnetic field necessary to reduce to zero the magnetic flux density of the magnetized ferromagnetic or ferrimagnetic material after saturation. In the single domain region, magnetic materials reach the highest coercivity; this is because all magnetic moments are oriented in the same direction.

Magnetic materials are classified as 'soft' or 'hard' depending on its coercivity value. A soft material refers to that one with low coercivity while a hard one will exhibit high coercivity. The coercivity for an assembly of randomly oriented single domain spheres with uniaxial magnetocrystalline anisotropy can be calculated by[13]:

$$H_c = \frac{0.958K_u}{M_s} \quad \textbf{(3)}$$

where:

K_u is the uniaxial anisotropy constant (erg/cm^3) and M_s (emu/cm^3) the saturation magnetization. The uniaxial anisotropy constant is used to describe the dependence of the internal energy on the direction of the spontaneous magnetization, as consequence, hard and easy directions of magnetization are present.

Accordingly to a Néel calculation for a random system of spherical, non-interacting particles with cubic anisotropy, the coercivity could be calculated by[9]:

$$H_c = \frac{0.64K_1}{M_s} \quad \textbf{(4)}$$

In equation (4), K_1 is the first anisotropy constant. Cobalt ferrite mainly possesses a positive cubic anisotropy.

2.4.2 Saturation Magnetization

A magnetic material reaches saturation when there is no change in maximum magnetization observed even when the external magnetic field is increased. Physically it means that all the magnetic moments are aligned with the magnetic field. It can be calculated based on the electronic configuration of the elements involved in the structure (TABLE 1). In the case of ferrimagnetic ferrites, the magnetization comes only from the divalent cation because Fe^{3+} cations have antiparallel arrangement and cancel themselves. Co^{2+} accounts for 3 magnetic moments[11] (TABLE 1) that come from its electronic configuration:

Co^{2+}: [Ar] $3d^7$

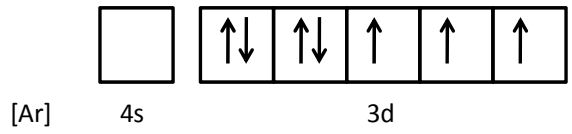

The alignment with the external magnetic field would be either by particle rotation or by magnetic moment rotation inside the particle. In order to avoid particle rotation, the powder should be immobilized into a polymeric matrix or tightly packed into the magnetometer holder.

TABLE 1: Magnetic moments of some simple ferrites (magnetic moment [μ_B])[11].

Ferrite	Measured	Calculated
$MnFe_2O_4$	4.6	5
$FeFe_2O_4$	4.1	4
$CoFe_2O_4$	3.7	3
$NiFe_2O_4$	2.3	2
γ - Fe_2O_3	2.3	2.5

Deviations from theoretical values can be attributed to several factors, namely:

- The ion distribution on the various sites may not be as perfect as predicted.
- The orbital magnetic contribution may not be zero as assumed.
- The directions of the spins may not be antiparallel in the interactions. In other words, they may be canted.

2.4.3 Remanence

After a material has been submitted to an external magnetic field, some particles remain magnetized. This magnetization is known as remanence. To demagnetize the material, a field equal of higher in magnitude than the coercivity must be applied in the opposite direction.

2.4.4 Squareness ratio

The squareness ratio is defined as:

$$S = \frac{M_r}{M_s} \tag{5}$$

where M_r and M_s are the remanence and saturation magnetization, respectively. A squareness ratio around one should be obtained if most of the magnetic moments remain magnetized after removing the magnetic field. For magnetic recording purposes, squareness ratio unity is desired in order to keep safe the information. Accordingly to Lee[14], the maximum squareness of a material with positive cubic anisotropy is 0.831. In the case of a negative cubic anisotropy the maximum squareness is 0.866.

2.4.5 Magnetic Anisotropy

Magnetocrystalline anisotropy energy is the work required to rotate the magnetic moments during the magnetization of a ferromagnetic material, due to the magnetocrystalline anisotropy. This magnetocrystalline anisotropy energy varies according to the crystal

orientation relative to the applied magnetic field. Easy axis of magnetization requires small applied fields to reach the saturation magnetization. For a cubic structure, the magnetocrystalline anisotropy energy (MAE) is expressed by:

$$E_{MAE} = k_1\left(\alpha_1^2\alpha_2^2 + \alpha_2^2\alpha_3^2 + \alpha_3^2\alpha_1^2\right) + k_2\left(\alpha_1^2\alpha_2^2\alpha_3^2\right) + \ldots \quad \textbf{(6)}$$

In the above equation, k_1 corresponds to the magnetocrystalline constant and α_i the direction cosines, which are the ratios of the individual components of the magnetization projected on each axis divided by the magnitude of the magnetization.

At low temperatures a competition between shape anisotropy and magnetocrystalline anisotropy can be observed. At room temperature, however, the magnetic properties are dominated by the shape anisotropy. This can be explained by the strong temperature dependence of the magnetocrystalline anisotropy constant[15]. The magnetocrystalline anisotropy energy has the same symmetry as the crystal structure. The shape of particles has a considerable effect on the switching behavior of magnetization. The shape anisotropy can dominate the magnetocrystalline anisotropy, thereby preventing the formation of domain walls inside the particle. The origin of surface anisotropy lies in the exchange interactions between the internal and surface atomic spins. With decreasing size of particles to nanometer scales, the ratio of surface–volume will be increased and the effect of surface anisotropy will grow. When the surface anisotropy constant becomes of the order of the exchange interaction coefficient, the coercivity of the medium will be increased considerably[16].

Following the law of approach to saturation, the magnetic anisotropy can be calculated by[17]:

$$M(H) = M_s\left(1 - \frac{0.07619K^2}{H^2 M_s^{\ 2}}\right) - \left(\frac{0.0384K^3}{H^3 M_s^{\ 3}}\right) \qquad \textbf{(7)}$$

where M_s is the saturation magnetization, K is the magnetic anisotropy, $M(H)$ is the magnetization at an specific applied field. The magnetic anisotropy constant[11] of some ferrites is shown in TABLE 2**;** large and positive anisotropy values mean more work is required to rotate the magnetic moments during the magnetization process.

TABLE 2: Magnetocrystalline anisotropy constant of some ferrites[11].

Ferrite	**Anisotropy constant, K_1 (ergs/cm^3)**
$FeFe_2O_4$	-1.1×10^3
$Co_{.8}Fe_{2.2}O_4$	$+3.9 \times 10^6$
$Co_{1.1}Fe_{1.9}O_4$	$+1.8 \times 10^6$
$Co_{.3}Zn_{.2}Fe_{2.2}O_4$	$+1.5 \times 10^6$
$Co_{.3}Mn_{.4}Fe_2O_4$	$+1.1 \times 10^6$
$Mn_{.45}Zn_{.55}Fe_2O_4$	-3.8×10^3
$MnFe_2O_4$	-28×10^3
$Ni_{.8}Fe_{2.2}O_4$	-39×10^3
$NiFe_2O_4$	-63×10^3
$Ni_{.7}Co_{.004}Fe_{2.2}O_4$	-10×10^3

2.5 Ferrites

2.5.1 Spinel structure of the ferrite

The spinel structure derives from the mineral $MgAl_2O_4$ whose structured was elucidated in 1915. Analogous to it, the spinel structure has the general formula MFe_2O_4, where M corresponds to a divalent metal. Divalent ions as Co^{2+}, Mn^{2+}, Ni^{2+}, and Zn^{2+} are commonly found in spinels. The spinel lattice[11] is composed of a close-packed oxygen arrangement with 32 oxygen atoms forming the unit cell. It has two types of interstices, called A and B sites, where the cations are accommodated. The site A is tetrahedral and the B site is octahedrally coordinated by oxygen atoms. The unit cell contains 64 tetrahedral sites, only 8 being occupied. In the other hand, from 32 octahedral sites half of them are occupied.

A spinel cell contains two types of subcells (shown in Figure 12) that alternate in a three-dimensional array to create a full cell. The full cell contains eight subcells.

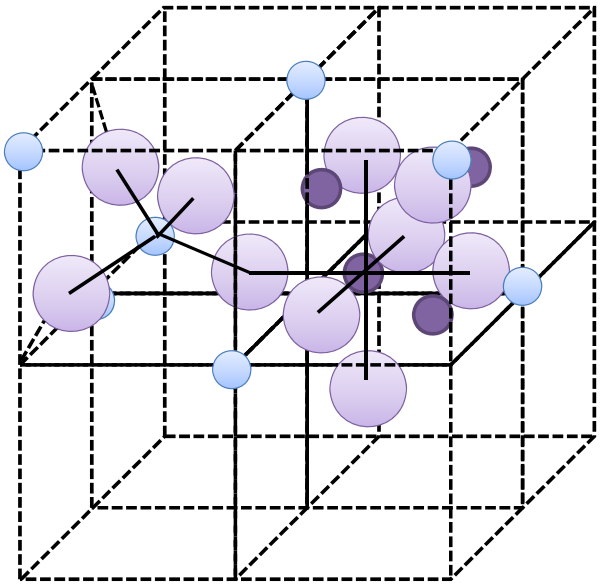

Figure 12: The spinel structure[11].

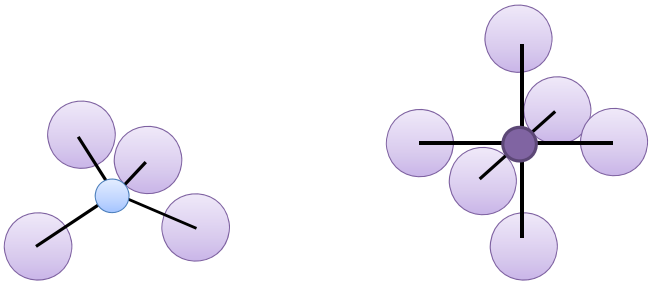

Figure 13: Tetrahedral site (left) and octahedral site (right) in the spinel structure.

The magnetic properties are also influenced by the interaction of cations in lattice sites A and B. Large angles and shorter distances between cations correspond to enhanced magnetic properties. Accordingly to it, A-B interactions are the strongest.

TABLE 3: Angles in the spinel structure for the different types of lattice site interactions[11].

AB	BB	AA
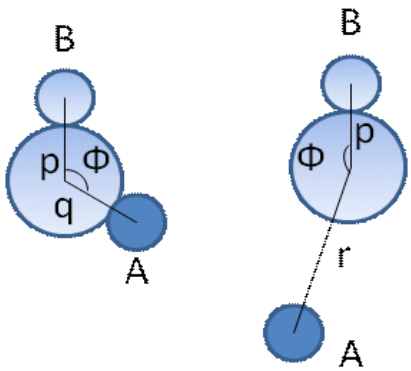	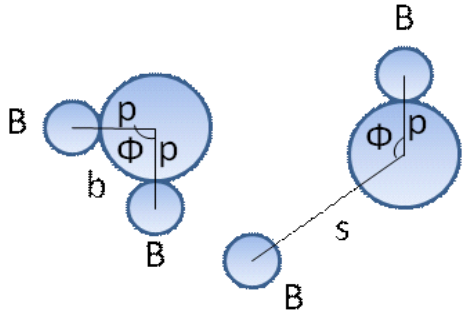	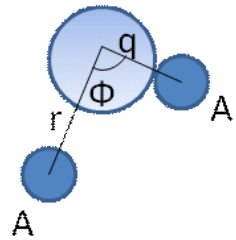
Φ = 125.15° 154.57°	**90° 125.03°**	**79.63°**

TABLE 4: Interionic distances in the spinel structure for the different types of lattice site interactions[11].

Distances M-O	Distances M-M
$p = a\left(\frac{5}{8} - u\right)$ $q = a\left(u - \frac{1}{4}\right)\sqrt{3}$ $r = a(1+u)\sqrt{11}$ $s = a\left(\frac{1}{3}u + \frac{1}{8}\right)\sqrt{3}$	$b = \left(\frac{a}{4}\right)\sqrt{2}$ $c = \left(\frac{a}{8}\right)\sqrt{11}$ $d = \left(\frac{a}{4}\right)\sqrt{3}$ $e = \left(\frac{3a}{8}\right)\sqrt{3}$ $f = \left(\frac{a}{4}\right)\sqrt{6}$

The interstices occupancy by the cations will depend on four specific factors. Those factors are listed below:

1. The ionic radii of the specific ions
2. The size of the interstices
3. Temperature
4. The orbital preference for specific coordination

Divalent ions are larger than trivalent ions because larger charge produces greater electrostatic attraction and pull the outer orbits inward. Because tetrahedral sites are smaller than octahedral, divalent ions prefers octahedral site. As the data in TABLE 6 shows, ions with larger radius cause expansion of the unit cell length[11].

TABLE 5: Ionic radius of metal ions in spinel ferrites[11].

Metal ion	Ionic radius (Å)
Mg^{2+}	0.78
Mn^{2+}	0.91
Mn^{3+}	0.70
Fe^{2+}	0.83
Fe^{3+}	0.67
Co^{2+}	0.82
Ni^{2+}	0.78
Cu^{2+}	0.70
Zn^{2+}	0.82
Cd^{2+}	1.03

TABLE 6: Lattice parameter of some cubic ferrites[11].

Ferrite	Lattice parameter (Å)
$MnFe_2O_4$	8.50
$FeFe_2O_4$	8.39
$CoFe_2O_4$	8.38
$NiFe_2O_4$	8.34

2.5.2 The cobalt ferrite

Cubic ferrites could be classified as normal, inverse, or mixed spinels. In the case of a normal spinel, the divalent ions occupy all the tetrahedral sites while the trivalent ions do the same with the octahedral sites. An example of a material with a normal spinel structure is $ZnFe_2O_4$. In the case of inverse spinels as cobalt ferrite, all tetrahedral sites are occupied by the trivalent ion (Fe^{3+}) while octahedral sites are equally occupied by divalent (Co^{2+}) and trivalent ions (Fe^{3+}), as seen in Figure 14 modified from Reference [10]. The five magnetic moments from octahedral Fe^{3+} accommodate anti-parallel to the five magnetic moments from tetrahedral Fe^{3+} canceling and leading to a ferrimagnetic behavior. The magnetization of the cobalt ferrite is attributed to the three magnetic moments from the cobalt atom.

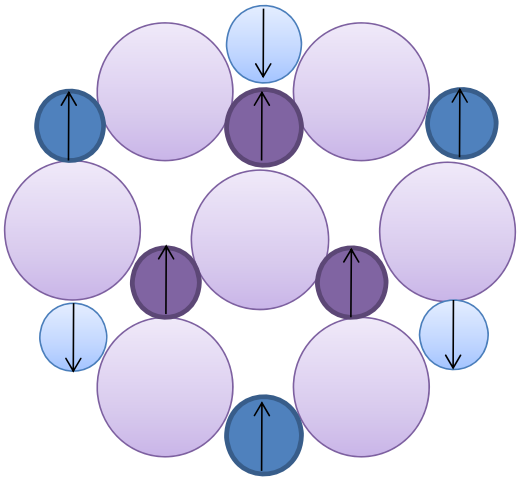

Figure 14: Cations arrangement in the lattice interstices of cobalt ferrite.

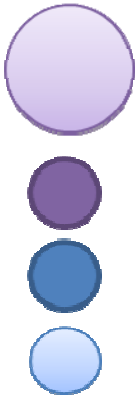

O^{2-}

Co^{2+} (octahedral)

Fe^{3+} (octahedral)

Fe^{3+} (tetrahedral)

The ferrite structure possesses good mechanical hardness in addition to chemical stability which makes it an excellent candidate for magnetic recording applications.

2.6 Crystals nucleation and growth processes

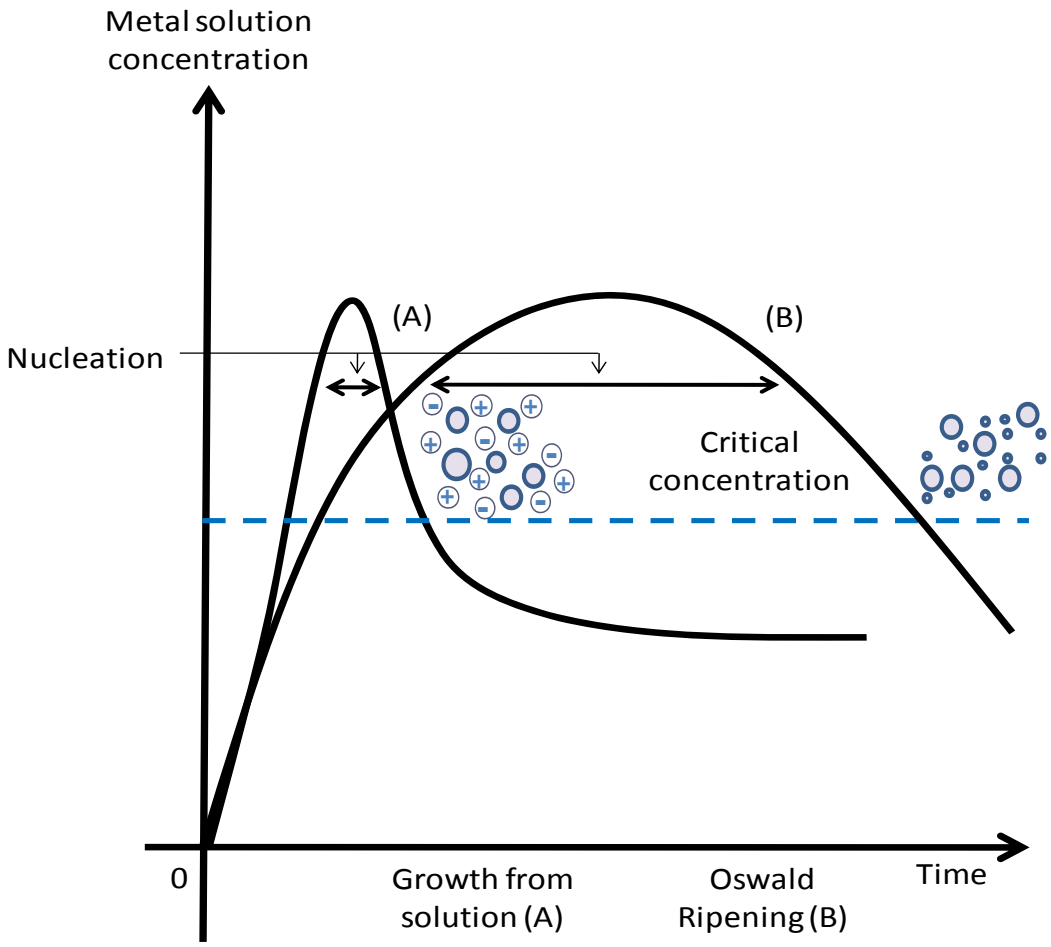

Figure 15: Nucleation and growth processes[18].

Based on the strong dependence of magnetic properties with crystal size, it is of paramount importance to have a control on nucleation and growth processes to attain highly monodisperse particles. Following the LaMer and Dinegar[18] diagram (a modification of it is shown in Figure 15), which was first proposed to explain the mechanism of formation of

monodispersed sulfur hydrosol, a blast of nucleation will occur when the metal solution concentration is above a critical concentration.

The key for nucleation is the degree of supersaturation. During this stage, the metal ions monomers are being consumed from solution to form the nuclei until the metal solution concentration falls below that critical concentration. Then, the growth stage begins and will end until they reach equilibrium. It is important that nucleation should be avoided during the growth process in order to obtain more homogeneous sizes. In our case, where single crystals are desired, the growth process cannot be by aggregation of much smaller subunits as the final product is polycrystalline. Growth by means of diffusion of metal ions from solution (A) or by Oswald Ripening[19] (B) where smaller particles dissolve and re-crystallize over the larger ones is necessary for the production of cobalt ferrite nanocrystals. The solubility of the nanoparticles is given by the Gibbs-Thompson equation[13]:

$$C_r = C_\infty e^{\left(\frac{2\gamma V_m}{rRT}\right)} \quad \textbf{(8)}$$

If $2\gamma Vm/rRT << 1$, C_r is approximated as:

$$C_r = C_\infty \left(1 + \frac{2\gamma V_m}{rRT}\right) \quad \textbf{(9)}$$

where C_r and C_∞ are the concentrations in equilibrium (solubility) with a particle of radius r and the bulk solid, respectively. V_m is the molar volume of a solid and γ is the specific surface energy.

2.7 Magnetic properties and particle size

There is a relationship between coercivity and particle size[20] that is based on the presence of magnetic domains. Magnetic particles would behave as single (SD) or multi-domain (MD) depending on particle size (as seen in Figure 16 [20]). This SD region is subdivided in two main regions characterized by their magnetic stability and they are known as the unstable and the stable regions. The unstable region corresponds to the superparamagnetic particles (SPM). It is a size-dependent issue where the thermal energy overcomes the anisotropy energy causing the spins rotate and randomize acting as paramagnetic (do not retain magnetization and coercivity after magnetic field removal).

The critical radius below which particles behave as single domain can be calculated by[21,22]:

$$r_c = \frac{9(AK_u)^{1/2}}{\mu_0 M_s^{\ 2}} \qquad \textbf{(10)}$$

A is the exchange stiffness (constant characteristic of the material related to the critical temperature for magnetic ordering), K_u is the uniaxial anisotropy constant; μ_0 is the vacuum permeability, and M_s the saturation magnetization. For the stable single domain region, a simple model developed by Stoner and Wohlfarth[23] assumes coherent spin rotation whereby all spins within the single-domain particle are collinear (the magnetization is uniform) and rotate in unison. The model predicts the field strength necessary to reverse the spin orientation direction or coercivity. In this stable region the magnetocrystalline energy

gradually overcomes the thermal energy and it is responsible for the increase in coercivity. The only way to magnetize a material is to rotate the spins, a process that involve high energies and, hence, high coercivity. Thus, SD grains are magnetically hard and have high coercivity and remanence magnetization. For the cobalt ferrite case, the limit between the single and multi-domain has been established to be around 40 nm with coercivity of 5.3 kOe at room temperature. For the multi-domain region, domain walls are present and coercivity tends to decrease with an increase in particle size. The magnetization process of a multi-domain particle is controlled by domain wall movement that is an energetically easy process. Based on the above considerations, a precise control on particle size will allow a fine tuning on magnetic properties, specifically coercivity, at the nanoscale.

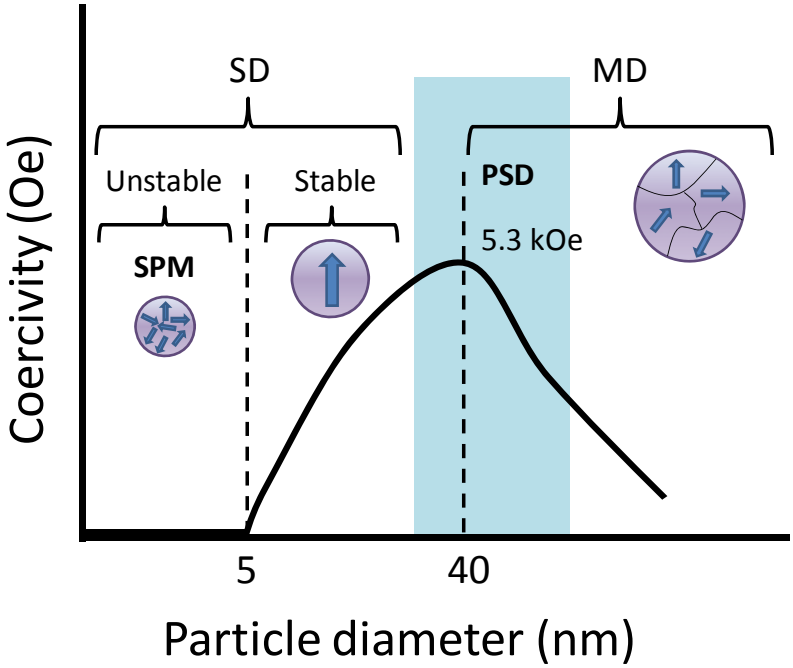

Figure 16: Dependence of coercivity with particle diameter for cobalt ferrite.

2.8 Fundamentals of Experimental Design Applied to Magnetic Properties of Materials

An experimental statistical design permits the simultaneous examination of the effects of independent variables (synthesis parameters) and the interactions between them on a response (dependent variable)[24,25], all with a minimum of experiments saving time and money. The independent variables are also called factors and may contribute to the value of the response variable[26]. The factor values are called levels of the factors. Each combination of levels from two or more factors is called a treatment combination. If at least one value of the response is observed at each treatment combination is called a factorial experiment. A factorial experiment combines all levels of a given factor with all levels of every other factor in the experiment. Accordingly, a 2^3 factorial design -that considered three factors (synthesis parameters) and two levels for each one- has 8 possible combinations was used to determine which synthesis parameters would exert more influence on the coercivity of ferrite nanocrystals. In addition to it, three replicates at the center of the cube will be used to estimate the experimental error (Figure 17). The levels of the synthesis parameters in the factorial design were defined based on the trends observed in the previous experiments.

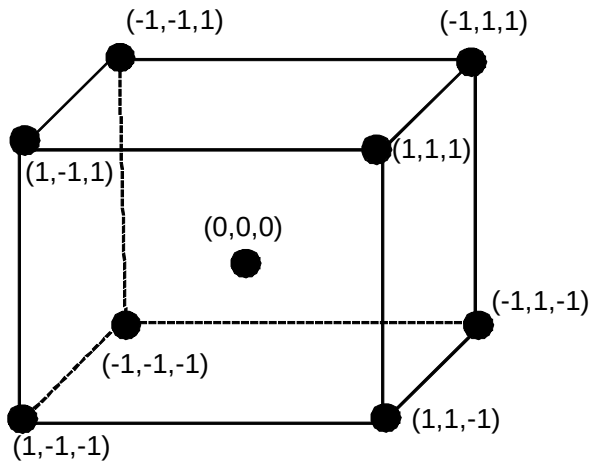

Figure 17: Experimental points for a 2^3 factorial design.

Advantages of factorial designs rely on more efficiency than with one factor at a time experiments and obtaining information regarding interaction between factors. The data collected from experimentation will be submitted to statistical analysis[27]. The analysis of variance (ANOVA) is used to quantify and evaluate the importance of possible sources of variation. It provides the basic information necessary for making statistical interference either in terms of tests of hypotheses (or tests of significance) or confidence interval estimation (F - test). The statistical results will have to be interpreted in terms of the original formulated hypotheses.

A test of a hypothesis is a rule to determine whether a hypothesis is rejected or not and it is based on sample statistics called test statistics. The hypothesis is usually stated in null form, since these are the only easily testable statements. The p-value of a test is the probability of obtaining a value of the test statistic that is at least as extreme as the calculated value when the null hypothesis is true. It is the smallest significance level at which the null hypothesis

can be rejected. Thus, if the agreed-upon value of α is less than the observed p value the null hypothesis is not rejected.

After determining which parameters have influence on coercivity, and based on the contour plots (a graphical representation of the synthesis parameters that shows interpolated values of the response – i.e. coercivity), additional designs were considered to refine the results. Central composite designs cover areas inside or outside the design cube so they will help to achieve this purpose and optimize coercivity. Composite designs (inscribed and face centered) were completed in order to facilitate the analysis through response surface regression. The central composite design is composed of three parts: 1) a factorial or cube from a 2^k factorial design, 2) an axial or 'star' consisting of 2k points on the axis of each factor, and 3) replications of the center point. The addition of star points to the existing factorial designs will help to complete such designs. In some cases the maximum may not have been reached, but the experimental design will indicate the direction to be followed in the experimental work.

Finally, a mathematical model can be derived from the data obtained from the analysis. In the case of three parameters evaluated, the general mathematical model should have the following form:

$$Y = B_0 + B_1X_1 + B_2X_2 + B_3X_3 + B_{12}X_1X_2 + B_{13}X_1X_3 + B_{23}X_2X_3 + B_{123}X_1X_2X_3 + E$$

Where: B_0 is the average of the response variable, X_1, X_2, and X_3 are the parameters evaluated in the design whereas X_1X_2, X_1X_3, and X_2X_3 are the interactions between them. E

is the experimental error. B_i coefficients are related to the effect of each variable or the corresponding interactions.

3 LITERATURE REVIEW

3.1 Ferrite synthesis

3.1.1 Cobalt ferrite synthesis: Possibilities and Limitations

Magnetic nanoparticles can be synthesized either by gas phase[28] or liquid phase methods. The present discussion will be focused on liquid phase approaches which are of our concern. Several chemical methods such as coprecipitation, sol-gel, thermal decomposition, hydrothermal processing, and reverse micelles have been reported for the synthesis of ferrite nanoparticles. Physical methods, such as ball milling, or ceramic routes have also been proposed for the synthesis of ferrites in solid state. The strengths and limitations of these approaches are discussed below.

Related literature was focused on the synthesis of cobalt ferrite in the superparamagnetic region (where no significant enhancement of coercivity is possible)[4,5,29-31] or polycrystalline multi-domain particles[32,33], in which case coercivity is expected to decrease. To our understanding, there is still a lack of a systematic attempt to restrict the growth of single nanocrystals within the magnetic single domain region where enhancement of coercivity could be achieved. Research works about cobalt ferrite nanoparticles have been published since the 1950's when Berkowitz and Schuele[8] prepared cobalt ferrite nanoparticles by thermal decomposition of the co-precipitated metal oxalates. At room temperature (300 K),

the magnetic measurements of the powders exhibited 2080 Oe as the highest coercivity for 35.5 nm nanocrystals. The thermal decomposition method has been widely used because high quality monodispersed and single crystal nanoparticles are obtained. Nevertheless, the required use of toxic solvents and surfactants is not desired in green-syntheses approaches.

In addition to the thermal decomposition method[34], a two-phase method known as reverse micelles[35-37] or water-in-oil microemulsions allows the formation of nanoparticles with narrow size distribution. The size of the nanoparticle is limited by the nanosized water droplets that are dispersed in an oil phase and stabilized by surfactants. It is also limited by the water to surfactant ratio. Particles between 4 nm and 150 nm have been reported. Surfactants as bis(2-ethylhexyl) sulfosuccinate (AOT), sodium dodecyl sulfate (SDS), polyvinylpirrolidone (PVP), and cetyltrimethylammonium bromide (CTAB) are typically used. A limitation of this technique relies on the difficulty to scale up and the effect of residual surfactants on magnetic properties.

The hydrolysis and condensation of metal alkoxides or alkoxide precursos, leading to dispersions of oxides particles in a 'sol', followed by the drying or 'gelled' of this 'sol' by solvent removal or by chemical reaction is known as the sol-gel method[38,39]. Cobalt ferrite nanoparticles prepared by sol-gel, with grain size around 14 nm and room-temperature coercivity of 1080 Oe, were produced by Gopalan[40]. Some disadvantages of the sol-gel method include contamination from byproducts as well as the need for post-treatment of the products.

The solvothermal or hydrothermal[41] processing requires a closed vessel (autoclave). It permits to reach temperatures over the boiling point due to the pressure created inside the vessel by heating. Extreme temperature and pressure leads high quality and usually polydisperse samples. A change in morphology and size could be noticed but not controlled as in the reverse micelle case.

In the High-energy ball milling process[32,42] the magnetic powder is placed in a jar with balls of a non-magnetic material. Those jars are submitted to a rotational speed and the impact of the powder with the balls creates defects, strain and can reduce or increase the crystal size. Liu and Ding[32] used cobalt ferrite powders, with three different sizes, as starting materials for ball milling. From magnetic measurements, the coercivity and saturation magnetization values achieved were 5.1 kOe and 70 emu/g, respectively. The increase in coercivity was attributed to the large residual strain and high density of defects in the 110 nm powders. This particle size was higher than the single domain limit (40 nm), which confirmed that coercivity does not only depend on crystal size. Prolonged milling times produced nanoparticles in an amorphous matrix which reduced the coercivity.

Particles prepared by the coprecipitation method[43-46] usually have low crystallinity and polydispersity but it is the simplest, cheapest, and most environmentally friendly procedure to produce magnetic nanoparticles. In consists on the coprecipitation of metal salts aqueous solutions by addition of a base. The control on size, shape, and composition also depends on the salts used (chlorides, nitrates, sulphates, etc.), temperature, pH, etc. This method can be easily modified because it is an open system, so control on flow-rate of the addition of

reactants into the alkaline solution could be adapted. Crystal sizes in the range of the single domain are typically obtained. There is no need to use surfactants or stabilizing agents for the cobalt ferrite synthesis, so the bare product could be isolated and processed later.

3.2 Ferrites and data storage systems

3.2.1 Current status

Hard disk drives (HDDs) have been used in computers since 1950's, but it was in the 1980's when they were introduced in personal computers. Today's date HDDs are widely used by consumers to store information and are found in MP3 players, video cameras, game consoles, among others. During 2000's, the HDDs capacity was doubled almost every 12-18 months. Until recently, longitudinal recording technology was employed to store information. In this type of technology, the magnetization that lies longitudinally (parallel to disk surface) are used to store information. Perpendicular recording (magnetization lies perpendicular to the disk surface) was first proposed by Shun-ichi Iwasaki in 1975[47]. More than 30 years have passed since the possibility of utilizing perpendicular recording magnetization was pointed out but longitudinal recording stayed competitive. Only recently, HDDs using perpendicular recording were successfully released. The need to find an alternative technology to get away from the superparamagnetic limit required by longitudinal recording intensified the research on perpendicular recording the last decade. Current products have areal density between 200 and 300 (Gb/in^2)[48], although demonstrations of 500-600 Gb/in^2 have been announced for perpendicular recording[49].

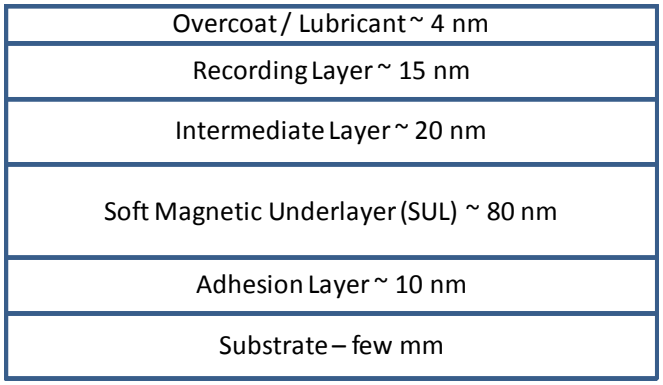

Figure 18: Different functional layers of perpendicular recording medium.

A perpendicular recording medium contains one or more layer of every functional layer but Figure 18 only includes one layer for simplicity. It consists of a substrate that is coated with an adhesion layer made of Ta, Ti, or an alloy of them. It helps to the adhesion of the other layers to the substrate. The soft underlayer (SUL) may be composed of many layers or it may be an antiferromagnetically coupled soft underlayer[50]. It helps in conducting the flux from the writing pole of the head to the trailing pole. The intermediate layer has at least two functions: 1) exchange-decoupling the SUL and the magnetic layer and, 2) provide epitaxial growth conditions for the recording layer. The function of the recording layer is to store information for long periods of time and to produce the signal when reading the information back. Carbon overcoats and lubricants help to prevent the disk from failures caused by chemical reactions or mechanical impacts.

3.2.2 Limitations and Challenges

CoCr, CoCr alloys, barium[51] and strontium ferrites, Co/Pd multilayers have been considered for perpendicular media. TABLE 7 summarizes the approximate requirements for high-density recording media and how they are related to recording performance. Candidate materials should exhibit the following characteristics: small grain size, well defined grain boundaries, high coercivity, thermal stability, anisotropy energy higher than that of the demagnetizing energy, high squareness ratio, lower noise, high signal to noise ratio (SNR). Co/Pd multilayers could show unit squareness but exhibited high transition noise. When comparing the performance of CoCrPtB and CoCrPt-oxide, CoCrPtB had a larger SNR but CoCrPt-oxide media[52] showed larger squareness and higher coercivity. For the cobalt ferrite case, the grain sizes lie beyond the superparamagnetic limit so thermal stability could be achieved. It also possesses high coercivity and large and positive first order magnetocrystalline anisotropy constant. The challenge consist of obtain well defined boundaries and will characterize them referring to signal to noise ratio. A good recording material should exhibit a balance between the previously mentioned factors.

The perpendicular coercivity[3,53], as well as the magneto-optical Kerr effect[54], reported for cobalt ferrite has increased the attractiveness of this material for high density magnetic recording and magneto-optical media, respectively.

TABLE 7: Main requirements for high-density recording media.

Parameter	Available products in 2007	500 Gbits/in.^{2}	Unit	Remarks
$M_r t$	0.7	0.7	memu/cm^3	Related to signal.
H_c	4000	6000	Oe	Related to storage, SNR, and T_{50}.
H_n	-2000	-3000	Oe	Related to thermal stability and erasure issues.
S	0.95-1	0.95-1	-	Related to dc noise.
S^*	0.5	0.5	-	Related to transition noise.
$\Delta\theta_{50}$	3.8	2-3	deg	Related to signal and noise.
Grain diameter D	7	5.7	nm	Related to SNR.
Grain size distribution	25%	15%	<D>/D	Related to SNR and thermal stability.
H_k	12000	19000	Oe	Related to writability.

4 METHODOLOGY

4.1 Experimental Procedures

4.1.1 Materials

All reagents were of analytical grade and used without further purification. The reagents used for the synthesis of pure cobalt ferrite are listed as follows:

- Sodium hydroxide, pellets, 98%, (Alfa Aesar).
- Iron (III) chloride hexahydrate, ACS, 97.0-102.0%, (Alfa Aesar).
- Cobalt (II) chloride hexahydrate, ACS, 98.0-102.0%, (Alfa Aesar).

In addition to the reagents mentioned above, transition metal salts where used for the TM-substituted cobalt ferrite syntheses. They are:

- Manganese (II) chloride tetrahydrate, ACS, 98.0-101.0%, (Alfa Aesar).
- Nickel (II) chloride hexahydrate, Reagent Plus® ,(Sigma-Aldrich).

The acid employed in the size-sensitive phase separation experiments was:

- Hydrochloric acid Trace Metal Grade, (Fisher Scientific).

Finally, the surfactants used to inhibit crystal growth included:

- Sodium oleate, (TCI America).
- Cetyl Trimethyl Ammonium Bromide (CTAB) High Purity Grade, (AMRESCO).
- Polyvinylpyrrolidone, average M.W. 58.000, K29-32, (ACROS ORGANICS).
- Sodium Dodecyl Sulfate (Fisher Scientific).
- Ethanol.

4.1.2 Conventional coprecipitation method

Ferrite nanocrystals are synthesized by the conventional coprecipitation method (Figure 19). In the conventional approach, an aqueous solution of 0.055 M Co (II) and 0.11 M Fe(III) was rapidly contacted with an excess of hydroxide (OH^-) ions. The hydrolysis reaction in the presence of an excess of OH^- ions leads to the formation of a paramagnetic Fe-Co hydroxide, which undergoes de-hydration and atomic re-arrangement conducive to a ferrite structure with no need of further annealing, according to:

$$2Fe^{3+} + Co^{2+} + 8OH^- \underset{\Delta}{\rightarrow} Fe_2Co(OH)_8 \underset{\Delta}{\rightarrow} CoFe_2O_4 + 4H_2O$$

The nucleation rate is quite high at the beginning of the precipitation process whereas the excess of OH^- ions provides a net negative surface charge to the nuclei limiting their further growth and aggregation. Under these conditions polydisperse particles of less than 30 nm in diameter are typically produced.

The reactant solution was mechanically stirred at 500 rpm and intensively heated to accelerate the dissolution/recrystallization stages involved with the ferrite formation. The intensive heating helped to reduce the reaction time dramatically. Cobalt ferrite nanocrystals were washed out with deionized water, dried at 80°C for 24 hours and characterized.

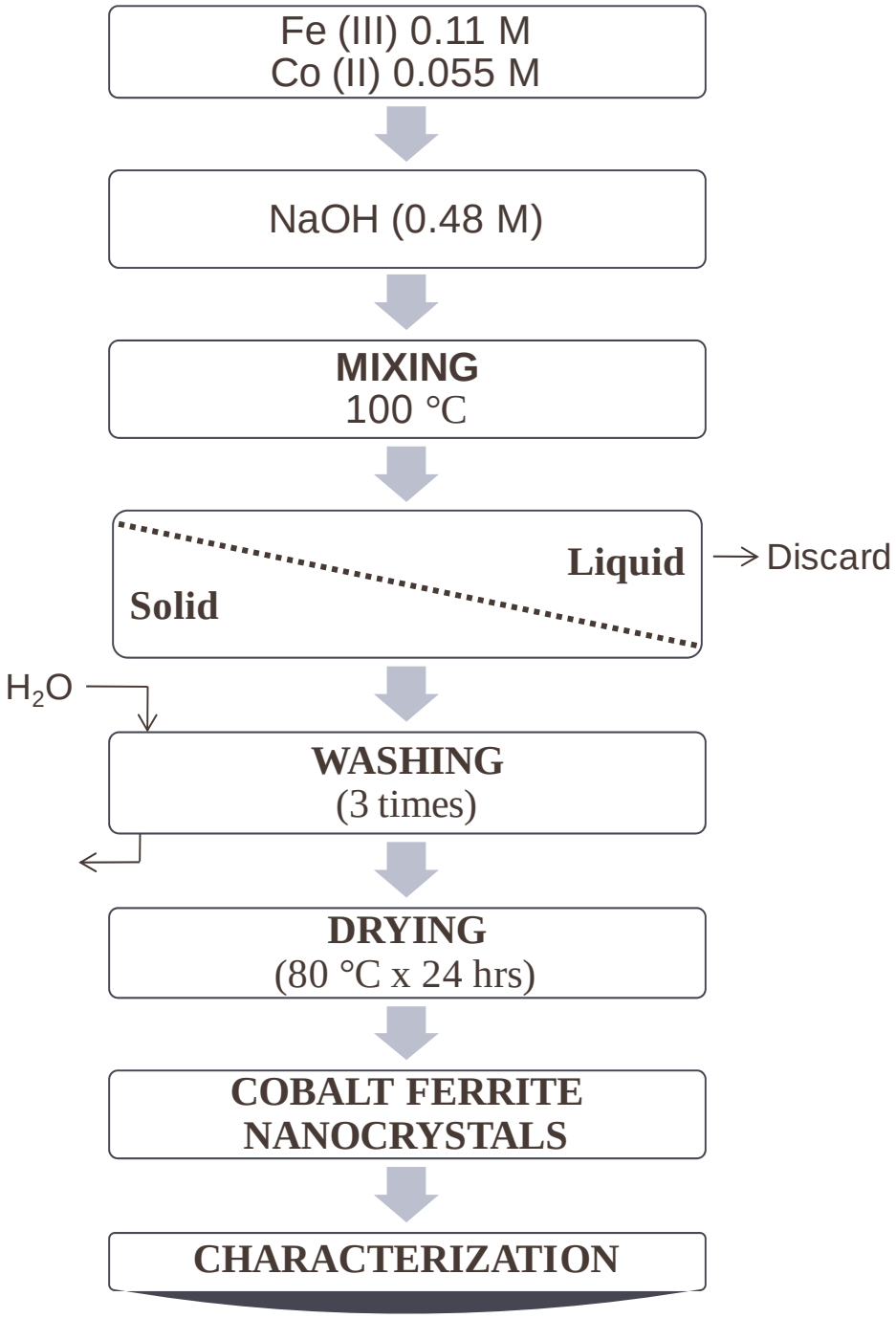

Figure 19: General Experimental Scheme: ***The Coprecipitation Method***

4.1.3 Modified coprecipitation method

In order to enhance the magnetic properties by changing the oversaturation conditions, the conventional co-precipitation route was modified by controlling the flow rate of addition of the metal ions solution to the alkaline one under intensive heating conditions. For this purpose, a micro-peristaltic pump with precise control of flow-rate was used.

4.1.4 Combined acid-washing and magnetically-assisted size-sensitive separation

4.1.4.1 Single acid washing process

The ferrite nanocrystals are produced using the modified coprecipitation method for one hour of reaction time. The reactants are contacted with the alkaline solution at a low and constant flow-rate (low flow-rates produce nanoparticles with high coercivity).

As-synthesized nanocrystals were first contacted with 5% w/w or 10% w/w HCl solutions for 30 minutes at a $\left(\frac{0.1\,g\ ferrite}{10\,mL\ acidic\ solution}\right)$ ratio. At the end of this acid treatment stage, the recovered solids were dispersed in water and submitted for the magnetically-assisted separation stage using a commercial N38 (field strength ≥ 1.2 T) neodymium permanent magnet. The particles suspension was contacted with the mentioned magnet for 2 minutes at the end of which, settled particles were separated from the suspended ones that remained in the supernatant. The solids in this supernatant represented the first fraction of the size-sensitive separation process. In turn, the magnetically settled particles were processed through the same water dispersion-magnetic separation cycle for two more times. The

fractions corresponding to the solids recovered from their corresponding supernatants and the last sediment were submitted for structural and magnetic characterization.

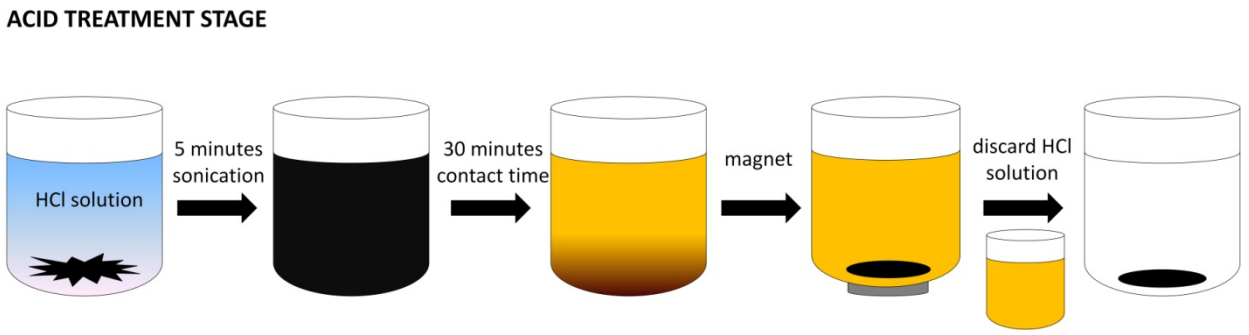

Figure 20: The acid-washing treatment stage.

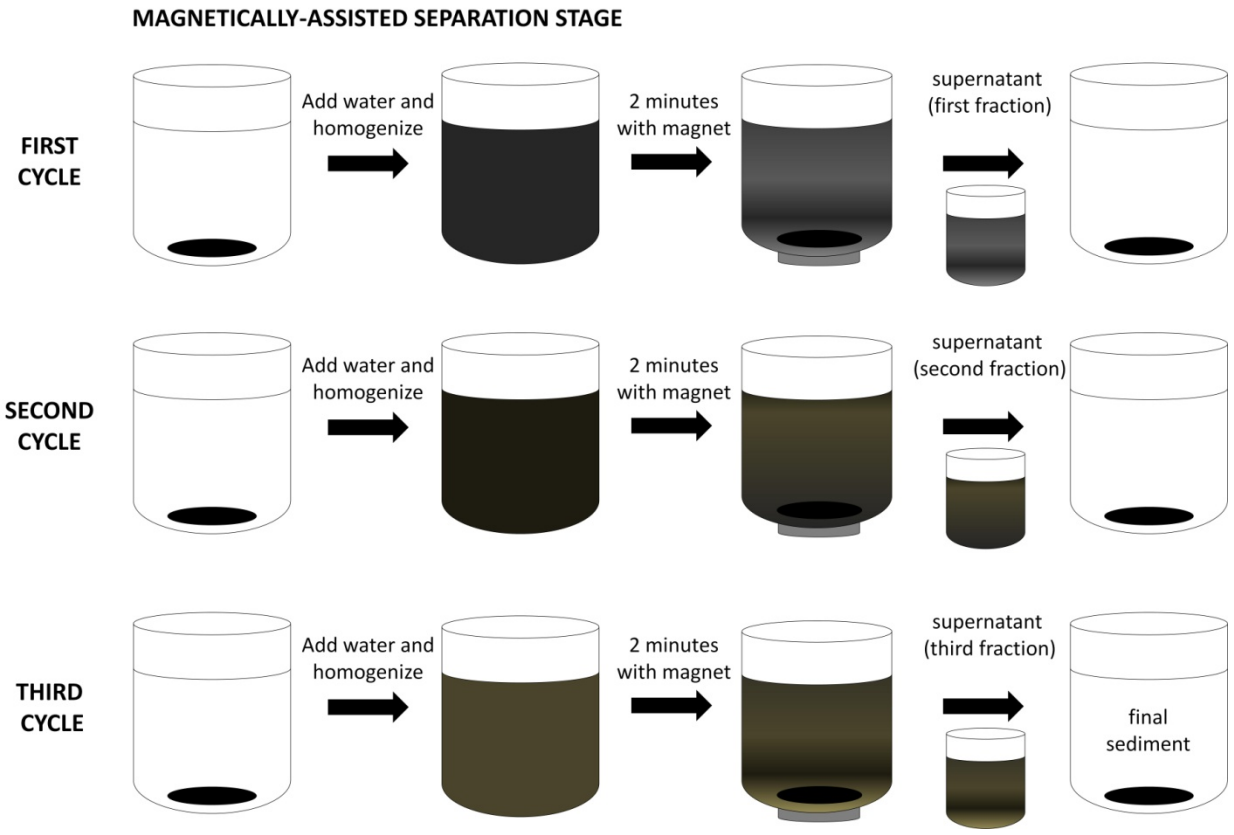

Figure 21: The magnetically-assisted separation.

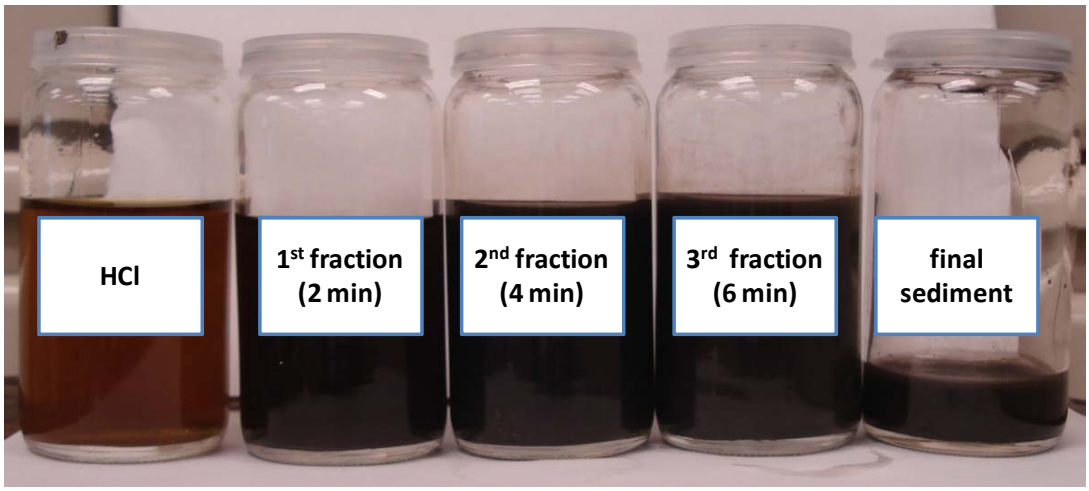

Figure 22: Images of the different fractions after the acid treatment and magnetically-assisted separation stages.

4.1.4.2 Double acid washing process

Five grams of ferrite synthesized by the modified coprecipitation method were used in the size-sensitive phase separation process and characterization. The ferrite to acidic solution ratio was the same than described in section 4.1.4 $\left(\frac{0.1\,g\ ferrite}{10\,mL\ acidic\ solution}\right)$. The fraction with the largest amount of particles was used as a starting material for a second size-sensitive separation cycle. This experimental procedure will be known as combined acid-washing and magnetically-assisted size-sensitive separation, double acid washing process.

4.1.5 Effect of the ferrite composition

4.1.5.1 Variation of the Fe/Co mole ratio

Cobalt ferrite nanocrystals with initial Fe:Co mole ratios of 3:1, 2:1, 1.7:1, and 1.4:1 were produced by the conventional and the modified coprecipitation method. The reaction time was kept constant at one hour.

4.1.5.2 Ni(II)- and Mn(II)-substituted cobalt ferrite

Cobalt ferrite nanocrystals prepared by the conventional coprecipitation method are synthesized in presence of Mn^{2+} and Ni^{2+}ions. Mn or Ni molar fractions between 0.1 and 1.0 were evaluated according to the stoichiometry: $TM_xCo_{1-x}Fe_2O_4$. The reaction time was one hour.

4.1.6 Heterogeneous nucleation experiments: Seed-mediated growth

Cobalt ferrite nanocrystals synthesized by the conventional (section 4.1.2) or modified (section 4.1.3) coprecipitation method (controlling flow-rate) will act as 'seeds' in the heterogeneous nucleation experiments. An IKA T-8 basic homogenizer was used to re-disperse the 'seeds' into aqueous solution. The homogenizer was used by 15 minutes at ~11000 rpm. Sodium hydroxide pellets were dissolved into the 're-dispersed seeds' aqueous solution followed by the addition of the metal ions solutions as in the coprecipitation

technique. Different amounts of seeds were evaluated according to the 'r' value: 0.25, 0.50, 0.75, and 1.0; where $r = \frac{g\ seeds}{g\ ferrite}$.

Figure 23: IKA T-8 basic homogenizer used to re-disperse the seeds in aqueous solution.

4.1.7 Size reduction by high-energy ball milling

Materials in this milling machine are pulverized by high energy impact (when the balls jump side to side of the jar), tangential impact (from the friction between ball-particle-ball or ball-particle-inner wall) and centrifugal impact (the balls stay around the inner wall by the centrifugal force and may overlap each other) forces. These types of impacts are related to the relative motion of the two different plates (main disk and secondary disk) in which the jars containing the sample are placed. Cobalt ferrite nanocrystals synthesized by the conventional and modified coprecipitation method were submitted to high-energy ball milling. A Fritch Pulverisseette-4 was used as the milling apparatus in our experiments;

tungsten carbide (WC) balls and jars were used to avoid contamination. The ball-milling assembly consisted of 2 jars of 45 mL with 17 balls of 10 mm diameter each. An initial ball to powder ratio (BPR) of 40:1 and milling times in the 20 minutes-10 hours range were selected. After every milling time, a small amount of sample was withdrawn from the tungsten carbide jar and submitted to characterization.

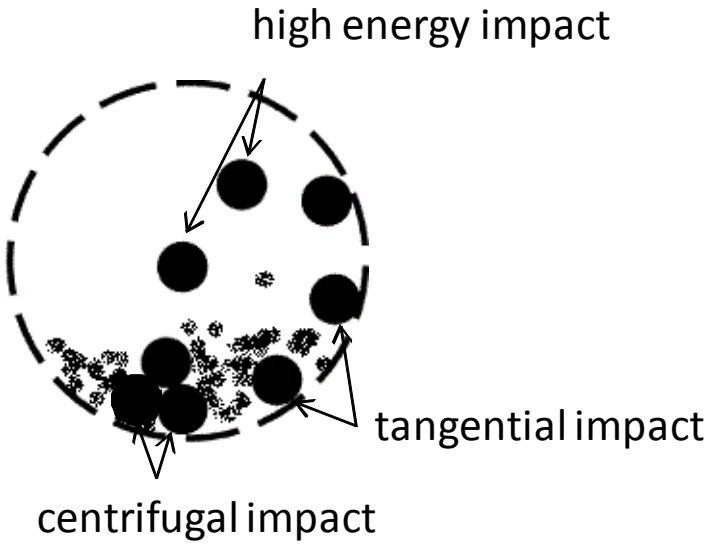

Figure 24: Fritsch Pulverisette-4 milling media (top) and the tungsten carbide jars, balls used for the milling of cobalt ferrite nanocrystals (center), and the three types of impacts involved in the milling process (bottom).

4.1.8 Shape modification by hydrothermal synthesis

Synthesis under high-pressure/temperature conditions achieved in an autoclave (Figure 25), allows the solvent to reach temperatures above the corresponding boiling point. The synthesis took place under pressurized conditions where the vapor pressure corresponding to each reaction temperature was kept constant in each experiment. A chemical reaction performed under those conditions is referred as solvothermal processing or hydrothermal when the solvent is water. In our experiments, we used the same reactants concentrations as in coprecipitation. Different temperatures were evaluated in the 100 ºC – 350 ºC range, at 50 ºC intervals. The schematic representation of the 4575 model HP/HT Pressure Reactor from Parr Instruments Company[55] is shown in Figure 26.

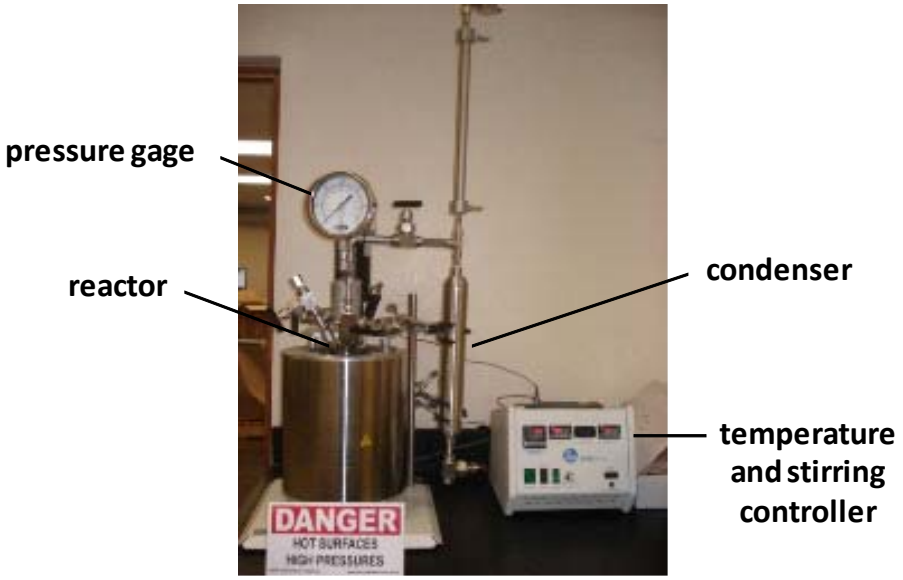

Figure 25: Autoclave reactor used for synthesis of cobalt ferrite by the hydrothermal method.

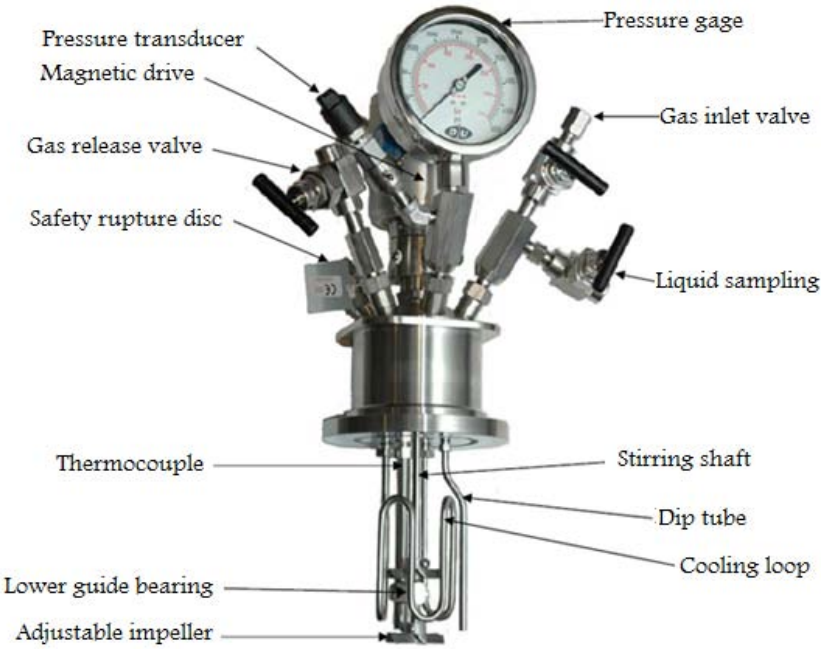

Figure 26: Schematic image of the 4575 model HP/HT Pressure Reactor from Parr Instruments Company.

4.1.9 Post-synthesis thermal treatment of ferrite powders

As an attempt to promote intergranular diffusion and hence, crystal growth, as-synthesized nanocrystals were thermally treated in a muffle furnace in the 600-900°C range. The treatment was extended by one hour in air.

4.1.10 Inhibition of crystal growth by using surfactants or polymers

The present research also addressed the determination of the superparamagnetic limits in cobalt ferrite nanoparticles. Accordingly, various types of surfactants were used in the synthesis of cobalt ferrite in order to inhibit crystal growth. Surfactants as oleic acid sodium salt (Na-oleate), cetyltrimethylammonium bromide (CTAB), sodium dodecyl sulfate (SDS), and polyvinylpyrrolidone (PVP) were evaluated. Their chemical and structural formula are shown in TABLE 8. Those surfactants were introduced into the same vessel with the sodium hydroxide solution, and heated as in the conventional coprecipitation method although for very short reaction times. Prolonged reaction times favored crystal growth. In a modified route, the boiling hydroxide and surfactant solution was removed from the heating source followed by its contact with the ionic solution containing iron (III) and cobalt (II).

TABLE 8: Surfactants and their chemical structure.

Surfactant	Chemical Formula	Structural Formula
Oleic acid sodium salt (Na-oleate)	$C_{18}H_{33}NaO_2$	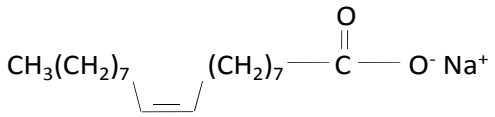
Cetyltrimethylammonium bromide (CTAB)	$CH_3(CH_2)_{15}N(CH_3)_3Br$	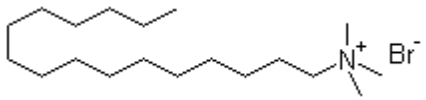
Sodium dodecyl sulfate (SDS)	$CH_3(CH_2)_{11}OSO_3Na$	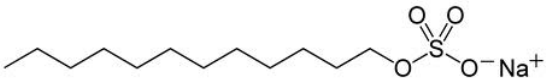
Polyvinylpyrrolidone M.W. 40000 (PVP)	$(C_6H_9NO)_n$	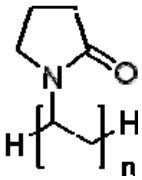

4.2 Characterization techniques

4.2.1 X-Ray Diffractometry (XRD)

In this technique, X-rays are produced when a beam of high electrons collide with a metal target. The target atoms go to excited states and lately decay back to their ground state emitting X-rays. Those X-rays are characteristic of the metal target. For our case, the target metal is Cu and usually consists of a few strong lines. The beam is filtered by using a monochromating crystal, which only allows observation of the $K_{\alpha 1}$ and $K_{\alpha 2}$ X-rays with wavelengths of 1.5405 Å and 1.544 Å, respectively.

Diffraction patterns are formed by constructive interference of diffracted beams (Figure 27). The crystal structure is related to the incident beam by the Bragg's Law.

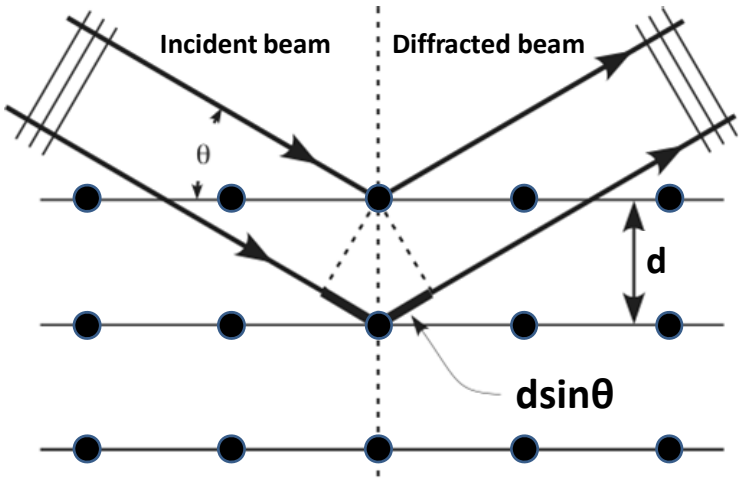

Figure 27: The diffraction phenomenon.

This law describes the angle ($2\theta_{hkl}$) formed between the incident beam and the diffracted beams. This equation has the form:

$$n\lambda = 2d_{hkl}\sin\theta_{hkl} \tag{11}$$

Where: λ is the wavelength of the incident radiation, d_{hkl} is an interplanar spacing, and θ is the diffraction angle. Diffracted electrons are used to determine crystallographic information about the sample such as crystal structure. The average crystallite size may also be determined by means of the Scherrer's equation shown below:

$$t = \frac{0.9\lambda}{B\cos\theta} \tag{12}$$

In equation (12), B corresponds to the full width at half maximum of the broadened diffraction line on the 2θ scale in radians.

Cobalt ferrite possesses a cubic structure so the lattice parameter can be determined clearing the following equation:

$$\frac{1}{d^2} = \frac{h^2 + k^2 + l^2}{a^2} \tag{13}$$

h, k, and l are the Miller indexes, d is the interplanar distance, and a the lattice parameter.

XRD analyses of our samples were performed in a Siemens D 500 powder X-Ray diffractometer located at the Engineering Science and Materials Department (Figure 28).

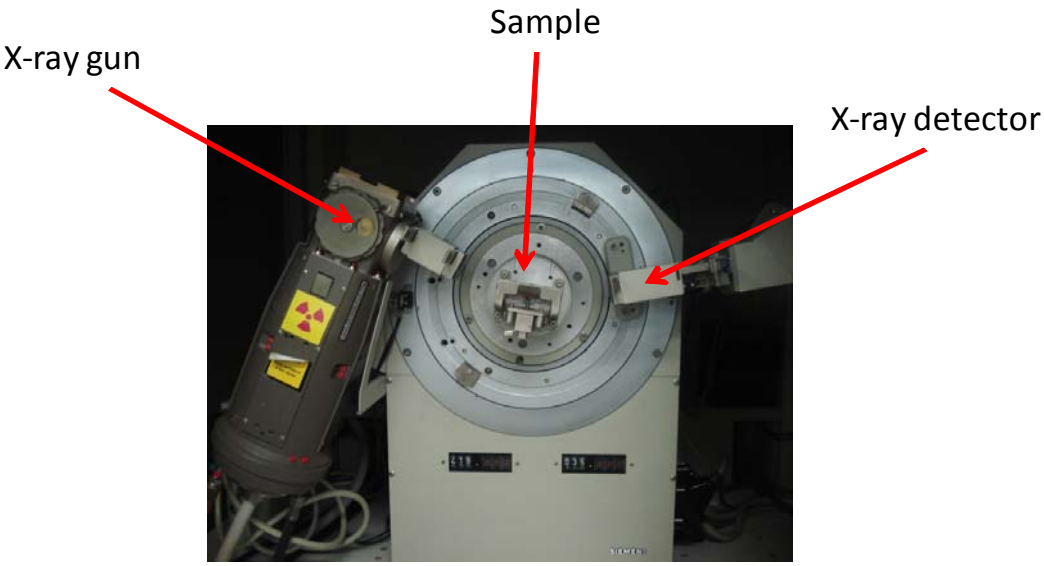

Figure 28: Siemens D500 X-Ray Diffractometer.

4.2.2 Vibrating Sample Magnetometry (VSM)

The vibrating sample magnetometer or VSM was invented in 1955 by Simon Foner at Lincoln Laboratory, MIT. The paper about his work was published shortly afterward in 1959[56]. A vibrating sample magnetometer operates on Faraday's Law of Induction, which tells us that a changing magnetic field will produce an electric field. This electric field can be measured and can tell us information about the changing magnetic field. A VSM is used to measure the magnetic behavior of magnetic materials.

A VSM operates by first placing the sample to be studied in a constant magnetic field. If the sample is magnetic, this constant magnetic field will magnetize the sample by aligning the magnetic domains, or the individual magnetic spins, with the field. The stronger the constant field, the larger the magnetization will be. The magnetic dipole moment of the sample will create a magnetic field around the sample, sometimes called the magnetic stray field. As the sample is moved up and down, this magnetic stray field is changing as a function of time and can be sensed by a set of pick-up coils. The alternating magnetic field will cause an electric field in the pick-up coils according to Faraday's Law of Induction. This electric field will be proportional to the magnetization of the sample.

The LakeShore 7400 Series Vibrating Sample Magnetometer (Figure 29) used in our work operates at a maximum magnetic field of 2.2 T with a magnet gap of 0.9 in.

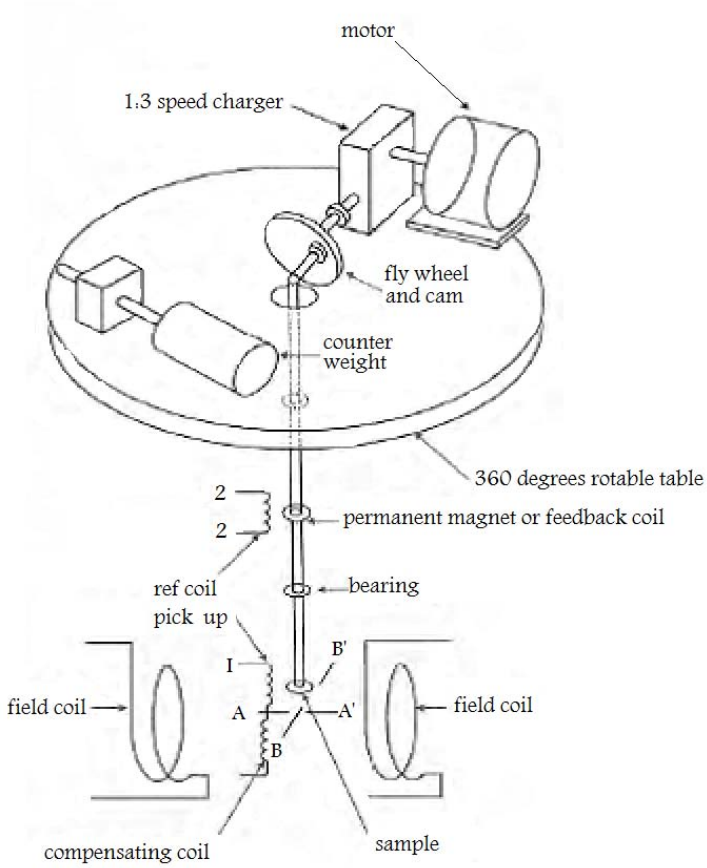

Figure 29: LakeShore 7400 Series Vibrating Sample Magnetometer (top) and schematic diagram of a vibrating sample magnetometer (bottom).

4.2.3 The Semiconducting Quantum Interference Device (SQUID)

The Magnetic Property Measurement System (MPMS®) from Quantum Design uses the Superconducting Quantum Interference Device (SQUID) technology. It will work in the 1.9 – 400 K temperature range at a maximum magnetic field of 7 T. A SQUID is a very sensitive magnetometer used to measure extremely weak magnetic fields, based on superconducting loops containing Josephson junctions to achieve superposition: each electron moves simultaneously in both directions. The Josephson junction is made up of two superconductors, separated by an insulating layer so thin that electrons can pass through. SQUIDs have been used for a variety of testing purposes that demand extreme sensitivity, including engineering, medical, and geological equipment. Because they measure changes in a magnetic field with such sensitivity, they do not have to come in contact with a system that they are testing.

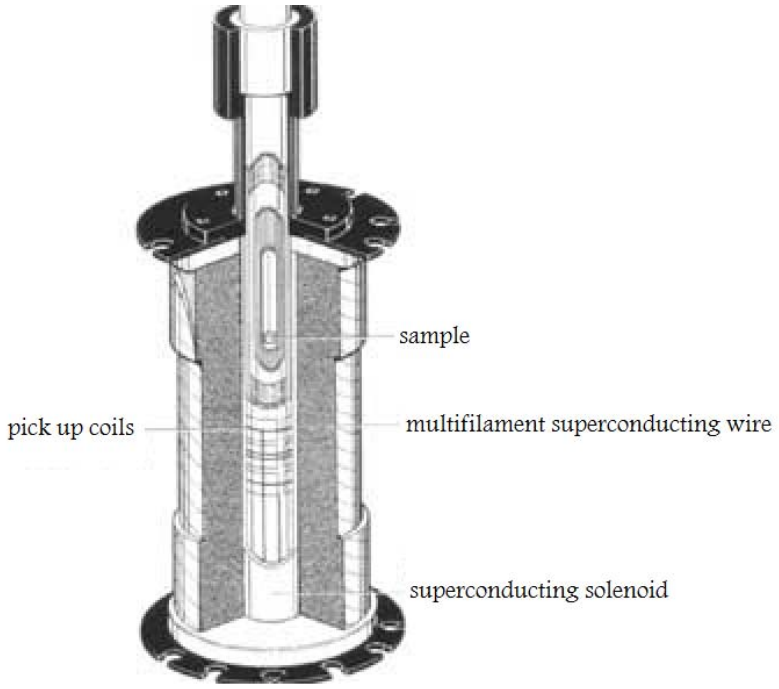

Figure 30: Quantum Design MPMSXL Superconducting Quantum Interference Device (top) and the general scheme of the device (bottom).

4.2.4 Scanning Electron Microscopy (SEM)

Accelerated electrons in an SEM carry significant amounts of kinetic energy, and this energy is dissipated as a variety of signals produced by electron-sample interactions when the incident electrons are decelerated in the solid sample. These signals include secondary electrons (that produce SEM images), backscattered electrons, diffracted electrons, photons, visible light, and heat. Secondary electrons and backscattered electrons are commonly used for imaging samples: secondary electrons are most valuable for showing morphology and topography on samples and backscattered electrons are most valuable for illustrating contrasts in composition in multiphase samples. SEM analysis is considered to be "non-

destructive"; that is, X-rays generated by electron interactions do not lead to volume loss of the sample, so it is possible to analyze the same materials repeatedly. The JEOL model JSM-5410 LV Scanning Electron Microscope was used in the present work.

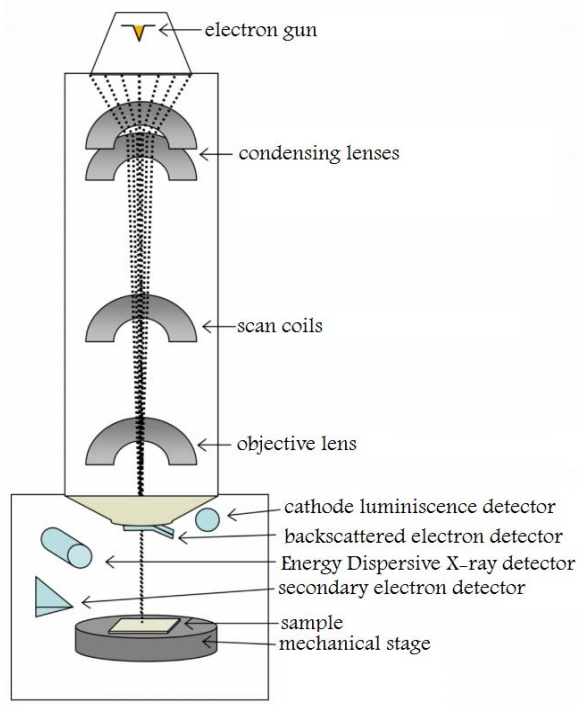

Figure 31: JEOL model JSM-5410 LV Scanning Electron Microscope (top) and general scheme of a scanning electron microscope (bottom).

4.2.5 High-Resolution Transmission Electron Microscopy (HR-TEM) and its analytical techniques: Electron Diffraction (ED) and Energy Dispersive X-Ray Spectroscopy (EDS)

Transmission electron microscopy analyses were carried out at two different places. The first one corresponds to the use of a Phillips CM 200 microscope located at the Materials Science and Engineering Department from the University of Wisconsin – Madison. The second microscope used is a JEOL 2011 located at the National High Magnetic Field Laboratory in Tallahassee, Florida.

The transmission electron microscope provides information about the structure of the specimen down to less than a nanometer. It is possible because the specimen is illuminated with a beam of high energy electrons. The interaction between the incident electrons and the atoms of the specimen leads to a variety of different signals. The information obtained (composition, structure, etc.) will depend on the kind of signal used to form the image. Important signals for our purposes are those that give rise to bright field images, electron diffraction patterns, and energy dispersive X-ray spectra. Bright field images and electron diffraction come from elastically scattered transmitted electrons, while X-ray comes from secondary signals. The elastically scattered electrons are made up of two general types of electrons: forward scattered and diffracted electrons. The forward scattered electrons travel in the direction of the incident electron beam. They have either or not scattered or, they have been scattered then re-scattered back into the incident beam direction. They are generally referred as transmitted beam and are used to form the bright field image. Diffracted electrons have been scattered elastically to form diffraction patterns by constructive interference.

Electrons are scattered into beams that exit the specimen traveling in different directions from the incident beam. For crystalline specimens, the allowed directions are related to the incident beam direction and the crystal structure by the Bragg's Law.

After an atom has been excited by a primary beam of electrons, it may relax to a ground state by a series of secondary processes. TEM are equipped with energy dispersive X-ray detectors for specimen composition determination. It can be used to determine which elements are present in the specimen by matching the energies of the strong peaks with the energies of the characteristic X-rays for the elements. The concentration of an element is directly related to the number of counts in a peak relative to all other elemental peaks.

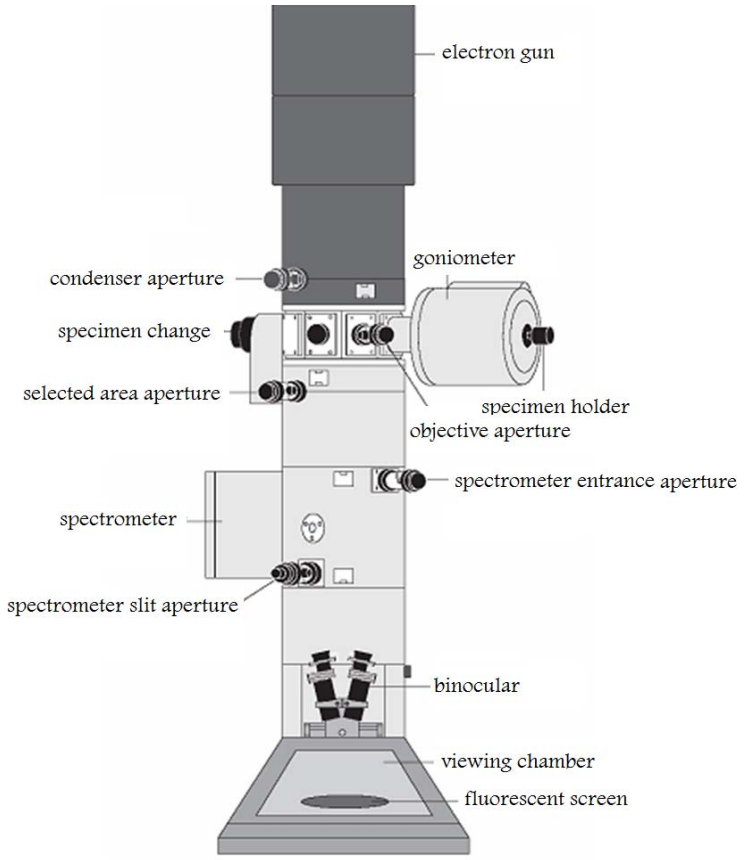

Figure 32: JEOL 2011 Transmission Electron Microscope (top) and general scheme of a transmission electron microscope (bottom).

4.2.6 Surface Area Analyzer (BET)

An isotherm is a plot of volume of gas adsorbed vs. pressure. The Brunauer, Emmet, and Teller (BET) type I isotherm is characteristic of solids on which only adsorbed monolayers are formed. An increase in gas pressure leads to a rise into the volume of gas adsorbed until a monolayer is formed, further increase of pressure does not result in more gas adsorbed. In a surface area analyzer, the sample contained in a cell is immersed in liquid nitrogen. The

nitrogen gas from a gas mixture that is continuously flowing through the sample becomes 'liquid like' due to the low temperature. Then, the adsorption takes place.

The equation for the surface area determination is:

$$S_t = K\left(1 - \frac{P}{P_0}\right) x V_a \qquad \textbf{(14)}$$

where:

S_t = total surface area of sample under analysis

K = a constant for nitrogen, assuming 'STP' conditions = 4.03

P/P_0 = 0.294 for a gas mixture of 30% N_2 / 70% He

V_a = volume of gas (N_2) adsorbed

Each cubic centimeter of N_2, adsorbed and then desorbed, by the sample is equivalent to a total surface area (S_t) of 2.84 m^2. The specific surface is found by dividing S_t by the weight of the sample in the cell in grams. Following the BET principle, the surface area can be calculated from the measurement of the volume of nitrogen gas adsorbed at liquid nitrogen temperature. The Horiba SA – 9600 series Surface Area Analyzer is available at the Engineering Science & Materials Department.

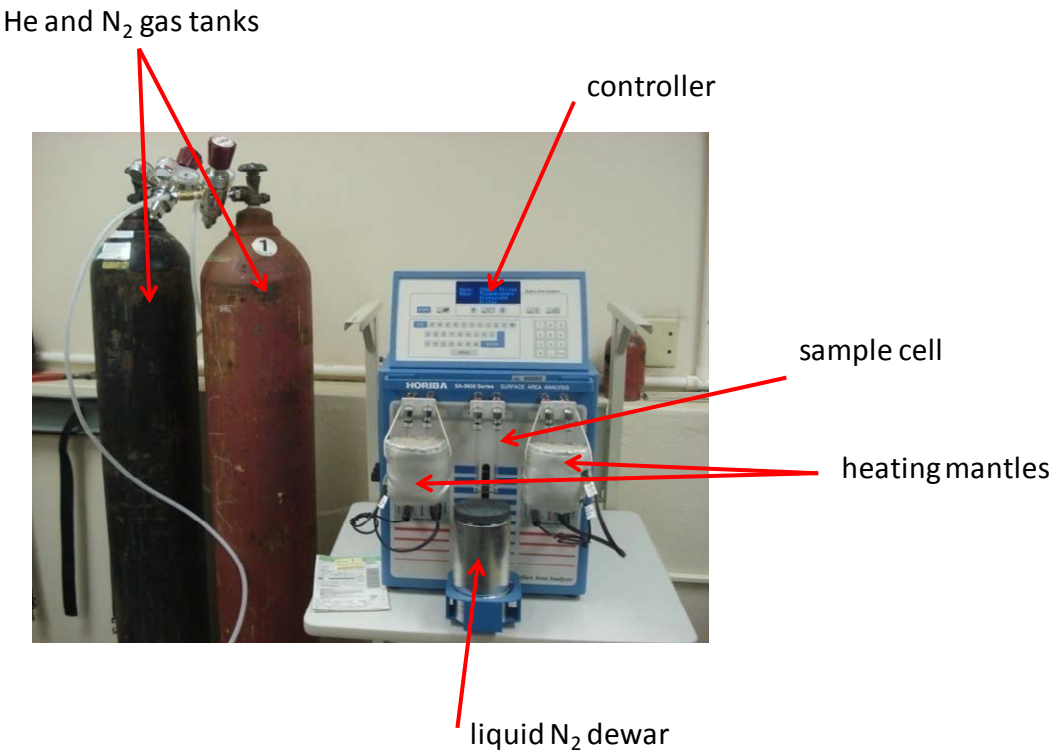

Figure 33: Horiba SA – 9600 series Surface Area Analyzer.

4.2.7 Mössbauer Spectroscopy

Mössbauer spectroscopy is a spectroscopic technique based on the recoil-free, resonant absorption and emission of gamma rays in solids. This resonant emission and absorption was first observed by Rudolf Mössbauer during his graduate studies in 1957, and is called the Mössbauer effect in his honor. Mössbauer received a Nobel Prize in 1961 for this work.

Like NMR spectroscopy, Mössbauer spectroscopy probes tiny changes in the energy levels of an atomic nucleus in response to its environment. Typically, three types of nuclear interaction may be observed: an isomer shift, also known as a chemical shift (a relative

measure describing a shift in the resonance energy of a nucleus due to the transition of electrons within its s orbital); quadrupole splitting (reflects the interaction between the nuclear energy levels and surrounding electric field gradient); and, magnetic or hyperfine splitting (result of the interaction between the nucleus any surrounding magnetic field), also known as the Zeeman effect. Due to the high energy and extremely narrow line widths of gamma rays, Mössbauer spectroscopy is one of the most sensitive techniques in terms of energy (and hence frequency) resolution.

Just as a gun recoils when a bullet is fired, conservation of momentum requires a free nucleus (such as in a gas) to recoil during emission or absorption of a gamma ray. If a nucleus at rest emits a gamma ray, the energy of the gamma ray is slightly less than the natural energy of the transition, but in order for a nucleus at rest to absorb a gamma ray, the gamma ray's energy must be slightly greater than the natural energy, because in both cases energy is lost to recoil. This means that nuclear resonance (emission and absorption of the same gamma ray) is unobservable with free nuclei, because the shift in energy is too great and the emission and absorption spectra have no significant overlap.

In its most common form, Mössbauer absorption spectroscopy, a solid sample is exposed to a beam of gamma radiation, and a detector measures the intensity of the beam transmitted through the sample. The atoms in the source emitting the gamma rays must be of the same isotope as the atoms in the sample absorbing them. The WEBRES spectrometer is available at the Engineering Science & Materials Department.

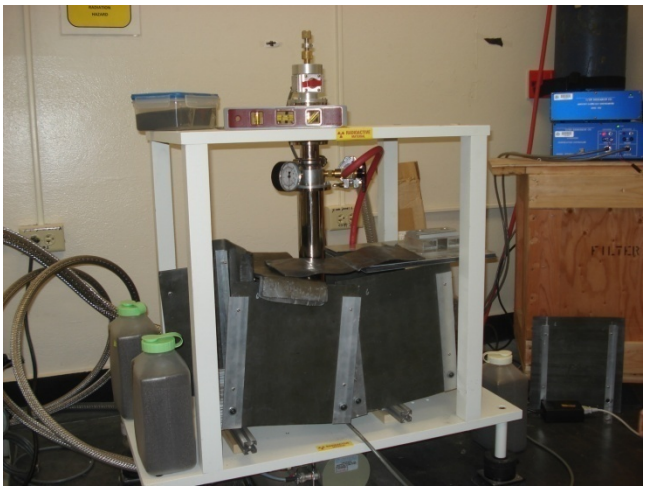

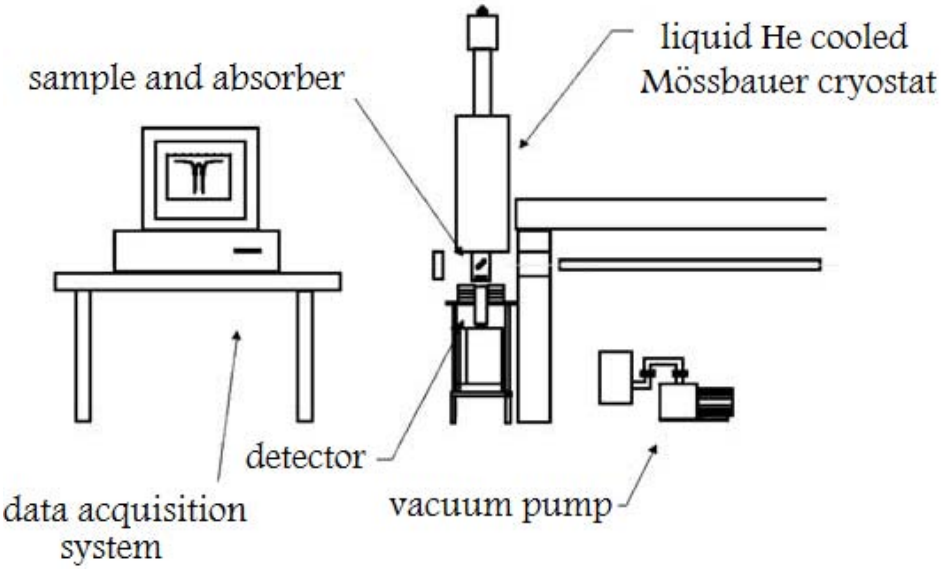

Figure 34: WEBRES spectrometer operating in the transmission mode, with a 50 mCi ^{57}Co source in a Rh matrix from Ritverc, GmbH (top) and the basic scheme of a Mössbauer spectrometer (bottom).

5 RESULTS AND DISCUSSION

5.1 Optimization of synthesis parameters

Since the crystal size corresponding to the superparamagnetic limit has been estimated at 5 nm, any effort to increase the coercivity in single crystals should consider the crystal growth above this critical value[29]. It is known that the crystal size is related to the relative interdependence between the nucleation and growth steps, which in turn can strongly be affected by the solution chemistry and precipitation conditions[8,57,58]. Synthesis parameters as reaction time, flow-rate of addition of reactants, and NaOH concentration are evaluated and discussed below. In order to evaluate the interaction between the synthesis parameters, an experimental design was developed.

5.1.1 Reaction time

A. XRD Analyses

XRD analyses confirmed the formation of the ferrite structure for a reaction time as short as five minutes. Under non-controlled flow-rate conditions, i.e. conventional coprecipitation approach, the average crystallite size was around 11 nm for reaction time from 5 to 180 minutes (Figure 35 and TABLE 9). The ferrite lattice parameter is in good agreement with the bulk value of 8.377 Å[59].

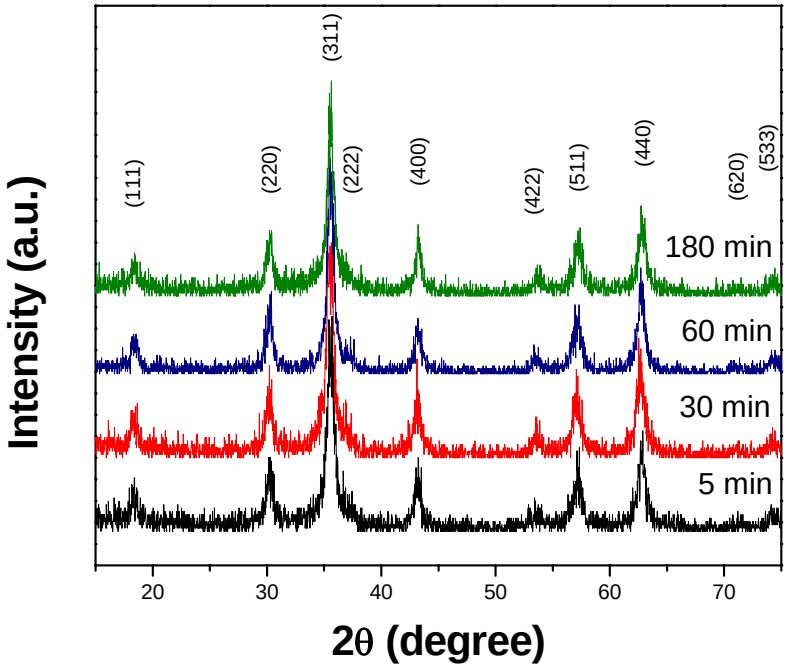

Figure 35: XRD patterns for $CoFe_2O_4$ powders synthesized at different reaction times with no control of flow-rate.

TABLE 9: Lattice parameter, 'a', and average crystallite size, 't', for $CoFe_2O_4$ powders synthesized at different reaction times.

Reaction Time (min)	a (± 0.01 Å)	t (± 0.8 nm)
5	8.37	11.3
30	8.39	11.1
60	8.38	11.4
180	8.37	11.2

B. TEM Analyses

TEM images of ferrite samples produced at 10 mL/min and 5 minutes and 60 minutes of reaction are shown in Figure 36 (a) and (b), respectively. Particles were polydisperse; however, the promotion of crystal growth by prolonging the reaction time was evidenced. The size distribution was not determined because of the aggregation of the particles but particle sizes between 10 nm and 50 nm were observed. Figure 36 (c) shows the electron diffraction (ED) patterns of nanocrystals produced at 10 minutes of reaction with no control on flow-rate. All crystallographic planes in the ED pattern are in good agreement with those of $CoFe_2O_4$, evidencing the good crystallinity of the product. A standardless TEM-EDS analysis reported Co, Fe and O atomic percents of 13.04%, 29.57%, and 57.39%, respectively. These results are very similar to the theoretical ferrite composition (Co = 14.28 %, Fe = 28.57 %, O = 57.14 %).

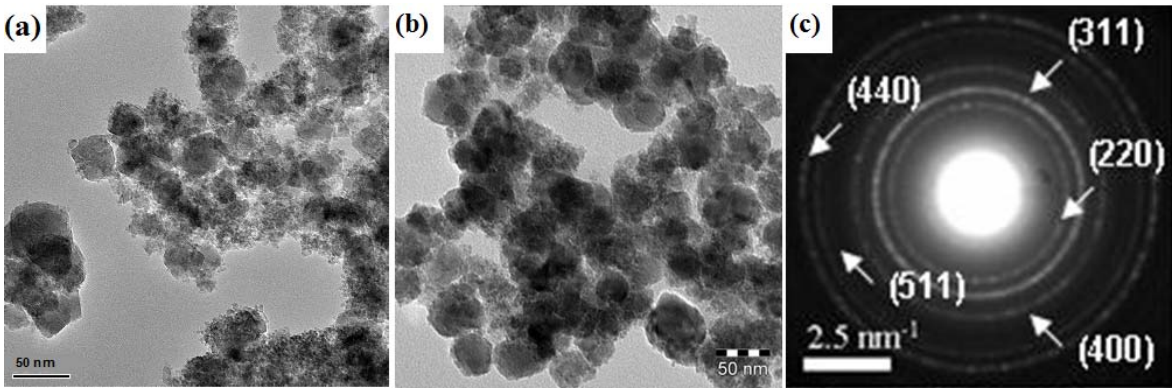

Figure 36: TEM pictures for $CoFe_2O_4$ nanoparticles produced after 5 minutes (a), and 60 minutes (b) of reaction. The flow-rate was 10 mL/min. (c) TEM-ED pattern for $CoFe_2O_4$ nanoparticles synthesized after 10 minutes of reaction.

C. M-H Measurements

Room-temperature M-H measurements confirmed the influence of crystal size on the magnetic properties of ferrite nanocrystals. As Figure 37 shows, the coercivity showed a rising trend from 316 Oe up to 805 Oe when the reaction time was prolonged from 5 minutes to 180 minutes. The corresponding maximum magnetization values did not exhibited a clear trend and ranged between 53 emu/g and 64 emu/g. The presence of superparamagnetic particles is suggested by the lack of saturation of the M-H profile. Although a long enough reaction time could have favored crystal growth, the variability in the superparamagnetic fraction in the powders could explain both, the low coercivity and magnetization values. TABLE 10 summarizes obtained results.

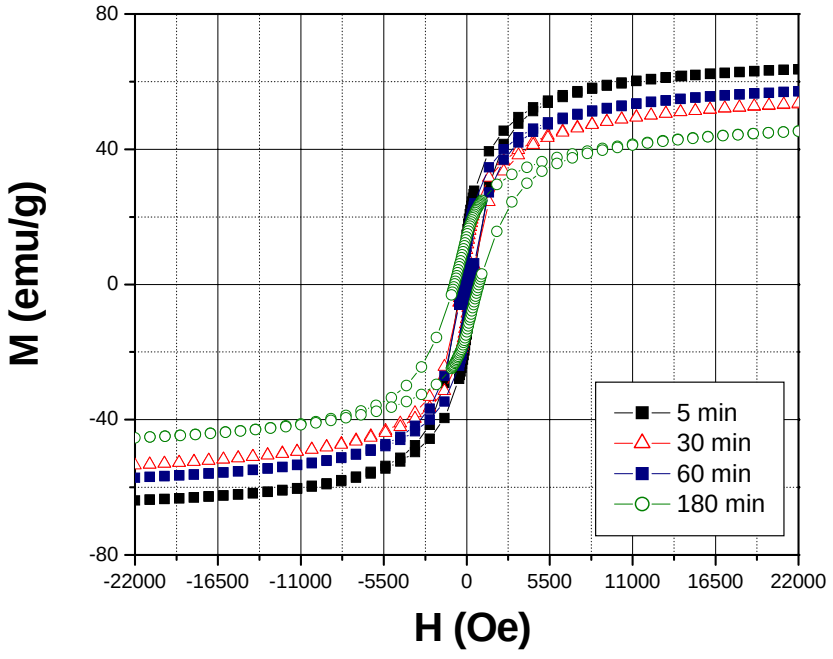

Figure 37: M-H plots (a) and loops (b) at 300K for $CoFe_2O_4$ synthesized at different reaction times with no control of flow-rate.

TABLE 10: Coercivity and magnetization for ferrite nanocrystals synthesized at different reaction times.

Reaction Time (min)	H_c (Oe)	M_{max} (emu/g)
5	316	53
30	316	57
60	405	64
180	805	45

5.1.2 Effect of flow-rate at which the reactants are mixed

A. XRD Analyses

Figure 38 shows the XRD patterns for the ferrites produced at different flow-rates of reactants additions and 60 minutes of reaction. As seen, the crystallinity of the ferrite products was very sensitive to the variation in flow-rate. Noisy XRD peaks were observed for samples synthesized over 1 mL/min flow-rate whereas well-defined and sharp peaks of the ferrite structure were observed for the solids synthesized at 1 mL/min.

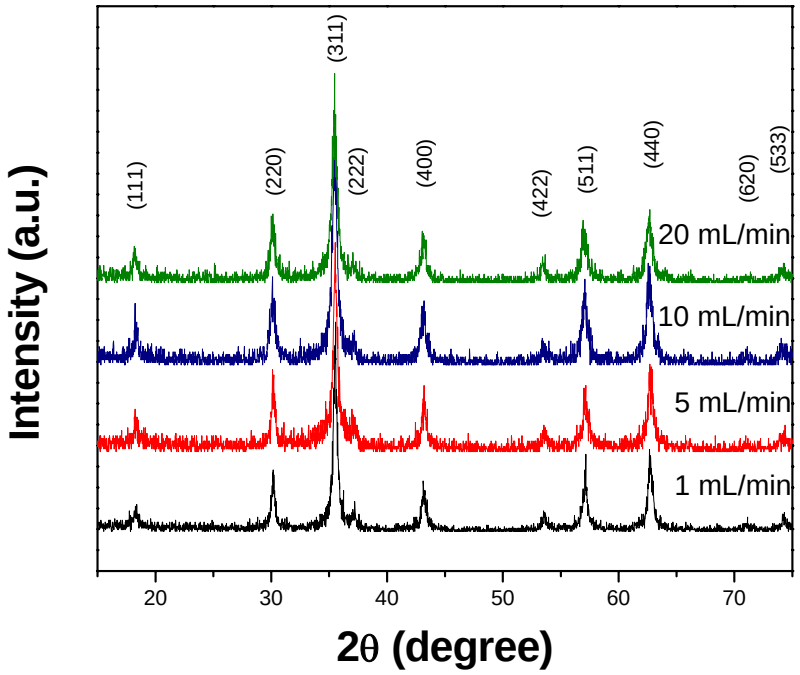

Figure 38: XRD patterns for $CoFe_2O_4$ powders synthesized at different flow rates. The reaction time was 60 minutes.

TABLE 11 summarizes the corresponding estimations of the lattice parameter and average crystallite size for the ferrite powders produced at different flow-rates. It is clear that crystal growth was promoted by controlling the flow-rate of the addition of reactants. The establishment of suitable heterogeneous nucleation conditions, where earlier nuclei should have acted as pre-existent seeds, could have promoted crystal growth. Average crystallite size varied from 18 nm to 14 nm for flow-rates between 1 mL/min and 20 mL/min, respectively. These sizes are larger than the average crystallite size obtained with no control of the flow-rate. The lattice parameter values are consistent with that of bulk Co-ferrite.

TABLE 11: Lattice parameter, 'a', and average crystallite size, 't', for $CoFe_2O_4$ nanoparticles synthesized at different flow rates of the addition of reactants.

Flow Rate (mL/min)	a (± 0.008 Å)	t (± 2 nm)
1	8.380	18
5	8.380	16
10	8.385	15
20	8.392	14

B. M-H Measurements

The coercivity was increased dramatically under controlled flow-rate conditions (Figure 39). This parameter increased from 405 Oe, (no control on flow rate), up to 4526 Oe for 1 mL/min, after 60 minutes of reaction. The corresponding maximum magnetization was 51 emu/g.

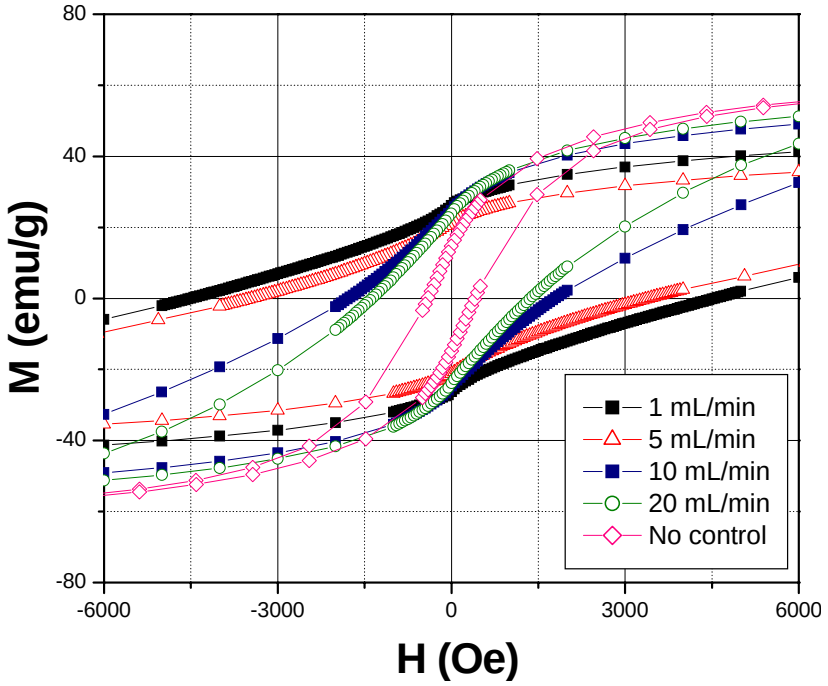

Figure 39: M-H loops at 300K for $CoFe_2O_4$ synthesized at different flow-rates. The reaction time was 60 minutes.

The precise values of coercivity and magnetization for those nanocrystals produced at different flow rates are listed in the following table. Based on information available from XRD and TEM analyses, the drastic enhancement in coercivity can be attributed to the promotion of crystal growth within the single domain region.

TABLE 12: Coercivity and magnetization values corresponding to the ferrite nanocrystals synthesized at different flow rates. The reaction time was 60 minutes.

Flow Rate (mL/min)	H_c (Oe)	M_{max} (emu/g)
1	4526	51
5	3428	44
10	1785	59
20	1368	61
No control	405	64

Figure 40 corresponds to a graph of coercivity and average crystallite size as function of flow rate. It clearly shows the inverse relationship of flow rate with coercivity and size. The slower flow rate (1 mL/min) promoted the biggest increment in size and hence, coercivity.

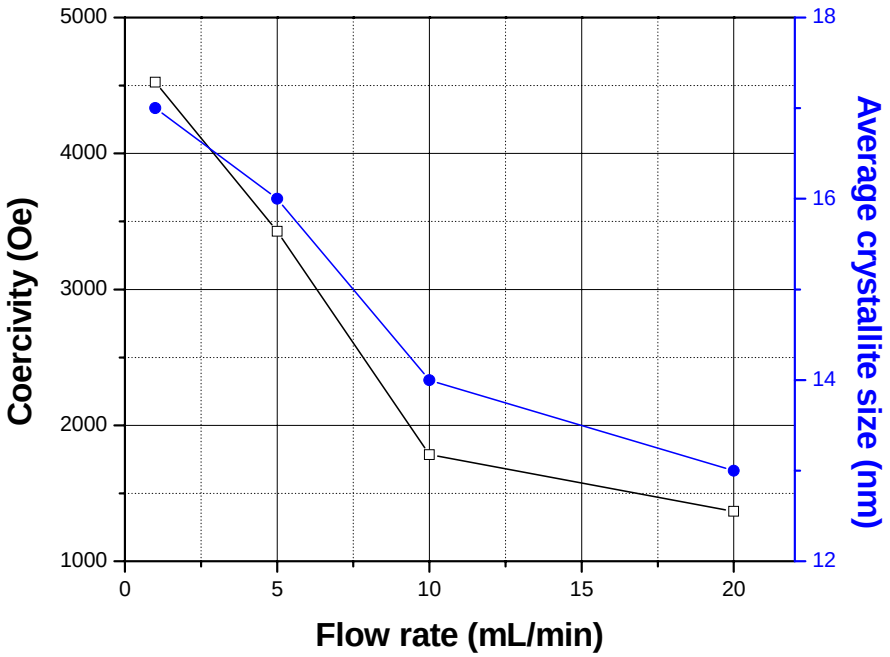

Figure 40: Cobalt ferrite coercivity and average crystallite size as function of flow rate.

5.1.3 Effect of NaOH concentration

A. XRD Analyses

Cobalt ferrite nanocrystals were synthesized at one hour reaction time by the conventional coprecipitation method at different NaOH concentration values. XRD analyses showed almost no difference in structure formation, specifically in average crystallite size and lattice parameter, when the NaOH concentration was in the 0.34 M - 0.54 M range.

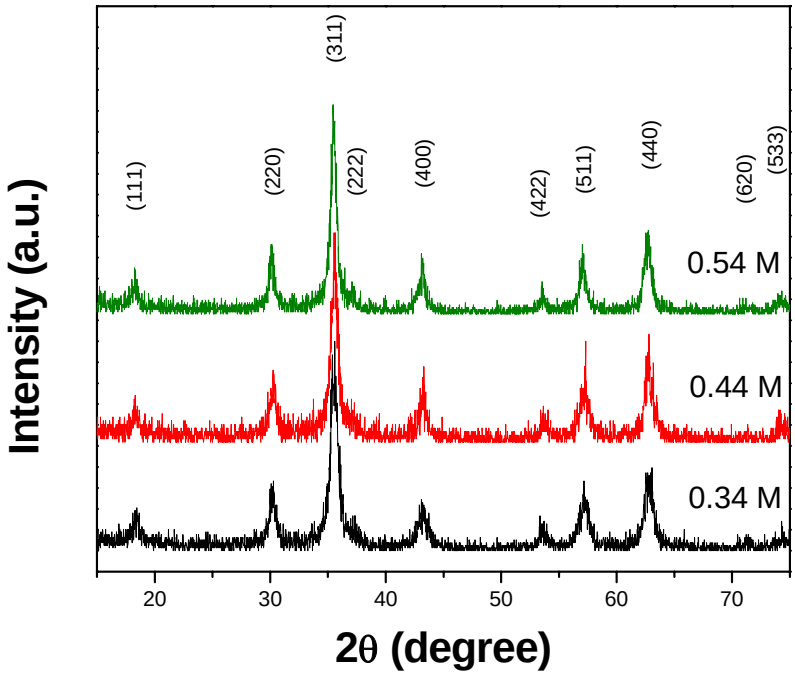

Figure 41: XRD patterns for $CoFe_2O_4$ powders synthesized at different NaOH concentrations. The reaction time was 60 minutes.

TABLE 13: Lattice parameter, 'a', and average crystallite size, 't', for $CoFe_2O_4$ nanoparticles synthesized at different NaOH concentrations.

NaOH concentration (M)	a (± 0.009 Å)	t (± 2 nm)
0.34	8.371	10
0.44	8.366	12
0.54	8.382	13

B. M-H Measurements

Room temperature M-H loops of cobalt ferrite showed an increasing trend in coercivity when the NaOH concentration increase from 0.34 to 0.54 M. The coercivity value of the nanocrystals synthesized at 0.54 M NaOH is almost three times the value of those synthesized at 0.34 M NaOH (see TABLE 14). It is known that an excess of OH^- ions can accelerate the de-hydration of the paramagnetic intermediate and the subsequent atomic re-arrangement stages in the ferrite. In addition to the conversion of the intermediate product into the ferrite, the alkaline medium probably helped to get rid of the non-magnetic layer on the nanocrystals surface.

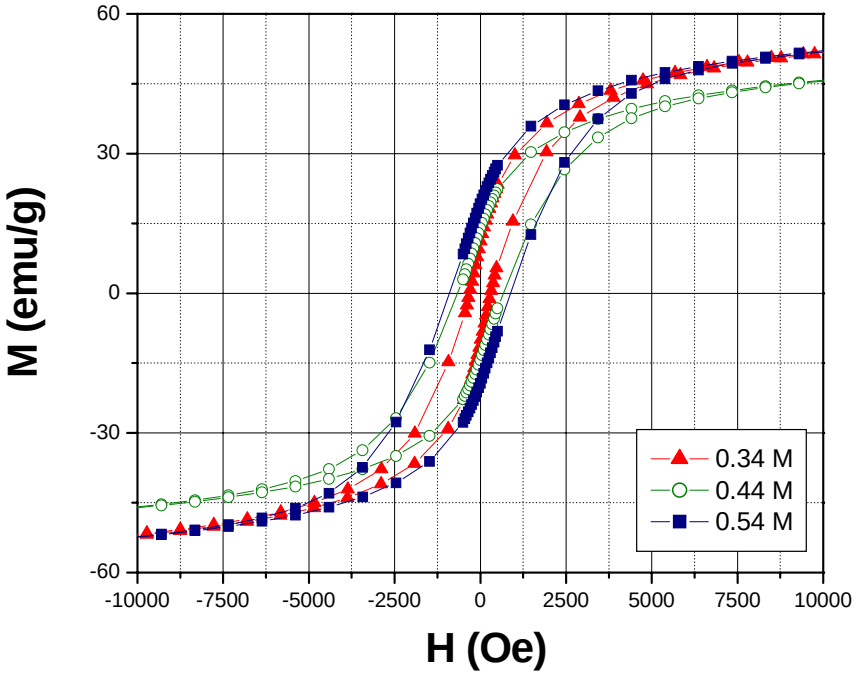

Figure 42: M-H loops at 300K for $CoFe_2O_4$ synthesized at different NaOH concentrations. The reaction time was 60 minutes.

TABLE 14: Coercivity, H_c, and magnetization, M_{max}, values corresponding to the ferrite nanocrystals synthesized at different NaOH concentrations. The reaction time was 60 minutes.

NaOH concentration (M)	H_c (Oe)	M_{max} (emu/g)
0.34	310	56
0.44	670	51
0.54	892	57

5.1.4 Experimental design

After studying the effect of the synthesis parameters on the corresponding coercivity based on a one-variable-at-the-time approach, it becomes indispensable to determine whether the interaction between selected parameters could influence the magnetic properties of the ferrite. A statistical experimental design can provide this kind of valuable information

A. 2^3 Factorial Design

In order to investigate the effect of the reaction time, flow-rate and NaOH concentration two levels for each one of these parameters (5 and 180 minutes, 0.85 and 20 mL/min, 0.34 M and 0.54M, respectively) were considered. TABLE 16 summarizes the experimental conditions and the obtained coercivity values (dependent variable). In this table, the high and low levels of the synthesis parameters are represented by the (+) and (-) signs (coded values), respectively. For example, 180 minutes and 5 minutes were the high and low level, respectively, for the reaction time. These experiments were complemented with three replicates at the center of the design to estimate the experimental error. Coercivity values

between 870 Oe (combination 'ab': 180 minutes of reaction, flow-rate 20 mL/min and NaOH 0.34M) and 4626 Oe (combination 'a': 180 minutes of reaction, flow-rate 0.85 mL/min and NaOH 0.34M), were achieved. In order to observe the wide range of coercivity that can be obtained just varying the parameters as suggested by the statistical design, the lowest and the highest coercivity values were selected and presented in Figure 43. The average crystallite size for the nanocrystals with the highest coercivity was estimated at 20 nm. A RT-coercivity of 4.6 kOe was achieved for cobalt ferrite nanocrystals. This value is close to the theoretical prediction of 5.3 kOe calculated for a system of noninteracting single domain cobalt ferrite particles with cubic anisotropy[9]. The statistical analysis of the obtained data suggested that both, the flow rate of addition of reactants and NaOH concentration were the most significant parameters at a level of confidence of 99% and 95%, respectively.

The mathematical model derived from the 2^3factorial design is:

$$Y = 2392 + 95*A - 1475*B - 329*C - 74*A*B + 69*A*C + 376*B*C - 47*A*B*C$$

The mathematical model could be used to predict the coercivity value for a given set of synthesis parameters using coded variables (between -1 and +1).

TABLE 15: Low and high levels employed in the 2^3 factorial design.

Parameter	Low level (-1)	High level (+1)
A: Reaction time (min)	5	180
B: Flow Rate (mL/min)	0.85	20
C: NaOH concentration (M)	0.34	0.54

TABLE 16: Experimental conditions for the 2^3 factorial design and the corresponding response: room-temperature coercivity, H_c.

Combinations	A B C Design	A: Reaction Time (min)	B: Flow Rate (mL/min)	C: NaOH (M)	H_c (Oe)
1	- - -	5	0.85	0.34	4518
A	+ - -	180	0.85	0.34	4626
B	- + -	5	20	0.34	871
AB	+ + -	180	20	0.34	870
C	- - +	5	0.85	0.54	2877
AC	+ - +	180	0.85	0.54	3448
BC	- + +	5	20	0.54	922
ABC	+ + +	180	20	0.54	1007

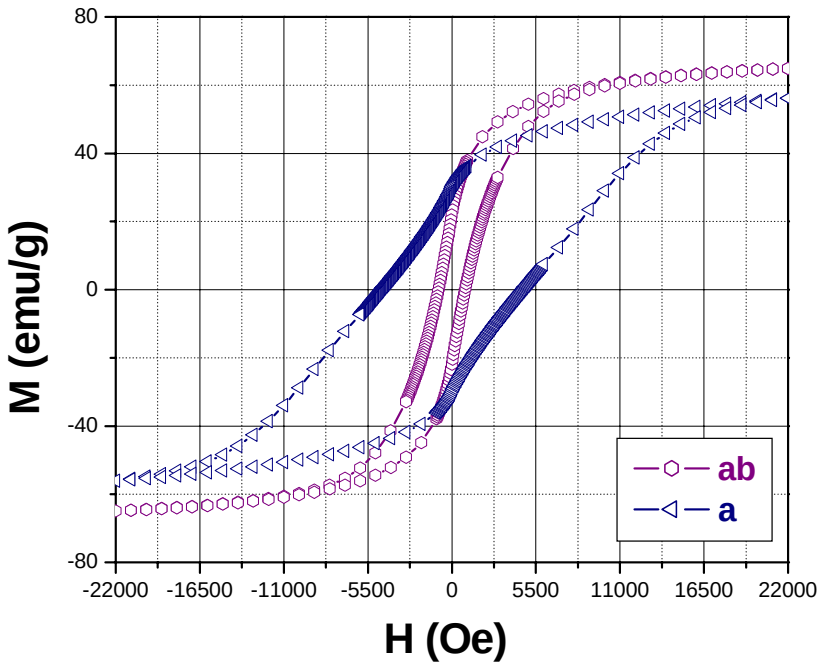

Figure 43: M-H loops at 300K for $CoFe_2O_4$ synthesized at different flow-rates (0.85 mL/min, combination 'a', or 20 mL/min, combination 'ab'). The corresponding reaction time and NaOH concentration were 180 minutes and 0.34M, respectively.

B. Complementary experimental designs

As the reaction time (A) was not significant, the 2^3 factorial design was collapsed into a 2^2 factorial design with two replicates in each point.

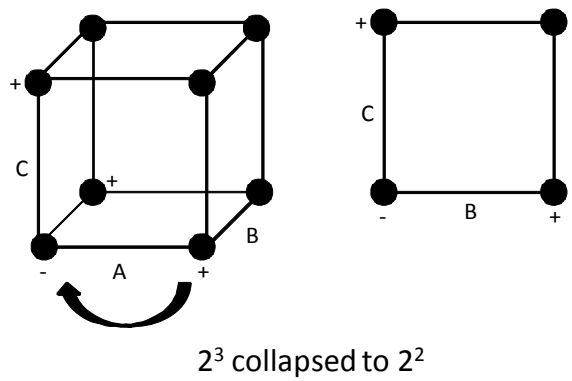

Figure 44: 2^3 factorial design collapsed to 2^2 factorial design.

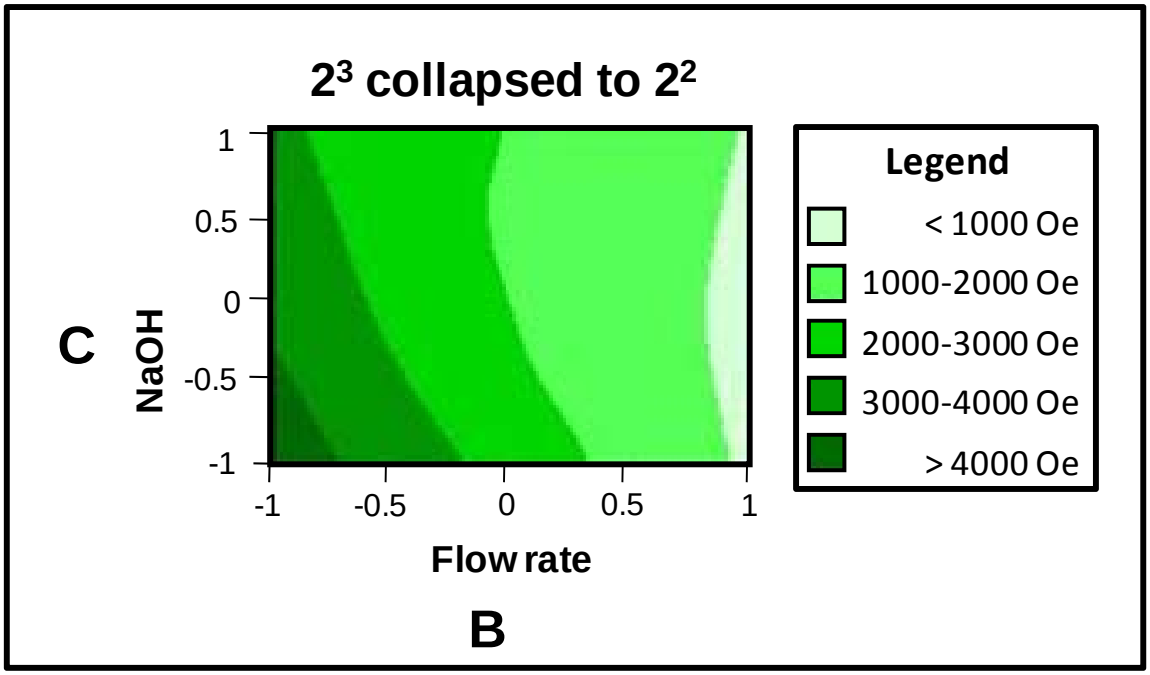

Figure 45: Contour plot of the collapsed 2^2 factorial design.

The contour plot from Figure 45 shows five different regions (tones of green). The lightest green shows the flow-rate and NaOH concentration conditions at which coercivity values of 1000 Oe and under can be obtained. Following an increasing trend on green intensity, regions with coercivity values between 1000-2000 Oe, 2000-3000 Oe, 3000-4000 Oe, and over 4000 Oe can be observed. After decoding the flow-rate and NaOH concentration limits corresponding to the darkest green, it became evident that coercivity over 4000 Oe should be achieved for a flow-rate of less than 4.2 mL/min and 0.38 M NaOH.

The mathematical model describing the 2^2 model is:

$$Y = 2392 - 1475*B - 329*C + 376*B*C$$

To facilitate the analysis of the data through response surface regression, it was decided to include new experimental designs. The different possible cases are illustrated in Figure 46.

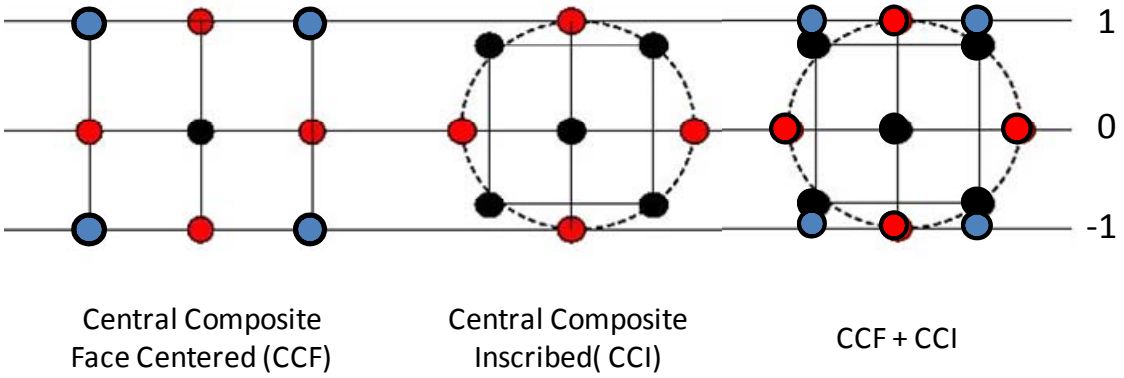

Figure 46: Experimental combinations for the additional experimental designs.

In this case, MINITAB software was used to analyze the data. For interpretation purposes in this study, P-values lower than 0.05 will indicate that a given source of variation is

statistically significant, i.e. coercivity changes significantly when the source of variation under analysis does.

TABLE 17: P-values corresponding to the analysis of CCF, CCI, and CCF + CCI experimental designs.

Experimental Design	P-values				
	B (Flow Rate)	C (NaOH Concentration)	B^2	C^2	BC
(a) Central Composite- Face Centered (CCF)	0.000	0.113	0.062	0.886	0.048
(b) Central Composite – Inscribed (CCI)	0.001	0.996	0.404	0.516	0.837
(c) CCF + CCI	0.000	0.257	0.043	0.513	0.069

CCF design (a) still indicated that both factors, flow rate (B) and NaOH concentration (C), should be controlled, while CCI design, (b), keeps only flow rate (B) as significant. However, the blend of the CCF and CCI designs, (c), suggested a fading effect of factor C. Although the p-value associated to the interaction is over 0.05, (i.e. 0.069) it is pretty close to it. A better insight in this aspect can be gathered from the contour plots (Figure 47), where an interaction between B and C seems evident: low flow-rate and low NaOH concentration cover the area of highest coercivity. Comparing contour plots from 2^2 factorial design and the blend between CCF + CCI it is evident that the region over 4000 Oe has been redefined. It means that the region comprising the highest coercivity has been narrowed in the CCF + CCI. This implies that contour plot corresponding to the 2^2 factorial design covered an area which has not necessarily coercivity over 4000 Oe as indicated.

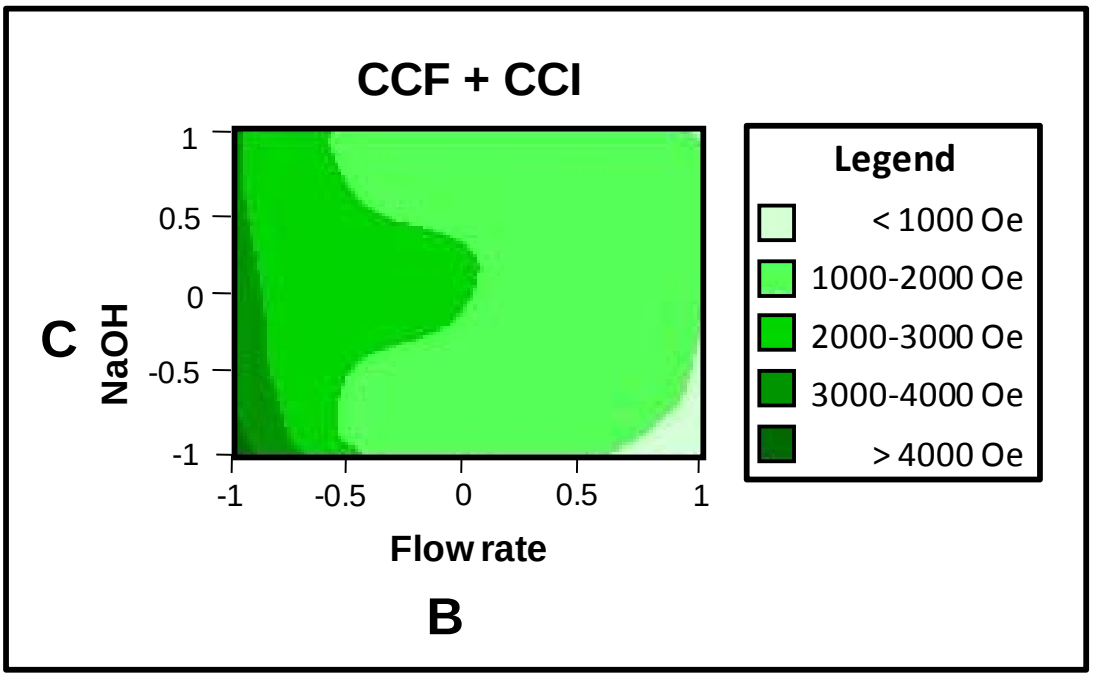

Figure 47: Contour plot of the CCF + CCI experimental design.

C. Maximization of the dependent variable: room-temperature coercivity

Coercivity values over 4000 Oe are represented by the darkest green area in the contour plot of Figure 47. The information in the contour plot clearly indicates that the lower the flow-rate and NaOH concentration the higher the coercivity. Based on this information, the cobalt ferrite synthesis at the lowest flow-rate (0.63 mL/min flow-rate, limited by the peristaltic pump) and a NaOH concentration as low as 0.29 M NaOH (we need to ensure that the complete formation of the ferrite will take place) were evaluated. It corresponds to (-1.02, -1.50) in coded values. Under these conditions, cobalt ferrite powders with a H_c of 3739 Oe, which was below to the value achieved by following the minimum synthesis parameters of

the (-1,-1) design, was obtained. The drop in coercivity could be consequence of an incomplete formation of the ferrite due to the lower NaOH concentration.

Under the above considerations, synthesis of cobalt ferrite under conditions between the minimum allowed by experimentation and minimum suggested from the (-1,-1) design was carried out. These parameters were: 0.74 mL/min of flow-rate and 0.315 M NaOH (coded: -1.01, -1.25). This time, the powders exhibited coercivity as high as 5373 Oe. This coercivity value was the highest obtained from direct synthesis without any additional treatment as was clearly suggested from the outputs of the experimental design.

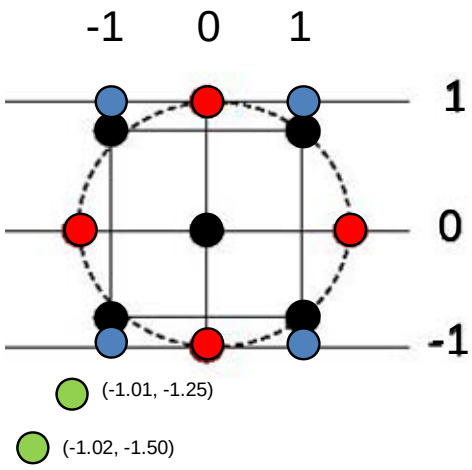

Figure 48: Experimental points for the maximization of coercivity experiments.

A mathematical model explains the dependence between the response variable with the synthesis conditions and their eventual interactions. In the present case, the mathematical model helped out to predict the coercivity value for a given set of flow-rate and NaOH

concentration levels. Our previous work allowed building the mathematical model obtained from the CCF + CCI design:

$Y = 1721.36 - 1264.53*B + 529.51*B^2 + 332.16*B*C$.

This mathematical model only takes into account the statistically significant parameters and interactions (those with p-values below 0.05).

Concluding remarks

The application of statistical design, minimizing the experimentation resources, led to maximization of coercivity in 17% comparing to the maximum coercivity obtained from one-variable-at-the-time approach. The significance of flow rate and NaOH concentration was confirmed. The statistical design showed the importance of the interaction between these factors, which cannot be determined by one-variable-at-the-time experiments.

It was obtained for a flow rate of 0.74 mL/min and 0.315 M NaOH. These synthesis parameters are out of range when compared to the pre-established levels. The optimized synthesis parameters were used for coercivity maximization purposes (i.e. size-sensitive phase separation).

5.2 Combined acid-washing and magnetically-assisted size-sensitive separation

Nanometric cobalt-ferrite ($CoFe_2O_4$) particles display unusual properties that increase its attractiveness for advanced technological applications ranging from biomedical treatment agents[60] to magnetic storage media. In particular, good chemical stability and mechanical hardness, large positive first order magnetocrystalline anisotropy constant and room-temperature high coercivity values makes this nano-size ferrite a promising candidate for magneto-optical recording media[53,61,62]. The modified size-controlled coprecipitation method to synthesize ferrite nanocrystals can allow a fine tuning on the average crystallite size within the single magnetic domain region; however, the product is still polydisperse in size[63]. On the other hand, superparamagnetism is a size-dependent phenomenon where thermal energy overcomes the aim of magnetic moment vectors to get magnetized when a magnetic field is applied. Therefore, superparamagnetic particles are easily demagnetized contributing with near-zero coercivity and low saturation magnetization. Accordingly, any attempt to achieve higher coercivity values in cobalt ferrite must consider the development of an alternative approach in order to obtain more homogeneous crystal sizes with less or null presence of superparamagnetic particles. Taking into account the strong influence of crystal size on coercivity, some efforts focused on size separation had been developed. Chinnasamy et al.[64] proposed a size-selection procedure that, although providing interesting results, was time consuming and required a variety of reagents as surfactants and solvents. We propose a rapid and simple size-sensitive phase separation treatment based on the size-dependence of

nanoparticles solubility in aqueous phase. In the case of particles with narrow size distribution, the dissolution behavior will depend on the ferrite degree of inversion and composition[65]. However, when moderately polydisperse nanocrystals are synthesized, the selective dissolution of tiny individuals can be expected according to the Oswald-Freundlich law[66] i.e., particles with smaller diameter will be more soluble than bigger ones. We will take advantage of this fact to get rid of the superparamagnetic or smaller particles that do make the coercivity of the powders to decrease. The selective dissolution of superparamagnetic particles will be complemented by a magnetically-assisted size-separation stage.

5.2.1 Single acid washing process

5.2.1.1 Effect of acid concentration (5% and 10% w/w)

A. XRD Analyses

Figure 49 shows the XRD patterns of the as-synthesized powders, i.e., before acidic treatment, and of those fractions recovered after 4 minutes or 6 minutes of magnetic separation. The final sediment corresponds to the settled solids at the end of the magnetic separation step. All XRD reflections correspond to the cubic spinel structure of cobalt ferrite. The corresponding average crystallite size varied from 16 ± 2 nm, in the as-synthesized sample, to 22 ± 2 nm in the fraction recovered after 6 minutes of magnetic separation. This enlargement on average crystallite size can be attributed to the preferential acidic dissolution of small nanoparticles, including the superparamagnetic ones, along with an efficient magnetically-assisted size classification. The average crystallite size for the same fraction

was 20 ± 2 nm when the as-synthesized cobalt ferrite nanoparticles were previously treated with a 5% w/w HCl solution. Evidently, less concentrated HCl solutions should have dissolved a minor fraction of the small individuals. In all cases, the lattice parameter varied between 8.33 ± 0.02 Å for the nanoparticles recovered at the end of the acidic dissolution and magnetic separation stages and 8.40 ± 0.02 Å for the as-synthesized ones.

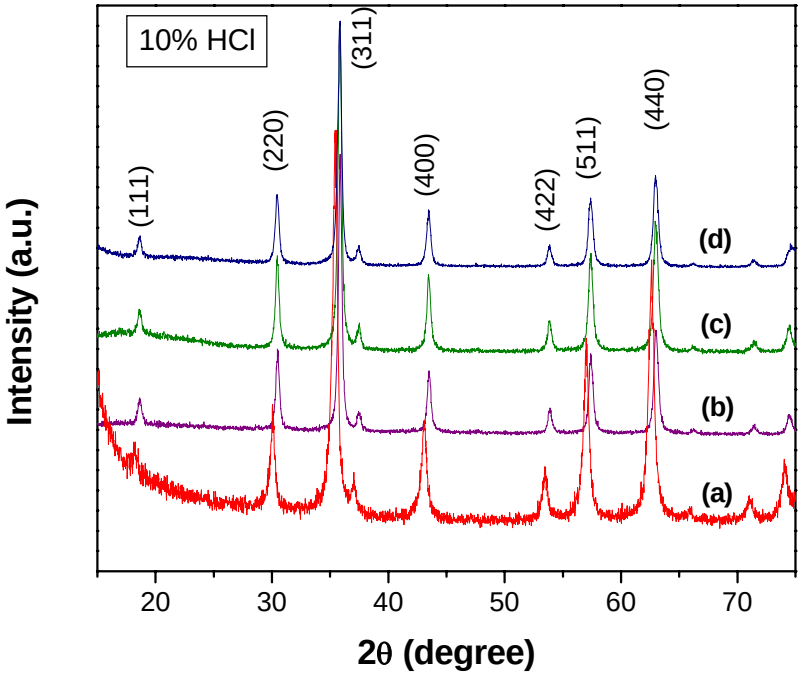

Figure 49: XRD patterns of $CoFe_2O_4$ powders before (a) and after acidic treatment with 10% HCl followed by magnetically-assisted separation. The patterns correspond to the solids contained in the fractions collected after 4 minutes, (b), and 6 minutes, (c), of magnetic separation and the sediment at the end of this stage, (d).

B. TEM and EDS Analyses

TEM images of Figure 50 correspond to the as-synthesized cobalt ferrite nanocrystals, (a), and the solids recovered after acidic treatment and 6 minutes (fraction 3) of magnetically-assisted separation with 5% and 10% HCl (b-c). The particle size in the as-synthesized sample ranged from 5 nm to 60 nm. In turn, sizes varying from 28 ± 14 nm to 30 ± 9 nm were observed in those fractions recovered after 6 minutes (fraction 3) of magnetic-separation treated with 5% and 10% HCl, respectively. Particles treated with 10% HCl exhibit narrower size distribution than those treated with 5% HCl. The full set of fractions for the 10% HCl case is shown in Figure 51. It is evident the increment in crystal size with an increment in separation time. The electron diffraction pattern and high resolution image from Figure 52 show the high crystallinity of the product. The (220), (311), and (440) crystallographic planes are clearly identified observed. The high resolution TEM image of a nanocrystals exhibit atomic planes with a interplanar distance around 2.5 Å corresponding to the (311) crystallographic plane.

TEM - Energy Dispersive Spectroscopy analyses were performed to measure the elemental composition and calculate the experimental Fe:Co mole ratio. TEM-EDS of cobalt ferrite nanocrystals suggested that selective dissolution of Fe could have taken place after contacting them with the 10% w/w HCl solution. The Fe:Co mole ratio decreased from 1.81:1 in the non-treated sample, down to 1.58:1 after the acidic treatment. No significant decrease in the Fe:Co atomic ratio was observed in those samples treated by a less concentrated 5% w/w HCl solution; the corresponding Fe:Co mole ratio was 1.80:1. The

selective dissolution of Fe in bulk ferrite was suggested by Figueroa's et al.[67]; they attributed the drop in the Fe:Co ratio to the removal of the less crystalline surface layer of iron oxide in cobalt ferrite produced by thermal decomposition.

As-synthesized particles show agglomeration while treated particles have better dispersion. It may be a result of electrostatic repulsion resulting from the chemisorption of charged species, in this case H^+, on the nanocrystals surfaces.

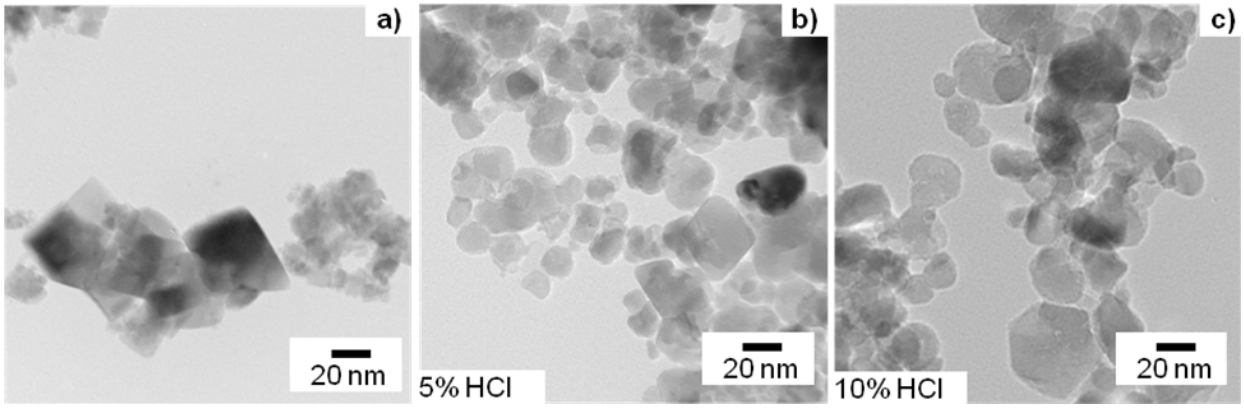

Figure 50: TEM images of $CoFe_2O_4$ powders before, (a), and after acidic treatment with 5% HCl v/v, (b,) or 10% HCl v/v, (c), followed by magnetically-assisted separation for 6 minutes.

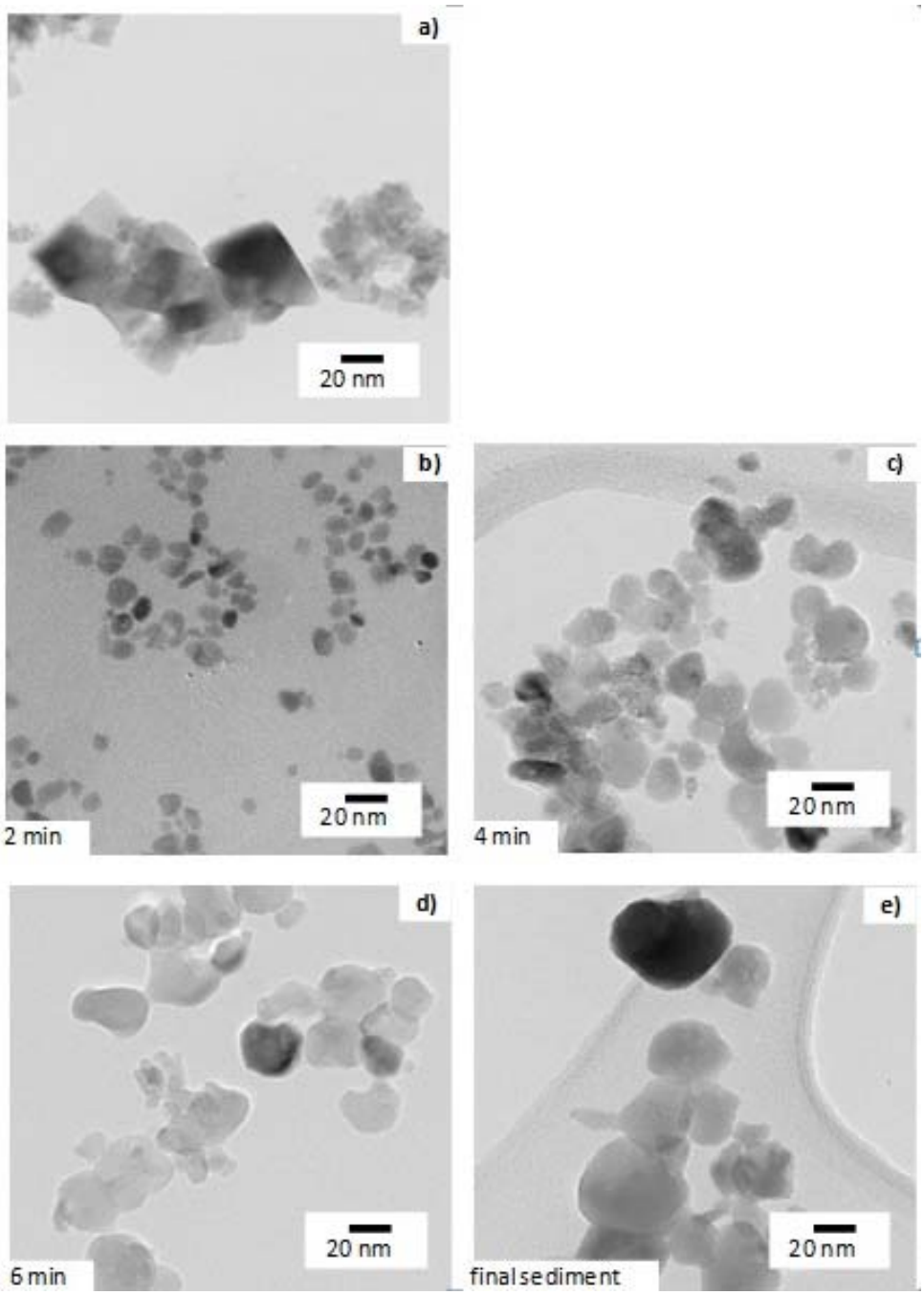

Figure 51: TEM images of $CoFe_2O_4$ powders before, (a), and after acidic treatment with 10% HCl followed by magnetically-assisted separation at different times (b-e). The images correspond to the solids contained in the fractions collected after 2 minutes, (b), 4 minutes, (c), and 6 minutes, (d), of magnetic separation and the sediment at the end of this stage, (e).

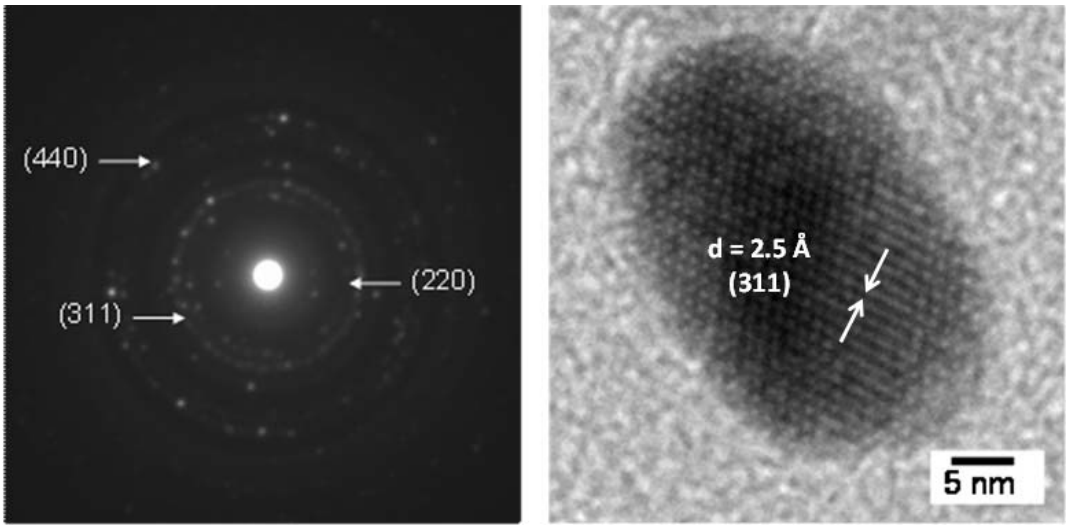

Figure 52: Electron diffraction pattern (ED) and High-resolution TEM image of a 16 nm cobalt ferrite nanocrystal showing high crystallinity.

C. M-H Measurements

Figure 53 shows the M-H loops for cobalt ferrite nanocrystals before and after treatment with HCl solutions and subsequent magnetic separation. The loops for the treated samples correspond to the fraction recovered at the end of the magnetic separation stage. The coercivity of the as-synthesized ferrite powders was 5.4 kOe. It was increased up to 8.0 kOe or 9.4 kOe after treating the powders with 5 % w/w or 10 % w/w HCl, respectively. The squareness ratio increases with the increase in coercivity up to 0.69 for the 9.4 kOe sample. The maximum magnetization of this high coercivity sample is 58 emu/g. The 'constricted loops' observed in the central part of the M-H loops suggest a mixture of soft and hard material in the powders. In this case, the soft material corresponds to the superparamagnetic fraction. In turn, the large room-temperature coercivity in these powders can be attributed to

the enlargement of their average crystal size caused by the removal of the superparamagnetic fraction during the acidic treatment and the subsequent size-sensitive magnetic separation stages. This interpretation is supported by the results provided by TEM and XRD analyses on these samples. Furthermore, the reduction in the Fe:Co atomic ratio in the size-selected cobalt ferrite particles, suggested by TEM-EDS analyses, could also be involved with the drastic change in coercivity. In this case, acidic treatment should have promoted the removal of a poorly crystalline and magnetically disordered surface layer of iron oxide. Recently, Limaye et al.[68] reported a coercivity value around 9.47 kOe. It was obtained from an oleic acid capped cobalt ferrite sample that exhibited 18 emu/g of saturation magnetization for an external applied field of 6 T. Such low magnetization value is attributed to the non-magnetic capping ligand which at the same time is the responsible for the high coercivity due to surface anisotropy. To our knowledge, this is the first time that such a combination of high coercivity, large magnetization, and squareness ratio for single domain cobalt ferrite nanocrystals has been reported.

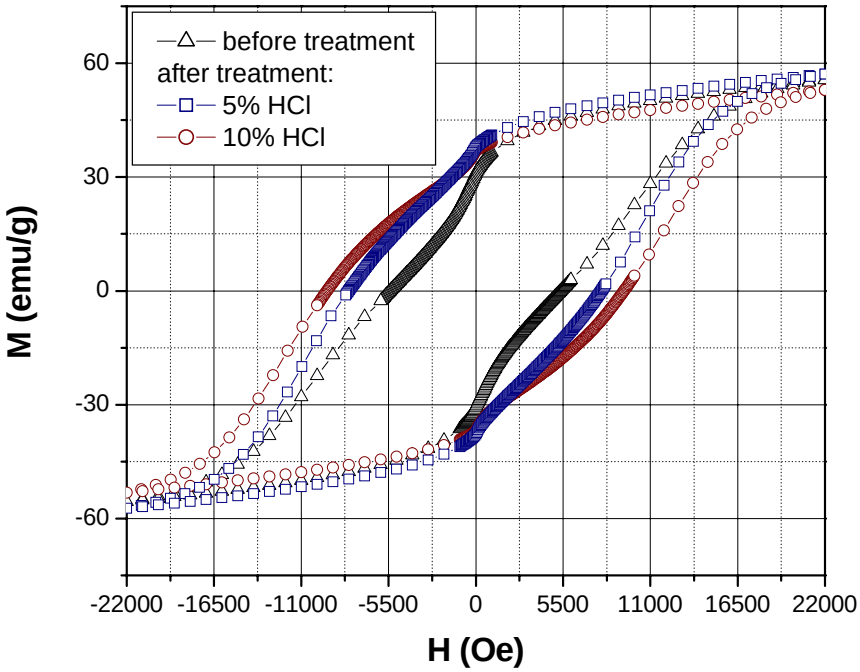

Figure 53: Room-temperature M-H loops of $CoFe_2O_4$ powders before and after acidic treatment followed by magnetically-assisted separation for 6 minutes. The HCl concentrations for the acidic treatment of the samples were 5% v/v and 10% v/v.

D. Mössbauer Spectroscopy Analyses

Mössbauer spectra for the cobalt ferrite powders without treatment and the sample recovered at the end of the magnetic separation stage are shown in Figure 54 (a) and (b), respectively. The spectrum of Figure 54 (a) clearly showed a broadened central peak, attributed to the presence of superparamagnetic particles, in addition to the hyperfine splitting typical of magnetically ordered iron species in the ferrite lattice. The relative abundance of the superparamagnetic portion was calculated at 19.3 % while the combined three magnetically split sites accounted for 81.7 % of the remainder of the cobalt ferrite. Data shown in Figure 54 (b) was fitted by using three components as indicated. No central peak was observed,

which suggest the complete removal of the superparamagnetic fraction after the acidic treatment and magnetic-separation stages. The internal magnetic field for the first site, which was assigned to Fe in the tetrahedral site (Fe^{Tetra1}), was 449.97 kOe with quadrupole splitting of -1.584 mm/s and isomer shift of 1.087 mm/s, while its relative abundance was 29.1%. The other two sites corresponded to Fe in the octahedral ferrite sites (Fe^{Oct1}). The first one was characterized with internal magnetic field of 481.13 kOe, quadrupole splitting of -0.974 mm/s and isomer shift of 0.024 mm/s with a relative abundance of 41.8 %. The second octahedral site, Fe^{Oct2}, was fitted with an internal magnetic field of 391.31 kOe, quadrupole splitting of -0.640 mm/s, isomer shift of 0.085 mm/s, and relative abundance of 29.1 %. The fittings are consistent with an inverse ferrite structure whereby Fe^{3+} cations randomly occupied both the tetrahedral and octahedral sites[69,70]. Based on these considerations and since an equal occupation of the tetrahedral and octahedral sites by Fe^{3+} cations did not take place, an incomplete inversion in synthesized cobalt ferrite nanocrystals can be considered. This partial inversion in ferrite structure can also account for the observed unusual coercivity value.

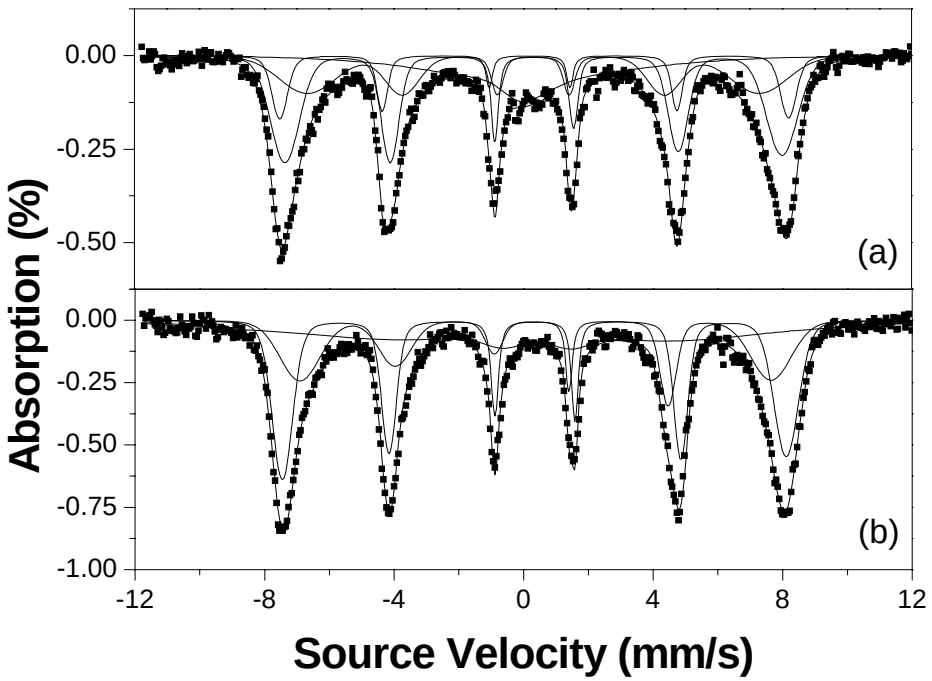

Figure 54: Room-temperature Mössbauer spectrum of the $CoFe_2O_4$ powders without acidic treatment, (a). The spectrum in (b) corresponds to the sample recovered at the end of the acidic treatment (HCl 10 % v/v) and magnetic separation stages.

Unusually high room temperature coercivity (9.4 kOe) and squareness ratio (0.69) have been achieved in cobalt ferrite nanocrystals. The large coercivity in these powders can be attributed to the enlargement of their crystal size favored by the suitable combination of size-controlled synthesis conditions and removal of the superparamagnetic fraction during the acidic treatment and subsequent size-sensitive magnetic separation stages. Acidic treatment should have also promoted the removal of a poorly crystalline and magnetically disordered surface layer of iron oxide from nanosize ferrite crystals.

5.2.2 Double acid washing process

As an attempt to explore the possibility of further enhancement of the ferrite coercivity by narrowing the size distribution even more, previously acid-washed ferrite powders were re-treated by following a similar acid-washing/magnetic separation cycles. Starting cobalt ferrite powders were prepared by the modified coprecipitation method at 0.81 mL/min flow-rate and a NaOH concentration of 0.315 M, which corresponds to the optimum concentration determined from the experimental design. The experimental procedure was the same as described in section 4.1.4.2. It was used a ferrite to acidic solution ratio of $\left(\frac{5.0\,g\ \ ferrite}{500\,mL\ HCl\,10\,\%\,v/v}\right)$.

A. XRD Analyses: First cycle

Figure 55 shows the XRD patterns of cobalt ferrite powders after the first cycle of size-sensitive phase separation. An increase in average crystallite size from 16 nm to 20 nm was achieved in the magnetically separated fractions. It was also observed a slight but significant decrease in lattice parameter from 8.383 Å, before treatment, to 8.365 Å for the first fraction. Those trends were very similar as those described and discussed in section 5.2.1, i.e., the powders recovered in each one of the size-selected fractions reported smaller lattice parameter than the powders before acidic treatment.

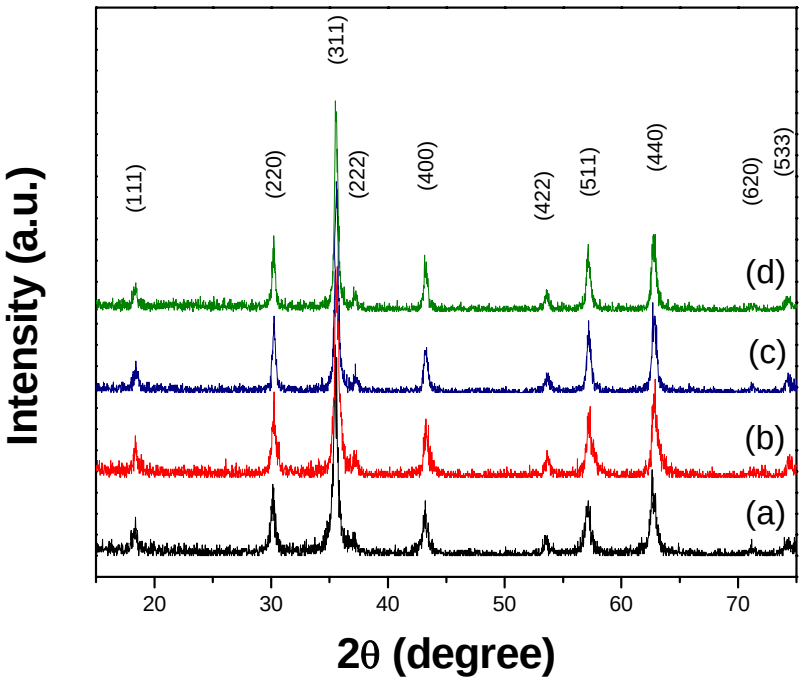

Figure 55: XRD patterns of $CoFe_2O_4$ powders before, (a), and after acidic treatment with 10% HCl followed by magnetically-assisted separation. The patterns correspond to the solids contained in the fractions collected after 2 minutes, (b), 4 minutes (c), and 6 minutes, (d) of magnetic separation.

B. M-H Measurements: First cycle

The coercivity was increased from starting 3.3 kOe up to 9.7 kOe for the third fraction after 6 minutes of magnetically-assisted settling. This increment is around three times its initial value. Again, observed 'constricted' hysteresis loops, shown in Figure 56 (b), are typical of a mixture of soft and hard magnetic materials[71]. In this case, this sort of 'necking' in the central part of the loop can be attributed to the co-existence of superparamagnetic single-domain cobalt ferrite nanoparticles. Fractions exhibiting larger coercivity values did not show this 'necking' confirming the removal of the superparamagnetic fraction.

The squareness ratio was enlarged from 0.50 (before treatment) up to 0.71 corresponding to the third fraction.

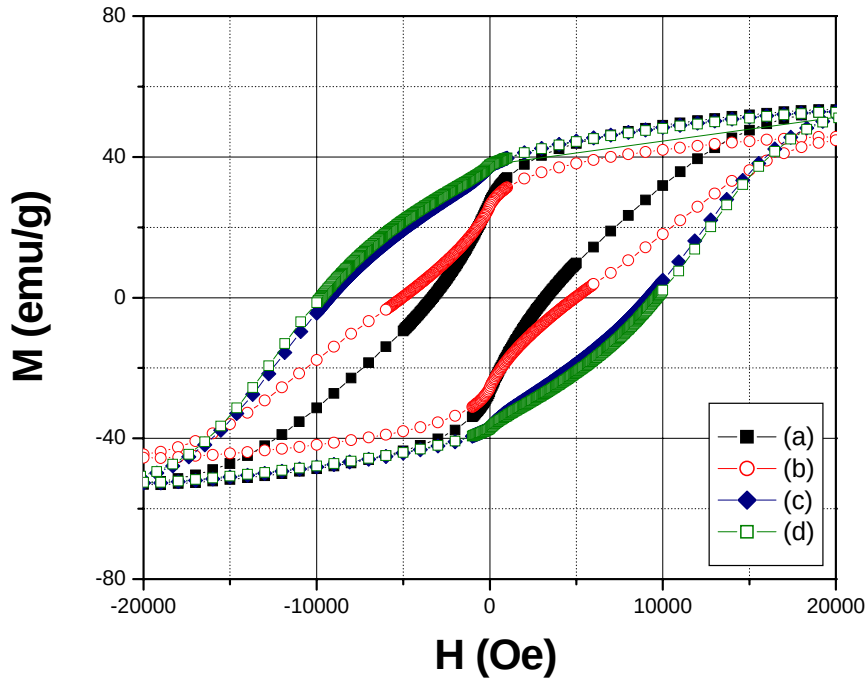

Figure 56: Room temperature M-H measurements of $CoFe_2O_4$ powders before (a) and after acidic treatment with 10% HCl followed by magnetically-assisted separation. The patterns correspond to the solids contained in the fractions collected after 2 minutes, (b), 4 minutes (c), and 6 minutes, (d) of magnetic separation.

C. XRD Analyses: Second cycle

The second settled fraction (corresponding to 4 minutes of settling time) was submitted to a second cycle of our size-sensitive phase separation process. This time, the ferrite to HCl ratio was $\left(\frac{0.8\,g\ ferrite}{800\,mL\ HCl\,10\%}\right)$. The XRD patterns of Figure 57 correspond to: (a) as-

synthesized cobalt ferrite, (c) the fraction corresponding to 4 minutes of settling time from the first cycle, (e) the fraction corresponding to 4 minutes of settling time generated during the second cycle, and (f) the fraction corresponding to 6 minutes settling time from the second cycle. As suggested by the enhanced intensity and sharpening of the diffraction peaks, an improvement in crystallinity was evident in those particles treated by the second cycle. In good agreement with the previous observations, the average crystallite size was as high as 23 nm for the 6 minutes-fraction. Evidently, a further acid washing would have eliminated more efficiently the superparamagnetic fraction in each fraction.

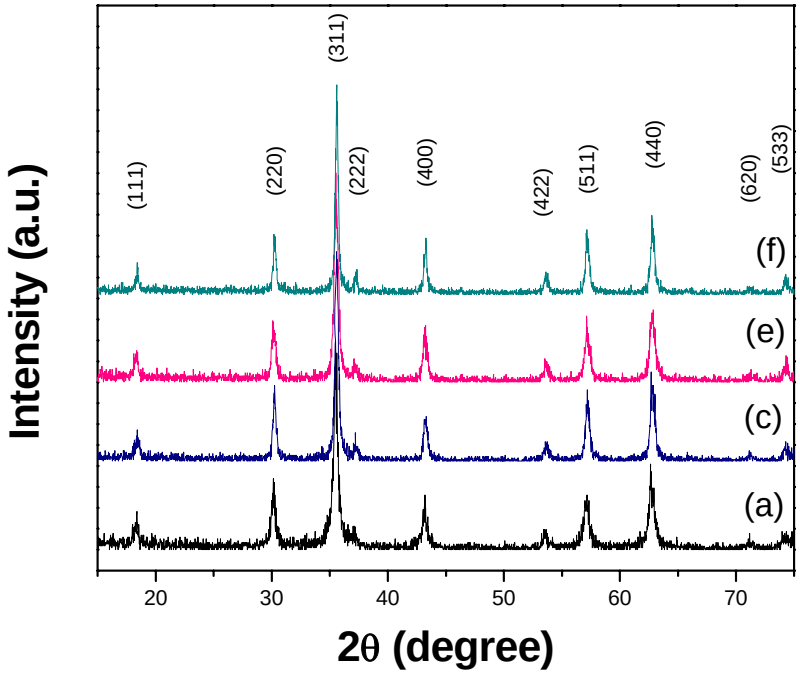

Figure 57: XRD patterns of $CoFe_2O_4$ powders submitted to two cycles of acid treatment and magnetically-assisted separation stages. Sample (a) corresponds to the ferrite before treatment, sample (c) corresponds to the second fraction of the first cycle, samples (e) and (f) are the fractions obtained after the second cycle of the size-sensitive phase separation. Average crystallite sizes of 16 nm and 23 nm were obtained for the sample before and after the two cycles of size-sensitive phase separation, respectively.

D. M-H Measurements: Second cycle

The initially 9.2 kOe achieved in the second fraction generated during the first separation cycle was increased up to 11.9 kOe. This pretty large coercivity was obtained in the third fraction produced during the second acid-washing/magnetic separation cycle. To our knowledge, it is the highest coercivity value reported to cobalt ferrite nanocrystals. In good agreement with our previous observations, this dramatic enhancement in coercivity can be attributed to the larger crystal size in the corresponding fractions and the more efficient removal of any remnant of superparamagnetic particles.

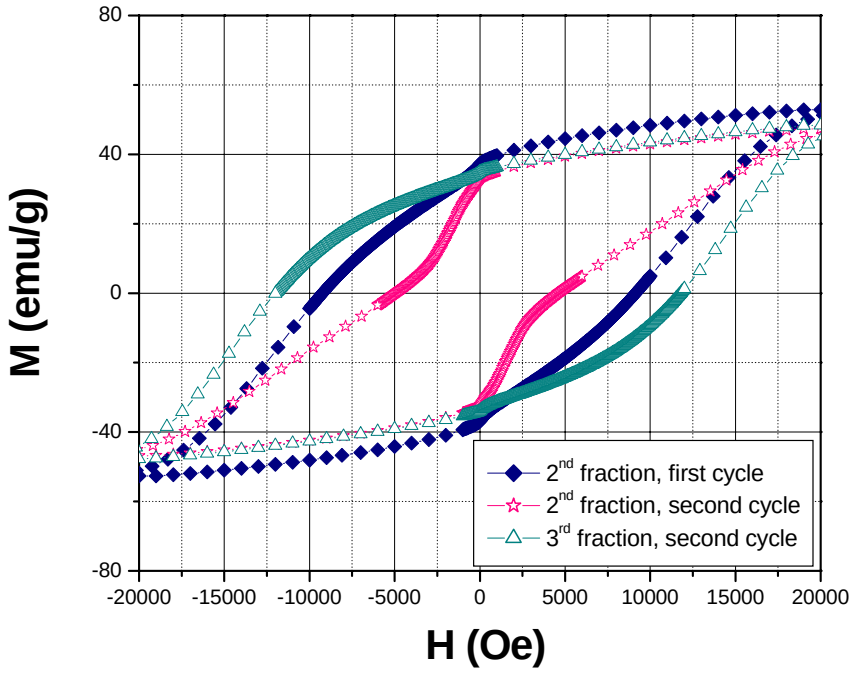

Figure 58: Room temperature M-H measurements of $CoFe_2O_4$ powders submitted to two cycles of acid treatment and magnetically-assisted separation stages.

A summary of the structural and magnetic properties of the powders treated by the two acid-washing/magnetic separation cycles is shown in TABLE 18 and TABLE 19, respectively.

TABLE 18: Structural properties of the sample submitted to the acid treatment and magnetically-assisted separation stages (1st and 2nd cycle).

Fraction	a (± 0.007 Å)	t (± 3 nm)
Before treatment (a)	8.383	16
1st fraction (b)	8.365	16
2nd fraction (c)	8.367	19
3rd fraction (d)	8.374	20
4th fraction	-	-

	Fraction	a (± 0.007 Å)	t (± 3 nm)
SECOND CYCLE	1st faction	-	-
	2nd fraction (e)	8.374	17
	3rd fraction (f)	8.367	23
	4th fraction	-	-

TABLE 19: Magnetic properties of the sample submitted to the acid treatment and magnetically-assisted separation stages (1st and 2nd cycle).

Fraction	H_c (Oe)	M_{max} (emu/g)	M_r/M_s
Before treatment (a)	3270	53	0.50
1st fraction (b)	4995	46	0.56
2nd fraction (c)	9191	53	0.70
3rd fraction (d)	9710	53	0.71
4th fraction	-	-	

	Fraction	H_c (Oe)	M_{max} (emu/g)	M_r/M_s
SECOND CYCLE	1st faction	-	-	
	2nd fraction (e)	4772	47	0.69
	3rd fraction (f)	11884	48	0.72
	4th fraction	-	-	

As seen in TABLE 19, the maximum saturation decreased from 53 emu/g to 48 emu/g. This later maximum magnetization corresponds to the 11.9 kOe sample. This drop in magnetization in the sample with the largest coercivity was expected from the inverse relationship of this parameter with coercivity (equation 4, page 18).

Concluding Remarks

The suitable combination of acid-washing and magnetically-assisted size-sensitive separation provides favorable conditions for the enlargement of average crystallite size and hence, increased coercivity. The enlargement in average crystallite size is consequence of the dissolution of the smaller and more soluble nanocrystals that contributes negatively to coercivity; in addition to the removal of the poorly crystalline layer on the surface of the nanocrystals. It was demonstrated those successive cycles of acid-washing and magnetically-assisted size-sensitive separation helps to improve coercivity even more.

5.3 Effect of the ferrite composition

5.3.1 Variation of the Fe:Co mole ratio

The magnetic properties of cobalt ferrite arise as consequence of diverse factors as crystal size[72], morphology[73], chemical composition[74,75], and/or cation distribution[76]. Pure cobalt ferrite ($CoFe_2O_4$) has inverse spinel structure $(Co_xFe_{1-x})[Co_{1-x}Fe_{1+x}]\ O_4$, where Co^{2+} ions have preference for the octahedral site (B) while Fe^{3+} ions distribute equally between tetrahedral [A] and octahedral sites. Substitution of metal ions by foreign cations (transition metals[77] or rare earth[78]) is a common practice when a change in A-B interaction is desired. Because the Fe_A^{3+}–Fe_B^{3+} super-exchange interaction is different from Co_A^{2+}–Fe_B^{3+}, any deviation from the stoichiometric Fe:Co mole ratio (2:1) will lead to an atomic rearrangement between A and B sites and/or creation of vacancies[79]. Consequently, a change in magnetic properties will take place. Among the preparation methods available for the production of magnetic nanoparticles (i.e. coprecipitation[43], sol-gel, hydrothermal[71], mechanical milling[70], organic precursor), the coprecipitation method was selected to produce these cobalt ferrite nanocrystals because the synthesis parameters can be easily modified in order to tune magnetic properties. On this basis, cobalt ferrite nanocrystals with different initial Fe:Co mole ratios (3:1, 2:1, 1.7:1, and 1.4:1) were synthesized and characterized structural, morphological, compositional, and magnetically. In addition to chemical composition, the effect of flow-rate of addition of reactants, which leads to crystal growth, was studied[80]. In addition to crystal growth, cation distribution, internal magnetic field,

morphology, and chemical composition, the presence of a secondary phase (α-Fe_2O_3), was identified as responsible of the observed wide range of magnetic properties.

Accordingly, cobalt ferrite nanocrystals with initial Fe:Co mole ratios of 3:1, 2:1, 1.7:1, and 1.4:1 were produced by the conventional and the modified coprecipitation methods. For this later case, the flow-rate at which the reactants were contacted was set to 0.67 mL/min. The reaction time was one hour in all our experiments.

A. XRD Analyses

The average crystallite size and lattice parameter of cobalt ferrite nanocrystals synthesized under the above described conditions are summarized in TABLE 20. The conventional, i.e. with no control on flow-rate, coprecipitation method (Figure 59) lead to the formation of nanocrystals with average crystallite size ranging between 11 and 12 nm regardless of the Fe:Co mole ratio. The control of the flow-rate of addition of reactants into the alkaline solution was conducive to a promotion of the crystal size (Figure 60), 'modified coprecipitation method'); the average crystallite size was between 15 and 19 nm. Excess of iron, (3:1 Fe:Co mole ratio), caused the formation of a secondary phase that was identified as hematite, α-Fe_2O_3, using the *Match! Phase Identification* from Powder Diffraction Software, (entry # 00-03-0800)[81]. Less crystalline powders were obtained when the Fe:Co mole ratio was decrease from 3:1 to 1.4:1. The lattice parameters for the 3:1 samples are below the bulk value of cobalt ferrite that could be due to some defect of Fe because of the formation of hematite.

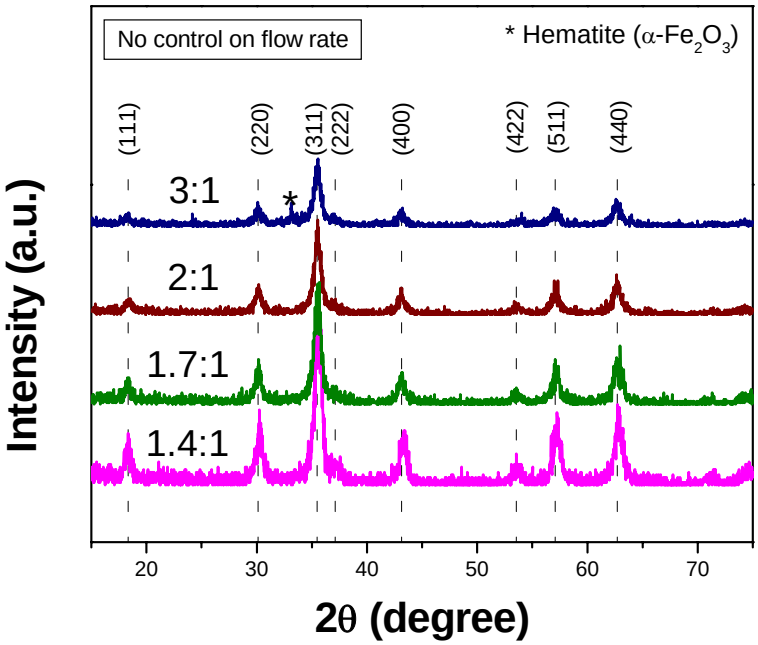

Figure 59: XRD patterns of cobalt ferrite nanocrystals synthesized without control on flow-rate at different Fe:Co mole ratios. The peak with the asterisk corresponds to hematite, α-Fe_2O_3 (entry # *00-03-0800 from Match!* software).

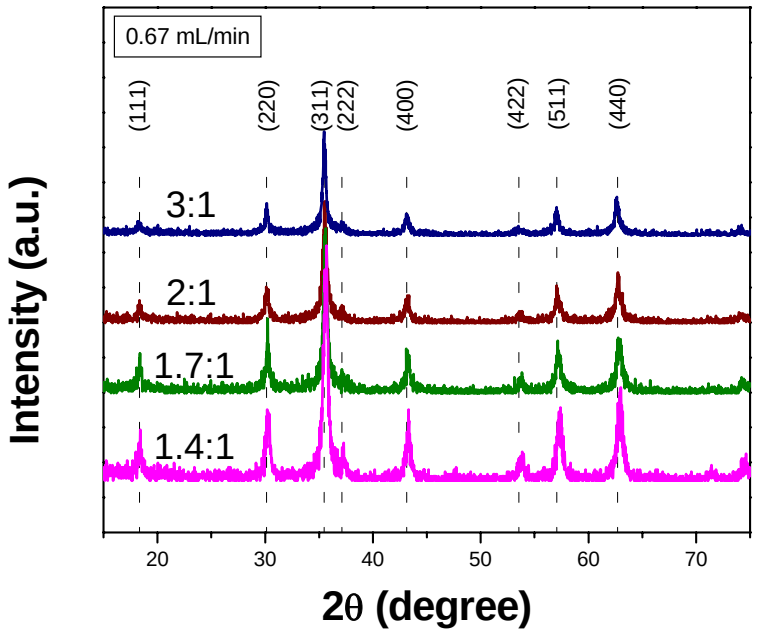

Figure 60: XRD patterns of cobalt ferrite nanocrystals synthesized at 0.67 mL/min and various Fe:Co mole ratios.

TABLE 20: Average crystallite size, 't', and lattice parameter, 'a', of cobalt ferrite synthesized at various Fe:Co mole ratios with and without control of the flow-rate.

	No control on flow-rate		Flow-rate: 0.67 mL/min	
Fe:Co mole ratio	**t (± 2 nm)**	**a (± 0.01 Å)**	**t (± 2 nm)**	**a (± 0.01 Å)**
3:1	11	8.39	19	8.39
2:1	12	8.38	15	8.38
1.7:1	11	8.38	17	8.37
1.4:1	11	8.36	15	8.35

B. TEM Analyses

Figure 61 (a) and (b) show the ferrite nanocrystals synthesized with (0.67 mL/min) and without control on flow-rate, respectively. Both samples were synthesized using a starting Fe:Co mole ratio of 1.4:1. The sample produced under flow-rate controlled conditions showed a mixture of small rounded particles and nearly squared particles with bigger size (@ 20 nm). As was also suggested by XRD data, the control on flow-rate would have promoted the crystal growth. Particles produced with no control on flow-rate were almost rounded and below 20 nm in diameter (Figure 62). A significant change in morphology and/or size was not observed. A size distribution analysis was not considered because of the particles agglomeration.

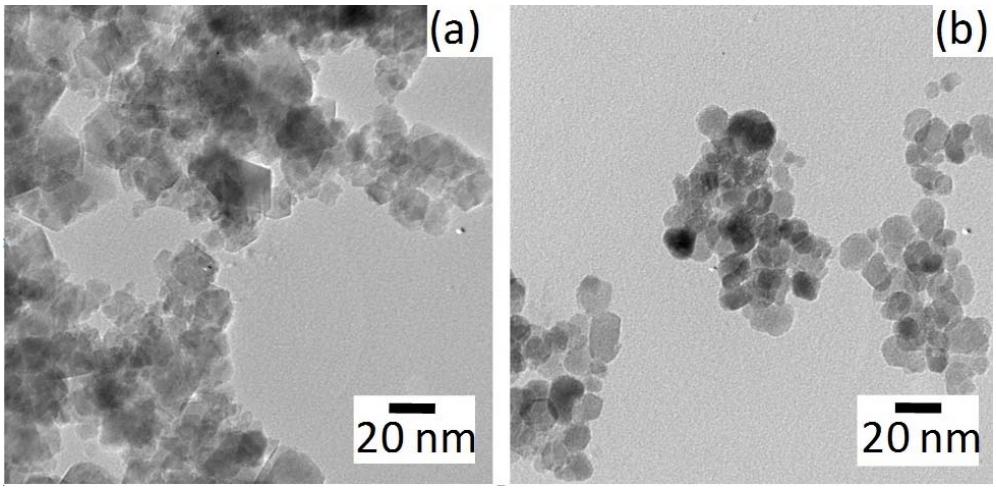

Figure 61: TEM images of cobalt ferrite nanocrystals produced with, (a), and without, (b), the flow-rate. The Fe:Co mole ratio was 1.4:1.

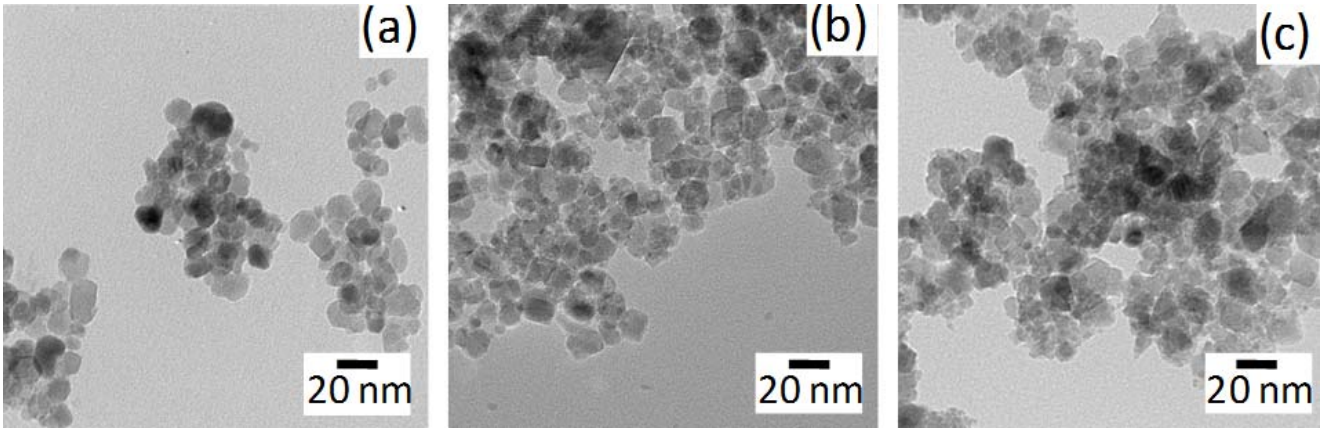

Figure 62: TEM images of cobalt ferrite nanocrystals synthesized without control on flow-rate at different Fe:Co mole ratios: 1.4:1 (a), 1.7:1 (b), and 2:1 (c).

C. EDS Analyses

TABLE 21 summarizes the nominal and experimental (measured) Fe:Co mole ratios in synthesized ferrite nanocrystals. The Fe:Co mole ratios represent an average from measurements at five different regions in the sample. For all cases, approximately 78% of the Fe present in starting solutions was incorporated into the ferrite structure. Based on the experimental Fe:Co mole ratios shown in TABLE 21, it can be concluded that control on flow-rate conditions does not affect the degree of Fe incorporation in the solid products. The intensive heating conditions during the synthesis, provided by the burner and the stainless steel reactor could be re-dissolving the iron from the ferrite structure thereby leading to the non-stoichiometry.

TABLE 21: Summary of Fe:Co mole ratios of cobalt ferrite synthesized with and without control on flow-rate.

	No control on flow-rate	**Flow-rate: 0.67 mL/min**
Nominal Fe:Co mole ratio	**Experimental Fe:Co mole ratio**	**Experimental Fe:Co mole ratio**
3:1	2.3:1 (± 0.3)	2.3:1 (± 0.2)
2:1	1.58:1 (± 0.08)	1.54:1 (± 0.08)
1.7:1	1.31:1 (± 0.08)	1.30:1 (± 0.06)
1.4:1	1.08:1 (± 0.04)	1.0:1 (± 0.1)

D. M-H Measurements

Coercivity and maximum magnetization of the as-synthesized samples are presented in TABLE 22. The maximum magnetization was measured for an external applied field of 1.9 T. Average crystallite sizes from cobalt ferrite synthesized without control on flow rate are quite similar. Thus, any change in magnetic properties could be attributed to the net effect of chemical composition. The corresponding M-H loops are contained in Figure 63. For this set of samples, the highest coercivity value (548 Oe) was obtained for the sample synthesized at a 3:1 Fe:Co mole ratio. This sample contained a secondary phase that was identified as hematite. The attained high coercivity value may result from the contribution of hematite to the surface anisotropy and interparticle interactions to the net anisotropy[82]. Having a mixture of phases, the interparticle interactions are different when compared to pure cobalt ferrite.

In our earlier work[72], it was noticed that Fe:Co mole ratios below the stoichiometric 2:1 were conducive to large coercivity values in samples synthesized under controlled flow-rate conditions. The M-H loops corresponding to samples synthesized controlling flow rate are contained in Figure 64. Taking into account that the flow-rate was kept constant in all the experiments of this series, any change in crystallite size could be attributed to the variation of the chemical composition in the synthesized powders. For instance, the sample synthesized at a starting Fe:Co mole ratio of 1.7:1, which reported an average crystallite size of 18 nm, exhibited a coercivity as high as 4412 Oe. In the case of the sample produced at a Fe:Co mole ratio of 3:1, the average crystallite size was 19 nm and reported 4249 Oe of coercivity.

A comparison between samples synthesized with and without control on flow rate at the same ferrite composition (Fe:Co 1.7:1) is shown in Figure 65. Also, as TABLE 22 shows, the maximum magnetization values in samples synthesized with and without control of flow-rate and various starting Fe:Co mole ratios, ranged between 42 emu/g and 60 emu/g. Furthermore, the corresponding squareness ratio increased as the coercivity did; this ratio was increased from 0.11 (H_c = 114 Oe, Fe:Co 1.4:1, no control of flow-rate) up to 0.51 in the sample with a coercivity of 4412 Oe (Fe:Co 1.7:1, 0.67 mL/min).

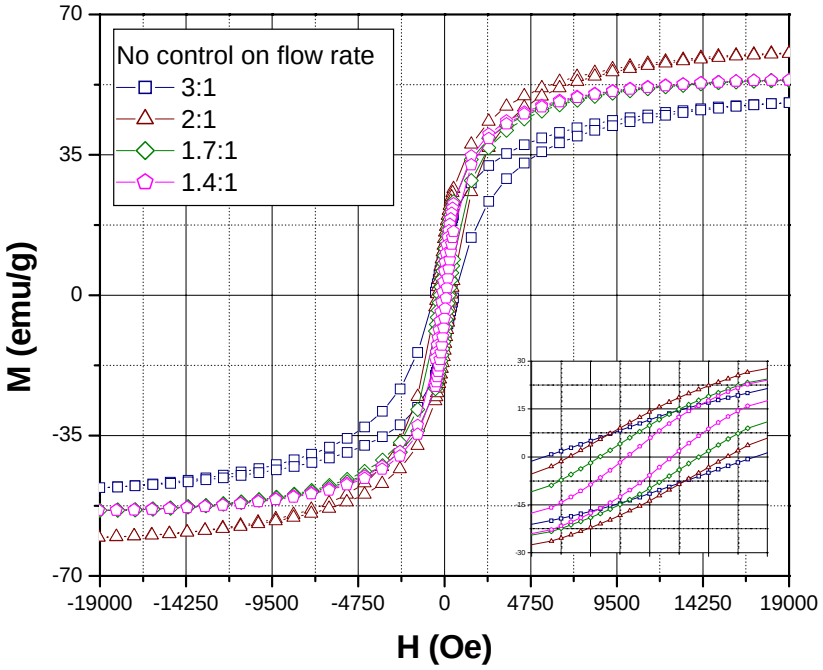

Figure 63: Room temperature M-H loops of cobalt ferrite nanocrystals produced without control on flow-rate and different Fe:Co mole ratios. The inset shows the loops around the origin.

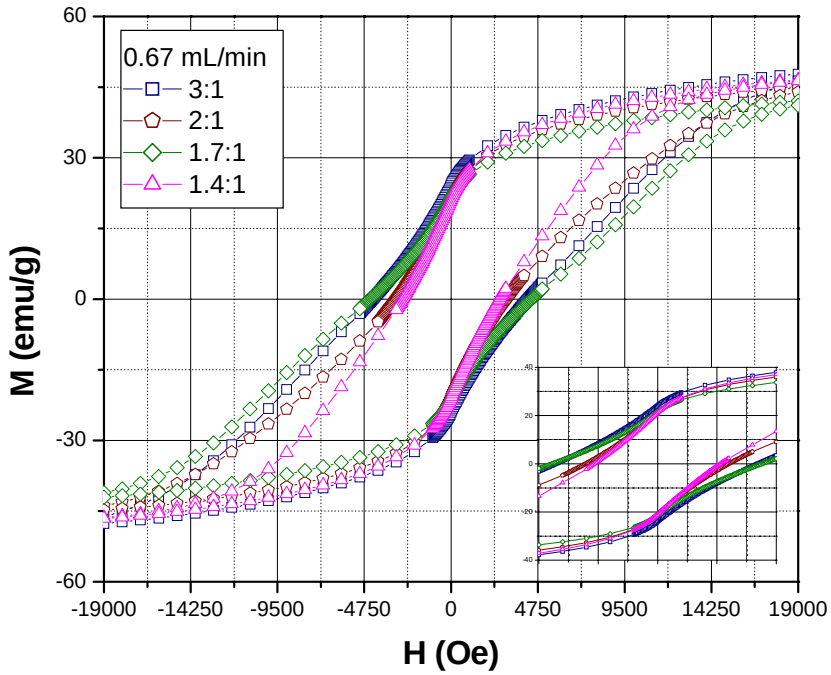

Figure 64: Room temperature M-H loops of cobalt ferrite nanocrystals synthesized at 0.67 mL/min and different Fe:Co mole ratios. The inset shows the loops around the origin.

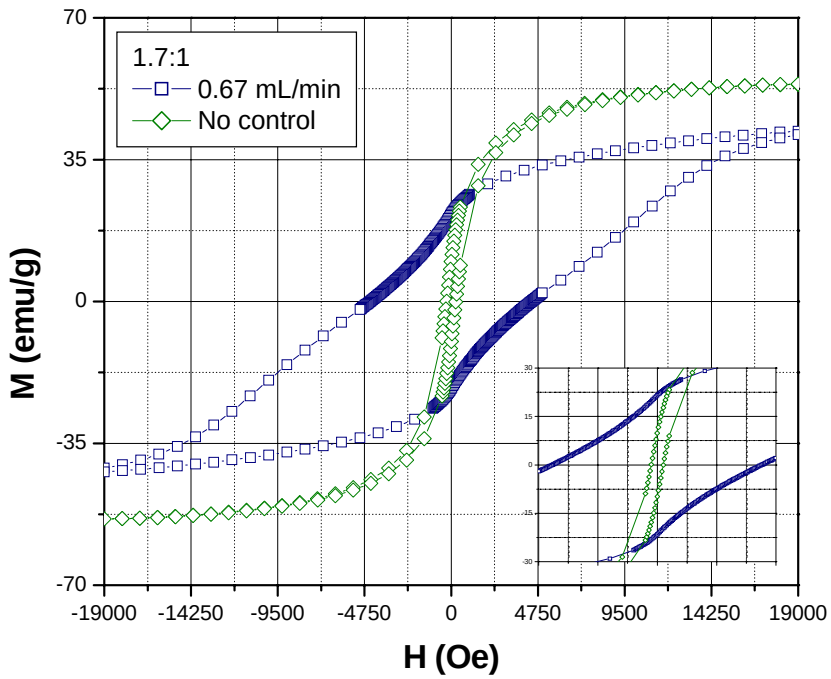

Figure 65: Room temperature M-H loops of cobalt ferrite nanocrystals synthesized under controlled, (a), and non-controlled flow-rate conditions, (b). The Fe:Co mole ratio was 1.7:1. The inset shows the loops around the origin.

TABLE 22: Coercivity, H_c, and maximum magnetization, M_{max}, of cobalt ferrite synthesized with and without control on flow-rate.

	No control on flow-rate			Flow-rate: 0.67 mL/min		
Nominal Fe:Co mole ratio	**H_c (Oe)**	**M_{max} (emu/g)**	**Squareness ratio**	**H_c (Oe)**	**M_{max} (emu/g)**	**Squareness ratio**
3:1	548	48	0.24	4249	48	0.50
2:1	402	60	0.23	3018	45	0.47
1.7:1	252	54	0.18	4412	42	0.51
1.4:1	114	54	0.11	2656	47	0.45

E. Mössbauer Spectroscopy Measurements

Mössbauer spectroscopy measurements will help to study the Fe cations environment and how their distribution between octahedral and tetrahedral sites changes in addition to the internal magnetic field. It is known that the surface to volume ratio increases at the nanoscale. Besides, this technique can also elucidate whether surface effects can be present. The effect of the nominal Fe:Co mole ratio and the flow-rate were on the above mentioned features were evaluated and discussed below.

i. Influence of the Fe:Co mole ratio on the Mössbauer parameters.

Figure 66 shows the unfitted Mössbauer spectra for cobalt ferrite samples synthesized at a Fe:Co mole ratio of 2:1, (a), 1.7:1, (b), and 1.4:1 (c). The samples were synthesized at 0.67 mL/min. As seen, spectrum (a) and (b) evidenced the presence of central doublet peaks. These doublets are not symmetrically located with respect to the zero for velocity position, and also exhibit a different relative intensity in comparison with the sextet peaks of the hyperfine splitting. These central doublet peaks are not detected in the spectrum corresponding to the sample synthesized at a Fe:Co mole ratio of 2:1 (spectrum ‘c’ in Figure 66). The absence of the central doublet peaks confirms the absence of non-magnetic material, in this case, superparamagnetic particles.

The fitting of the spectra corresponding to the ferrite synthesized at a Fe:Co mole ratios of 2 and 1.7 were carried out with the hyperfine field distribution model, with four sites. They are

shown in Figure 67. Samples were synthesized at 0.67 mL/min. The HFD model used to fit the experimental data considers four sites in the magnetic structure of the ferrite.

H_f corresponds to the internal magnetic field. It is responsible for the hyperfine splitting of the nuclear levels. RA % is the relative abundance percentage of the Fe ion for each site in the magnetic structure of the ferrite. IS represents the isomer shift which is related to the s – electron density in chemical bonds. QQ represents the quadrupole splitting. The 3/2 state in Fe is degenerate with respect to an asymmetric electrostatic field, and in such a field these levels will be split into ± 3/2 and ±1/ 2 levels. One can observe transitions either to or from these two levels to the ground state, and this is the quadrupole splitting. FWHM is the full width at half maximum peak-height and corresponds to nuclear transitions. h_1/h_3 and h_2/h_3 are the ratios between peaks from the hyperfine splitting.

The doublet peaks at the central part of the corresponding spectrum is attributed to the phenomenon of superparamagnetic relaxation, arising from particles with single domain attributes. Given the broad aspects of this component, we can confirm some distribution of particle size within these superparamagnetic fraction, with some of them having their blocking temperature close to 298 K (room temperature conditions).

The most remarkable discrepancy between the two spectra of Figure 67 relies on both, the relative abundances in each sub-sites, and the internal magnetic field of the octahedral and tetrahedral cationic positions. Based on the features of each Mössbauer spectrum, the superparamagnetic components in each sample was estimated in 17% of the total material; and therefore suggests that the synthesis process did not affect the particle distribution. The

corresponding internal magnetic field of the octahedral and tetrahedral Fe are found to be very similar in both samples; however, the fourth component of the spectrum 'b' (Fe:Co 1.7:1), with an internal magnetic field of 352.8 kOe, accounted for 10% of the sample, which was very high when compared to the component but for sample 'a' (Fe:Co 2:1) where the internal magnetic field was 409 kOe representing an abundance of 0.9% in the sample. The surface cations (Site-4) exhibit smaller internal magnetic field and broadened absorption lines indicating a more disordered state at the surface (spin canting) being responsible for lack of magnetization saturation and higher coercivity value due to surface anisotropy[83].

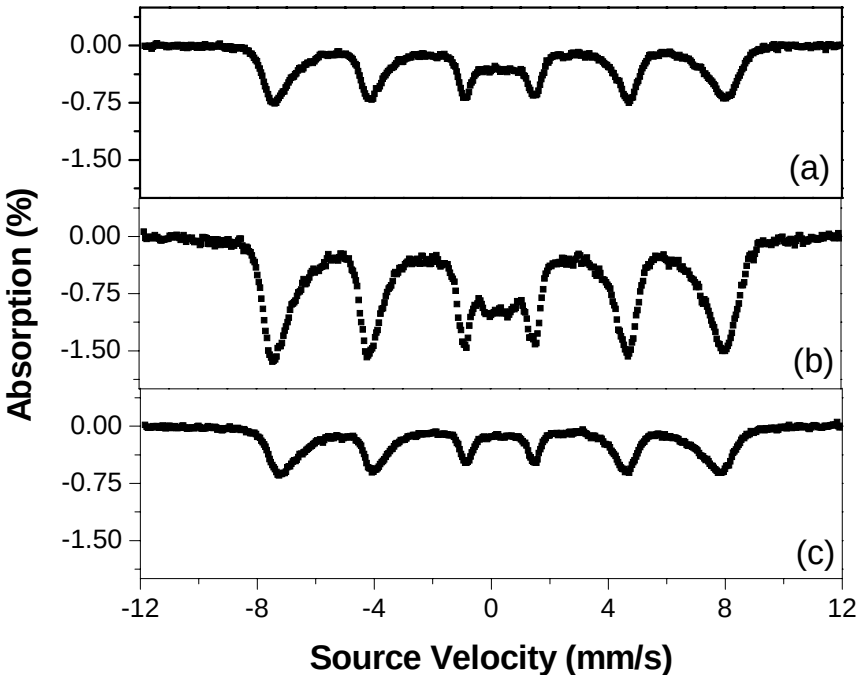

Figure 66: Unfitted Mössbauer spectra of cobalt ferrite nanocrystals synthesized at 0.67 mL/min and Fe:Co mole ratios of 1.4:1, (a), 1.7:1, (b), and 2:1, (c).

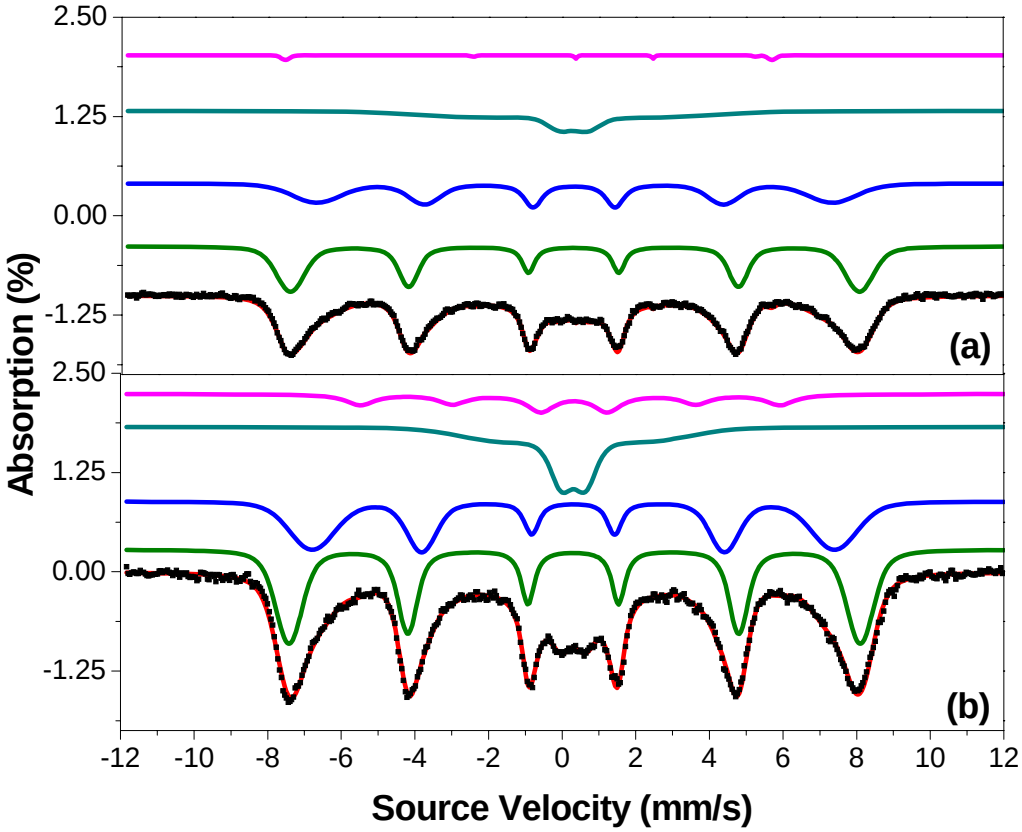

Figure 67: Fitted Mössbauer spectra corresponding to cobalt ferrite nanocrystals synthesized at 0.67 mL/min and nominal Fe:Co mole ratios of 2:1, (a,) and 1.7:1, (b). The green, blue, cyan, and magenta fittings correspond to sites 1, 2, 3, and 4, respectively.

TABLE 23: Mössbauer parameters for sample synthesized at 2:1 Fe:Co mole ratio and 0.67 mL/min flow-rate.

2:1 0.67 mL/min	H_f (kOe)	RA %	IS (mm/s)	QQ (mm/s)	FWHM (mm/s)	h_1/h_3	h_2/h_3
Site-1	479.22	44.96	0.318	3.744e-2	0.379	3.149	2.101
Site-2	434.24	36.71	0.317	1.283e-2	0.521	1.790	1.372
Site-3	148.47	17.45	0.198	-0.207	0.469	1.561	0.000
Site-4	409.84	0.88	0.245	-2.333	4.743e-2	0.000	0.000

TABLE 24: Mössbauer parameters for sample synthesized at 1.7:1 mole ratio and 0.67 mL/min flow-rate.

1.7:1 0.67 mL/min	H_f (kOe)	RA %	IS (mm/s)	QQ (mm/s)	FWHM (mm/s)	h_1/h_3	h_2/h_3
Site-1	479.96	40.70	0.321	3.795e-2	0.402	2.951	2.025
Site-2	438.80	31.84	0.303	7.084e-3	0.393	3.663	2.634
Site-3	127.00	17.31	0.319	2.728e-2	0.547	0.735	0.000
Site-4	352.80	10.15	0.270	-0.110	0.900	0.650	0.569

ii. Effect of the flow-rate on the Mössbauer parameters

Figure 68 shows the unfitted Mössbauer spectra of cobalt ferrite nanocrystals produced at a 1.4:1 Fe:Co mole ratio with, (a), and without control of the flow-rate, (b). Each spectrum was fitted based on the hyperfine field distribution model, with four sites. The relevant parameters obtained for the best fits and the least χ^2 values, are listed in TABLE 25 and TABLE 26. Visual examination of the two spectra did not reveal a major difference between them. The parameters showed in these tables suggested the relative amounts of the component fitted as sub-site 4 is negligible making any further consideration of this site unnecessary. Figure 69 shows the Mössbauer spectra of Figure 68 but after fitting the experimental data to the Fe sub-sites within the ferrite lattice. Site-1 is attributed to Fe cations in the octahedral position of the spinel structure, while site-2 corresponds to the Fe located in the tetrahedral position. The internal magnetic fields for these sites were estimated at 469.077 kOe, and 435.561 kOe, respectively. The corresponding quadrupole splitting

values for the spectrum of Figure 69 (a) suggested minimal distortion of these sites. In turn, sites-3 and 4 are attributed to surface cations.

Regarding the analysis of the spectrum corresponding to the sample synthesized without control of flow-rate, Figure 69 (b), the internal magnetic field values corresponding to the Fe-sites were higher than those for the powders synthesized at 0.67 mL/min (Figure 69-a). Furthermore, the relative abundance of Sites-1 and 2 in the samples synthesized without control of flow-rate (42.32 and 41.26%, respectively) followed an antagonistic trend when compared to the same parameters for the samples produced at 0.67 mL/min (36.80% and 42.75%) ; i.e., there are more Fe cations in Site-1 when the powders are synthesized with no control of the flow-rate. In other words, the control of the flow-rate during the synthesis of the cobalt ferrite nanocrystals will not only affect the average crystallite size but also the distribution of Fe ions within A- and B- sites in the spinel structure. This un-expected change in the atomic distribution should also be involved with the magnetic properties observed in those high-coercivity samples.

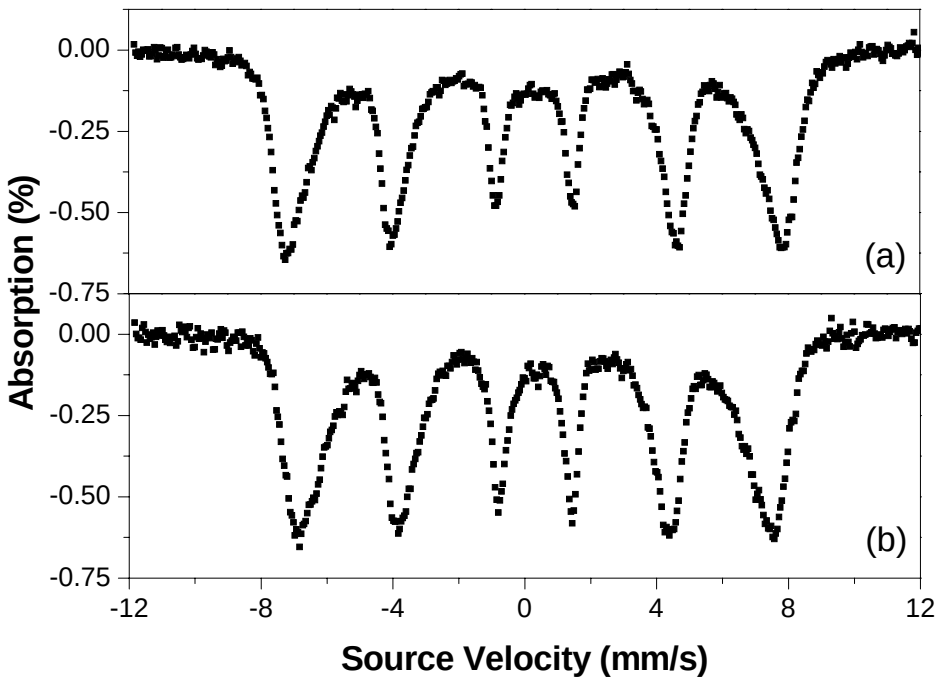

Figure 68: Unfitted Mössbauer spectra of cobalt ferrite nanocrystals produced at 1.4:1 Fe:Co mole ratio and 0.67 mL/min, (a), and without control of the flow-rate, (b).

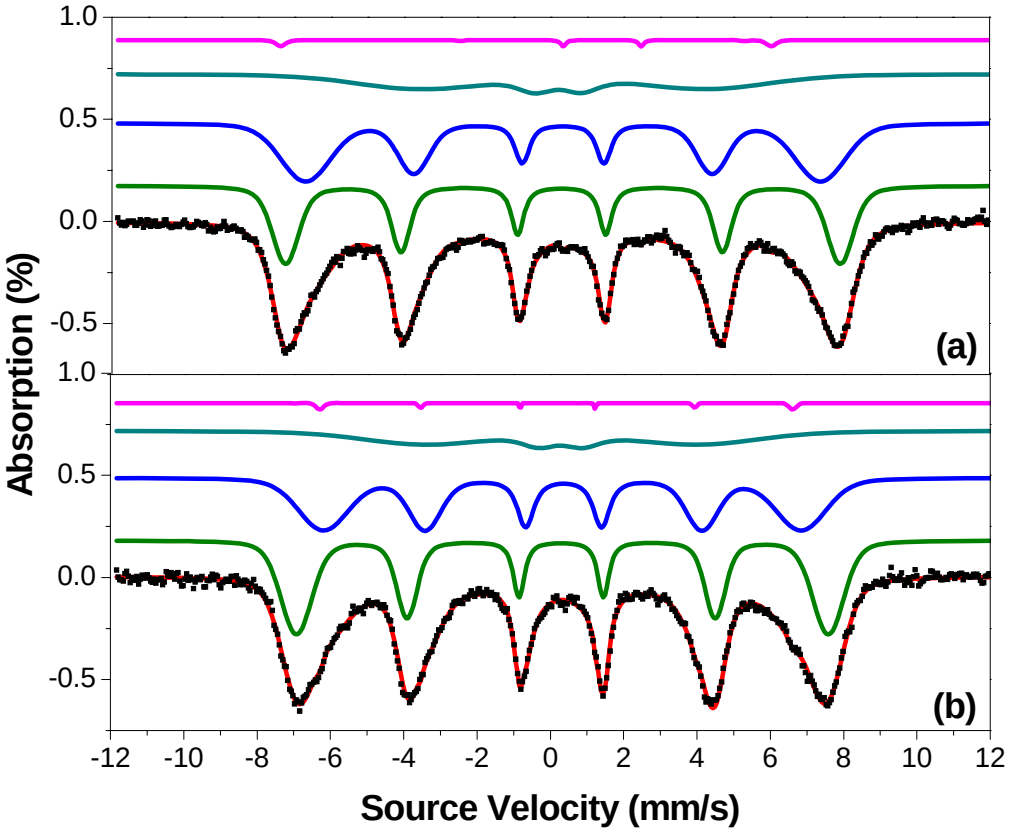

Figure 69: Fitted spectra with the sub-sites indicated. The sub-sites are listed arranged from the last to the first from top to bottom. They correspond to cobalt ferrite nanocrystals produced at a nominal Fe:Co mole ratio of 1.4:1, controlling (a) and not controlling (b) the flow-rate. The green, blue, cyan, and magenta fittings correspond to Site 1, 2, 3, and 4, respectively.

TABLE 25: Mössbauer parameters for sample synthesized at 1.4:1 mole ratio and 0.67 mL/min flow-rate.

Fe:Co 1.4:1 0.67 mL/min	**H_f (kOe)**	**RA %**	**IS (mm/s)**	**QQ (mm/s)**	**FWHM (mm/s)**	**h_1/h_3**	**h_2/h_3**
Site-1	469.08	36.80	0.314	0.03498	0.381	2.803	1.807
Site-2	435.56	42.75	0.334	0.000161	0.369	4.000	2.311
Site-3	245.20	19.46	0.266	0.122	0.900	2.895	0.05639
Site-4	414.69	0.99	0.364	-2.081	0.149	1.581	0.197

TABLE 26: Mössbauer parameters for sample synthesized at 1.4:1 mole ratio without control on flow-rate.

Fe:Co 1.4:1 No control on flow-rate	H_f (kOe)	RA %	IS (mm/s)	QQ (mm/s)	FWHM (mm/s)	h_1/h_3	h_2/h_3
Site-1	448.64	42.32	0.312	0.032	0.315	3.710	2.163
Site-2	403.07	41.26	0.344	-0.3.52e-2	0.451	2.596	1.782
Site-3	231.23	15.87	0.291	7.22e-2	0.900	3.006	0.000
Site-4	398.81	0.56	0.180	-4.07e-2	1.254e-4	4.000	1.700

Concluding remarks

Approximately 78% of the Fe present in starting solutions was incorporated into the ferrite structure. The synthesis under flow-rate controlled conditions did not affect the degree of Fe incorporation in the solid products. The highest coercivity from these experiments was found for low flow-rate and Fe:Co 1.7:1. Mössbauer measurements revealed that this particular sample had an additional contribution of 10% from Site-4. This site is associated to surface cations. These surface cations are in a disordered state and will be responsible of surface anisotropy in the nanocrystals. The contribution of site-4 for all other samples was negligible; i.e., the environment of Fe cations would be practically the same across the whole particle. Mössbauer analyses also confirmed the strong influence of the flow-rate on the Fe cation distribution between tetrahedral and octahedral sites within the spinel structure. Accordingly, the remarkable enhancement of the coercivity in produced ferrite nanocrystals will be a

consequence not only of the enlargement in crystal size but also on the combined effect of the variation in the Fe distribution within sites A- and B- and the enhancement of the surface anisotropy effect.

5.3.2 Transition metals-substituted cobalt ferrite

The cationic distribution and interaction between them will affect and tailor the magnetic properties of ferrites. Accordingly, transition metal (TM) ions were used to substitute Co ions according to $TM_xCo_{1-x}Fe_2O_4$, where 'x' corresponds to the atomic fraction of transition metal. Ni^{2+} and Mn^{2+} were selected as Co substituting species based on the similitude between the ionic radius of Co^{2+}, Ni^{2+} and Mn^{2+} (TABLE 5). In addition to the ionic radii, the coordination number and magnetic nature of Mn and Ni species were taken into account**.** Introducing foreign ions into the spinel structure will cause a change into the superexchange interaction (occurs via intermediate atoms or ions, in this case, oxygen). It is a type of inter-particle interaction that allows the magnetic moments in a solid to interact with each other. This interaction will vary depending on the element causing changes into the magnetic properties (coercivity and saturation magnetization) due to different electronic configuration. All ferrite samples were prepared by the conventional coprecipitation method, i.e. with no control on flow-rate. Other synthesis conditions were one hour of reaction and 0.34 M NaOH.

5.3.3 Co substitution by Mn species

A. XRD analyses

Mn atomic fractions 'x' between 0.0 and 1.0 were evaluated. As the summary of structural and magnetic properties of TABLE 27 and TABLE 28 suggests there was no a remarkable crystal growth by increasing the incorporation of Mn ions; the average crystallite size

changed from 11 nm and 14 nm when 'x' varied from 0.0 to 1.0, respectively. The substitution of Co^{2+} by Mn^{2+} should cause an increment in the cubic lattice parameter, 'a', attributed to the slightly larger ionic radius of Mn (0.91 Å) with respect to Co (0.82 Å). This expected enlargement of the lattice parameter of the ferrite was suggested by the shift of the ferrite XRD peaks towards smaller diffraction angles when the amount of Mn ions, 'x', was increased. Consequently, the variation of the lattice parameter with the degree of substitution, 'x', should follow the linearity predicted by the Vegard's rule. This linear trend was verified as shown in Figure 71, which also confirms the actual incorporation of Mn ions into the ferrite lattice.

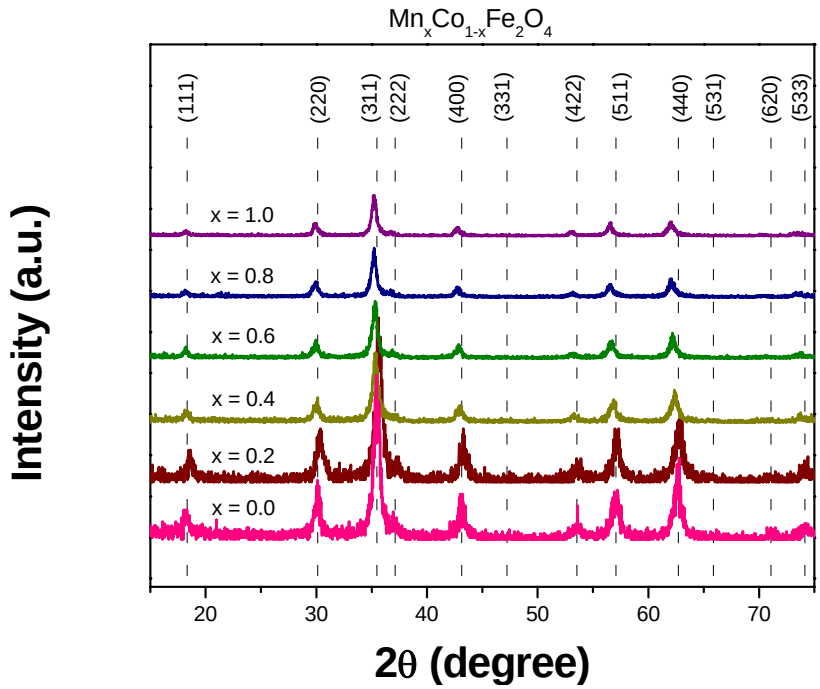

Figure 70: XRD patterns of Mn-substituted cobalt ferrite powders synthesized at different Mn atomic fraction, 'x', values.

TABLE 27: Average crystallite size, 't', and lattice parameter, 'a' of Mn-substituted cobalt ferrite.

Mn atomic fraction (x)	t (± 1 nm)	a (± 0.03 Å)
0.0	11	8.39
0.1	12	8.39
0.2	12	8.36
0.3	11	8.41
0.4	13	8.42
0.5	12	8.42
0.6	13	8.44
0.7	12	8.45
0.8	13	8.46
0.9	14	8.47
1.0	14	8.46

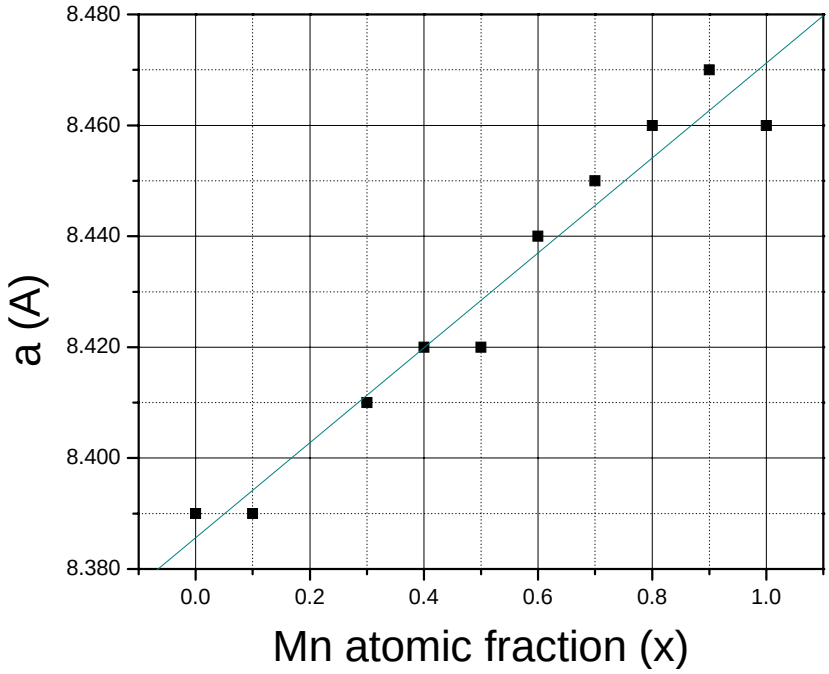

Figure 71: Variation of lattice parameter with Mn atomic fraction in cobalt ferrite.

B. M-H Measurements

M-H room temperature measurements of Mn-substituted cobalt ferrite show a decreasing trend in coercivity with a rising 'x'. Since the crystallite sizes were comparable in all samples, the drop in coercivity was attributed to the actual the substitution of Co by Mn ions in the ferrite structure. This ionic substitution should also cause the magnetocrystalline anisotropy constant of the corresponding ferrite to decrease[11]; the magnetic anisotropy constant gradually decreases from hard $CoFe_2O_4$ to soft $MnFe_2O_4$ magnetic material. In turn, the high magnetization values are attributed to the substitution of Co^{2+} ions (each one contributing with 3 Bohr magnetons) by Mn^{2+} ions that contribute with 5 Bohr magnetons.

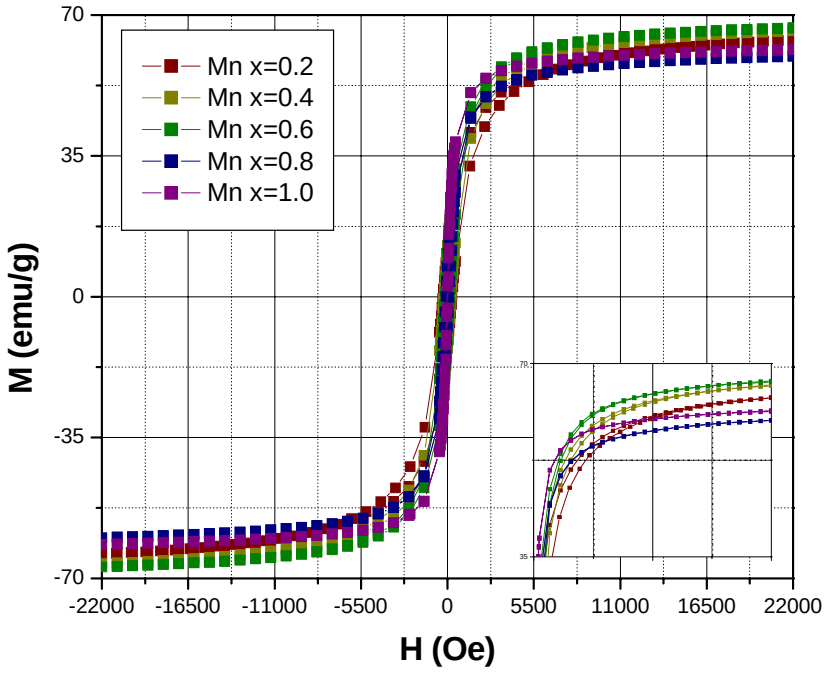

Figure 72: Room temperature M-H loops for Mn-substituted cobalt ferrite synthesized at different Mn atomic fractions, 'x'.

TABLE 28: Coercivity, H_c, maximum magnetization, M_{max}, and squareness ratio of Mn-substituted cobalt ferrite powders synthesized at different 'x' values.

Mn atomic fraction (x)	H_c (Oe)	M_{max} (emu/g)	Squareness ratio M_r/M_s
0.0	403	65	0.23
0.1	334	64	0.22
0.2	292	64	0.21
0.3	280	66	0.20
0.4	244	66	0.19
0.5	210	66	0.18
0.6	171	67	0.17
0.7	141	65	0.16
0.8	102	60	0.12
0.9	60	61	0.09
1.0	18	62	0.04

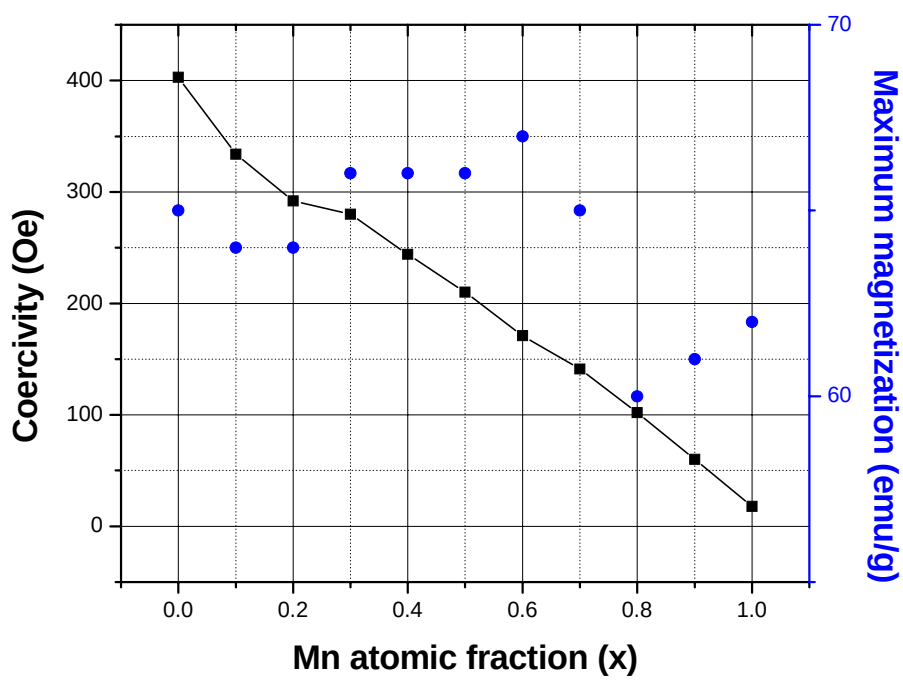

Figure 73: Variation in coercivity and maximum magnetization as a function of Mn atomic fraction, 'x'.

Figure 73 summarizes the variation in coercivity and maximum magnetization with the Mn atomic fraction values, 'x', in the cobalt ferrite. As seen, the increment in Mn^{2+} incorporation into the ferrite structure caused a decrease in coercivity that was attributed due to the decrease in magnetocrystalline anisotropy of the ferrite. An increasing trend in maximum magnetization is observed up to x = 0.6 as expected from the substitution of Co by Mn ions. A further increase in the Mn atomic fraction caused a drop in magnetization. This decrease of M_{max} at larger amounts of Mn can be due to an atomic rearrangement between A and B sites which affects the superexchange interaction.

5.3.4 Co substitution by Ni species

A. XRD Analyses

Figure 74 shows the XRD patterns of the samples synthesized at various Ni atomic fractions, 'y'. The corresponding structural properties are presented in TABLE 29. As seen, the average crystallite size was systematically increased from 11 nm to 18 nm in the 0.0 - 0.8 'y' range. Substitution of Co by Ni will cause a decrease in lattice parameter, attributed to a smaller ionic radius down to 8.34 Å corresponding to pure nickel ferrite (Figure 75). The nickel incorporation will retard the ferrite formation for atomic fractions over y = 0.8. It was confirmed by the poor crystallinity in samples synthesized at 'y' 0.9 and 1.0 even for reaction times as large as three hours.

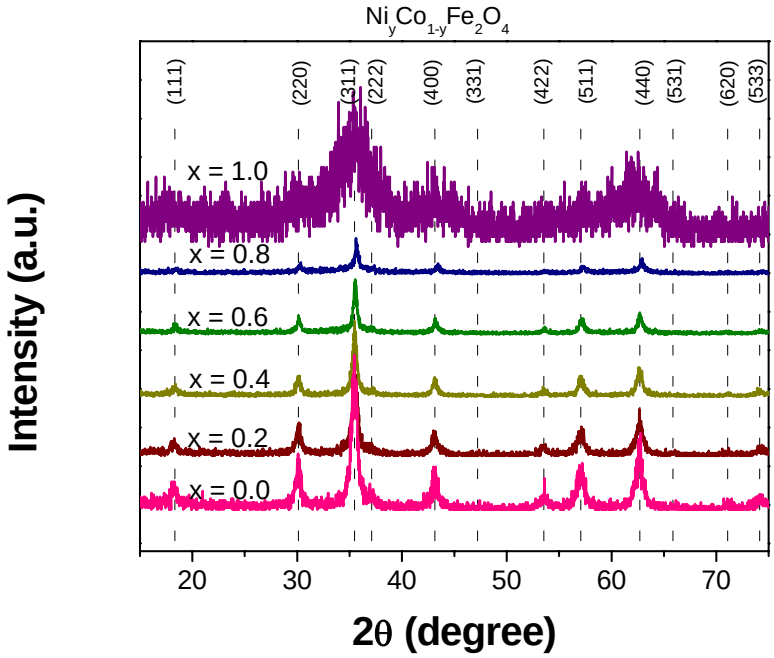

Figure 74: XRD patterns of Ni-substituted cobalt ferrite at different Ni atomic fraction, 'y', values.

TABLE 29: Average crystallite size, 't', and lattice parameter, 'a' in Ni-substituted cobalt ferrite nanocrystals.

Ni atomic fraction (y)	t (± 3 nm)	a (± 0.01 Å)
0.0	11	8.39
0.1	12	8.39
0.2	12	8.38
0.3	13	8.38
0.4	15	8.39
0.5	15	8.38
0.6	17	8.38
0.7	17	8.38
0.8	18	8.35
0.9	16	8.36
1.0	7	8.38

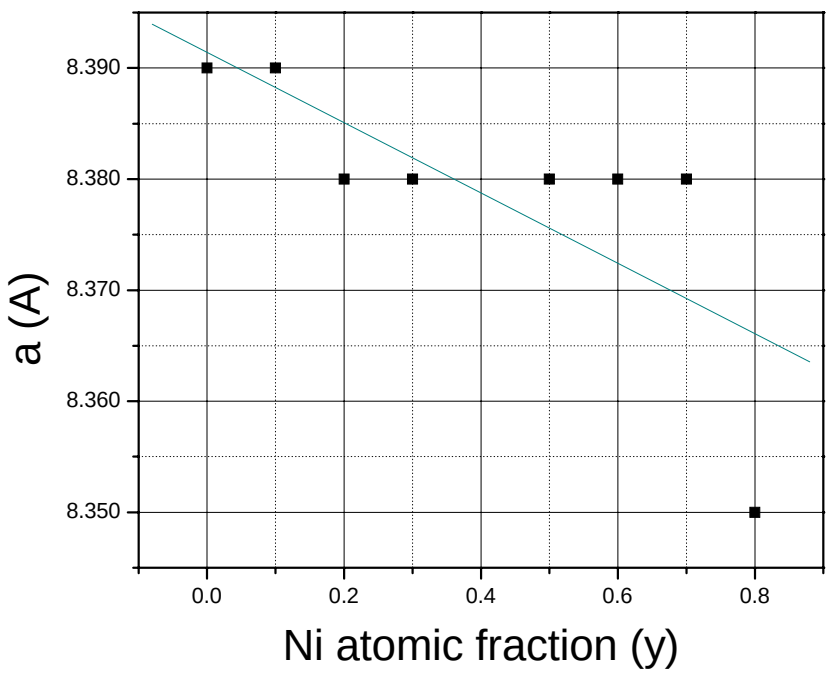

Figure 75: Variation of lattice parameter, 'a', as a function of Ni atomic fraction, 'y'.

B. M-H Measurements

TABLE 30 shows the values of maximum magnetization, M_{max}, and coercivity, H_c, of the ferrite samples synthesized at various Ni atomic fractions, 'y'. Although a decrease in coercivity could be expected from the incorporation Ni ions in bulk cobalt ferrite structure [84] our results, on the contrary, evidenced a rise in coercivity up to 2583 Oe in the sample synthesized at 'y' = 0.8 (Figure 76).

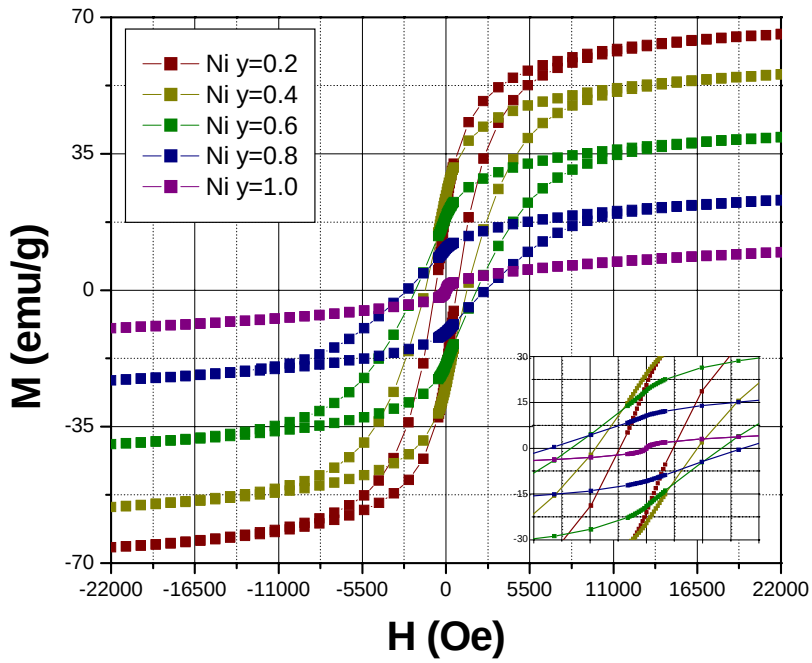

Figure 76: Room temperature M-H loops of Ni-substituted cobalt ferrite at different Ni atomic fractions, 'y'.

TABLE 30: Summary of magnetic properties of Ni-substituted cobalt ferrite powders.

Ni atomic fraction (y)	H_c (Oe)	M_{max} (emu/g)	Squareness ratio M_r/M_s
0.0	403	65	0.23
0.1	479	63	0.26
0.2	714	59	0.32
0.3	1022	58	0.38
0.4	1360	56	0.44
0.5	1719	47	0.47
0.6	2005	39	0.48
0.7	2465	33	0.49
0.8	2583	23	0.46
0.9	712	22	0.32
1.0	14	10	1.7E-02

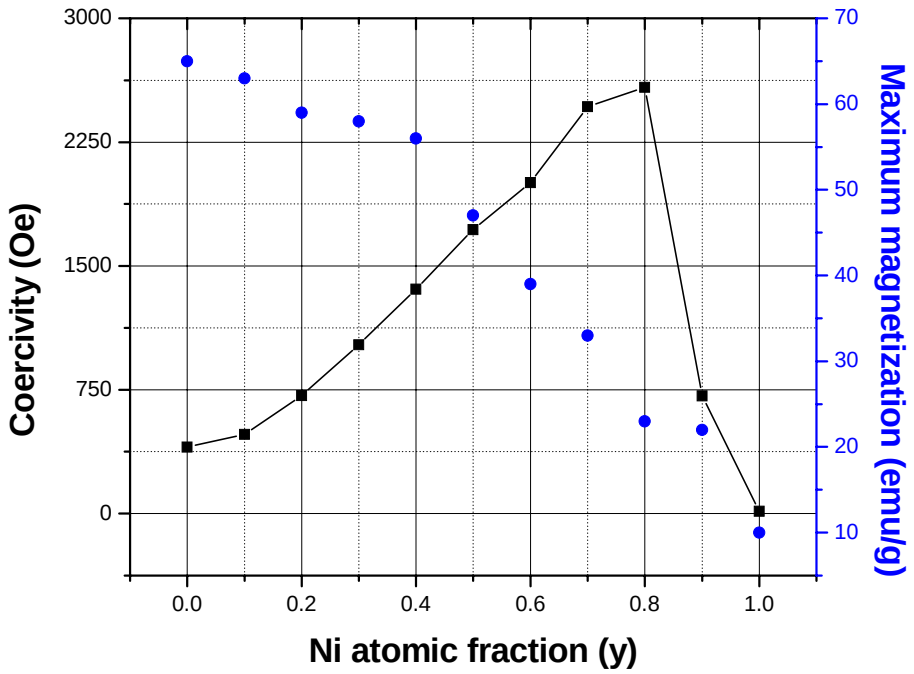

Figure 77: Variation in coercivity and maximum magnetization as a function of Ni atomic fraction, 'y'.

Figure 77 shows the relation between coercivity and maximum magnetization and the Ni atomic fraction, 'y'. As seen, the coercivity increased as the Ni atomic fraction did up to 'y' = 0.8. The incomplete ferrite formation above this point is the responsible for the drop in coercivity above 'y' 0.8. The decrease in magnetization can be attributed to the substitution of Co^{2+} (3 magnetic moments/ion) by Ni^{2+} (2 magnetic moments/ion).

Since the variation in the chemical composition of the ferrite cannot explain the trends in coercivity, other possibilities including variation in crystal size, or particular redistributions of Ni and Co ions in the A and B sites in the spinel structure should be taken into account. As suggested by the XRD measurements, the average crystallite size in synthesized powders

was increased from 11 nm up to 18 nm in the 0 - 0.8 ‘y’ range. Accordingly, the observed rise in coercivity in these samples could be related to this enlargement in crystal size promoted by the incorporation of Ni.

Concluding remarks

The substitution of Co^{2+} by foreign cations (Mn^{2+} and Ni^{2+}) led to a variation in coercivity and maximum magnetization. The incorporation of increasing amounts of Mn^{2+} into the ferrite structure caused an increase in magnetization due to substitution of Co^{2+} by Mn^{2+} which accounts with five magnetic moments while Co^{2+} contributes with only three of them. A decrease in coercivity was laid to a decrease in magnetic anisotropy of the ferrite by the incorporation of Mn^{2+}.

The variation in coercivity and magnetization values followed an opposite trend when Co^{2+} was substituted by Ni^{2+}. Substitution of a cation which accounts with three magnetic moments (Co^{2+}) by a cation that contributes with only two (Ni^{2+}) explained the decrease in magnetization. The enlargement of crystallite size with the increase in the Ni atomic fraction can explain the rise in coercivity in the Ni-substituted cobalt ferrite nanocrystals.

5.4 Heterogeneous nucleation Seed-mediated crystal growth

Synthesis under heterogeneous nucleation-promoted conditions is based on the premise that previously synthesized cobalt ferrite crystals will act as seeds; i.e., fresh ionic solution (monomers) will crystallize over the seeds promoting crystal growth and hence, a change in the corresponding magnetic properties. We must consider that condensation of monomers onto the seeds surface (heterogeneous nucleation) will be accompanied of self-nucleation of monomers (homogeneous nucleation)[85]. Accordingly, freshly precipitated ferrite crystals were be used as seeds in a subsequent precipitation stage and the products of these seeding experiments were re-used in a 2nd or 3rd re-seeding experiments.

5.4.1 Effect of the ferrite/seed weight ratio, 'r'

Cobalt ferrite seeds were produced by the conventional coprecipitation method. The NaOH concentration and reaction time were 0.34 M and 1 hour, respectively.

A. XRD Analyses

There were no remarkable changes in the XRD patterns corresponding to the seeds and seeded products of cobalt ferrite; all diffraction peaks were assigned to the spinel ferrite structure. For instance, Figure 78 shows the XRD patterns for the powders synthesized at a ferrite/seeds w/w ratio, 'r', of 1.0 after seeding and re-seeding cycles. TABLE 31

summarizes obtained results. As seen, the average crystallite sizes did not report a significant change (+/- 2 nm) even after seeding and re-seeding steps.

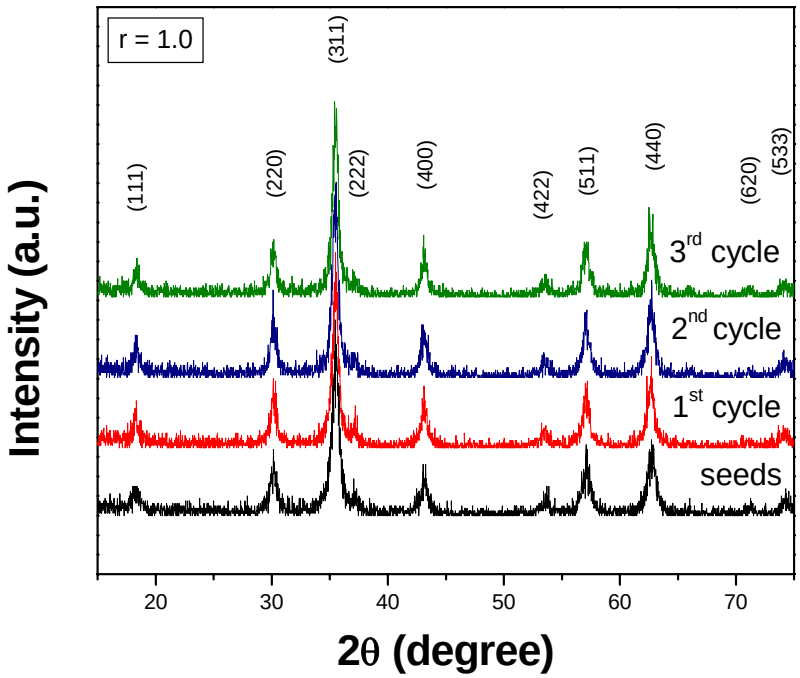

Figure 78: XRD patterns of seeds and seeded products of cobalt ferrite at a starting ferrite/seeds w/w ratio, 'r', of 1.0.

TABLE 31: Average crystallite size, 't', and lattice parameter, 'a', in cobalt ferrite nanocrystals after seeding and re-seeding processes at different 'r' values.

r = 0.25	**t (± 1 nm)**	**a (± 0.01 Å)**
Seeds	11	8.37
1st cycle	11	8.37
2nd cycle	11	8.39
3rd cycle	13	8.37
r = 0.50	**t (± 1 nm)**	**a (± 0.008 Å)**
Seeds	12	8.387
1st cycle	12	8.378
2nd cycle	13	8.394
3rd cycle	12	8.389
r = 0.75	**t (±1 nm)**	**a (± 0.007 Å)**
Seeds	11	8.383
1st cycle	12	8.385
2nd cycle	13	8.382
3rd cycle	13	8.381
r = 1.0	**t (± 1 nm)**	**a (± 0.008 Å)**
Seeds	11	8.373
1st cycle	13	8.387
2nd cycle	13	8.387
3rd cycle	13	8.387

B. M-H Measurements

Although noticeable structural changes were not detected, the coercivity in seeded ferrites was enhanced to some extent after every seeding cycle; the most remarkable change was observed after the first seeding cycle. Figure 79 shows the M-H loops corresponding to the seeds and seeded products for a 'r' value of 1.0. In turn, Figure 80 plots the variation in the coercivity of the samples produced at the end of the three seeding/re-seeding cycles and the

corresponding maximum magnetization as a function of 'r'. The samples were synthesized without control of flow-rate. The rising trend in both parameters with 'r', clearly suggest the promotion of the heterogeneous nucleation. Therefore, the minimum variation in the average crystallite size as estimated from XRD analyses can be a consequence of the important superparamagnetic fraction in the seeded or re-seeded powders. This superparamagnetic fraction would affect the magnetization value but would not overcome the effect of larger particles on the coercivity. On this basis, a 'r' value of 1.0 was selected for subsequent seeding/re-seeding experiments under flow-rate controlled conditions.

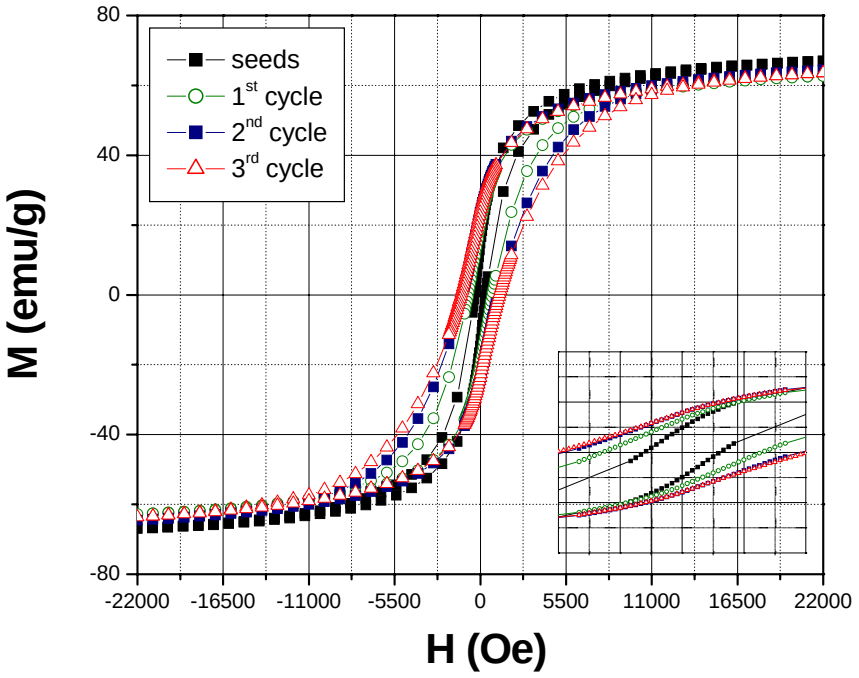

Figure 79: Room temperature M-H loops of cobalt ferrite nanocrystals treated by three cycles of seeding and re-seeding at r = 1.0.

TABLE 32: Coercivity, H_c, and magnetization, M_{max}, values of cobalt ferrite nanocrystals treated by seeding and re-seeding cycles at different 'r' values.

r = 0.25	**H_c (Oe)**	**M_{max} (emu/g)**
Seeds	443	55
1st cycle	735	60
2nd cycle	700	60
3rd cycle	785	58
r = 0.50	**H_c (Oe)**	**M_{max} (emu/g)**
Seeds	365	63
1st cycle	900	61
2nd cycle	928	61
3rd cycle	1075	59
r = 0.75	**H_c (Oe)**	**M_{max} (emu/g)**
Seeds	385	67
1st cycle	837	63
2nd cycle	1098	62
3rd cycle	1100	63
r = 1.0	**H_c (Oe)**	**M_{max} (emu/g)**
Seeds	366	67
1st cycle	772	63
2nd cycle	1151	64
3rd cycle	1229	64

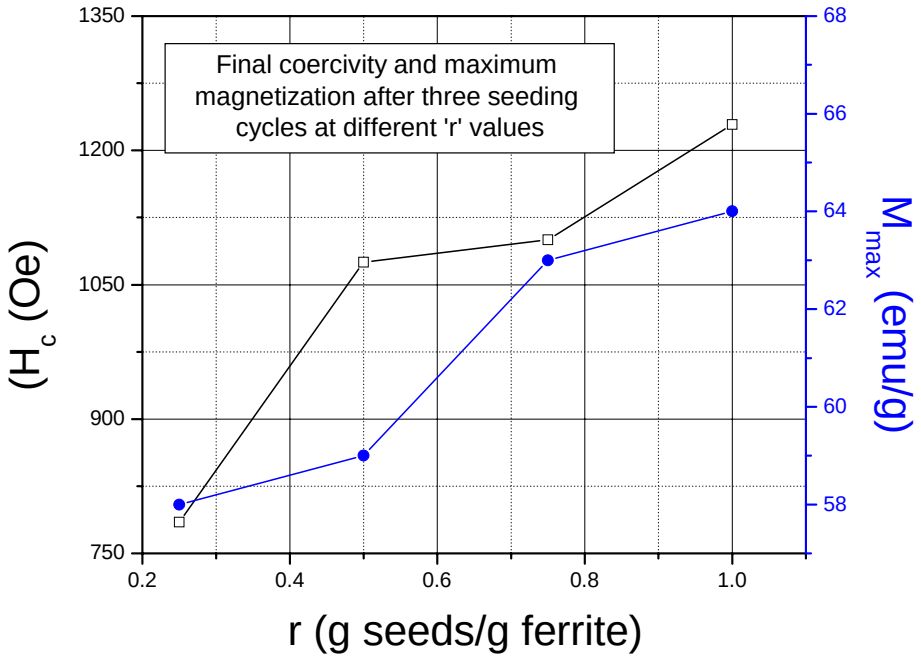

Figure 80: Variation in coercivity, H_c, and maximum magnetization, M_{max}, of cobalt ferrite crystals as a function of the ferrite/seed w/w ratio, 'r'. The samples correspond to the third re-seeding cycle.

5.4.2 Seeding and re-seeding experiments at ‘r’=1.0 and flow-rate controlled synthesis conditions

The synthesis under flow-rate controlled conditions was considered as an attempt to combine the enhancement effect on crystal growth of this route with heterogeneous nucleation promoted by the seeded-assisted synthesis approach. Figure 81 shows the XRD patterns of the samples produced after seeding and re-seeding for two times under a constant flow-rate of 0.81 mL/min. Only the peaks corresponding to the ferrite structure were observed. TABLE 33 summarizes the variation in average crystallite size and lattice parameter after each seeding cycle. It was observed a noticeable enlargement of crystal size (17 - 18 nm) in comparison with the values obtained without control of the flow-rate (11 - 13 nm). This effect was attributed to the promoting effect of low flow-rates as discussed in previous sections. Nevertheless, no drastic variation in average crystallite size was observed after the first seeding step. Despite of this minimum variation in size, the coercivity values exhibited a rising trend after each seeding cycle. It was increased from 3961 Oe, in starting seeds, up to 5605 Oe after the 3rd re-seeding cycle (TABLE 34). Once again, promoted heterogeneous nucleation where the seeds worked as pre-existing nuclei could explain this remarkable rise in coercivity. The maximum magnetization values did not suffer major changes and varied between 55 emu/g – 57 emu/g in all samples.

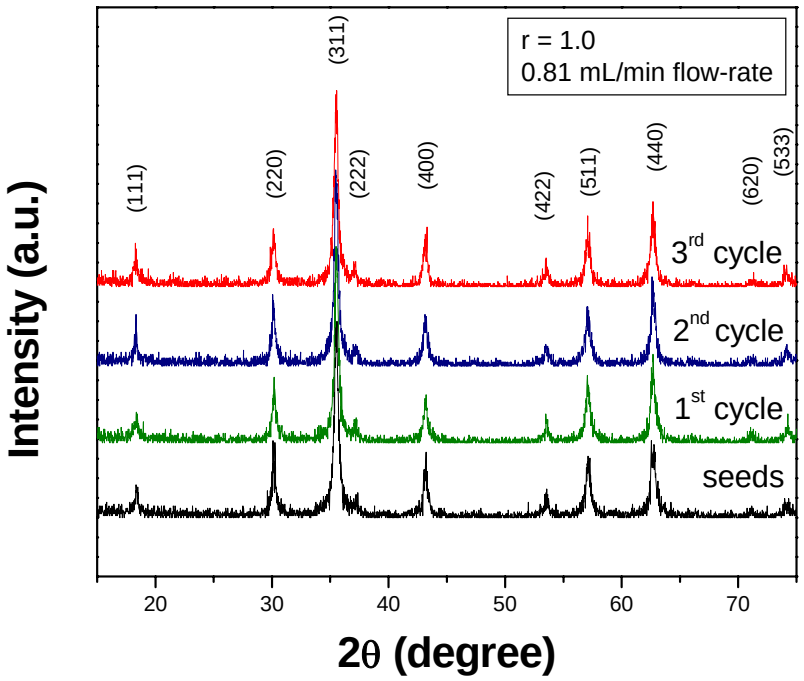

Figure 81: XRD patterns of cobalt ferrite treated by seeding and re-seeding cycles (r = 1.0) under flow-rate controlled synthesis conditions (0.81 mL/min).

TABLE 33: Average crystallite size, 't', and lattice parameter, 'a', of cobalt ferrite nanocrystals treated by seeding and re-seeding (r = 1.0) at 0.81 mL/min.

r = 1.0 0.81 mL/min	**t (± 1 nm)**	**a (± 0.003 Å)**
Seeds	17	8.379
1st cycle	18	8.380
2nd cycle	18	8.384
3rd cycle	17	8.383

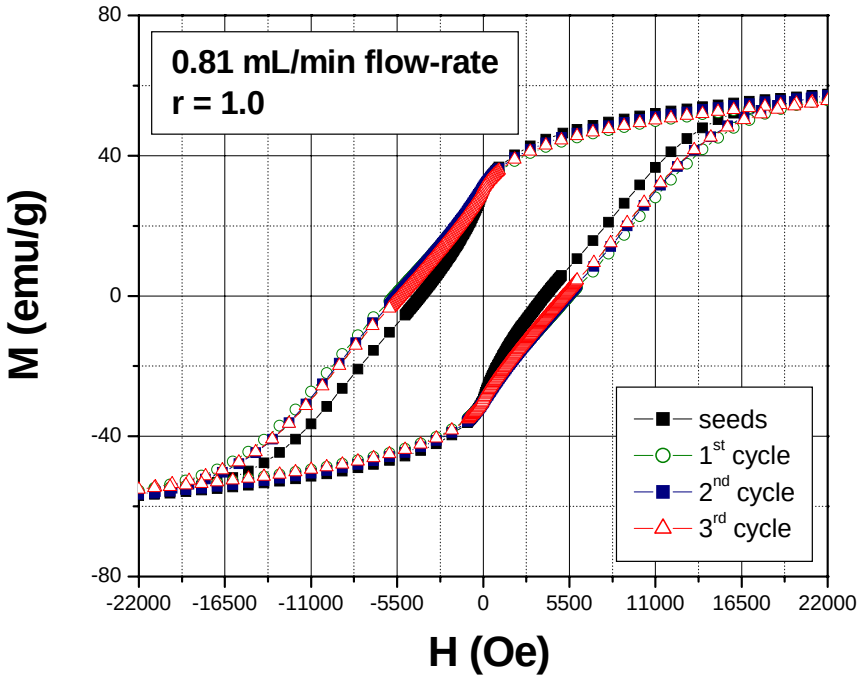

Figure 82: Room temperature M-H loops of cobalt ferrite nanocrystals treated by seeding and re-seeding cycles (r = 1.0) and 0.81 mL/min.

TABLE 34: Coercivity, H_c, and magnetization, M_{max}, values of cobalt ferrite nanocrystals treated by seeding and re-seeding cycles at different 'r' values and 0.81 mL/min.

r = 1.0 0.81 mL/min	H_c (Oe)	M_{max} (emu/g)
Seeds	3961	57
1st cycle	5218	55
2nd cycle	5416	57
3rd cycle	5605	56

5.4.3 Seeding-assisted synthesis of Ni-substituted cobalt ferrite (‘r’=1.0)

Previous results evidenced the promoting effect of seeding on crystal growth and the corresponding coercivity. Accordingly, synthesis under seeding-assisted conditions was carried out for Ni-substituted (‘y’ = 0.7) cobalt ferrite as an attempt to explore whether the heterogeneous nucleation effect, promoted by seeding, would allow a further enhancement in coercivity in this ferrite. These experiments were carried out without control on flow rate.

A. XRD Analyses

The XRD patterns of the Ni-substituted cobalt ferrite (y = 0.7) synthesized after three seeding cycles at r = 1.0 are shown in Figure 83. Again, only peaks corresponding to the ferrite structure were observed. TABLE 35 summarizes the structural properties of the synthesized samples. The average crystallite size was increased from 16 nm in the seeds to 19 nm in seeded samples. There was no a noticeable variation in crystal size after the first seeding cycles. Probably, the formation of superparamagnetic particles in each seeding cycle could have affected this average size value.

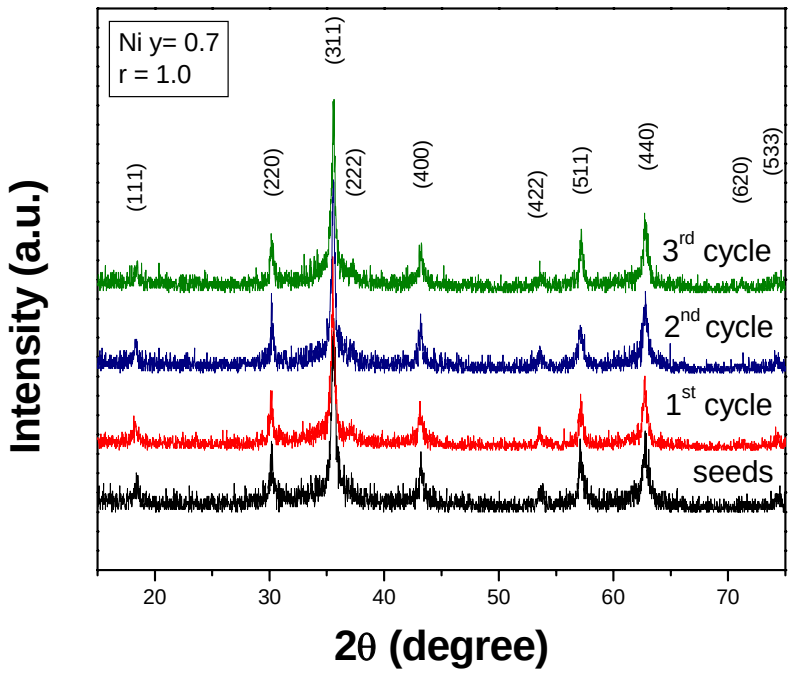

Figure 83: XRD patterns of Ni-substituted cobalt ferrite (y = 0.7) treated by seeding and re-seeding cycles and r = 1.0.

TABLE 35: Average crystallite size, 't', and lattice parameter, 'a', of Ni-doped cobalt ferrite nanocrystals (y = 0.7) submitted to seeding and re-seeding processes at 'r' = 1.0.

Ni –substituted Co ferrite, 'y' = 0.7	t (± 2 nm)	a (± 0.006 Å)
Seeds	16	8.373
1st cycle	18	8.381
2nd cycle	19	8.374
3rd cycle	18	8.370

B. M-H Measurements

M-H loops at room temperature of seeded Ni-substituted cobalt ferrite samples are shown in Figure 84. TABLE 36 summarizes the corresponding magnetization and coercivity values. As observed, the rise in coercivity was not as dramatic as for pure cobalt ferrite although it was systematically increased after each seeding cycle from 2382 Oe up to 3164 Oe. Based on the information provided by XRD, the enlargement on crystallite size with seeding could be the main reason behind this moderate increase in coercivity. On the other hand, the maximum magnetization values were not significantly affected and varied between 30 emu/g and 34 emu/g. The suggested increase in the amount of superparamagnetic particles after each seeding cycle can also explain this modest change in magnetization.

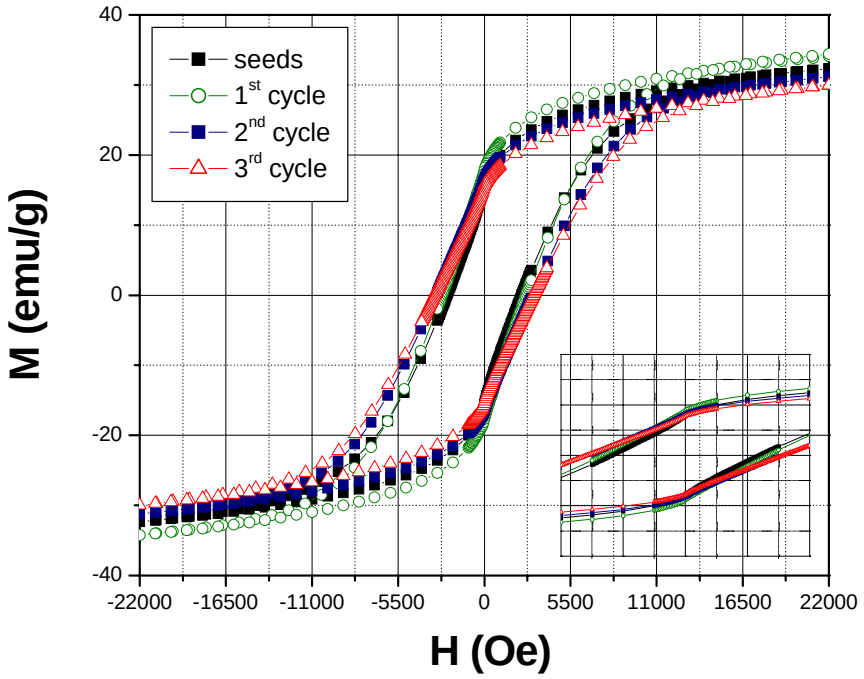

Figure 84: Room temperature M-H loops of Ni-substituted cobalt ferrite (y = 0.7) treated by seeding and re-seeding cycles at 'r' = 1.0.

TABLE 36: Coercivity, H_c, and magnetization, M_{max}, values of Ni-substituted cobalt ferrite (y = 0.7) treated by seeding and re-seeding cycles at 'r' = 1.0.

Ni –substituted Co ferrite, 'y' = 0.7	H_c (Oe)	M_{max} (emu/g)
Seeds	2382	32
1st cycle	2674	34
2nd cycle	3083	31
3rd cycle	3164	30

Concluding Remarks

It has been proved the effectiveness of the seed-mediated growth process by promoting of the heterogeneous nucleation. The optimum 'r' value was 1.0 that was conducive to an increase in coercivity of 236% with respect to the value in starting seeds. This approach was also effective under flow-rate controlled conditions but the increase in coercivity was in a lesser extent (42% over the seed value); an enhancement of the generation of superparamagnetic particles in each seeding cycle could explain this minor change in coercivity.

5.5 Crystal size reduction by high-energy

High-energy ball milling could be either used to synthesized materials starting from precursors followed by size reduction of it or may be used to reduced the size from a previously synthesized material. The high-energy impacts produced from the movement of the disks on which the milling jars and media (balls) are placed are the responsible of the production of new materials and/or size reduction. Sinha and Pradhan[86] synthesized and reduced the particle diameter of Cd-Zn ferrite to 7 nm after 25 hours ball milling. Abdahllah *et al.*[87] produced MnCo ferrite starting from Co ferrite and Mn ferrite and reduced it to 7.58 ± 0.03 nm.

The high-energy impacts could cause strain into the ferrite modifying coercivity due to the additional energy from strain anisotropy. The strain anisotropy is described by the magnetostatic energy:

$$E_a^{strain} = -\frac{3}{2}\lambda_s \sigma S \cos^2 \theta' \qquad \textbf{(15)}$$

where: λ is the saturation magnetostriction, σ is the strain value by surface unit, S the particle surface, and θ' the angle between magnetization and the strain tensor axis.

Our aim is to reduce crystal size from previously synthesized cobalt ferrite, as an effort to reach the superparamagnetic limit, and evaluate the effect of particle size reduction and strain on the corresponding magnetic properties.

5.5.1 Effect of high-intensity ball milling time on structural, specific surface area and magnetic properties of cobalt ferrite powders

Cobalt ferrite samples exhibiting different average crystallite sizes (12 nm and 18 nm) were processed by high-energy ball milling at different milling times. The first ferrite sample was synthesized by the conventional coprecipitation method (no control on flow-rate) whereas the second was produced by the modified coprecipitation method at 0.71 mL/min. The NaOH concentration was and 0.315 M in both cases.

In addition to XRD analyses, milled powders were analyzed in a BET surface area analyzer to determine the corresponding specific surface area at different milling times. The external specific surface area[88] of spheres, SSA, with diameter '*t*' (or cubes with edge length '*t*') and density ρ was estimated by:

$$SSA = \frac{6}{\rho t} \qquad \textbf{(16)}$$

This equation does not take into account interparticle overlapping (aggregation) only agglomeration. The density[89] of cobalt ferrite was 5.304 g/cm^3 and the diameter was considered as the same estimated using the Scherrer's equation. The specific surface area calculated by equation 16 will be compared with the values obtained from experimental BET measurements.

A. XRD Analyses

XRD patterns from the 12 nm and 18 nm cobalt ferrite powders before milling process (0 min) and after several milling times (30 min, 60 min, and 300 min) are shown in Figure 85

and Figure 86, respectively. Peak broadening became evident after prolonged milling time; this broadening suggests the decrease in crystallite size. The average crystallite size of the 12 nm powders showed a just minor decrease (10 nm) even after 10 hours of milling. The 18 nm samples exhibited a more noticeable drop in the average crystallite size; it decreased down to 10 nm at the end of the 10 hours milling period. Evidently, the impact and abrasion forces generated inside the milling jar should have broken up the crystals even at the nanoscale. Figure 85 and Figure 86 also evidenced the shift of the XRD peaks towards smaller diffraction angles. This shift in diffraction angle could be attributed to uniform strain, which would be reflected in the increase of the interplanar distance[32,90]. The corresponding interplanar distance, *d*, corresponding to the (440) peak, was increased from 1.483 Å to 1.486 Å when the milling time was prolonged up to 10 hours. XRD analyses suggest that high-energy ball milling could effectively contribute to induce distortion in the unit cell while favoring certain decrease in crystal size.

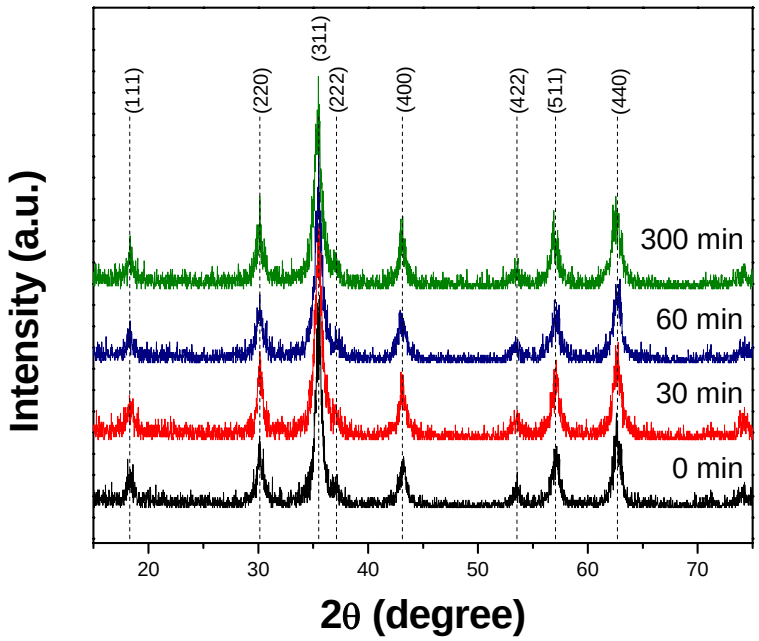

Figure 85: XRD patterns of 12 nm-cobalt ferrite nanocrystals ball-milled at different times.

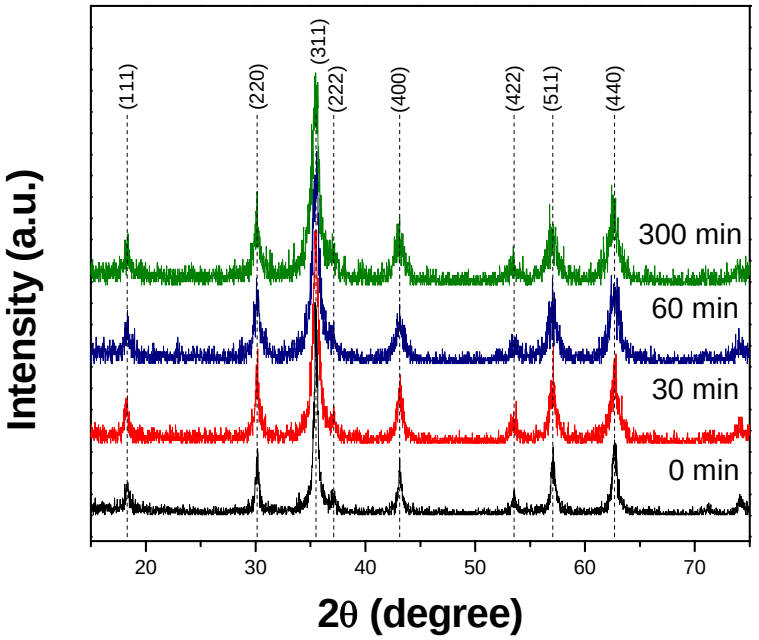

Figure 86: XRD patterns of 18 nm-cobalt ferrite nanocrystals ball-milled at different times.

B. BET-Specific Surface Area of ball-milled powders

TABLE 37 and TABLE 38 show the calculated and experimental specific surface area values for the 12 nm and 18 nm samples, respectively, ball-milled at different times. As observed, the calculated and the measured BET specific surface area were very similar in the starting powders, which suggest that individual, non-aggregated nanocrystals were produced. However, the discrepancy between these two values became remarkable after prolonging the milling time. The decreasing trend in specific surface area with milling time can be attributed to strong interparticle aggregation promoted by intensive milling. A similar aggregation phenomenon has been observed in different materials after intensive ball-milling [91-93]. Furthermore, comparison of Figure 87 and Figure 88 and the corresponding tables, suggests that the aggregation of the nanocrystals was slightly more pronounced in the 18 nm sample.

The 18 nm sample shows an initial reduction in SSA below 50 minutes milling time that could be attributed to aggregation. A small increment in SSA is mainly attributed to crystal size reduction in the range between 50 and 180 minutes. Aggregation is the dominant mechanism at long milling times. For the case of the 12 nm sample, the crystal size reduction is not significant and aggregation predominates since the beginning of the milling process.

The aggregation effect was also suggested by the TEM analyses of both ball-milled samples. Figure 90 and Figure 91 evidenced the strong aggregation of those nanocrystals after 5 hours of milling.

TABLE 37: Variation in average crystallite size, 't', lattice parameter, 'a', and specific surface area (SSA) measurements of ball-milled cobalt ferrite nanocrystals with initial average crystallite size of 12 nm.

Milling time (min)	t (± 1 nm)	A (± 0.02 Å)	Calculated SSA (m^2/g)	BET SSA (m^2/g)
0	12	8.38	99.06	96.45
20	11	8.38	109.40	77.21
30	10	8.38	113.69	71.27
40	10	8.38	116.74	69.22
50	10	8.39	119.08	71.25
60	10	8.39	111.23	73.39
180	10	8.39	121.51	65.36
300	9	8.40	131.23	62.15
600	10	8.40	124.04	59.39

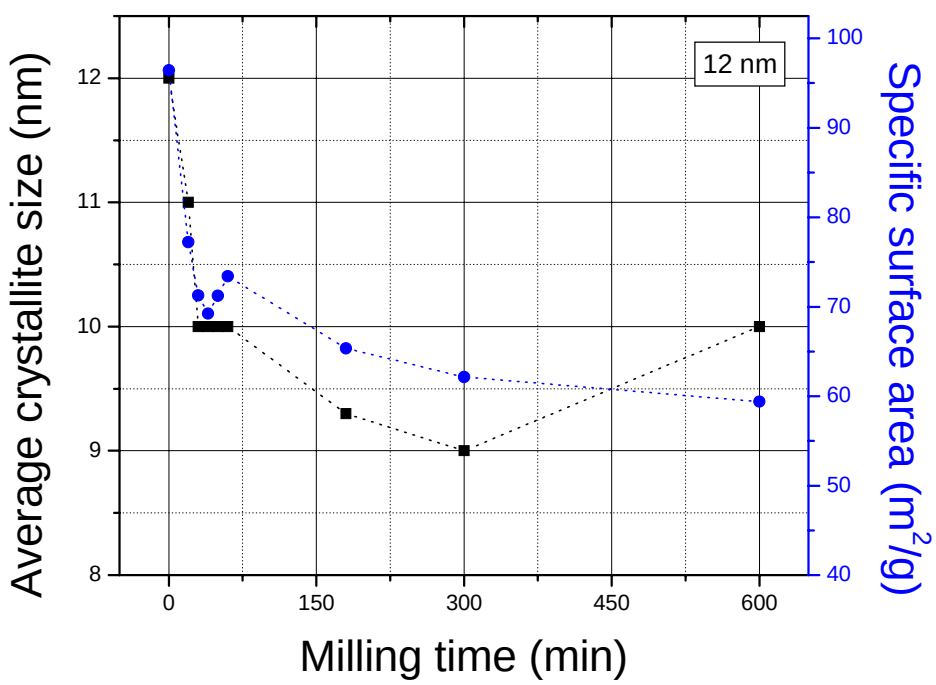

Figure 87: Average crystallite size and surface area versus milling time of cobalt ferrite with initial average crystallite size of 12 nm. The dot line shown in the figure is a visual guide to show the decreasing trend in both, average crystallite size and SSA.

TABLE 38: Variation in average crystallite size and surface area as a function of milling time of 12 nm-cobalt ferrite. The dot line shown in the figure is a visual guide to show the decreasing trend in both, average crystallite size and SSA.

Milling time (min)	t (± 3 nm)	A (± 0.01 Å)	Calculated SSA (m^2/g)	BET SSA (m^2/g)
0	18	8.39	66.11	71.35
20	14	8.38	92.27	62.36
30	12	8.39	97.18	55.72
40	12	8.38	99.58	52.26
50	11	8.39	102.10	54.41
60	10	8.39	121.51	59.38
180	9	8.39	140.87	63.5
300	10	8.39	121.51	58.73
600	10	8.41	124.04	55.11

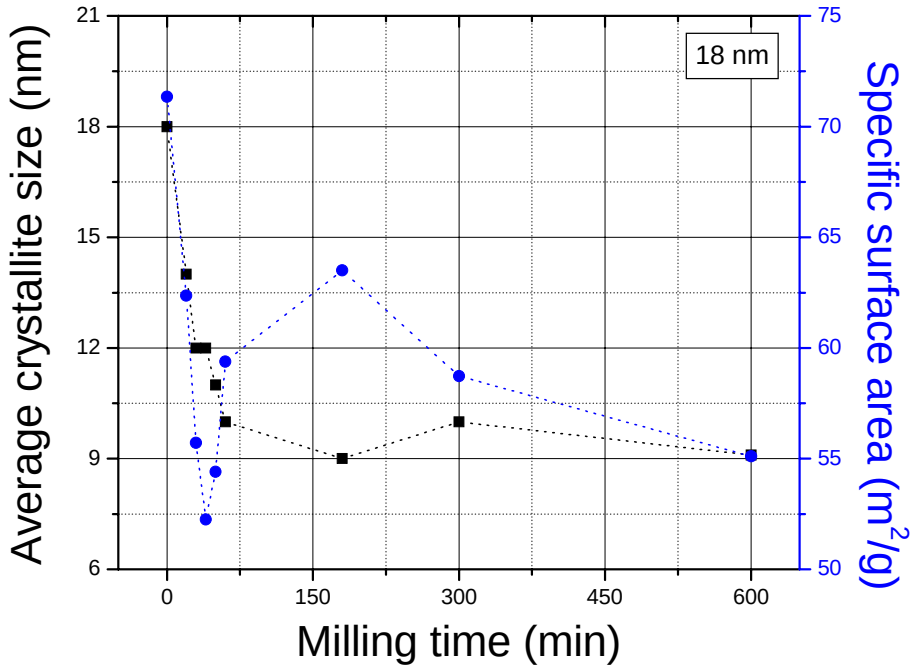

Figure 88: Variation in average crystallite size and surface area as a function of milling time of 18 nm-cobalt ferrite particles.

C. TEM Images

High resolution TEM images of both samples before milling are shown in Figure 89; small crystal sizes are nearly rounded while bigger ones are nearly squared.

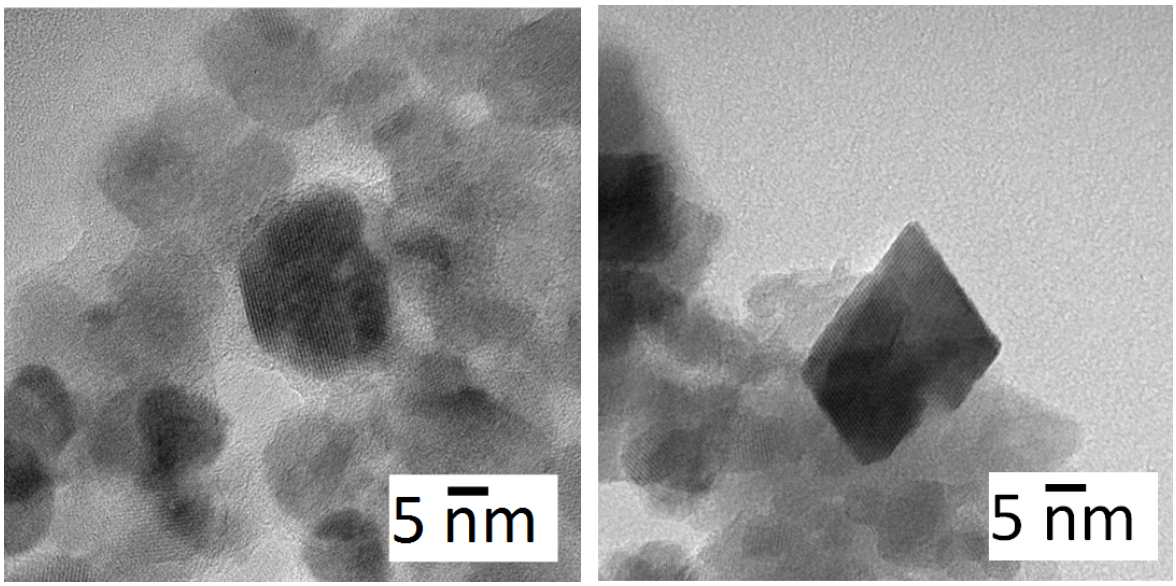

Figure 89: High-Resolution TEM images of cobalt ferrite with average crystallite sizes of 12 nm (left) and 18 nm (right) before milling.

Figure 90 shows the TEM images of the cobalt ferrite with average crystal size of 12 nm before and after 5 hours of milling; interparticle aggregation is evident. The same behavior was observed in the 18 nm cobalt ferrite particles (Figure 91). These images clearly explained the discrepancy between the calculated and measured SSA values: the longer the milling, the more pronounced the particle aggregation and drop in SSA.

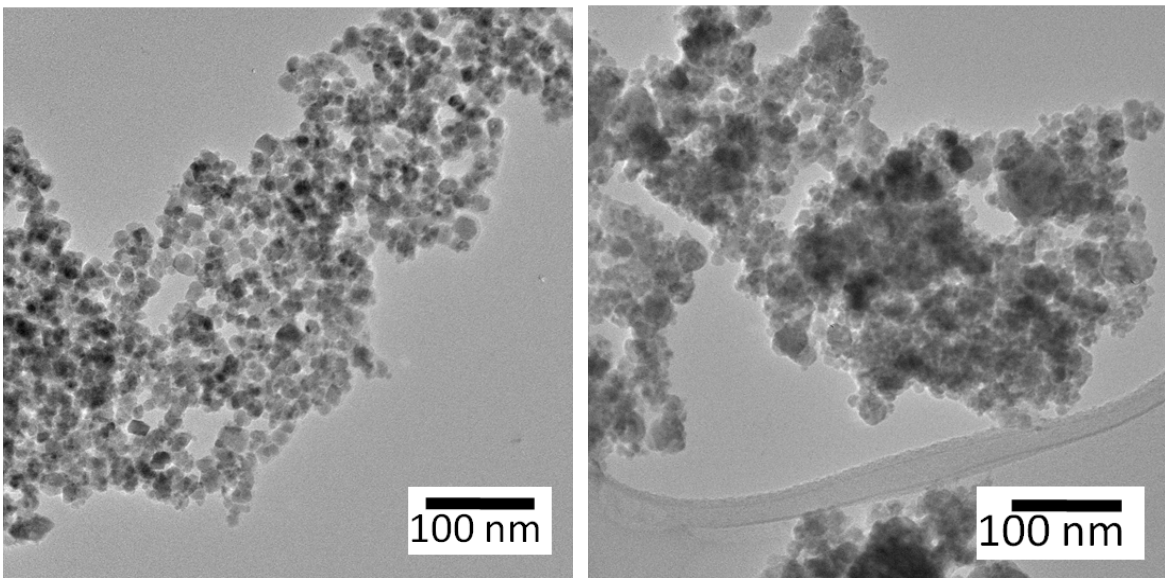

Figure 90: TEM images of cobalt ferrite nanocrystals before (left) and after 5 hours of high-intensity ball milling (right). The average crystallite in the starting sample was 12 nm.

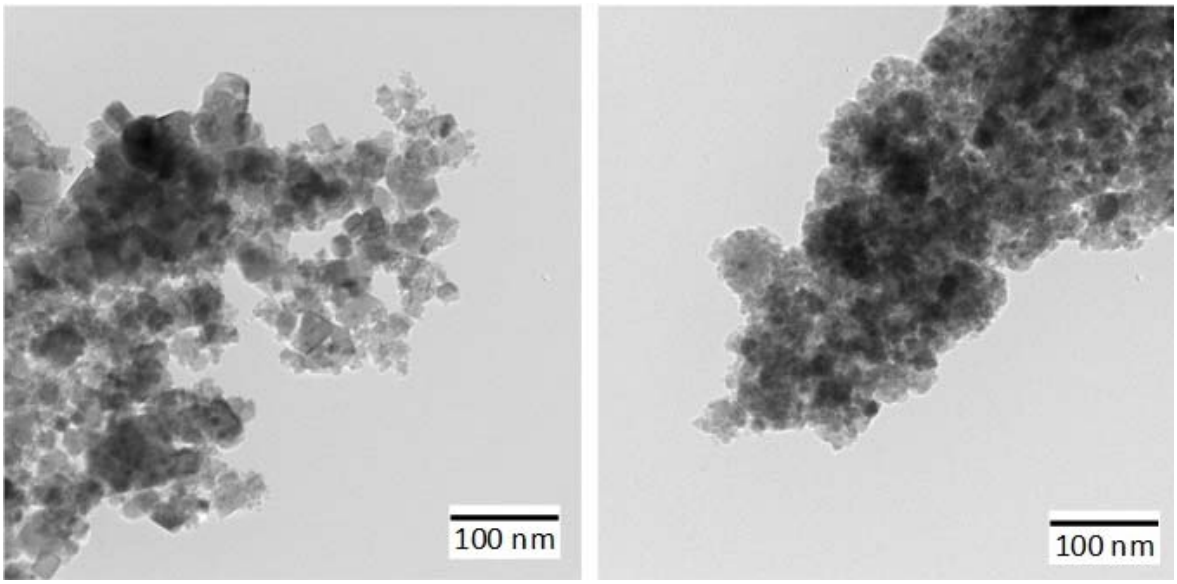

Figure 91: TEM images of cobalt ferrite nanocrystals before (left) and after 5 hours of high-intensity ball milling (right). The average crystallite in the starting samples was 18 nm.

D. M-H Measurements

Room temperature M-H measurements of 12 nm cobalt ferrite nanocrystals submitted to high-energy ball milling are shown in Figure 92 and the summary of magnetic properties is summarized in TABLE 39. A careful examination of the coercivity values shows that milling time increases coercivity in a 25%, which is accompanied by a decrease in crystal size. This increase in coercivity could be explained by the introduction of strain into the ferrite structure, a fact that was suggested by XRD measurements. The strain is a type of defect into the crystalline structure caused by the high-energy impacts. On the other hand, the 18 nm sample suffered a continuous reduction in coercivity with increasing in milling time. This trend was in agreement with the observed decrease in crystal size at prolonged milling times. After 10 hours milling time the coercivity reaches the same value than the 12 nm sample, i.e., 491 Oe. The corresponding M-H loops and magnetic properties are shown in Figure 94 and TABLE 40, respectively. The maximum magnetization is not greatly affected by the milling process. It kept in the ranges of 55 - 61 emu/g and 52 - 55 emu/g for the 12 and 18 nm samples, respectively.

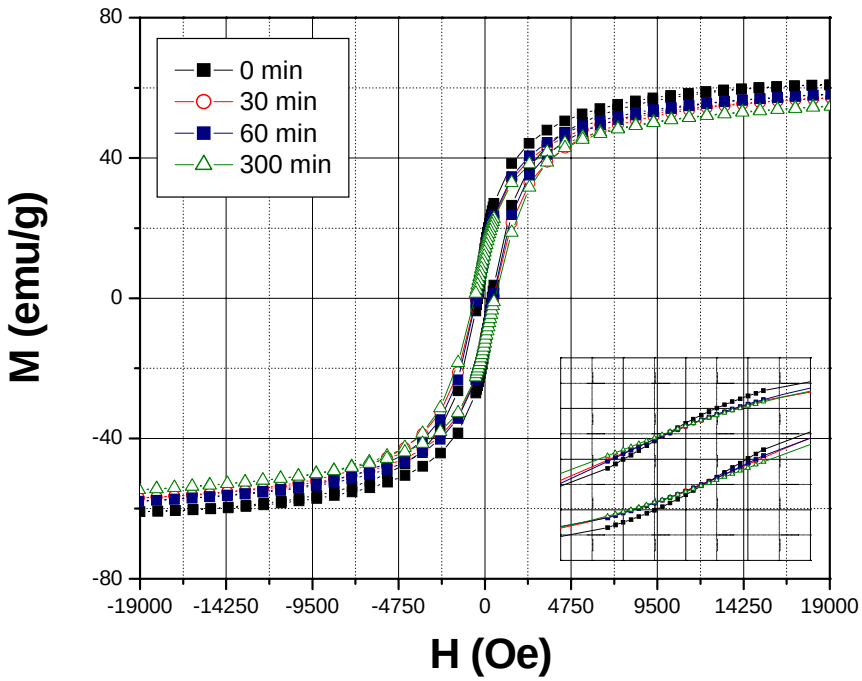

Figure 92: Room temperature M-H measurements of ball-milled cobalt ferrite nanocrystals with an initial average crystallite size of 12 nm.

TABLE 39: Coercivity, H_c, and maximum magnetization, M_{max}, of cobalt ferrite submitted to high-energy ball milling. The initial average crystallite size was 12 nm.

Milling time (min)	H_c (Oe)	M_{max} (emu/g)
0	394	61
20	470	58
30	483	58
40	480	57
50	466	58
60	462	59
180	495	59
300	560	55
600	491	56

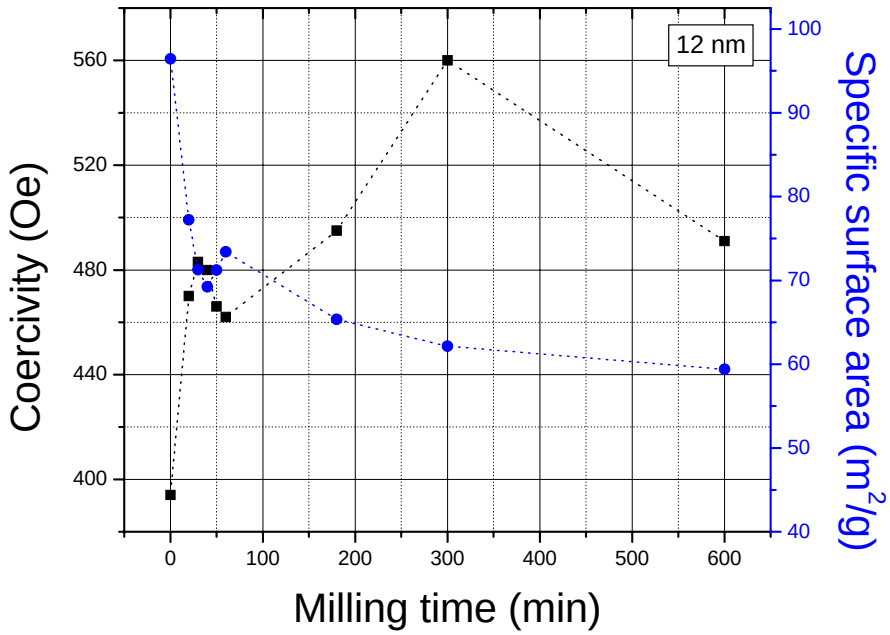

Figure 93: Variation in coercivity and specific surface area with milling time of cobalt ferrite with initial average crystallite size of 12 nm.

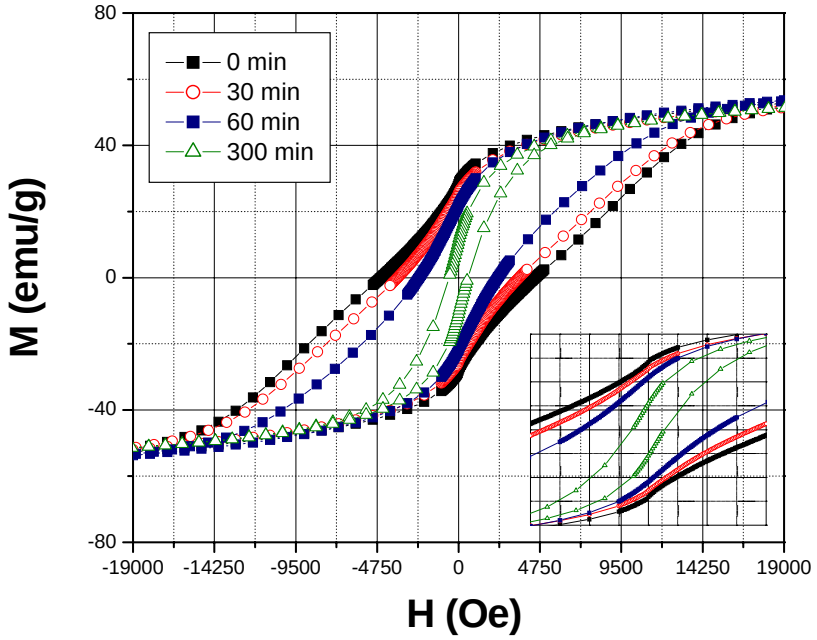

Figure 94: Room temperature M-H loops of ball-milled cobalt ferrite nanocrystals with initial average crystallite size of 18 nm. The inset shows the MH data around the origin.

TABLE 40: Coercivity, H_c, and maximum magnetization, M_{max}, of cobalt ferrite submitted to high-energy ball milling. The initial average crystallite size was 18 nm.

Milling time (min)	H_c (Oe)	M_{max} (emu/g)
0	4506	53
20	4011	55
30	3539	53
40	2974	54
50	2748	55
60	2290	55
180	708	55
300	555	52
600	491	53

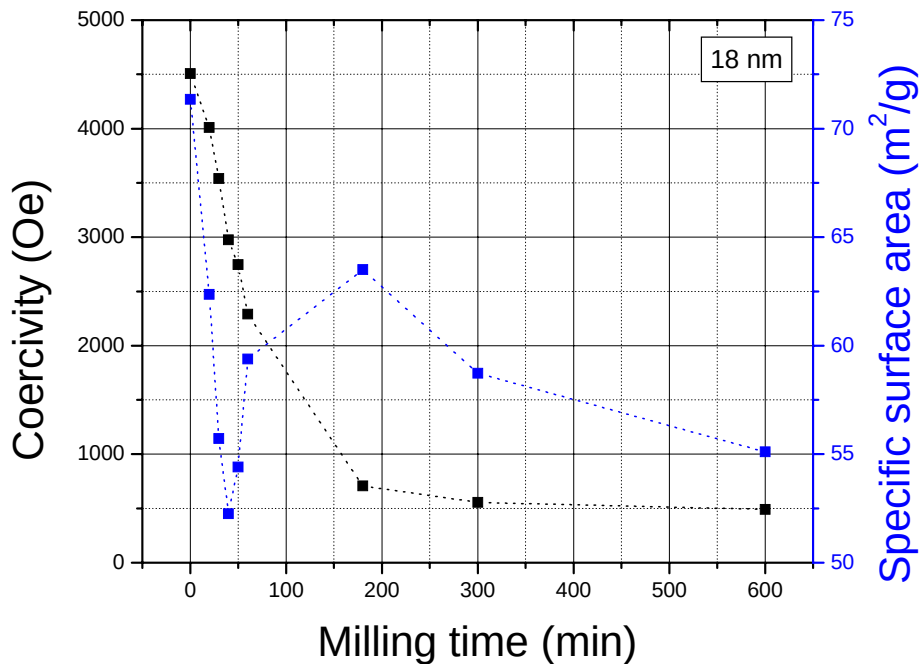

Figure 95: Variation in coercivity and specific surface area with milling time of cobalt ferrite with initial average crystallite size of 18 nm.

Concluding Remarks

Both sets of samples exhibited different trends. The high-energy ball milling of the 12 nm cobalt ferrite sample was governed by the introduction of strain which finally conducted to an increment in coercivity. A decrease in coercivity was found for the cobalt ferrite nanocrystals with initial average crystallite size of 18 nm; this trend was attributed to the continuous reduction in average crystallite size by prolonging milling time.

5.6 Shape modification by hydrothermal synthesis

Hermetic reaction vessels allow the achievement of temperatures over the boiling point of the solvent along with higher pressures. These extreme conditions should affect the rate of the dissolution-recrystallization processes involved with the formation of the ferrite crystals and, consequently, induce changes in the composition, size or shape of the final solid products. In particular, any shape different from spherical will introduce a shape anisotropy and hence, a variation in magnetic properties of the particles should also be expected[94]; it will be easier to magnetize a non-spherical sample along a long axis than along a short axis due to the demagnetizing field. The demagnetizing field is smaller in the longer direction because the dipoles at the surface of the sample are more spaced.

A. XRD Analyses

XRD patterns of cobalt ferrite synthesized at different temperatures are shown in Figure 96. The reaction time was 60 minutes in all experiments and the internal pressure was the vapor pressure at the synthesis temperature. Very well defined and sharp peaks corresponding to ferrite structure were observed that evidenced the high crystallinity of the powders. As TABLE 41 shows, the average crystallite size was increased from 12 nm up to 16 nm when the synthesis temperature varied from 100°C to 350°C. Evidently, higher temperatures should have promoted the dissolution - recrystallization mechanism involved with the crystal formation. Also, the dissolution of smaller individuals at higher temperatures should have

favored the formation of larger crystals. Temperatures between 150 °C and 250 °C led to lattice parameters smaller than the bulk. In contrast, temperatures between 300 °C and 350 °C were conducive to ferrite powders with a lattice parameter comparable to the bulk.

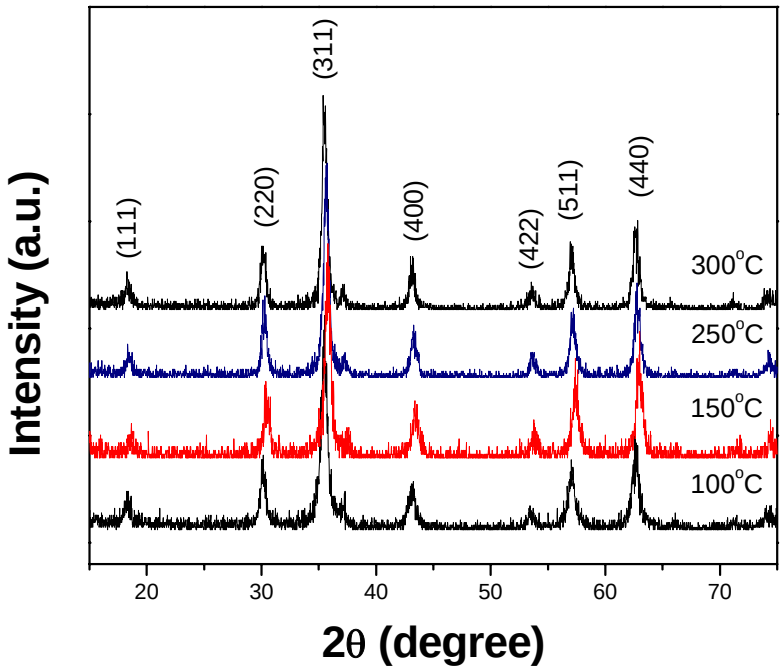

Figure 96: XRD patterns of cobalt ferrite synthesized by the hydrothermal method at different temperatures.

TABLE 41: Summary of structural properties of cobalt ferrite powders produced by the hydrothermal process.

Temperature (°C)	Vapor Pressure (psi)	t (±1 nm)	a (± 0.02 Å)
100	20	12	8.38
150	60	13	8.34
200	220	14	8.36
250	600	15	8.37
300	1270	15	8.39
350	2440	16	8.39

B. TEM Images

TEM images of cobalt ferrite synthesized at 250 °C and 350 °C are shown in Figure 97 and Figure 98, respectively. These images revealed the highly monodispersity of squared-like particles in the nanometric size range. The high crystallinity of these nanoparticles is evidenced in the High Resolution TEM image of the sample produced at 350 °C; the lattice fringes can be clearly observed. The crystal size, calculated averaging 100 particles, is around 22 ± 6 nm.

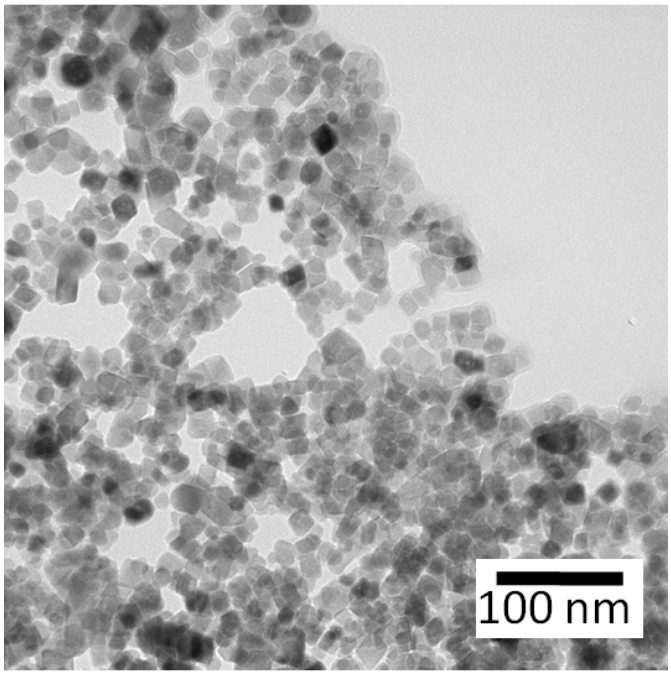

Figure 97: TEM image of cobalt ferrite synthesized by hydrothermal method at 250 ºC.

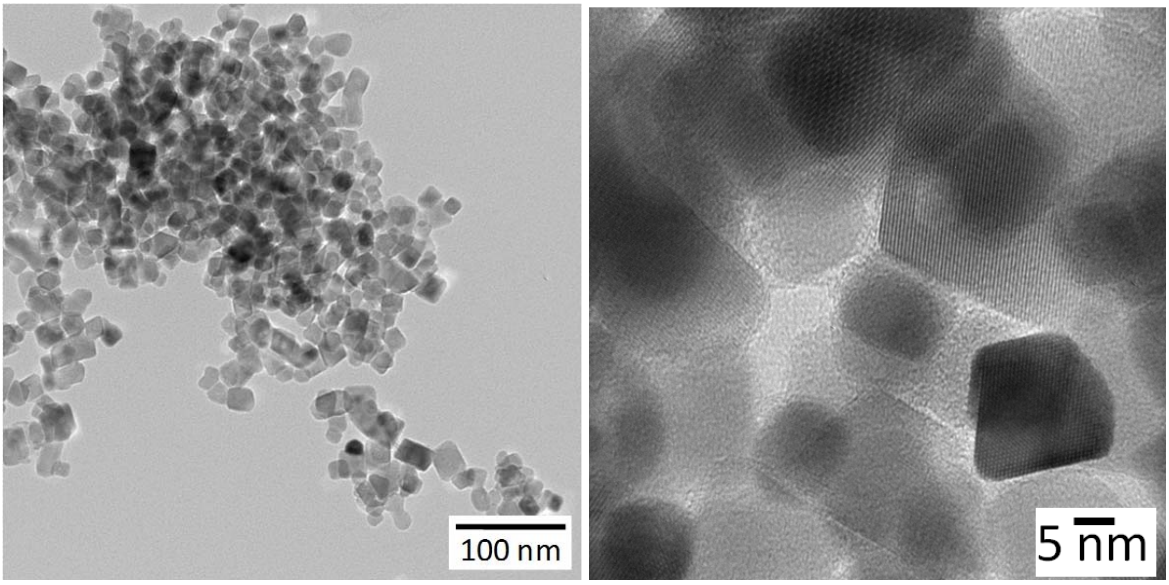

Figure 98: TEM image of cobalt ferrite synthesized by the hydrothermal method at 350 ºC (left). Right-hand figure shows the corresponding High-Resolution TEM image.

C. M-H Measurements

Room temperature M-H loops corresponding to cobalt ferrite nanocrystals produced by the hydrothermal process at 250°C, 300°C, and 350 °C are shown in Figure 99. The rise in magnetization with synthesis temperature became evident. The maximum magnetization reached 75 emu/g when the synthesis temperature was 350°C. This value is near to the bulk value of 80 emu/g. Such high magnetization could be consequence of well crystallized particles without surface defects such as canted spins or poorly crystallized surface as suggested for the nanoparticles produced at 100 ^{o}C by the conventional co-precipitation method. As seen in TABLE 42, coercivity values are in the range of 670 and 815 Oe, when the synthesis temperature varies between 100°C and 350 °C. These coercivity values are above the ones obtained by the co-precipitation method under similar synthesis conditions.

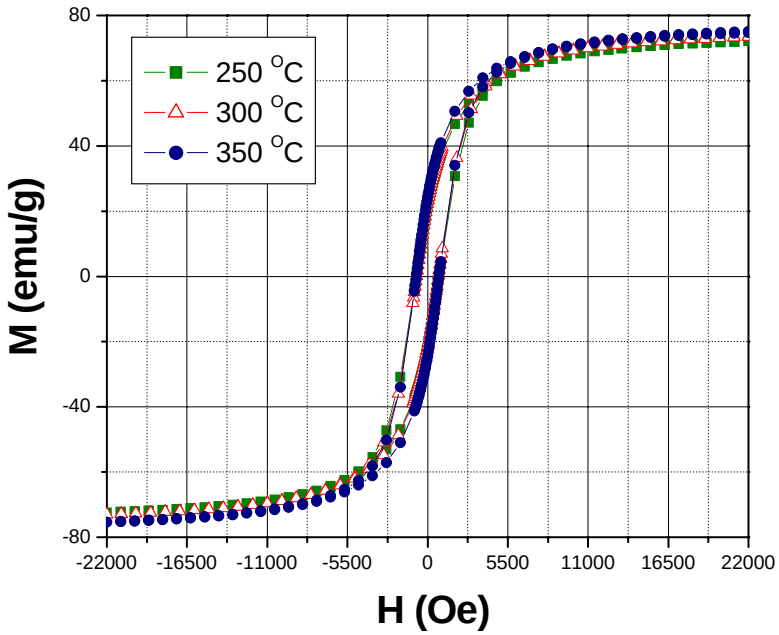

Figure 99: Room temperature M-H measurements of cobalt ferrite synthesized by the hydrothermal method at different temperatures.

TABLE 42: Summary of magnetic properties of cobalt ferrite synthesized by the hydrothermal process.

Temperature (°C)	Vapor Pressure (psi)	H_c (Oe)	M_{max} (emu/g)	Squareness ratio M_r/M_s
100	20	670	63	0.29
150	60	815	67	0.32
200	220	802	70	0.31
250	600	775	72	0.30
300	1270	747	73	0.30
350	2440	773	75	0.32

5.6.1 Comparison between nanoparticles synthesized by coprecipitation and hydrothermal processes

The main features of the samples synthesized by conventional coprecipitation and the hydrothermal processes are compared in TABLE 43. The high temperature and hence, high pressure reached in the hydrothermal process lead to highly stoichiometric cobalt ferrite. The size and shape was also modified; well-crystallized and square-shaped nanoparticles were synthesized in the autoclave contrasting with smaller spherical particles typical of coprecipitation synthesis. The better crystallized particles produced through the hydrothermal route also exhibited improved magnetization and coercivity values. The larger crystallite size and the contribution of shape anisotropy contributed to attain the higher coercivity values in these samples. The high quality of the product obtained by the hydrothermal process is also responsible of the observed high magnetization, very close to the bulk value of 80 emu/g.

TABLE 43: Comparison between main features of the nanoparticles synthesized by conventional coprecipitation and hydrothermal processes.

Synthesis method	**Coprecipitation**	**Hydrothermal Synthesis**
Synthesis Temperature (°C)	100	350
Vapor Pressure (psi)	--	2440
Fe:Co mole ratio (measured by EDS)	1.58:1	1.96:1
Particle shape	Spherical 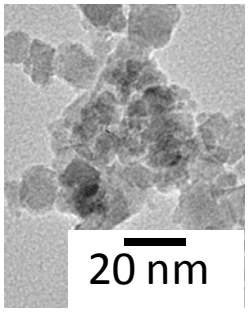	Squared 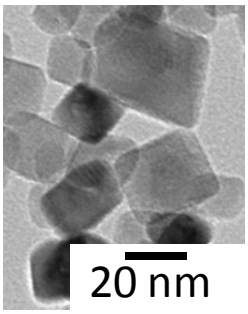
t (nm)	12	16
a (± 0.005 Å)	8.384	8.393
H_c (Oe)	402	773
M_{max} (emu/g)	60	75
Squareness ratio (M_r/M_s)	0.23	0.32

Concluding Remarks

Cobalt ferrite nanocrystals were produced successfully by the hydrothermal process. These nanocrystals exhibited enhanced magnetic properties due to the high crystallinity and shape modification when compared to the coprecipitation method. The introduction of shape anisotropy will cause an increase in the total anisotropy energy and hence, coercivity within the single domain region. Synthesis temperatures above 350 °C would lead to particle sizes even bigger, corresponding to the multi-domain region where the coercivity decreases.

5.7 Post-synthesis thermal treatment of ferrite powders

Samples of cobalt ferrite nanocrystals were thermally treated at different temperatures under atmospheric conditions to evaluate the variation in the crystallinity and hence, in the corresponding magnetic properties. Cobalt ferrite powders synthesized at 0.85 mL/min and 0.48 M NaOH concentration were thermally treated for one hour in air in the temperature range of 500°C – 900 °C, in order to promote particle growth by intergranular diffusion. This effort was intended to produce particles at the bulk scale where magnetic properties correspond to those of the magnetic multi-domain region.

A. XRD Analyses

Figure 100 shows the XRD patterns of the cobalt ferrite samples treated at 700 °C and 900 °C in air. The sharpening of the diffraction peaks evidenced the crystal growth with increase in thermal treatment temperature. The average crystallinity size was not determined using the Scherrer's equation due to the limitation of this approach when crystal sizes higher than 100 nm are involved[90]. The lattice parameter was only slightly modified by the treatment temperature when compared to the bulk value of 8.377 Å.

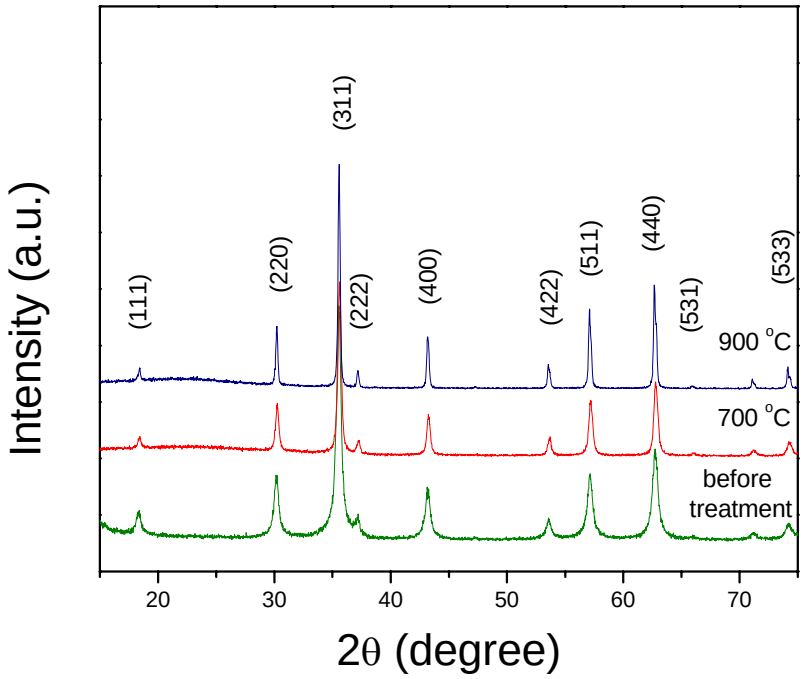

Figure 100: XRD patterns of cobalt ferrite powders thermally treated in air at various temperatures. The XRD pattern of the starting powder synthesized under flow-rate controlled conditions is also included for comparison purposes.

TABLE 44: Lattice parameter of cobalt ferrite nanocrystals submitted to thermal treatment in air.

Thermal Treatment Temperature (°C)	a (±0.009 Å)
Before treatment	8.378
500	8.358
600	8.368
700	8.368
900	8.380

B. Morphological Analyses

i. **SEM Images**

Although SEM images are not of high magnification, an increment in particle size can be noticed when the treatment temperature increases. Larger particles (@200 nm) could be observed in the sample treated at 900 °C. Such increment in particle size is attributed to intergranular diffusion, a process that is enhanced at higher temperature.

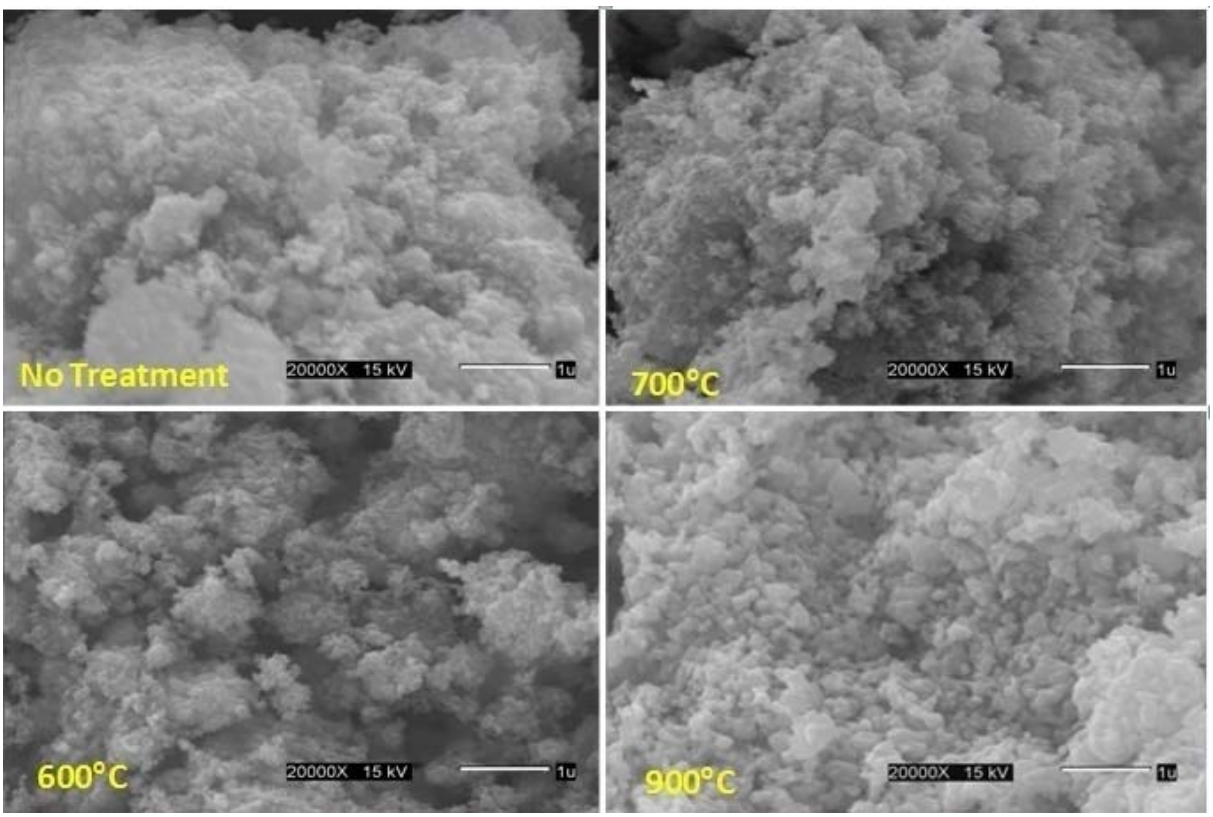

Figure 101: SEM images of cobalt ferrite submitted to thermal treatment at different temperatures.

ii. **TEM Images**

Figure 102 shows the TEM image and the electron diffraction pattern corresponding to a single crystal of cobalt ferrite treated at 900 °C. The electron diffraction pattern evidences the high crystallinity of the selected single crystal. The single crystal in the red box is oriented along the [02-1] zone axis (see APPENDIX A. for determination of beam direction).

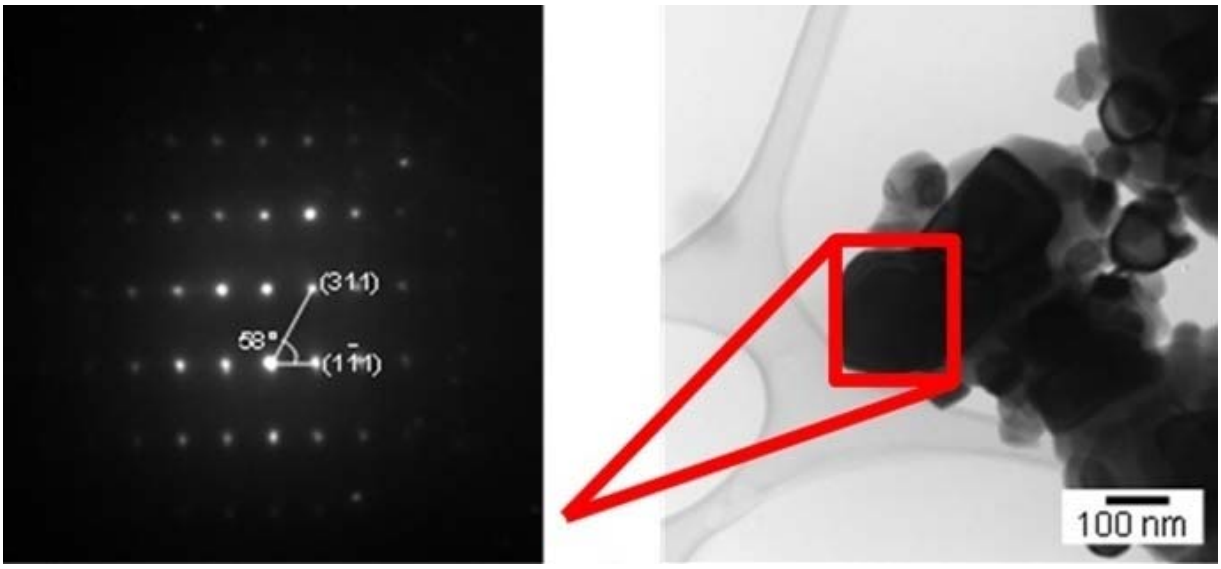

Figure 102: Electron diffraction pattern (ED) and TEM image of cobalt ferrite submitted at 900 ºC thermal treatment in air.

D. M-H Measurements

The data of Figure 103 and TABLE 45 shows the drop in coercivity with a rising temperature. This decrease in coercivity is attributed to the enlargement of the ferrite crystals and the establishment of multiple magnetic domains. The maximum magnetization increased

gradually with annealing temperature till reaching 79 emu/g, which is very close to the bulk value of 80 emu/g.

TABLE 45: Summary of magnetic properties of cobalt ferrite nanocrystals submitted to thermal treatment in air.

Thermal Treatment Temperature (°C)	H_c (Oe)	M_s (emu/g)	Squareness ratio
Before treatment	3653	54	0.49
500	750	63	0.34
600	1003	66	0.41
700	1212	72	0.46
900	823	79	0.45

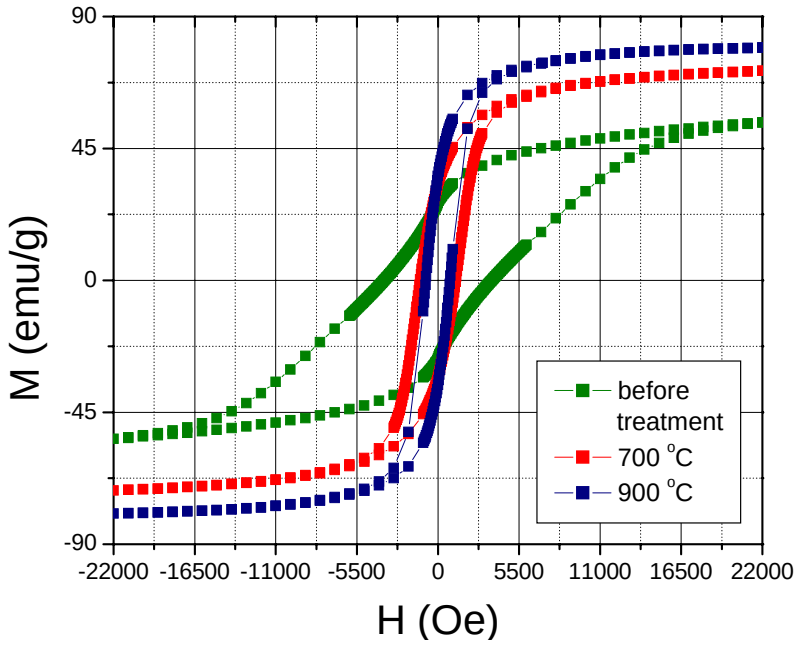

Figure 103: M-H room temperature loops of cobalt ferrite submitted to thermal treatment.

Concluding Remarks

The desired particle growth and the corresponding ‘jump’ to the multi-domain region were achieved by intergranular diffusion due to high temperature treatment. Reduction in coercivity value, in addition to the rise in magnetization values, confirms the switch to the multi-domain region.

5.8 Inhibition of crystal growth: Use of surfactants or polymers during the ferrite crystal formation

The use of surfactants or polymers comes from the necessity to produce extremely small particles, which could help us to determine the actual superparamagnetic limit in the cobalt ferrite. Surfactants were used to inhibit crystal growth, because of expected surface interaction between polar groups and nanoparticles, as well as prevent nanoparticles aggregation through strong steric interactions promoted by the adsorption of surfactants, polymers, or other organic species (‘capping ligands’). These surfactant and polymers have long chains that confer a physical impediment preventing particle growth and/or aggregation. Four surfactants were evaluated: Oleic acid sodium salt (Na-oleate), Cetyltrimethylammonium bromide (CTAB), Sodium dodecyl sulfate (SDS), and Polyvinylpyrrolidone M.W. 40000 (PVP). The corresponding chemical formula and structure were presented in TABLE 8.

.

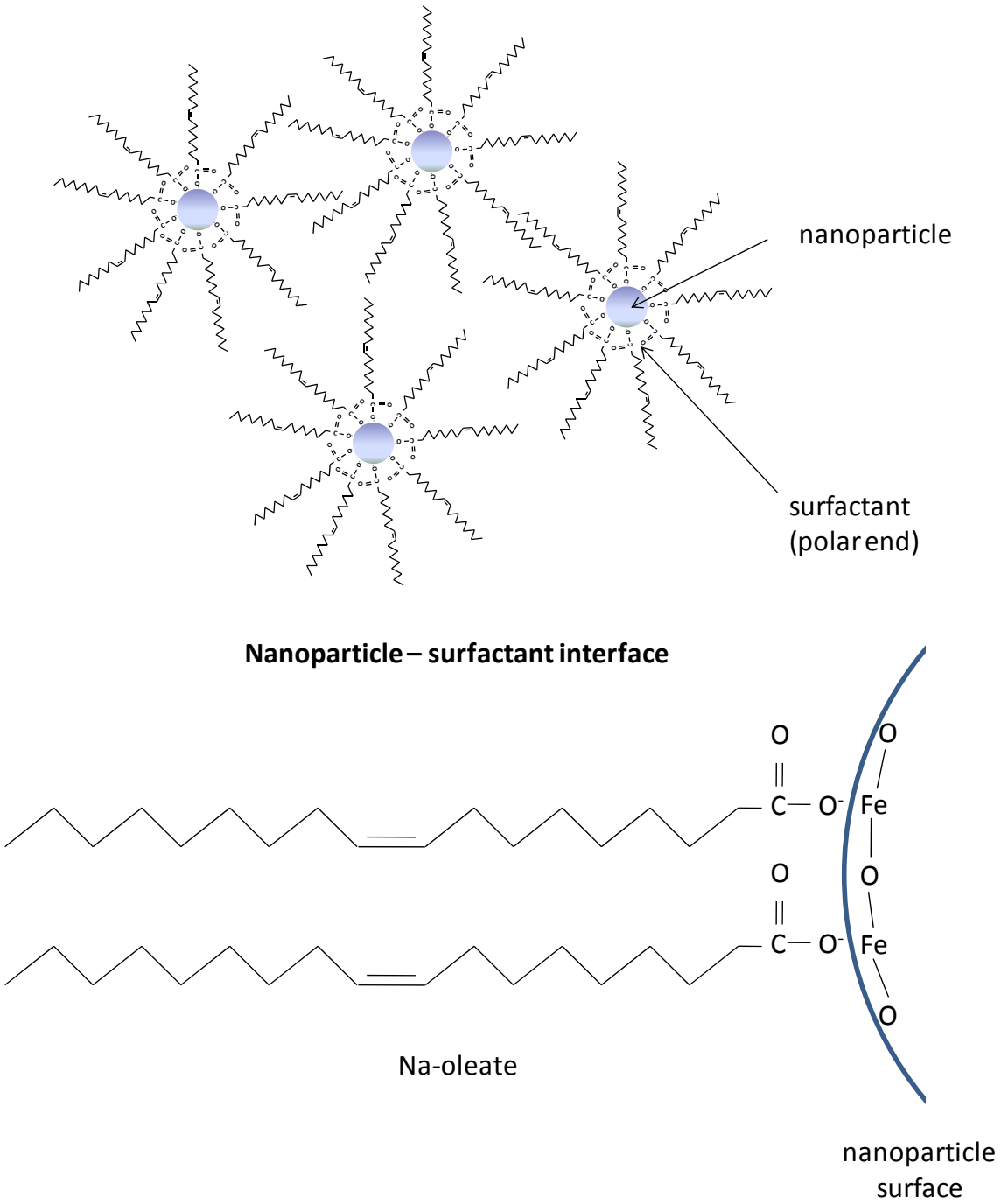

Figure 104: Mechanism of inhibition of crystal growth by means of steric effect enhanced by surfactants adsorption onto nanoparticles surface.

5.8.1 Effect of the type of surfactant

A. XRD Analyses

The synthesis of cobalt ferrite nanoparticle was carried out at the same conditions for conventional coprecipitation method but in presence of 0.011 M surfactant solutions in water. In the case of PVP, 1 g was added to the boiling 0.48 M hydroxide solution (1 g of PVP corresponds to 1.25 x 10^{-4} M). A reaction time as short as five minutes was considered in order to prevent any remarkable crystal growth. The corresponding XRD patterns are shown in Figure 105. The average crystallite sizes were in the range of 10 to 11 nm.

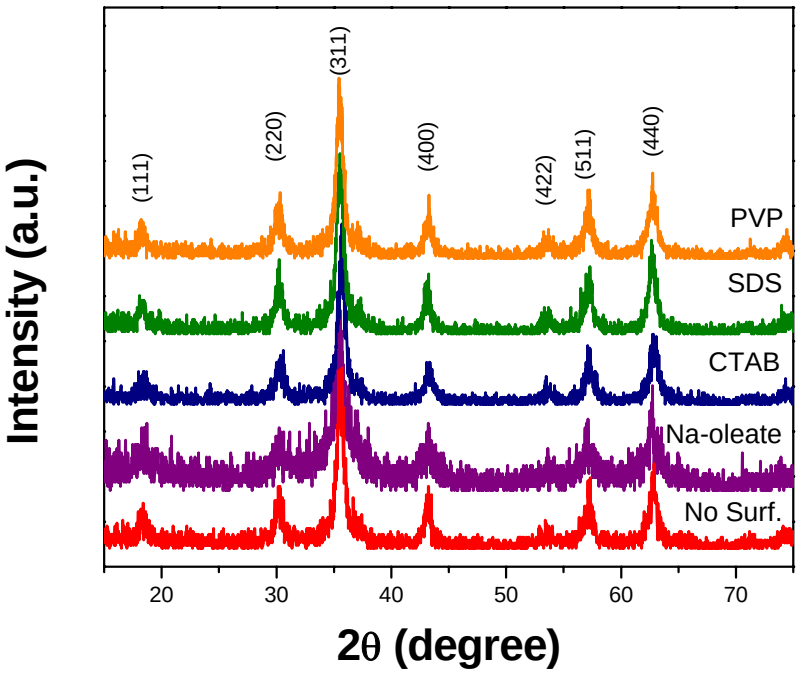

Figure 105: XRD patterns of cobalt ferrite synthesized using Na-oleate, CTAB, SDS, and PVP.

TABLE 46: Average crystallite size, 't', and lattice parameter, 'a', of cobalt ferrite nanocrystals produced using different types of surfactants.

Sample	t (± 1 nm)	a (± 0.01 Å)
No Surfactant	11	8.37
0.011 M Na-oleate	11	8.38
0.011 M CTAB	10	8.36
0.011 M SDS	11	8.38
*1 g PVP	11	8.38

B. M-H Measurements

M-H loops corresponding to cobalt ferrite synthesized in presence of different surfactants are shown in Figure 106. The evaluation criterion to assess the surfactant effectiveness was based on the magnetization that can be achieved; adsorbed surfactant should lower the interparticle exchange interaction and cause a drop in magnetization[68]. The lowest magnetization was exhibited by the sample synthesized in presence of Na-oleate. The maximum magnetization was reduced less than the half value of the uncoated ferrite ensuring that the bonding of the Na-oleate to the surface took place. Also, technical literature suggests the fast and effective coating of magnetite particles by oleate groups comes from the chemisorption of it onto the particle surface[95,96]. Accordingly, Na-oleate was selected for additional experiments.

TABLE 47: Magnetic properties of cobalt ferrite synthesized using different types of surfactants.

Sample	H_c (Oe)	M_{max} (emu/g)
No Surfactant	316	53
0.011 M Na-oleate	486	24
0.011 M CTAB	252	53
0.011 M SDS	315	55
*1 g PVP	342	52

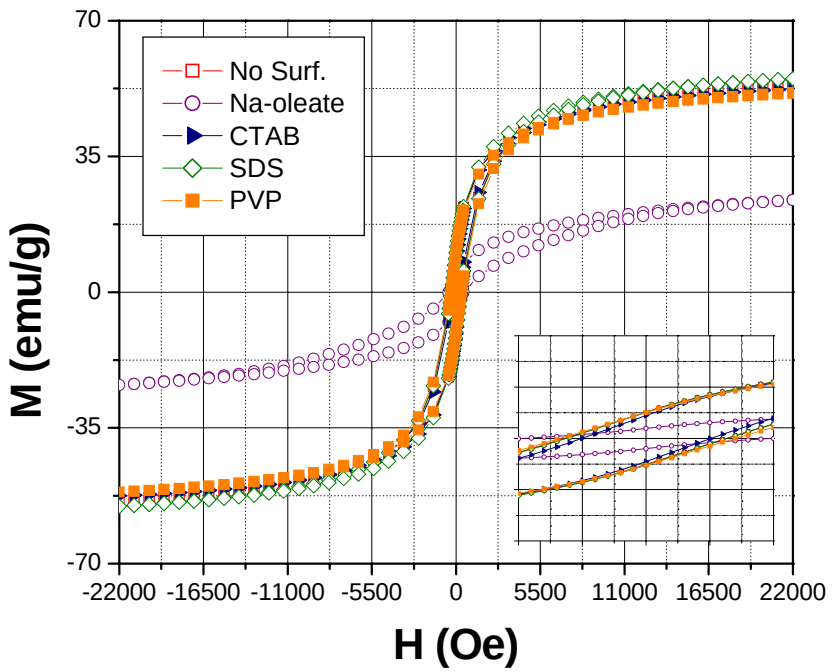

Figure 106: Room temperature M-H loops of cobalt ferrite synthesized using different types of surfactants.

5.8.2 Synthesis of superparamagnetic particles by inhibition of crystal growth using Na-oleate

As discussed above, a reaction time as short as five minutes was conducive to the formation of ferrite nanocrystals in the 10 nm - 11 nm range, which suggested a very fast formation and growth of earlier ferrite nuclei. Therefore, as an attempt to avoid crystal growth, the cobalt ferrite powder was removed right after the metal solution contacted the boiling NaOH + Na-oleate solution. Recovered product was rapidly washed with deionized water and ethanol and submitted to characterization by XRD and VSM.

A. XRD Analyses

Figure 107 shows the XRD patterns of cobalt ferrite nanocrystals synthesized with and without Na-oleate and recovered right after the metal solution was fully added into the boiling alkaline solution. As seen, very broad diffraction peaks were observed in the sample synthesized in presence of Na-oleate. The corresponding average crystallite size was estimated at 4 nm; this was the smallest crystallite size we achieved so far. The average crystallite size was 9 nm when the synthesis took place with no addition of the surfactant. This result suggests that the ferrite formation was interrupted in the nucleation stage, with practically no time for the nuclei to grow any further.

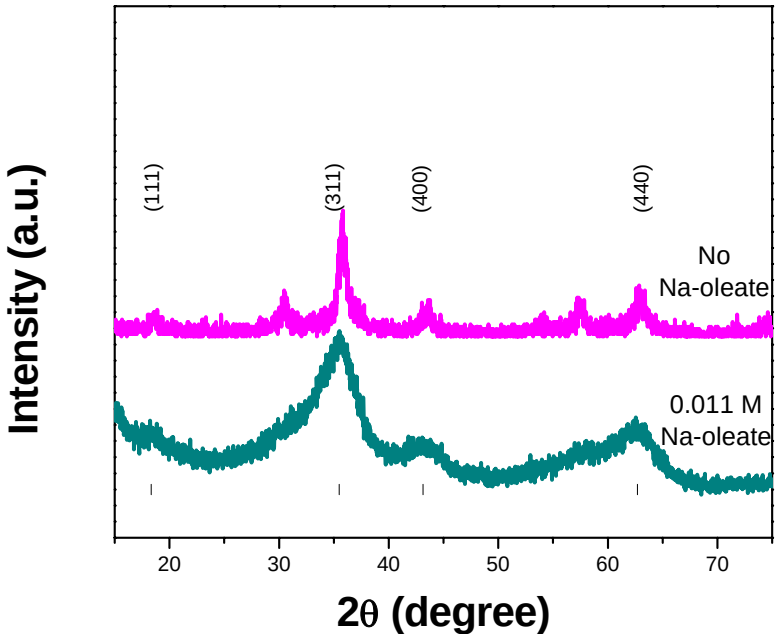

Figure 107: XRD patterns of cobalt ferrite produced with and without 0.011M Na-oleate. The ferrite powders were removed right after the metal solution was fully added into the boiling hydroxide solution.

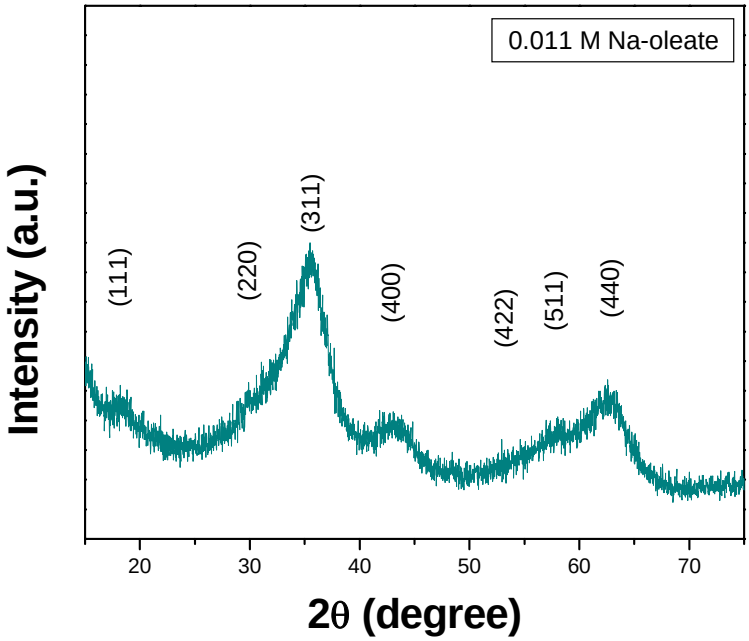

Figure 108: XRD pattern corresponding to the 4 nm cobalt ferrite nanocrystals.

The extremely small crystal size was also confirmed by TEM analyses. TEM images from Figure 109 confirmed the formation of nanocrystals with a diameter around 4 nm.

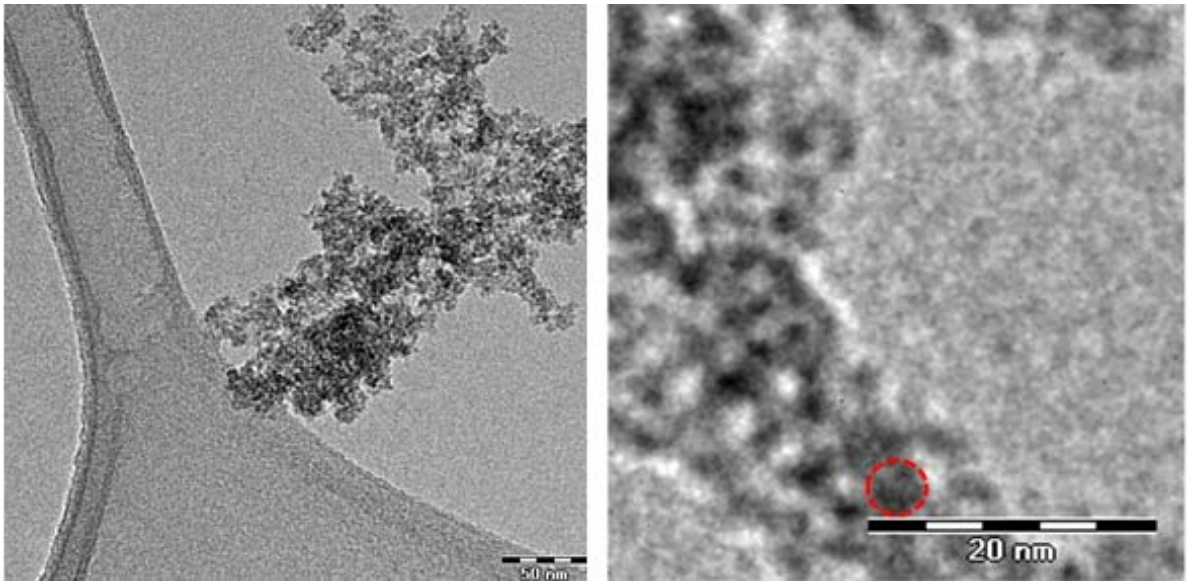

Figure 109: TEM images of cobalt ferrite nanocrystals synthesized in presence of 0.011 M Na-oleate.

B. Fourier Transform Infrared (FT-IR) Spectroscopy Measurements

Infrared spectra were collected using a Bruker IFS 66v/S FT-IR spectrometer. Figure 110 show the normalized Infrared spectra of bare and Na-oleate coated cobalt ferrite nanocrystals synthesized at 0 and 5 minutes of reaction time. The band corresponding to the Metal – Oxygen vibration is located at 575 cm^{-1} and is present in both samples. The broad band located around 3300 cm^{-1} is attributed to the O – H stretching. The presence of Na-oleate on the sample surface was confirmed by the presence of two bands in the 1610-1550 cm^{-1} and

1400-1300 cm^{-1} regions. These bands were assigned the carboxilate anion (COO^-) stretching. The C – H stretching band was also detected in the 2962-2853 cm^{-1} range. It is important to notice that the bands are more intense when the reaction time is prolonged due to better ferrite formation.

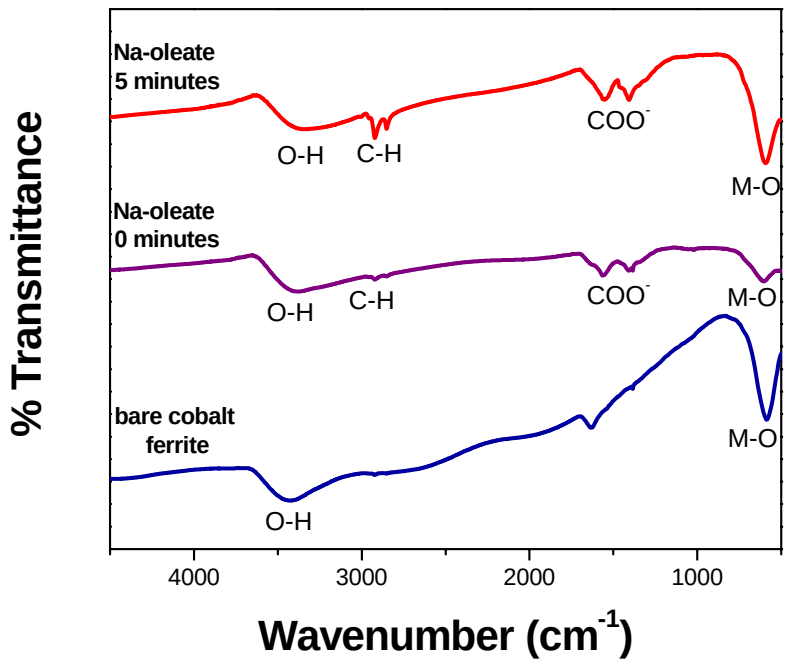

Figure 110: Infrared spectra of bare and Na-oleate coated cobalt ferrite.

C. M-H Measurements

The M-H loops of Figure 111 and the data showed in TABLE 48, indicated that the 9 nm nanoparticles exhibited a coercivity of 189 Oe whereas the 4 nm ones reported a coercivity as low as 3 Oe. The later value falls within the experimental error of the instrument; i.e. these particles practically did not show any coercivity.

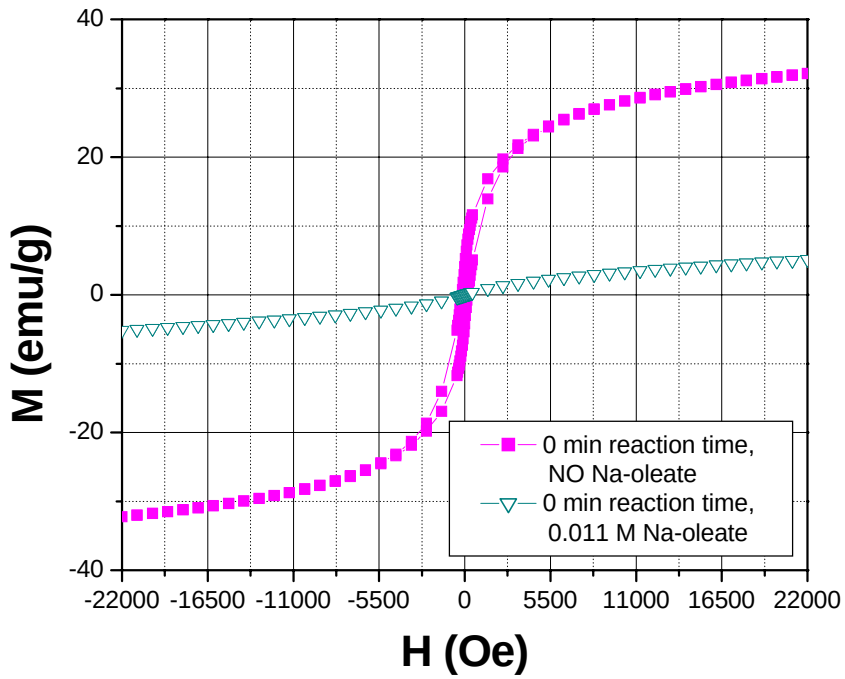

Figure 111: M-H loops of cobalt ferrite synthesized with and without Na-oleate.

TABLE 48: Magnetic properties of cobalt ferrite nanocrystals produced with and without Na-oleate.

Sample	H_c (Oe)	M_{max} (emu/g)
0 min reaction time, 0.48 M NaOH	189	32
0.011 M Na-oleate, 0 min reaction time, 0.48 M NaOH	3	5

Superparamagnetic particles behave as ferrimagnetic below its blocking temperature so increased coercivity is expected. In order to confirm the superparamagnetic nature of the 4 nm nanocrystals, it was analyzed using a SQUID magnetometer at 2 K (see Figure 112). It exhibited a coercivity value around 17.4 kOe.

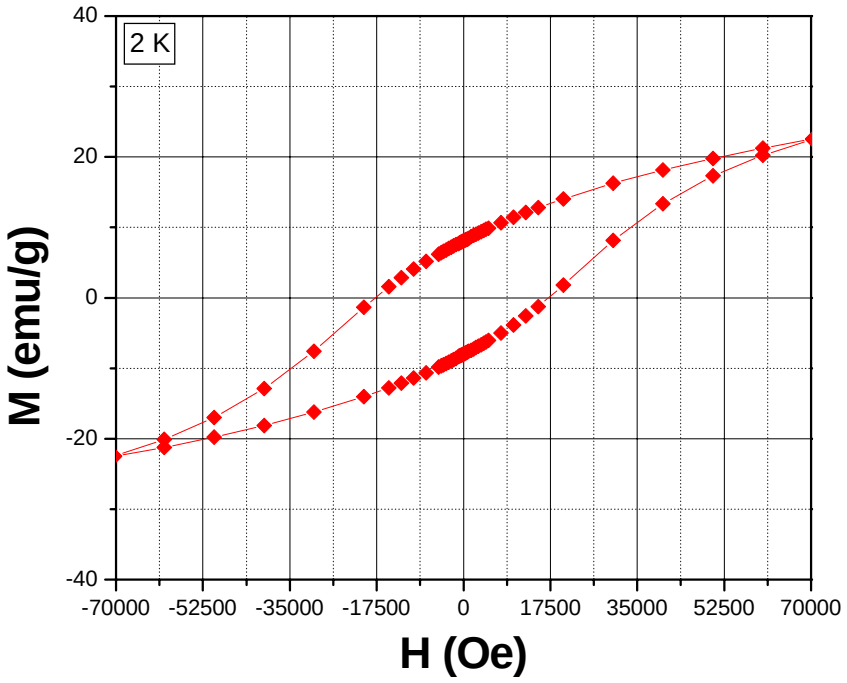

Figure 112: M-H loops at 2 K of 4 nm cobalt ferrite powders.

C. Mössbauer Spectroscopy Measurements

The presence of the quadrupole splitting in the Mössbauer spectrum of the 4 nm cobalt ferrite nanocrystals (Figure 113) may suggest the superparamagnetic nature of the synthesized crystals. Electric quadrupole interaction occurs if at least one of the nuclear states involved possesses a quadrupole moment eQ (which is the case for nuclear states with spin I > 1/2) and if the electric field at the nucleus is inhomogeneous. In the case of ^{57}Fe the first excited state (14.4 keV state) has a spin I = 3/2 and therefore also an electric quadrupole moment. It can be visualized by the precession of the quadrupole moment vector about the field gradient axis sets in and splits the degenerate I = 3/2 level into two substates with magnetic spin quantum numbers $m_I = \pm 3/2$ and $\pm 1/2$. The energy difference between the two substates

ΔE_Q is observed in the spectrum as the separation between the two resonance lines[97]. On this basis, the superparamagnetic nature of the 4 nm nanocrystals can be proposed.

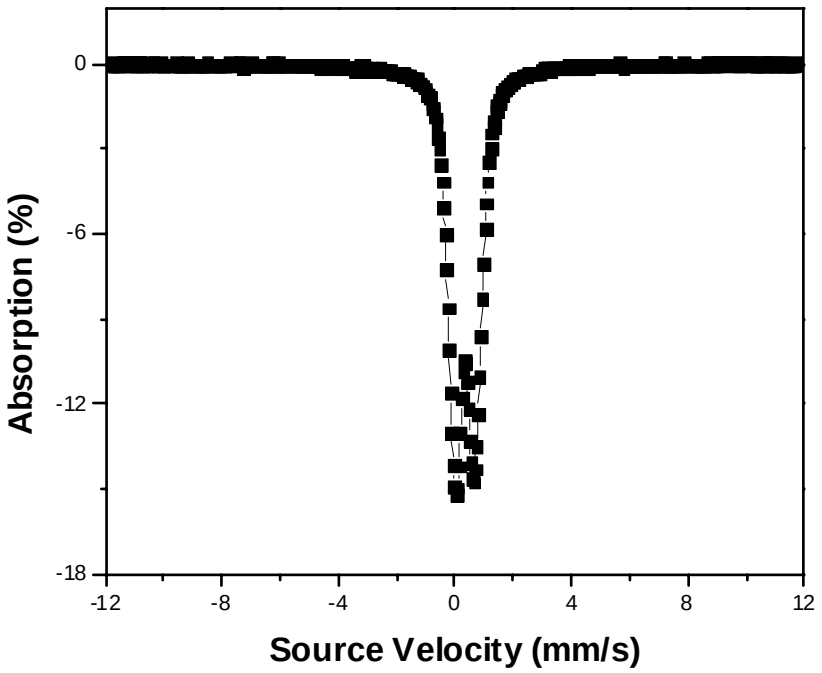

Figure 113: Mössbauer spectrum of cobalt ferrite synthesized using Na-oleate.

Concluding Remarks

A variety of surfactants was evaluated in order to inhibit crystal growth by means of steric repulsion. Due to the fast formation and growth of earlier ferrite nuclei, the surfactant may interact with the nanocrystal surface very fast. This interaction was effective for the Na-oleate surfactant. Further experiments led to the formation of 4 nm superparamagnetic cobalt ferrite. The superparamagnetic nature of this ferrite was confirmed by VSM, SQUID, and Mössbauer Spectroscopy measurements.

5.9 ZFC/FC and M-T measurements as a function of ferrite crystal size

In order to study the magnetic properties as function of crystal size in a deeper way, cobalt ferrite nanocrystals with different crystal sizes where selected from previous sections. The superparamagnetic sample was submitted to Zero-Field-Cooled / Field-Cooled (ZFC/FC) measurements to determine blocking temperature. This sample was analyzed in a Quantum Design MPMSXL Superconducting Quantum Interference Device. The powders were fixed in a solid matrix of poly(styrene-divinylbencene) as described by Calero and Rinaldi[34]. In turn, the ferrimagnetic samples were submitted to M-T measurements in a VSM to determine the corresponding demagnetization temperature. Finally, the M-H loops of the different samples were also measured in the SQUID unit at 2K and 300K.

A. XRD Analyses

As expected, the sharpening and intensity of the XRD peaks (Figure 114) were enhanced for larger average crystallite sizes.

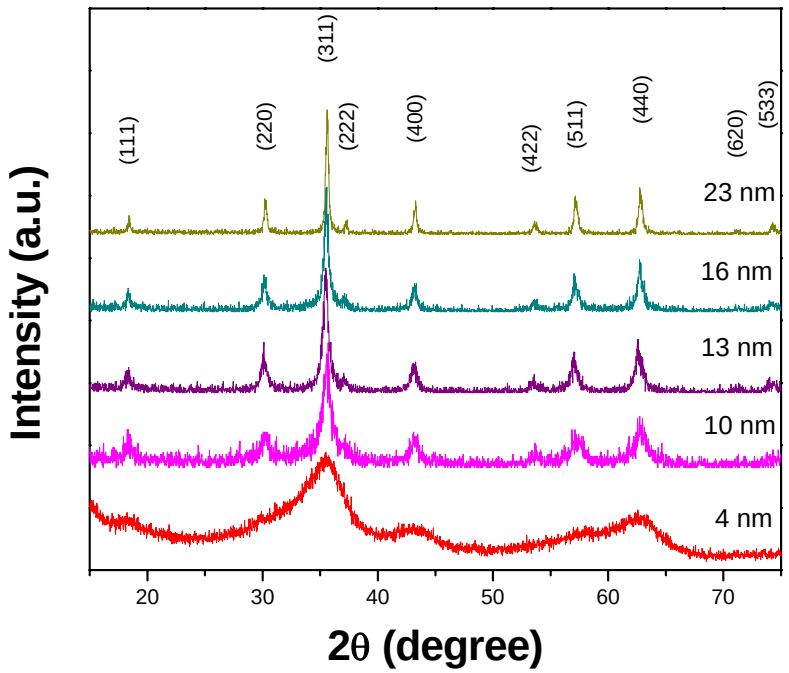

Figure 114: XRD patterns of cobalt ferrite with different average crystallite sizes.

B. Magnetic Measurements

B.1. ZFC/FC Measurements for the 4 nm cobalt ferrite nanocrystals

The ZFC/FC magnetization curves were performed using a Quantum Design SQUID unit, under an external magnetic field of 100 Oe and in the temperature range from 300 K to 2 K. ZFC/FC profile (Figure 115) indicated that these 4 nm particles are blocked at temperatures below 115 K. It means that superparamagnetic particles at room temperature behave as ferromagnets at temperature below the blocking temperature[58]; in this case, 115 K.

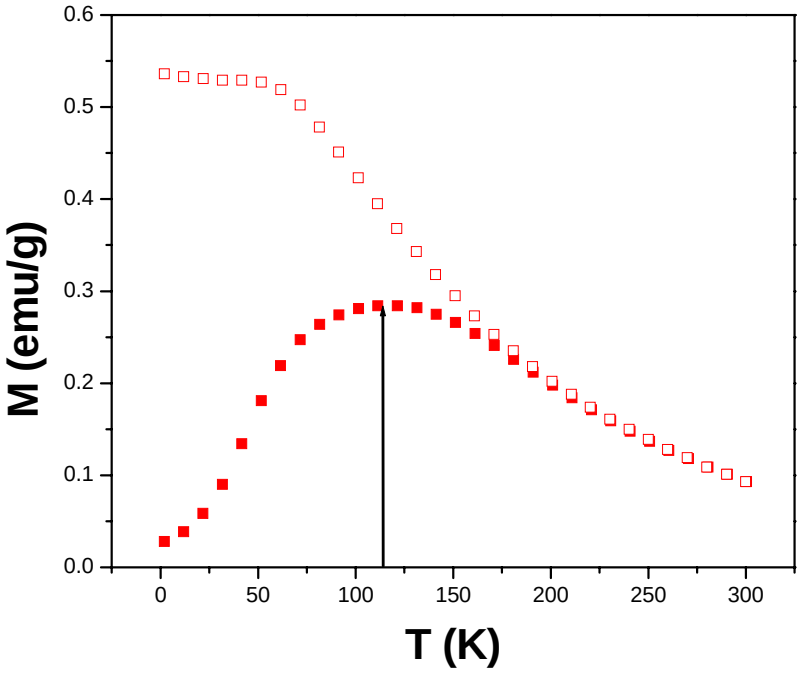

Figure 115: Zero-field-cooled (closed symbols) and field-cooled (open symbols) (ZFC/FC) magnetization curves of 4nm-cobalt ferrite crystals.

B.2. M-H Measurements at 2 K and 300 K

As the M-H loop of Figure 116 and the data given in TABLE 49 evidenced, the coercivity a 2K of the 23 nm samples reached a value as high as 30 kOe. To our knowledge, this is the highest coercivity value reported for cobalt ferrite nanocrystals at 2 K. Sun[98] and Meron[59] reported 20 kOe and 15 kOe, respectively for highly monodisperse cobalt ferrite, measured at 10 K. The maximum magnetization also increases at low temperatures due to the absence of thermal energy responsible of spin rotation and randomization.

As expected, the coercivity decreases with the rise in temperature (Figure 117); since thermal energy is been supplied to the system, less energy is needed to reverse the particle's

magnetization. This trend can be easily observed in the Figure 118, where the M-H loops at 2 K and 300 K of the 23 nm sample measurements are shown.

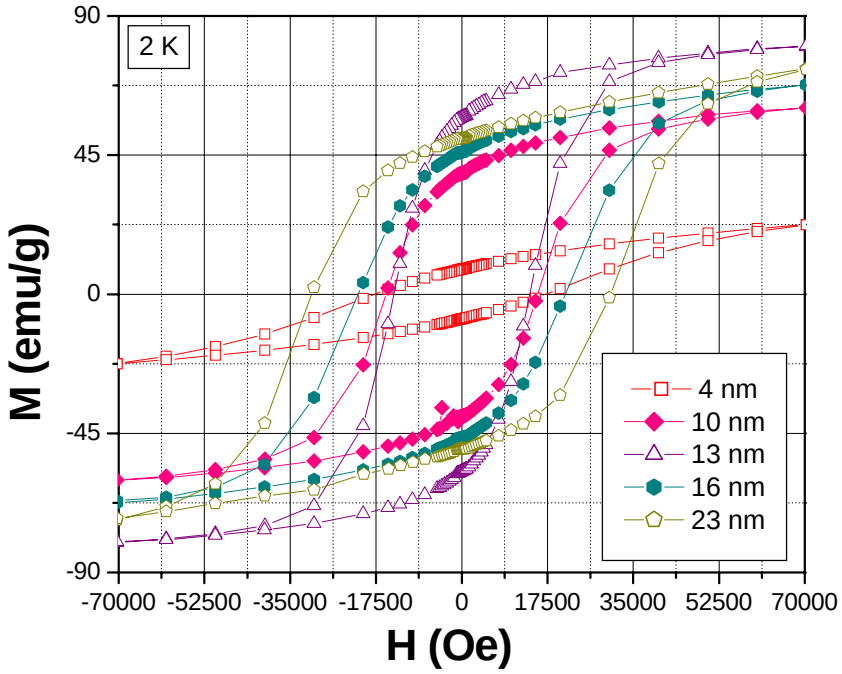

Figure 116: M-H loops at 2 K of cobalt ferrite powders with different average crystallite sizes.

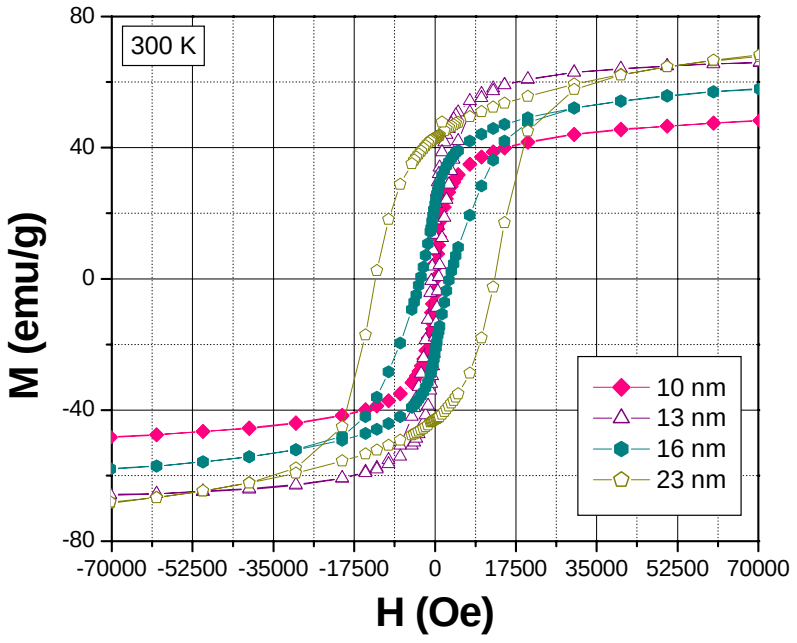

Figure 117: M-H loops at 300 K of cobalt ferrite powders with different average crystallite size.

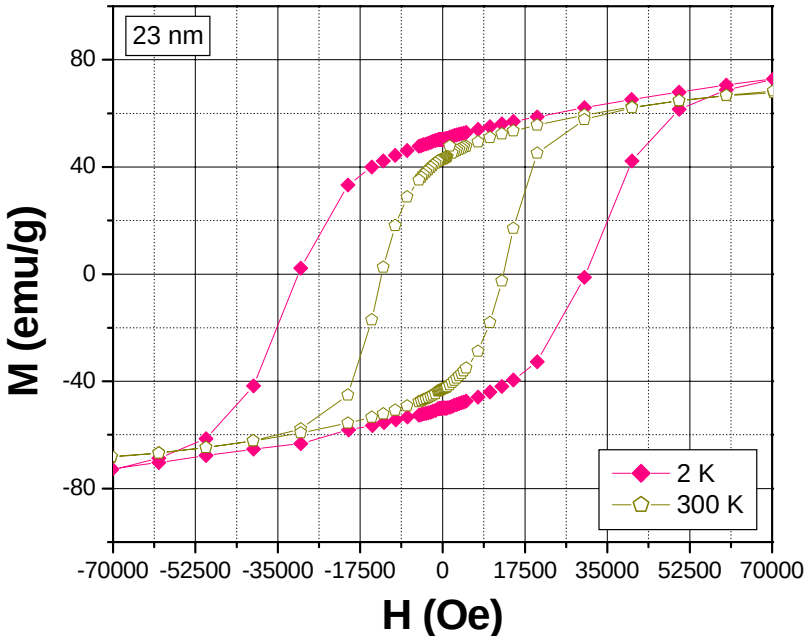

Figure 118: M-H loops of 23 nm cobalt ferrite nanocrystals analyzed in a Quantum Design SQUID unit at 2 K and 300 K. The external magnetic field was 7 T.

TABLE 49: Magnetic properties of cobalt ferrite with different crystal sizes measured at 2 K and 300 K.

Measurement Temperature (K)	Average crystallite size, 't' (nm)	H_c (Oe)	M_{max} (emu/g)
2	4	17406	22
	10	15989	60
	13	13831	80
	16	21153	68
	23	30255	73
300	10	199	48
	13	776	66
	16	3114	58
	23	12903	68

B.3. M-T Measurements

The room-temperature ferrimagnetic nanocrystals were submitted to M-T measurements in order to determine the demagnetization temperature for an external magnetic field of 5000 Oe. All the demagnetization temperatures lie between 779 and 819 K for coercivity values between 199 Oe and 12903 Oe (Figure118). These temperatures are tabulated in TABLE 50. As seen, the shift in demagnetization temperature is not so significant when comparing with mixed ferrites, e.g., Mn-Zn ferrite[99].

The M-T curve for the 10 nm-crystal size sample shows the usual profile where the magnetization decreases with increasing temperature. On the contrary, those samples with crystal sizes over 10 nm show an increase in magnetization with temperature. This unusual shape occurs when the molecular field on *b*-site ions is less than on *a*-site ions, as a result M_b

decreases more rapidly with temperature than M_a and, therefore, the net magnetization $M = M_a + M_b = |M_a| - |M_b|$ increases[100]. This trend is more noticeable as the crystal size increases.

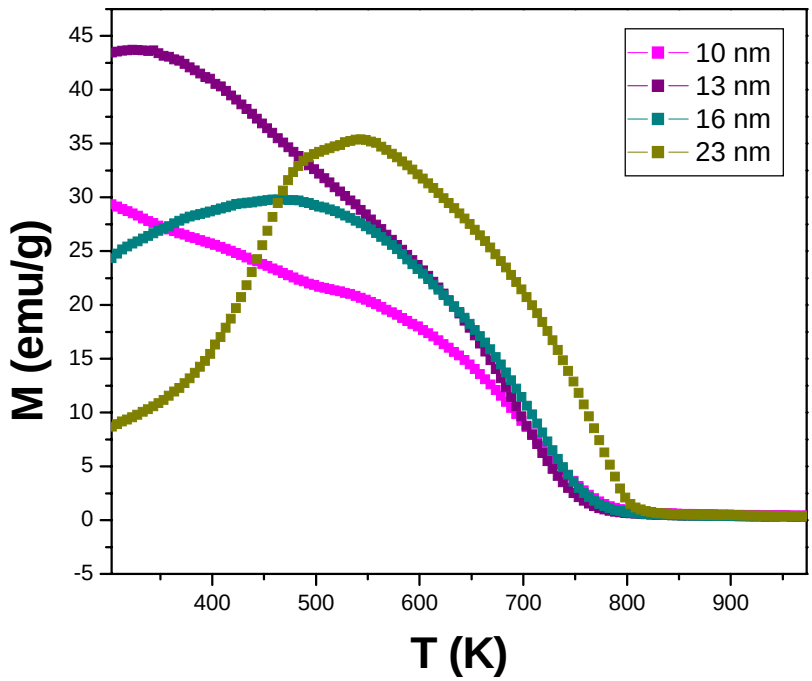

Figure 119: M-T measurements for cobalt ferrite with different sizes. The external magnetic field was 5000 Oe.

TABLE 50: Demagnetization temperature, T_d, of cobalt ferrite with different crystal sizes. The external magnetic field was 5000 Oe.

Average crystallite size, 't' (nm)	T_d (K)
10	803
13	779
16	790
23	819

Ferrite powders were re-analyzed by X-Ray Diffraction after finishing with the M-T measurements. The corresponding X-Ray Diffraction patterns of Figure 120 evidenced the pretty sharp peaks suggesting a remarkable crystal growth at the end of the M-T measurements. The observed crystal growth should have taken place through intergranular diffusion process promoted at high temperatures. It was also interesting to detect a secondary crystalline phase corresponding to CoO co-existing with the main ferrite peaks. The formation of this Co(II) oxide is consequence of the disproportionation[101] of cobalt ferrite upon annealing during the M-T measurements. This phase was not present in those samples submitted to thermal treatment, discussed in section 5.7, where the annealing in air lasted only 1 hour, a very short period compared to the 24 hours-duration of the M-T measurements. Evidently, the enlargement in crystal size during the M-T measurements should also be taken into account to explain the observed variation in the demagnetization temperature in our samples.

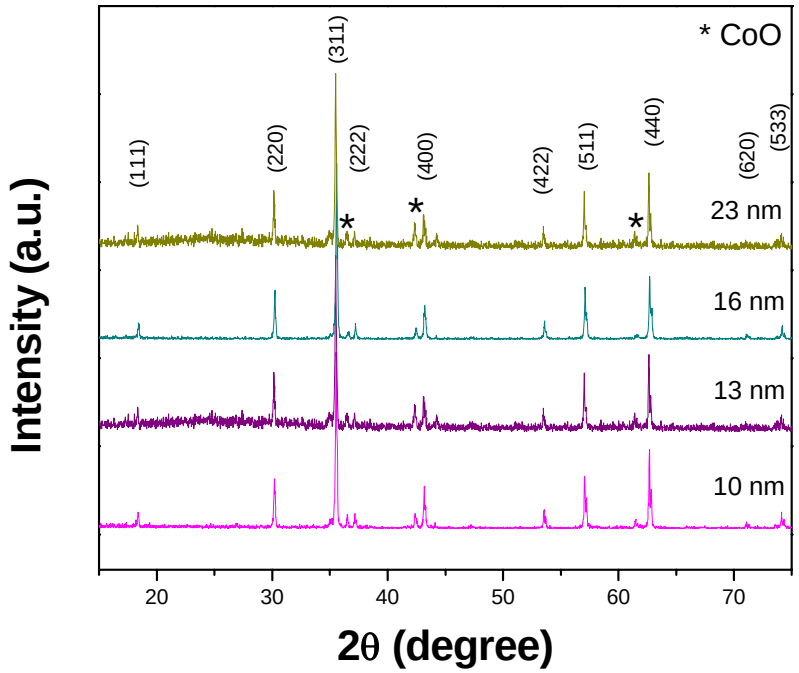

Figure 120: XRD patterns of cobalt ferrite samples after M-T measurements.

Concluding Remarks

The magnetic properties of cobalt ferrite were studied as function of crystal size. The blocking temperature of the superparamagnetic sample was determined to be 115 K. M-H measurements at two different temperatures showed coercivity values in the range of 0 to 30 kOe. For our knowledge, this is the first time that a 2 K-coercivity value of 30 kOe in 23 nm-cobalt ferrite samples has been reported. The demagnetization temperature was determined for those samples that are ferrimagnetic at temperatures over 400 K. The demagnetization temperature ranges between 779 and 819 K. Although only moderate, this rise in the demagnetization temperature in the samples with higher coercivities was expected due to the corresponding high remanence values.

5.10 Revisited dependence of coercivity with particle size

It has been proved and revised the strong dependence of coercivity with particle size. Different approaches as experimental design, transition metal doping, size-sensitive phase separation method, and surfactants discussed above were the essential tools to obtain particles with a wide range of sizes. They helped us to achieve the main objective of this research: to determine the limits of the single domain and multi-domain regions as a function of the composition, structure, and crystal size in ferrimagnetic ferrites. It is important to notice that the theoretical coercivity values have been greatly surpassed. An experimental plot of coercivity versus particle size summarizes some of the values obtained and it is shown in Figure 121.

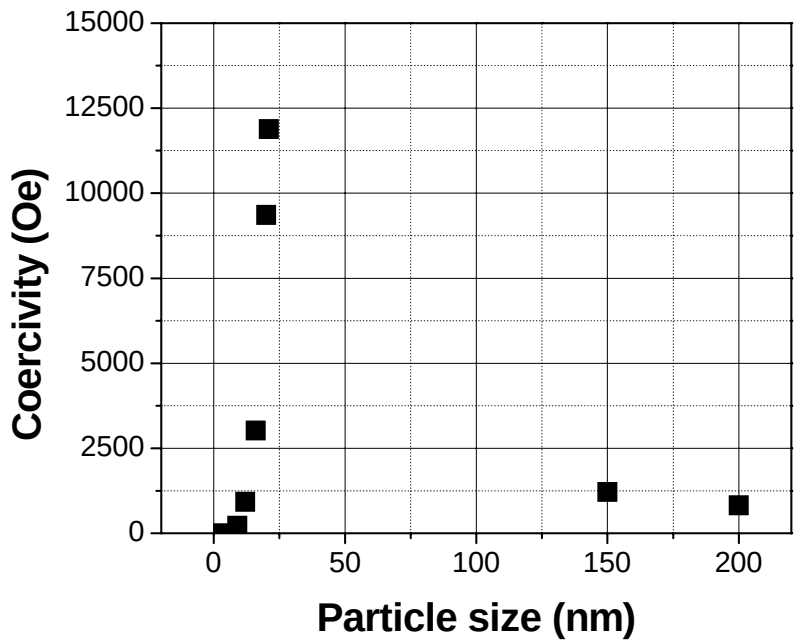

Figure 121: Variation of coercivity with particle size in cobalt ferrite particles synthesized in the present study.

GENERAL CONCLUSIONS

Tuning on magnetic properties of cobalt ferrite at the nanoscale was achieved by controlling crystal size, chemical composition, and cations distribution. Average crystallite sizes ranging between 4 and 23 nm were successfully synthesized. The corresponding room-temperature coercivity values varied between 3 Oe and 11.9 kOe. The 23 nm-nanocrystals exhibited coercivity as high as 11.9 kOe, which is reported here for the first time. The corresponding magnetization and squareness ratio were 48 emu/g and 0.72, respectively.

The suitable combination of flow-rate controlled synthesis complemented by acid-washing and magnetically-assisted size-sensitive separation processes provided favorable conditions for the enhancement of nanoparticles monodispersity and tailoring of the corresponding magnetic properties. Smaller and more soluble nanocrystals that contribute negatively to coercivity (superparamagnetic particles) were selectively dissolved during the acid washing step. This selective dissolution of the superparamagnetic fraction took place in addition to the removal of the poorly crystalline layer on the surface of the nanocrystals.

The effect of the nominal Fe:Co mole ratio in starting solutions on the structural and magnetic properties of the nanocrystals was also investigated. Our findings revealed the cationic distribution in the ferrite was dependent on the nominal Fe:Co mole ratio whereas the contribution of the surface cations, and hence the surface anisotropy, became remarkable under flow-rate controlled synthesis conditions. Accordingly, the colossal coercivity attained in nanometric cobalt ferrite crystals became possible not exclusively by control of crystal

size, but also through promotion of the mentioned effects: surface anisotropy and atomic rearrangements of Fe species within the ferrite lattice. Complementary work evidenced that the substitution of Co^{2+} by transition metal cations (Mn^{2+} and Ni^{2+}), with and without control of flow-rate, also allowed the modification of the magnetic properties in the products.

High-energy ball milling was used as an attempt to reduce the nanoparticle size and evaluate the effect of milling on the structural and magnetic properties of cobalt ferrite nanocrystals. Size reduction below 10 nm was not possible by this means. However, it was found that high-energy ball milling of the 12 nm-cobalt ferrite sample induced strain and cell distortion in the nanocrystals, which explained the observed increment in coercivity.

Different types of surfactants were evaluated in-synthesis to inhibit crystal growth and aggregation. 4 nm-cobalt ferrite crystals were produced by using Na-oleate. The superparamagnetic behavior of these nanocrystals was confirmed by M-H measurements and Mössbauer Spectroscopy techniques.

The transition to the magnetic multi-domain region in cobalt ferrite was achieved by intergranular diffusion-promoted crystal growth by thermal treatment in air at high temperatures. Single crystals larger than 100 nm were obtained by this route. As expected for multi-domain particles, the coercivity values decreased in larger crystals whereas the magnetization was enhanced up to 79 emu/g, which is very close to the magnetization in bulk cobalt ferrite, (80 emu/g).

The temperature dependence of the magnetic properties of cobalt ferrite was studied as function of crystal size. The blocking temperature of the 4 nm-superparamagnetic sample

was determined to be 115 K. The 23 nm sample (room-temperature coercivity of 11.9 kOe) reported a 2 K-coercivity as high as 30 kOe coercivity. The demagnetization temperature was determined for those samples that are ferrimagnetic at temperatures over 400 K. The demagnetization temperature ranges between 779 and 819 K. Although only moderate, this rise in the demagnetization temperature in the samples with higher coercivities was expected due to the corresponding high remanence values.

6 REFERENCES

(1) Sun, C.; Lee, J. S.; Zhang, M. Magnetic nanoparticles in MR imaging and drug delivery. *Adv. Drug Delivery Rev.* **2008**, *60*, 1252-1265.

(2) Arulmurugan, R.; Vaidyanathan, G.; Sendhilnathan, S.; Jeyadevan, B. Mn-Zn ferrite nanoparticles for ferrofluid preparation: Study on thermal-magnetic properties. *J. Magn. Magn. Mater.* **2006**, *298*, 83-94.

(3) Terzzoli, M. C.; Duhalde, S.; Jacobo, S.; Steren, L.; Moina, C. High perpendicular coercive field of $CoFe_2O_4$ thin films deposited by PLD. *J. Alloys Compd.* **2004**, *369*, 209-212.

(4) Song, Q.; Zhang, Z. J. Shape Control and Associated Magnetic Properties of Spinel Cobalt Ferrite Nanocrystals. *J. Am. Chem. Soc.* **2004**, *126*, 6164-6168.

(5) Hyeon, T.; Chung, Y.; Park, J.; Lee, S. S.; Kim, Y.; Park, B. H. Synthesis of Highly Crystalline and Monodisperse Cobalt Ferrite Nanocrystals. *J. Phys. Chem. B* **2002**, *106*, 6831-6833.

(6) Khedr, M.; Omar, A.; Abdel-Moaty, S. Magnetic nanocomposites: Preparation and characterization of Co-ferrite nanoparticles. *Colloids Surf., A* **2006**, *281*, 8-14.

(7) Li, S.; John, V. T.; O'Connor, C.; Harris, V.; Carpenter, E. Cobalt-ferrite nanoparticles: Structure, cation distributions, and magnetic properties. *J. Appl. Phys.* **2000**, *87*, 6223-6225.

(8) Berkowitz, A. E.; Schuele, W. J. Magnetic Properties of Some Ferrite Micropowders. *J. Appl. Phys.* **1959**, *30*, S134.

(9) Neel, L. *C.R. Acad. Sci. Paris* **1947**, *224*, 1488.

(10) Callister, Jr., W. *Materials Science and Engineering an Introduction*; 6º ed.; John Wiley & Sons, Inc.: New Jersey, 2003.

(11) Goldman, A. *Modern Ferrite Technology*; Van Nostrand Reinhold: New York, 1990.

(12) Landau, L.; Lifschitz, E. M. *Physik Z. Sowjetunion* **1935**, *8*, 153-169.

(13) Sugimoto, T. *Monodispersed Particles*; 1º ed.; Elsevier Science, 2001.

(14) Lee, E. W.; Bishop, J. E. L. Magnetic behaviour of single-domain particles. *Proc. Phys. Soc.* **1966**, *89*, 661-675.

(15) Kröll, M.; Blau, W. J.; Grandjean, D.; Benfield, R. E.; Luis, F.; Paulus, P. M.; de Jongh, L. J. Magnetic properties of ferromagnetic nanowires embedded in nanoporous alumina membranes. *J. Magn. Magn. Mater.* **2002**, *249*, 241-245.

(16) Zoriasatain, S.; Azarkharman, F.; Sebt, S.; Akhavan, M. Magnetic anisotropies in FeCo fine particles. *J. Magn. Magn. Mater.* **2006**, *300*, 525-531.

(17) Grössinger, R. A critical examination of the law of approach to saturation. I. Fit procedure. *Phys. Stat. Sol. (A)* **1981**, *66*, 665-674.

(18) LaMer, V. K.; Dinegar, R. H. Theory, Production and Mechanism of Formation of Monodispersed Hydrosols. *J. Am. Chem. Soc.* **1950**, *72*, 4847-4854.

(19) Sugimoto, T. *Fine Particles: Synthesis, Characterization, and Mechanisms of Growth*; 1º ed.; CRC Press, 2000.

(20) Luborsky, F. E. Development of Elongated Particle Magnets. *J. Appl. Phys.* **1961**, *32*, S171.

(21) O'Handley, R. C. *Modern Magnetic Materials: Principles and Applications*; Wiley-Interscience, 1999.
(22) Bedanta, S.; Kleemann, W. Supermagnetism. *J. Phys. D: Appl. Phys.* **2009**, *42*, 013001.
(23) Stoner, E. C.; Wohlfarth, E. P. A Mechanism of Magnetic Hysteresis in Heterogeneous Alloys. *Trans. R. Soc. Lond. A* **1948**, *240*, 599 -642.
(24) Prado, C.; Garrido, J.; Periago, J. F. Urinary benzene determination by SPME/GC-MS: A study of variables by fractional factorial design and response surface methodology. *J. Chromatogr. B* **2004**, *804*, 255-261.
(25) Yang, W.; Hsieh, C. Fractional factorial design applied to optimize experimental conditions for preparation of ultrafine lanthanum-doped strontium titanate powders. *J. Mater. Res.* **1999**, *14*, 3410-3416.
(26) Chung, C. A. *Simulation Modeling Handbook: A Practical Approach*; 1º ed.; CRC Press, 2003.
(27) Hicks, C. R.; Jr, K. V. T. *Fundamental Concepts in the Design of Experiments*; 5º ed.; Oxford University Press, USA, 1999.
(28) Fujii, E.; Torii, H.; Tomozawa, A.; Takayama, R.; Hirao, T. Iron oxide films with spinel, corundum and bixbite structure prepared by plasma-enhanced metalorganic chemical vapor deposition. *J. Cryst. Growth* **1995**, *151*, 134-139.
(29) Moumen, N.; Bonville, P.; Pileni, M. P. Control of the Size of Cobalt Ferrite Magnetic Fluids: Mössbauer Spectroscopy. *J. Phys. Chem.* **1996**, *100*, 14410-14416.
(30) Tirosh, E.; Shemer, G.; Markovich, G. Optimizing Cobalt Ferrite Nanocrystal Synthesis Using a Magneto-optical Probe. *Chem. Mater.* **2006**, *18*, 465-470.
(31) Lee, J.; Park, J. Y.; Kim, C. S. Growth of ultra-fine cobalt ferrite particles by a sol–gel method and their magnetic properties. *J. Mater. Sci.* **1998**, *33*, 3965-3968.
(32) Liu, B. H.; Ding, J. Strain-induced high coercivity in $CoFe_2O_4$ powders. *Appl. Phys. Lett.* **2006**, *88*, 042506.
(33) Gonzalez-Sandoval, M. P.; Beesley, A. M.; Miki-Yoshida, M.; Fuentes-Cobas, L.; Matutes-Aquino, J. A. Comparative study of the microstructural and magnetic properties of spinel ferrites obtained by co-precipitation. *J. Alloys Compd.* **2004**, *369*, 190-194.
(34) del Castillo, V.; Rinaldi, C. Effect of Sample Concentration on the Determination of the Anisotropy Constant of Magnetic Nanoparticles. *IEEE Trans. Magn.* **2010**, *46*, 852-859.
(35) Calero-DdelC, V. L.; Rinaldi, C. Synthesis and magnetic characterization of cobalt-substituted ferrite ($Co_xFe_{3-x}O_4$) nanoparticles. *J. Magn. Magn. Mater.* **2007**, *314*, 60-67.
(36) Eastoe, J.; Hollamby, M. J.; Hudson, L. Recent advances in nanoparticle synthesis with reversed micelles. *Adv. Colloid Interface Sci.* **2006**, *128-130*, 5-15.
(37) Mathew, D. S.; Juang, R. An overview of the structure and magnetism of spinel ferrite nanoparticles and their synthesis in microemulsions. *Chem. Eng. J.* **2007**, *129*, 51-65.
(38) Gul, I.; Maqsood, A. Structural, magnetic and electrical properties of cobalt ferrites prepared by the sol-gel route. *J. Alloys Compd.* **2008**, *465*, 227-231.
(39) Sajjia, M.; Oubaha, M.; Prescott, T.; Olabi, A. Development of cobalt ferrite powder preparation employing the sol-gel technique and its structural characterization. *J. Alloys Compd.* **2010**, *506*, 400-406.

(40) Gopalan, E. V.; Joy, P.; Al-Omari, I.; Kumar, D. S.; Yoshida, Y.; Anantharaman, M. On the structural, magnetic and electrical properties of sol-gel derived nanosized cobalt ferrite. *J. Alloys Compd.* **2009**, *485*, 711-717.
(41) Byrappa, K.; Adschiri, T. Hydrothermal technology for nanotechnology. *Prog. Cryst. Growth Charact. Mater.* **2007**, *53*, 117-166.
(42) Ding, J.; Miao, W. F.; McCormick, P. G.; Street, R. High-coercivity ferrite magnets prepared by mechanical alloying. *J. Alloys Compd.* **1998**, *281*, 32-36.
(43) Zi, Z.; Sun, Y.; Zhu, X.; Yang, Z.; Dai, J.; Song, W. Synthesis and magnetic properties of $CoFe_2O_4$ ferrite nanoparticles. *J. Magn. Magn. Mater.* **2009**, *321*, 1251-1255.
(44) Chinnasamy, C. N.; Jeyadevan, B.; Shinoda, K.; Tohji, K.; Djayaprawira, D. J.; Takahashi, M.; Joseyphus, R. J.; Narayanasamy, A. Unusually high coercivity and critical single-domain size of nearly monodispersed $CoFe_2O_4$ nanoparticles. *Appl. Phys. Lett.* **2003**, *83*, 2862-2864.
(45) Qu, Y.; Yang, H.; Yang, N.; Fan, Y.; Zhu, H.; Zou, G. The effect of reaction temperature on the particle size, structure and magnetic properties of coprecipitated $CoFe_2O_4$ nanoparticles. *Mater. Lett.* **2006**, *60*, 3548-3552.
(46) Kim, Y. I.; Kim, D.; Lee, C. S. Synthesis and characterization of $CoFe_2O_4$ magnetic nanoparticles prepared by temperature-controlled coprecipitation method. *Phys. B* **2003**, *337*, 42-51.
(47) Iwasaki, S. Perpendicular Magnetic Recording - Evolution and Future -. *IEEE Trans. Magn.* **1984**, *20*, 657-662.
(48) Hsu, Y.; Nikitin, V.; Hsiao, D.; Chen, J.; Zheng, Y.; Pentek, A.; Loo, J.; Jiang, M.; Yuan, S.; Alex, M.; Luo, Y.; Salo, M.; Okada, T.; Maruyama, Y.; Mitsuoka, K. Challenges for perpendicular write heads at high recording density. *IEEE Trans. Magn.* **2007**, *43*, 605-608.
(49) Gao, K. Z.; Heinonen, O.; Chen, Y. Read and write processes, and head technology for perpendicular recording. *J. Magn. Magn. Mater.* **2009**, *321*, 495-507.
(50) Acharya, B. R.; Zhou, J. N.; Zheng, M.; Choe, G.; Abarra, E. N. Anti-parallel coupled soft under layers for high-density perpendicular recording. *IEEE Trans. Magn.* **2004**, *40*, 2383-2385.
(51) Morisako, A.; Matsumoto, M.; Naoe, M. Sputtered hexagonal Ba-ferrite films for high-density magnetic recording media. *J. Appl. Phys.* **1996**, *79*, 4881-4883.
(52) Hikosaka, T.; Komai, T.; Tanaka, Y. Oxygen effect on the microstructure and magnetic properties of binary CoPt thin films for perpendicular recording. *IEEE Trans. Magn.* **1994**, *30*, 4026-4028.
(53) Yin, J.; Ding, J.; Liu, B.; Miao, X.; Chen, J. High perpendicular coercivity co-ferrite films with (111) texture using pulsed laser deposition. *J. Magn. Magn. Mater.* **2007**, *310*, 2537-2539.
(54) Kim, K. J.; Lee, H. S.; Lee, M. H.; Lee, S. H. Comparative magneto-optical investigation of d–d charge–transfer transitions in Fe_3O_4, $CoFe_2O_4$, and $NiFe_2O_4$. *J. Appl. Phys.* **2002**, *91*, 9974-9977.
(55) Parr Instruments Company Operating Instruction Manual for 4570 HP/HT Pressure Reactors. *http://www.parrinst.com/doc_library/members/397M.pdf.*
(56) Foner, S. Versatile and Sensitive Vibrating-Sample Magnetometer. *Rev. Sci. Instrum.* **1959**,

30, 548.
(57) Chinnasamy, C.; B. Jeyadevan, B.; Perales-Perez, O.; Shinoda, K.; Tohji, K.; Kasuya, A. Growth dominant co-precipitation process to achieve high coercivity at room temperature in $CoFe_2O_4$ nanoparticles. *IEEE Trans. Magn.* **2002**, *38*, 2640-2642.
(58) Perales-Perez, O.; Sasaki, H.; Kasuya, A.; Jeyadevan, B.; Tohji, K.; Hihara, T.; Sumiyama, K. Production of monodispersed particles by using effective size selection. *J. Appl. Phys.* **2002**, *91*, 6958-6960.
(59) Meron, T.; Rosenberg, Y.; Lereah, Y.; Markovich, G. Synthesis and assembly of high-quality cobalt ferrite nanocrystals prepared by a modified sol-gel technique. *J. Magn. Magn. Mater.* **2005**, *292*, 11-16.
(60) Kim, D.; Nikles, D. E.; Johnson, D. T.; Brazel, C. S. Heat generation of aqueously dispersed $CoFe_2O_4$ nanoparticles as heating agents for magnetically activated drug delivery and hyperthermia. *J. Magn. Magn. Mater.* **2008**, *320*, 2390-2396.
(61) Wang, Y.; Ding, J.; Yi, J.; Liu, B.; Yu, T.; Shen, Z. High coercivity Co-ferrite thin films on SiO_2 (100) substrate. *J. Magn. Magn. Mater.* **2004**, *282*, 211-215.
(62) Yan, C.; Cheng, F.; Liao, C.; Kuang, J.; Zhigang Xu; Chen, L.; Zhao, H.; Liu, Z.; Wang, Y.; Tao Zhu; He, G. Sol-gel synthesis, magnetic and magneto-optical properties of $CoFe_{2-x}Tb_xO_4$ nanocrystalline films. *J. Magn. Magn. Mater.* **1999**, *192*, 396-402.
(63) Cedeño-Mattei, Y.; Perales-Perez, O.; Tomar, M. S.; Roman, F.; Voyles, P. M.; Stratton, W. G. Tuning of magnetic properties in cobalt ferrite nanocrystals. *J. Appl. Phys.* **2008**, *103*, 07E512.
(64) Chinnasamy, C.; Jeyadevan, B.; Perales-Perez, O.; Shinoda, K.; Tohji, K.; Kasuya, A. In *2003 Nanotechnology Conference and Trade Show - Nanotech 2003, Febrary 23, 2003 - Febrary 27, 2003*; 2003 Nanotechnology Conference and Trade Show - Nanotech 2003; Computational Publications: San Francisco, CA, United states, 2003; Vol. 3, págs. 134-136.
(65) Sileo, E. E.; García Rodenas, L.; Paiva-Santos, C. O.; Stephens, P. W.; Morando, P. J.; Blesa, M. A. Correlation of reactivity with structural factors in a series of Fe(II) substituted cobalt ferrites. *J. Solid State Chem.* **2006**, *179*, 2237-2244.
(66) Letellier, P.; Mayaffre, A.; Turmine, M. Solubility of nanoparticles: Nonextensive thermodynamics approach. *J. Phys.: Condens. Matter* **2007**, *19*, 436229.
(67) Figueroa, C. A.; Sileo, E. E.; Morando, P. J.; Blesa, M. A. Dissolution of Nickel Ferrite in Aqueous Solutions Containing Oxalic Acid and Ferrous Salts. *J. Colloid Interface Sci.* **2000**, *225*, 403-410.
(68) Limaye, M. V. High Coercivity of Oleic Acid Capped $CoFe_2O_4$ Nanoparticles at Room Temperature. *J. Phys. Chem. B* **2009**, *113*, 9070-9076.
(69) Sawatzky, G. A. Cation Distributions in Octahedral and Tetrahedral Sites of the Ferrimagnetic Spinel $CoFe_2O_4$. *J. Appl. Phys.* **1968**, *39*, 1204-1205.
(70) Manova, E.; Kunev, B.; Paneva, D.; Mitov, I.; Petrov, L.; Estournès, C.; D'Orléan, C.; Rehspringer, J.; Kurmoo, M. Mechano-Synthesis, Characterization, and Magnetic Properties of Nanoparticles of Cobalt Ferrite, $CoFe_2O_4$. *Chem. Mater.* **2004**, *16*, 5689-5696.
(71) Zhao, L.; Zhang, H.; Xing, Y.; Song, S.; Yu, S.; Shi, W.; Guo, X.; Yang, J.; Lei, Y.; Cao, F. Studies on the magnetism of cobalt ferrite nanocrystals synthesized by hydrothermal method.

J. Solid State Chem. **2008**, *181*, 245-252.
(72) Cedeño-Mattei, Y.; Perales-Pérez, O.; Uwakweh, O. N. C.; Xin, Y. Colossal room-temperature coercivity in size-selected cobalt ferrite nanocrystals. *J. Appl. Phys.* **2010**, *107*, 09A741.
(73) Olsson, R. T.; Salazar-Alvarez, G.; Hedenqvist, M. S.; Gedde, U. W.; Lindberg, F.; Savage, S. J. Controlled Synthesis of Near-Stoichiometric Cobalt Ferrite Nanoparticles. *Chem. Mater.* **2005**, *17*, 5109-5118.
(74) Globus, A.; Monjaras, R. Influence of the deviation from stoichiometry on the magnetic properties of Zn-rich NiZn ferrites. *IEEE Trans. Magn.* **1975**, *11*, 1300-1302.
(75) Salazar-Alvarez, G.; Olsson, R. T.; Sort, J.; Macedo, W. A. A.; Ardisson, J. D.; Baró, M. D.; Gedde, U. W.; Nogués, J. Enhanced Coercivity in Co-Rich Near-Stoichiometric $Co_xFe_{3-x}O_{4+\delta}$ Nanoparticles Prepared in Large Batches. *Chem. Mater.* **2007**, *19*, 4957-4963.
(76) Henderson, C. M. B.; Charnock, J. M.; Plant, D. A. Cation occupancies in Mg, Co, Ni, Zn, Al ferrite spinels: a multi-element EXAFS study. *J. Phys.: Condens. Matter* **2007**, *19*, 076214.
(77) Krieble, K.; Lo, C. C. H.; Melikhov, Y.; Snyder, J. E. Investigation of Cr substitution in Co ferrite ($CoCr_xFe_{2-x}O_4$]) using Mössbauer spectroscopy. *J. Appl. Phys.* **2006**, *99*, 08M912.
(78) Tahar, L. B.; Artus, M.; Ammar, S.; Smiri, L.; Herbst, F.; Vaulay, M.; Richard, V.; Grenèche, J.; Villain, F.; Fiévet, F. Magnetic properties of $CoFe_{1.9}RE_{0.1}O_4$ nanoparticles (RE=La, Ce, Nd, Sm, Eu, Gd, Tb, Ho) prepared in polyol. *J. Magn. Magn. Mater.* **2008**, *320*, 3242-3250.
(79) Töpfer, J.; Dieckmann, R. Point defects and deviation from stoichiometry in $(Zn_{x-y/4}Mn_{1-x-3y/4}Fe_{2+y})_{1-\delta/3}O_4$. *J. Eur. Ceram. Soc.* **2004**, *24*, 603-612.
(80) Cedeño-Mattei, Y.; Perales-Pérez, O. Synthesis of high-coercivity cobalt ferrite nanocrystals. *Microelectron. J.* **2009**, *40*, 673-676.
(81) *Match! - Phase Identification from Powder Diffraction Software. Entry # 00-03-0800.*
(82) Xu, P.; Han, X.; Zhao, H.; Liang, Z.; Wang, J. Effect of stoichiometry on the phase formation and magnetic properties of $BaFe_{12}O_{19}$ nanoparticles by reverse micelle technique. *Mater. Lett.* **2008**, *62*, 1305-1308.
(83) Papaefthymiou, G. C. Nanoparticle magnetism. *Nano Today* **2009**, *4*, 438-447.
(84) Maaz, K.; Karim, S.; Mashiatullah, A.; Liu, J.; Hou, M.; Sun, Y.; Duan, J.; Yao, H.; Mo, D.; Chen, Y. Structural analysis of nickel doped cobalt ferrite nanoparticles prepared by coprecipitation route. *Phys. B* **2009**, *404*, 3947-3951.
(85) Kousaka, Y.; Nomura, T.; Alonso, M. Simple model of particle formation by homogeneous and heterogeneous nucleation. *Adv. Powder Technol.* **2001**, *12*, 291-309.
(86) Sinha, M.; Pradhan, S. Synthesis of nanocrystalline Cd-Zn ferrite by ball milling and its stability at elevated temperatures. *J. Alloys Compd.* **2010**, *489*, 91-98.
(87) Abdallah, H.; Moyo, T.; Msomi, J. In *International Conference on the Applications of the Mössbauer Effect, ICAME 2009, July 19, 2009 - July 24, 2009*; Journal of Physics: Conference Series; Institute of Physics Publishing: Vienna, Austria, 2010; Vol. 217.
(88) Papelis, C.; Um, W.; Russell, C. E.; Chapman, J. B. Measuring the specific surface area of natural and manmadeglasses: effects of formation process, morphology, and particle size. *Colloids Surf., A* **2003**, *215*, 221-239.

(89) *Match! - Phase Identification from Powder Diffraction Software. Entry # 00-022-1086.*
(90) Cullity, B.; Stock, S. *Elements of X-Ray Diffraction*; 3º ed.; Prentice Hall, 2001.
(91) Fadda, S.; Cincotti, A.; Concas, A.; Pisu, M.; Cao, G. Modelling breakage and reagglomeration during fine dry grinding in ball milling devices. *Powder Technol.* **2009**, *194*, 207-216.
(92) Zhang, D.; Cai, R.; Zhou, Y.; Shao, Z.; Liao, X.; Ma, Z. Effect of milling method and time on the properties and electrochemical performance of $LiFePO_4$/C composites prepared by ball milling and thermal treatment. *Electrochim. Acta* **2010**, *55*, 2653-2661.
(93) Zeng, Q. Influence of milling conditions on magnetic properties of $Nd(Fe,Mo)_{12}N_x$ compounds. *J. Magn. Magn. Mater.* **1999**, *192*, 321-324.
(94) Goh, S. C.; Chia, C. H.; Zakaria, S.; Yusoff, M.; Haw, C. Y.; Ahmadi, S.; Huang, N. M.; Lim, H. N. Hydrothermal preparation of high saturation magnetization and coercivity cobalt ferrite nanocrystals without subsequent calcination. *Mater. Chem. Phys.* **2010**, *120*, 31-35.
(95) Jiang, W.; Wu, Y.; He, B.; Zeng, X.; Lai, K.; Gu, Z. Effect of sodium oleate as a buffer on the synthesis of superparamagnetic magnetite colloids. *J. Colloid Interface Sci.* **2010**, *347*, 1-7.
(96) Zhang, L.; He, R.; Gu, H. Oleic acid coating on the monodisperse magnetite nanoparticles. *Appl. Surf. Sci.* **2006**, *253*, 2611-2617.
(97) Miller, J. S.; Drillon, M. *Magnetism: molecules to materials*; Wiley-VCH, 2003.
(98) Sun, S.; Zeng, H.; Robinson, D. B.; Raoux, S.; Rice, P. M.; Wang, S. X.; Li, G. Monodisperse MFe_2O_4 (M = Fe, Co, Mn) Nanoparticles. *J. Am. Chem. Soc.* **2004**, *126*, 273-279.
(99) Calderón-Ortiz, E. Composition- and size- controlled synthesis of Mn-Zn ferrite nanocrystals for potential magnetocaloric applications. MS Thesis, University of Puerto Rico: Mayagüez Campus, 2008.
(100) von Ranke, P. J.; de Oliveira, N. A.; Alho, B. P.; Plaza, E. J. R.; de Sousa, V. S. R.; Caron, L.; Reis, M. S. Understanding the inverse magnetocaloric effect in antiferro- and ferrimagnetic arrangements. *J. Phys.: Condens. Matter* **2009**, *21*, 056004.
(101) Desautels, R.; Van Lierop, J.; Cadogan, J. In *International Conference on the Applications of the Mössbauer Effect, ICAME 2009, July 19, 2009 - July 24, 2009*; Journal of Physics: Conference Series; Institute of Physics Publishing: Vienna, Austria, 2010; Vol. 217.

APPENDIX A.

Indexing single crystal spot patterns and determination of beam direction (zone axis).

H	K	l	$\|hkl\|^2$	$\|hkl\|$	g_1=111 ratios	g_1=002 ratios
1	1	1	3	1.732	1	
2	0	0	4	2	1.154	1
2	2	0	8	2.828	1.632	1.414
3	1	1	11	3.316	1.914	1.658
2	2	2	12	3.464	2	1.732
4	0	0	16	4	2.309	2
3	3	1	19	4.358	2.516	2.179
4	2	0	20	4.472	2.581	2.236
4	2	2	24	4.898	2.828	2.449

Length measured from diffraction pattern:

g_1= 0.32 in.

g_2 = 0.61 in.

g_2/ g_1 ratio = 1.906

g_1= (111)

Implies that g_2 = {311} from ratios

Determine the angles between the possible combinations of (111) with {311}. They are determined the following way:

$$\begin{bmatrix} 3 & -1 & 1 \end{bmatrix} \begin{bmatrix} (a)^2 & 0 & 0 \\ 0 & (a)^2 & 0 \\ 0 & 0 & (a)^2 \end{bmatrix} \begin{bmatrix} 3 \\ -1 \\ 1 \end{bmatrix}$$

$$[3-11]\begin{bmatrix}(0.8391)^2 & 0 & 0\\ 0 & (0.8391)^2 & 0\\ 0 & 0 & (0.8391)^2\end{bmatrix}\begin{bmatrix}3\\ -1\\ 1\end{bmatrix}$$

$$[3-11]\begin{bmatrix}0.704 & 0 & 0\\ 0 & 0.704 & 0\\ 0 & 0 & 0.704\end{bmatrix}\begin{bmatrix}3\\ -1\\ 1\end{bmatrix}$$

$$[3-11]\begin{bmatrix}2.112\\ -0.704\\ 0.704\end{bmatrix} = 6.336 + 0.704 + 0.704 = \sqrt{7.774} = 2.78\ nm$$

$$[111]\begin{bmatrix}0.704 & 0 & 0\\ 0 & 0.704 & 0\\ 0 & 0 & 0.704\end{bmatrix}\begin{bmatrix}1\\ 1\\ 1\end{bmatrix}$$

$$[111]\begin{bmatrix}0.704\\ 0.704\\ 0.704\end{bmatrix} = 0.704 + 0.704 + 0.704 = \sqrt{2.112} = 1.45\ nm$$

$$[3-11]\begin{bmatrix}0.704 & 0 & 0\\ 0 & 0.704 & 0\\ 0 & 0 & 0.704\end{bmatrix}\begin{bmatrix}1\\ 1\\ 1\end{bmatrix}$$

$$[3-11]\begin{bmatrix}0.704\\ 0.704\\ 0.704\end{bmatrix} = 2.112 - 0.704 + 0.704 = 2.112\ nm$$

$$\theta = \cos^{-1}\left(\frac{2.112}{2.78*1.45}\right) = 58.4°$$

Angle between (111) and (311) = 29° NO

Angle between (111) and (-311) = 122° NO

Angle between (111) and (3-11) = 58° YES

Determination of the beam direction:

(111) x (3-11)

$$\begin{bmatrix} 1 & 1 & 1 \\ 3 & -1 & 1 \end{bmatrix} = (1-1 \quad 1+3 \quad -1+3) = (0\ 4-2) = [0\ 2\ -1]$$

[0 2 -1] beam direction or zone axis